ISSN 2525-2461

Vietnam Journal of Science, Technology and Engineering

MARCH 2020 • VOL.62 NUMBER 1

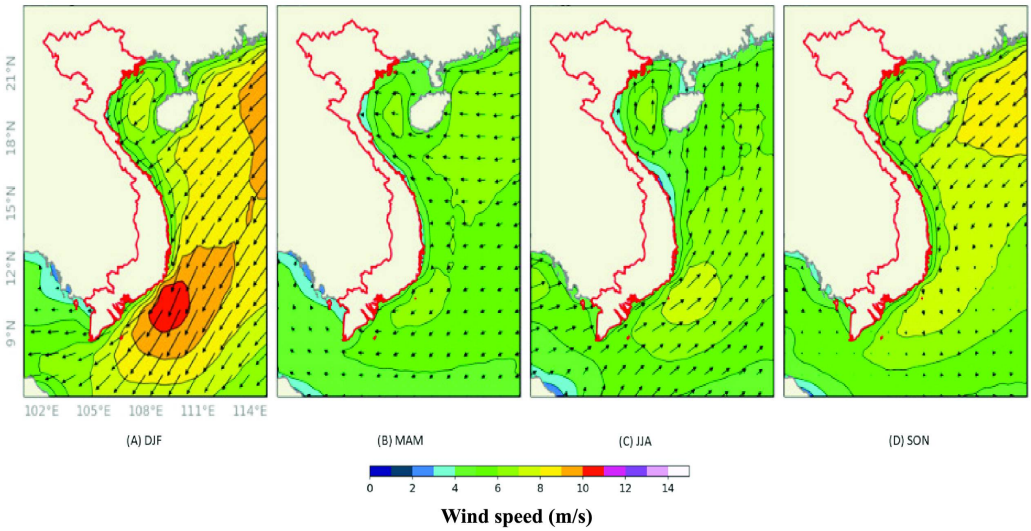

Evaluation of resource spatial-temporal variation, dataset validity, infrastructures and zones for Vietnam offshore wind energy

Characteristics and antifungal activity of CuO-ZnO nanocomposites synthesised by the sol-gel technique

VIETNAM JOURNAL OF SCIENCE, TECHNOLOGY AND ENGINEERING * MARCH 2020 * VOL.62 NUMBER 1
vietnamscience.vn

Vietnam Journal of Science, Technology and Engineering (VJSTE) **is a quarterly double-blind peer-reviewed academic journal. VJSTE publishes research articles and review articles in all areas of science, technology and engineering with the focus on the life sciences and environmental sciences including the following topics:**

- **Agriculture**
- **Medicine**
- **Pharmacology**
- **Biology**
- **Biotechnology**
- **Ecology**
- **Climatology.**

CLASSIFICATION SCHEME

1. **Mathematics and Computer Science**
   - 1.1. Mathematics
   - 1.2. Computer Science
   - 1.3. Computational Science
2. **Physical Sciences**
   - 2.1. Physics
   - 2.2. Chemistry
   - 2.3. Engineering
3. **Life Sciences**
   - 3.1. Agriculture
   - 3.2. Medicine
   - 3.3. Pharmacology
   - 3.4. Biology
   - 3.5. Biotechnology
4. **Geosciences**
   - 4.1. Geography
   - 4.2. Geology
   - 4.3. Geophysics
   - 4.4. Oceanography
5. **Environmental Sciences**
   - 5.1. Ecology
   - 5.2. Climatology

CONTENTS

MARCH 2020 • VOL.62 NUMBER 1

8

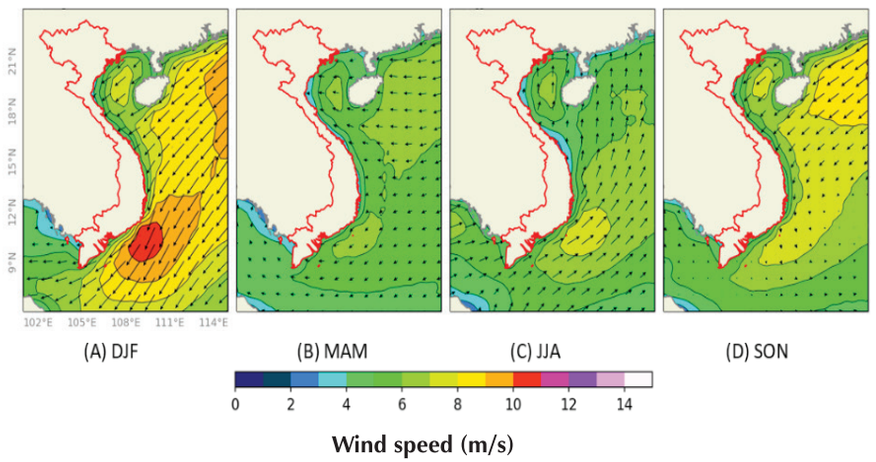

CONTENTS

MARCH 2020 • VOL.62 NUMBER 1

LIFE SCIENCES

ENVIRONMENTAL SCIENCES

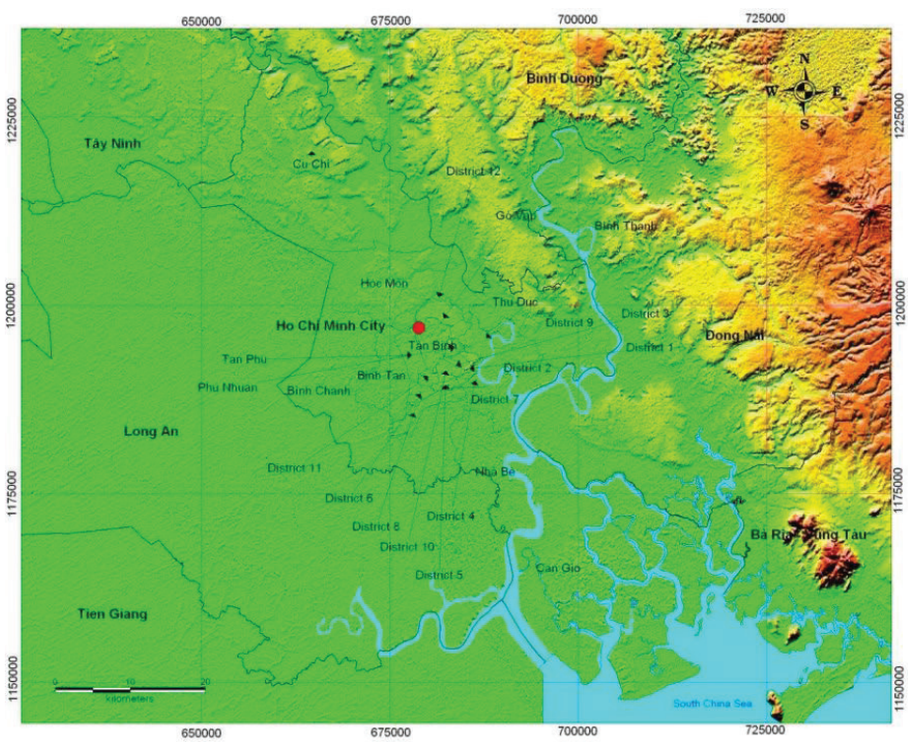

Evaluation of resource spatial-temporal variation, dataset validity, infrastructures and zones for Vietnam offshore wind energy

Vu Dinh Quang[1, 2], Van Quang Doan[3], Van Nguyen Dinh[4], Nguyen Dinh Duc[1, 2*]

[1]*Vietnam Japan University, Vietnam National University, Hanoi, Vietnam*
[2]*University of Engineering and Technology, Vietnam National University, Hanoi, Vietnam*
[3]*Center for Computational Sciences, University of Tsukuba, Japan*
[4]*MaREI Centre for Marine and Renewable Energy, ERI, University College Cork, Ireland*

Received 15 November 2019; accepted 20 January 2020

Abstract:

The shortage of reliable datasets and resource assessments, resource variations, and lack of marine planning are the technical challenges facing offshore wind energy development in Vietnam. This pioneering paper comprehensively addresses these challenges by first screening available datasets to select cross-calibrated multi-platform (CCMP) data and validating them with measurements. The resource is divided into four zones of 100 NM-width from the coastline. The wind energy density (WED) and capacity factor (CF) are calculated using an 8 MW reference turbine. The assessment of the zoned resource and infrastructures is based on the location of synchronous power sources and ports, along with the variation of WED and CF. Zone 3, comprising of the Binh Thuan and Ninh Thuan seas, the southern part of Zone 2 (Phu Yen and Khanh Hoa), and the northern part of Zone 4 (Ba Ria and Vung Tau) are found to have the highest wind energy potential, where the annual accumulated WED is 80 GWh/km^2. The five year CF and average wind speed in Phu Quy island were 54.5% and 11 m/s, respectively. These zones, with moderate resource variation and excellent ports are the most suitable for offshore wind energy development. Zones 1 and 4 are recommended for far-offshore wind farms. This work is useful to various environmental groups and is a crucial input to marine and power planning.

Keywords: **CCMP data, marine and power planning, offshore wind energy, ports, spatial and temporal variation, Vietnam sea.**

Classification numbers: **1.3, 2.3**

Introduction

Countries around the world are facing the problems of environmental pollution and energy security and renewable energy emerges as an optimal method to solve those problems [1]. The use of wind energy has had positive impacts on society and the environment, including the reduction of greenhouse gas emissions, job opportunities, and the promotion of sustainable development [2]. Offshore wind power productivity can be 1.5 times that of onshore plants because offshore wind speeds are greater and more stable [3]. In addition to providing electricity to the grid, offshore wind power plants can help improve the quality of life in island areas far from the shore [4] and potentially supply power to gas for renewable fuels [2].

Resulting from rapid economic development, the energy demands made by the industrial, transportation, commercial, and residential sectors of Vietnam have significantly increased and most of the country's electricity is generated by hydropower and fossil fuel power until now [5]. However, recently there has been an exhaustion of sites for hydropower plants and a revelation of negative impacts caused by hydropower to the local environment and ecology [6]. From the latest national Power Development Plan (PDP) in Vietnam [7, 8], so-called the "*Adjusted PDP VII*" that projects into 2030, coal-fired power is expected to grow strongly from a share of 33% (12.9 GW) in 2015 to 43% (55.1 GW) in 2030, which is abnormally high. The share of renewable energy (excluding large hydropower plants) installed capacity will be 9.9% in 2020 (1% from wind) and 21% (5% from wind) in 2030, which is very low in comparison with the country's potential.

The exploitation of renewable energy sources seems to be the only way to reduce the large share of coal-fired power in Vietnam. The country is likely to have a huge opportunity for developing offshore wind energy [9] because of its more than 3,000 km of coastline and 1 million km^2 sea area. Vietnam offshore wind is seated in the top ten of global potential markets,

*Corresponding author: Email: ducnd@vnu.edu.vn

as reported by the Global Wind Energy Council [10]. However, besides political impetus [11], there are a number of major domestic technical obstacles to offshore wind policymakers and developers in Vietnam. The first two obstacles are (i) the shortage of reliable offshore wind, metocean, and seabed data sets and (ii) the severe lack of a comprehensive assessment of offshore wind resources and infrastructures.

Doan, et al. [12] made the first attempt to simulate the offshore wind over an area limited to southern Vietnam using a numerical simulation model, however, it was without validation of the simulated wind data. A second and more complete attempt was made with the recent use of numerical simulations validated by two sets of wind data obtained from (i) six ground-based weather stations on islands off the coast of Vietnam and (ii) QuikSCAT (Quick Scatterometer), an Earth observation satellite with a coarse spatial resolution of 25 km [13]. The absence of up-to-date marine planning, where the offshore wind development zones and foreshore grid connections have never been studied and designated, is the third major obstacle to offshore wind policymakers and developers in Vietnam. In a first initiative, maps of potential offshore wind zones in Vietnam with 30 m and 60 m water-depth contours were proposed [14].

There are many studies that assess wind energy potential around the world by using data obtained from satellites and wind observation stations [15]. Such datasets were used in Kirklareli, Turkey [16], in Turkey [17], and in Tehran, Iran with data from a period between 1995 and 2005 [18]. Measured data were utilised to assess the wind energy potential in Malaysia from ten meteorological stations over ten years [19], in Egypt [20, 21], and in Oman based on a five-year hourly wind dataset obtained from weather stations [22]. Statistical methods were used in Morocco [23, 24] and in Jordan [25] via Weibull distributions. Not only wind characteristics, but also wind power generation, was investigated in Jordan [25], Nigeria [26], and Ireland [27]. Offshore wind resources have been accessed by many countries. Wind speed and rose, energy rose and density, and air density of a south-western sea area in South Korea were analysed from meteorological mast data [28]. The potential application of the hyper-temporal satellite Advanced Scatterometer data for offshore wind farm site selection in Irish waters was investigated and the data was validated by *in situ* measurements from five weather buoys [29]. Thus, the use of data from satellite observations and from measurements to assess wind energy potential is widely accepted. In this work, cross-calibrated multi-platform [30] data are used after validation with measurement data.

The great challenge behind wind energy is its high dependence on wind speed that fluctuates greatly at all time scales, that is, minutes, hours, days, months, seasons, and years [31]. Understanding the temporal variations of the wind is of key importance to the integration and optimal utilization of wind in a power system [32]. Wind power assessment, therefore, plays a key role in dealing with the stochastic and intermittent nature of wind and the challenges involved with the planning and balancing of supply and demand in any electricity system [32, 33]. Such spatiality in power sources and transmission is apparent in Vietnam, where renewable generation capacities are mostly installed in the south and the major demand centres are in the southern and northern regions [34].

A large geographic spread of installed capacity can reduce wind power variability and smooth its production. It is essential to understand the wind power spatiality in order to address power system constraints in systems with large and growing wind power penetrations [35]. The spatial and temporal correlation of wind power across ten European Union countries was examined from three years of hourly wind power generation data [35]. A spatial analysis of offshore wind resources in Africa revealed that more than 90% of the resources are concentrated in coastal zones associated with three African power pools and suggested that a joint and integrated development within these power pools could offer a promising approach to utilising offshore wind energy in Africa [36].

The major challenges to government and national marine authorities are how to manage the planning, consent, installation, and operation of offshore wind projects and how to integrate those activities effectively into other activities and strategies such as natural/cultural heritage site designations, military/aviation, shipping, fishing, and ports or harbour restrictions [2]. In this context, marine spatial planning (MSP) is a new way of looking at how the marine area is used and preparation of how best to use it in the future [37]. The increasing number of uses and users of the ocean leads to more conflicts, whereas zoning the ocean in space and time has been shown to reduce these conflicts [38]. Additionally, planned use of the marine environment can minimise losses and maximise gains for conflicting sectors [39]. Such lessons can be learned from the Great Barrier Reef Marine Park (GBRMP) [40] and the ongoing MSP development in Europe.

In an objective summary, this paper aims at addressing the number of technical challenges to the development of offshore wind in Vietnam. The CCMP data validated with measurement data from seven meteorological stations were the input to contend with the shortage of reliable wind data. The severe lack of resource assessment is initially addressed by evaluating the temporal and spatial variation of offshore wind speed and directions over seasonal, annual, and inter-annual periods. Based on the approach of time and space zoning [38], the lessons learned, expert consultations, temporal variation of temperature, and the offshore wind resource, the ocean area 100 NM off the coastline of Vietnam is classified into four zones. Prior to evaluating the offshore wind resource and infrastructures in this work, a set of criteria and data including temporal variation in temperature, synchronous power sources and transmission, seaport facility, offshore wind power, and density and capacity factors are discussed. Such validated wind data, infrastructure data, and the evaluation of resource potential, density, temporal, and spatial variations will be input for further work by

policymakers, energy and marine planners, industry developers, and researchers. Such initial zoning and zone evaluation will be crucial, in combination with other sectors, to the development of MSP and power plan in the country.

Methodology

The methodology of this paper is depicted in Fig. 1. The first step, after selecting a dataset, is to validate the dataset by comparing their surface wind speed probability distribution with that of the measurement data from seven meteorological stations. If the comparison shows that the dataset is usable, the next step is to extrapolate the wind speed at different heights and evaluate the temporal and spatial variations of wind speed and direction. Using that evaluation and zoning criteria, the potential offshore wind area is divided into four zones for marine and energy planning and management. The last two steps are to calculate the wind energy potential, capacity factor, power distributions, and to evaluate their temporal and spatial variations for each zone. Prior to these steps, information on how wind power would be converted is required, which can be input by power curves of the reference wind turbines. In this study, a LEANWIND 8 MW turbine [41] is selected as the reference.

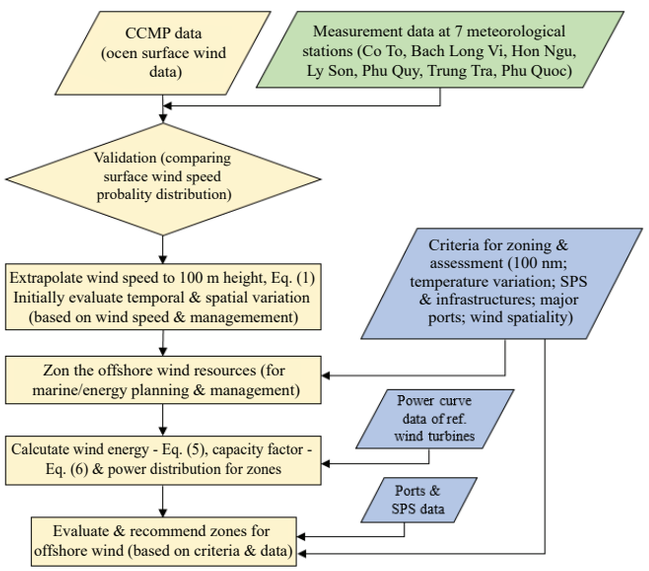

Fig. 1. Methodology flowchart of the study. SPS: synchronous power source.

Dataset selection and validation

The surface wind dataset is used in research obtained from the CCMP project published by the U.S. National Aeronautics and Space Administration (NASA) [30, 42]. This project aimed to obtain multi-instrument ocean surface wind velocity, which is used to analysis meteorology and oceanography. This dataset is built from combining cross-calibrated satellite winds from remote sensing systems by using variational analysis (VA) [42]. This method creates a gridded surface wind analysis with high spatial resolution (0.25 degrees) that can minimize the deviation of data. The cross-calibrated satellite wind data from the CCMP dataset contains data from a number of microwave satellite instruments. These microwave radiometers, such as the special sensor microwave imager sounder (SSMIS) and WindSat [43], were used to gather information about wind speed. Microwave scatterometers, such as QuikScat and SeaWinds, were also applied to obtain wind speed and directions by the development of a geophysical model function. Wind velocity is observed and analysed at 10 meters above sea level. The spatial resolution of the dataset was 0.25 degrees in latitude and 0.25 degrees in longitude. Especially important, the dataset has a high temporal resolution of 6 h and a timespan of 25 years, from 02 July 1987 to 31 December 2011, as listed in Table 1. Because the entire CCMP data over the course of 25 years is very large, this study used wind data from the last five years of the dataset (from 2007 to 2011). The CCMP dataset was then validated by comparison with the observed data from several meteorological stations located in Vietnam. The temporal resolution of measured data for comparison with CCMP is 6 hours; similar to that of the CCMP data. The measurement stations are also placed at a height of 10 m above sea level. Thus, the two datasets have a similar temporal resolution and height. In this study, the surface wind speed probability distribution between the CCMP data and the measurement data from seven meteorological stations along the coast and on several islands for five years (from 2007 to 2011) is compared.

Table 1. Information of the CCMP dataset [30].

Region	Global
Northernmost latitude (degree)	78
Southernmost latitude (degree)	-78
Westernmost longitude (degree)	0
Easternmost longitude (degree)	360
Time span	1987-Jul-02 to 2011-Dec-31
Spatial resolution (Latitude × Longitude)	0.25°× 0.25°
Temporal resolution (hour)	6

Estimation of wind energy potential

In order to assess the relevant wind energy potential to the wind turbines, the wind speed at various heights is required. The CCMP dataset used in this research contains wind speed at 10 meters in height above sea level. The wind power law, commonly used for extrapolating wind speed from the sea surface to specific heights [24, 44, 45], is adopted as follows:

$$v_2 = v_1 \left(\frac{z_2}{z_1}\right)^{\alpha} \quad (1)$$

where the parameter α is the power law exponent, v_1 is wind speed at height z_1, and v_2 is wind speed at hub height z_2. According to Davenport [46] and Hsu [47], the magnitude of the power law exponent was found to be approximately 0.1 under natural conditions of the sea. It is noted that this theoretical extrapolation approach is for a preliminary

assessment, particularly at a larger scale and spatial variation. Future research to obtain measurements and higher resolution data for wind profiles at turbine hub height are recommended before planning the offshore wind development zones and marine spaces.

Wind turbines convert the kinetic energy of wind into electrical energy. By operation classification, there are two basic types of wind turbines: vertical axis and horizontal axis, where the horizontal axis wind turbines are more popular than the vertical axis ones. The power output of a horizontal axis wind turbine is calculated by using following equation [48, 49]:

$$P(v) = \begin{cases} 0, & v < v_i \\ P_f(v), & v_i \le v < v_r \\ P_r, & v_r \le v < v_o \\ 0, & v_o \le v \end{cases} \quad (2)$$

where the parameters P_r, v_i, v_r, and v_o are the rated power, cut-in wind speed, rated wind speed and cut-out wind speed of the reference wind turbine, respectively, and $p_f(v)$ is the nonlinear relationship between wind speed and electric power:

$$P_f(v) = \frac{1}{2} \times \rho \times A \times C_p \times v^3 \quad (3)$$

In Eq. (3), A is rotor swept area of the reference wind turbine, ρ is the air density and C_p is the overall efficiency coefficient, valued between 0.3 and 0.5, which varies with both wind speed and rotational speed of the turbine.

The energy conversion output of a wind turbine over a time period can be determined from:

$$\mathrm{E_{out}} = \sum_{t=1}^{N} \mathrm{P(v)} \times \mathrm{T_t} \quad (4)$$

where T_t is the temporal resolution (h) and N is the number of spans in the time period.

Energy production from the wind farm over the time period is calculated as follows:

$$E_{\mathrm{windfarm}} = \sum_{i=1}^{N_t} E_{\mathrm{out}} \quad (5)$$

where N_t is the number of wind turbines in the wind farm.

The capacity factor represents the ratio between the actual electrical energy output and the maximum possible electrical energy during the time period and depends on both wind turbines and site characteristics. The annual CF is defined as follows:

$$CF = \frac{E_{out}}{E_r} \times 100\% \quad (6)$$

where the annual maximum possible electrical energy is defined as follows:

$$E_r = P_r \times (24h/day) \times (365days) \quad (7)$$

Zoning and assessment criteria of offshore wind resource zones

Based on the beneficial approach of time and space zoning discussed in [38], the lessons learned from the GBRMP [40], and from the ongoing MSP development in Europe and other countries [38], the following set of criteria is proposed to initially zone the offshore wind resources in Vietnam and to assess the zones:

(a) *Sea area of 100 nautical miles (185.2 km) from the coastline:* this distance is adopted as it is the maximum distance that offshore wind farm can be deployed in the near future at economical costs.

(b) *Temporal variation in temperature over the year:* this affects the characteristics of coastal and marine biology and human activities at sea, including fishing and tourism.

(c) *Synchronous power sources and main electricity transmission lines:* synchronous power sources are hydropower, gas, and oil-fired power plants. Main electricity transmission lines include 500 and 220 kV lines. These power infrastructures are essential to the spatial distribution and intermittency of renewable energy sources in criterion (e) and the delay in expansion/upgrading the electricity grid required [34].

(d) *Existing or potential major seaports and container terminals:* these are the key elements of the supply chain required for the assembly, transportation, and installation of offshore wind turbines components including the blades, towers, substructure, and foundations [2]. In order to accommodate installation vessels, offshore developers require a port draft of up to 10 m, quayside of up to 300 m, and water way of up to 200 m [50]. The transportation of monopiles using heavy lift cargo vessels and their installation by jack-up vessels require drafts of about 9.5 m and 5.8 m to Chart Datum of water, respectively [51]. The overall lengths for heavy lift cargo vessels approach 170 m [51].

(e) *Temporal and spatial variation of wind resources:* parameters characterising the quality of wind resources directly obtained from wind data are wind speed and wind direction. Temporal variation means the change of wind speed over months, seasons, and years. Both wind speed and its temporal variation govern the energy output of a wind turbine as in Eq. (4), and consequently control the capacity factor, as defined in Eq. (6). Both wind speed and its spatial and temporal variation influence the energy production of wind farms as shown in Eq. (5), and the energy storage and the integration of the wind farms into the grid. At larger scales, spatial and temporal variation affect the stability and operation of the national/regional power system [32, 35].

The theoretical potential of wind energy is however limited by a number of constraints including ecology, supply chains, other sectors, and political and natural reasons. In identifying the unsuitable areas for onshore wind in Vietnam, exclusion criteria

including high altitude, political areas (cities, urban centres, road, railway, airport, etc.), water areas, protected areas, and living areas, were used [11]. When studying offshore wind potential, a number of exclusion criteria for onshore wind are not applicable or need to be updated, and new criteria should be defined for finer zoning and practical assessment in future studies.

Results and discussion

Data validation

The CCMP dataset was compared with the observed data from seven meteorological stations. The locations of the seven meteorological stations are shown in Table 2 and Fig. 2. Fig. 3 shows the wind speed probability distribution of both the CCMP data and measurement data. The shape of the probability distribution of the CCMP data is very close to the measured data. Notably, the shape of the distributions of the two data sources are almost identical at the Co To, Hon Ngu, and Ly Son stations. From Fig. 3, it can also be seen that the area around Phu Quy island has the largest wind speed. Phu Quy is a part of the Ninh Thuan province. In the North Sea, Bach Long Vi island also has strong wind in that area.

Table 2. Location of meteorological stations of Vietnam.

No.	Station	Latitude	Longitude
1	Co To	20.98	107.77
2	Bach Long Vi	20.13	107.72
3	Hon Ngu	18.8	105.77
4	Ly Son	15.38	109.15
5	Phu Quy	10.52	108.93
6	Truong Sa	8.65	111.92
7	Phu Quoc	10.22	103.97

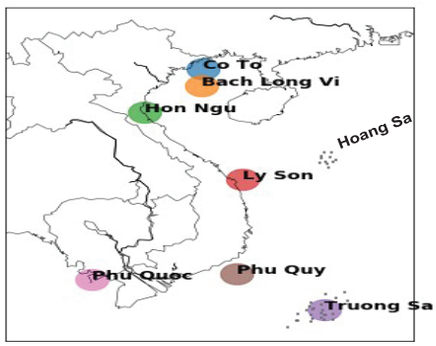

Fig. 2. Location of meteorological stations on the map.

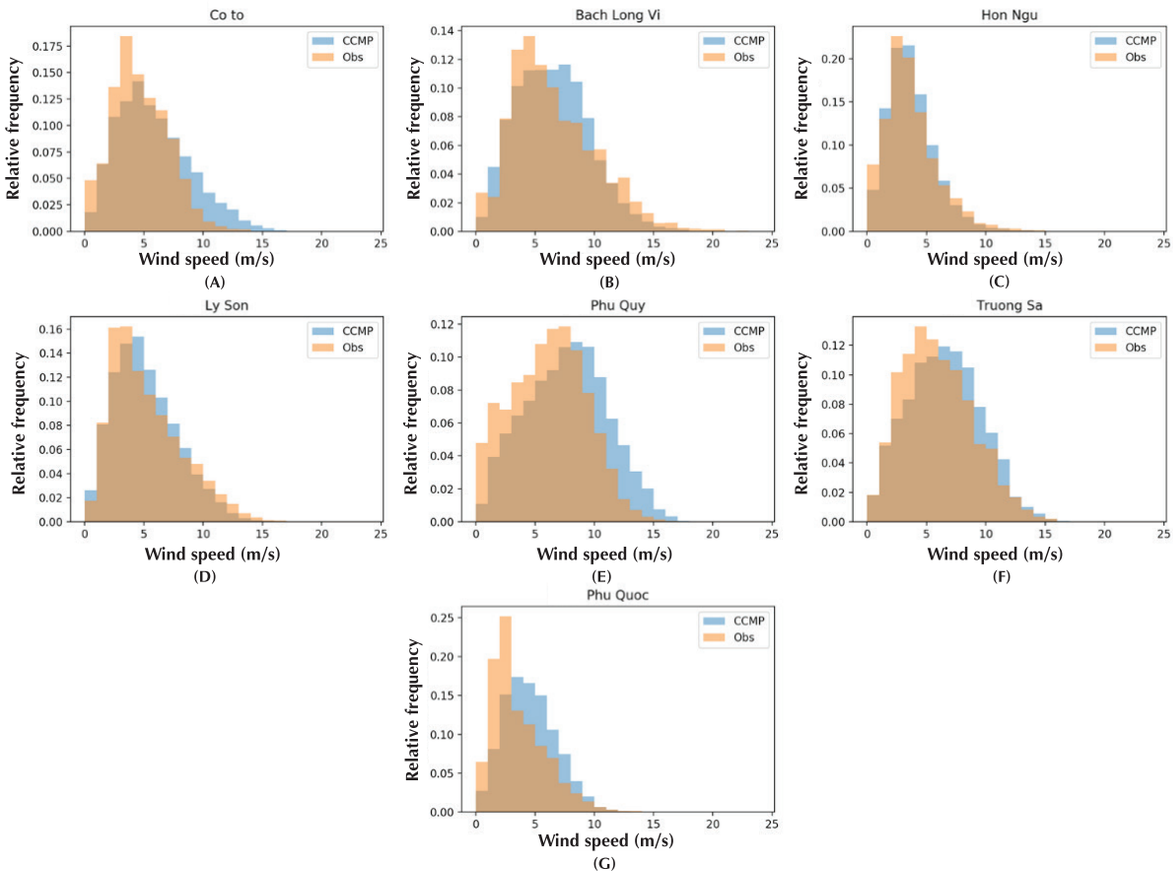

Fig. 3. Surface wind speed probability distribution of the CCMP data and observed data from the seven meteorological stations over the five-year period 2007-2011.

Evaluation of spatial and temporal variation of offshore wind resources

The seasonal variation of wind speed and direction over the period 2007 to 2011 can be evaluated from Fig. 4, where the study considers four seasons: winter being December - January - February (DJF), spring including March - April - May (MAM), summer including June - July - August (JJA), and autumn including September - October - November (SON). In the winter months, the north-eastern monsoon is stronger than the winds during the other seasons in Vietnam. The south-western monsoon is quite strong in the summer months June - July - August (JJA).

Figure 5 shows the wind speed at a turbine hub elevation of 100 m averaged from 2007 to 2011, however this data was not verified due to the shortage of measured data. In the offshore areas around Phu Quy island, the wind speed is largest with an average of about 11 m/s. It is approximately 9 m/s at Tonkin Gulf in the northern sea. The inter-annual wind speed of the four islands: Bach Long Vi, Ly Son, Phu Quy, and Phu Quoc, from 2007 to 2011, are shown in Fig. 6, which is obtained by plotting the monthly averaged wind speed over five years. The largest wind speed is about 12 m/s in Phu Quy island in January. The lowest wind speed range is from 2.765 to 7.347 m/s during this period in Phu Quoc. The mean wind speed ranges from 3.578 to 9.682 m/s and from 2.91 to 9.275 m/s in Bach Long Vi and Ly Son, respectively.

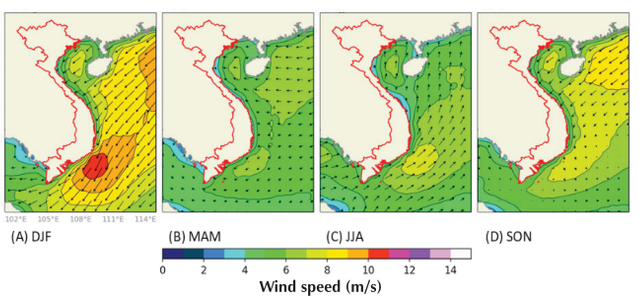

Fig. 4. Seasonal average surface wind speed within five years from 2007 to 2011.

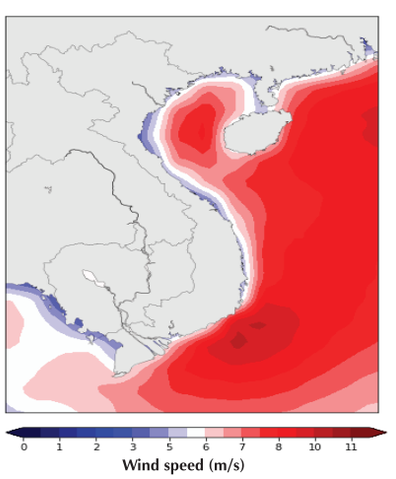

Fig. 5. Wind speed average at 100 m above sea level from 2007 to 2011.

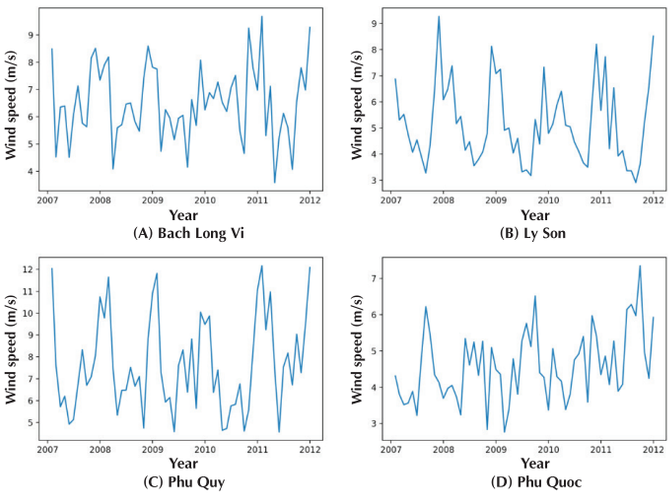

Fig. 6. Inter-annual wind speed at the four islands over the period 2007-2011.

Zoning and assessment of zone infrastructures for offshore wind energy

Based on the consultation with marine and island management experts along with the criteria discussed in the above section, the offshore wind resource in Vietnam was first classified into four zones with their boundaries shown in Fig. 7. Zone 1 is the region with the coldest winter of the four zones and consists of eight provincial sea areas extending from Quang Ninh province to Ha Tinh province. Zone 2, where the winter is moderately cold, has a sea area comprising of seven coastal provinces starting from Quang Binh to Binh Dinh. Zone 3 is less affected by the winter monsoon and is made up of five provincial seas from Phu Yen to Ba Ria - Vung Tau. Zone 4 is the sea region from Ho Chi Minh city to the Kien Giang province, is the least affected by the winter, and has the highest average temperature over the year.

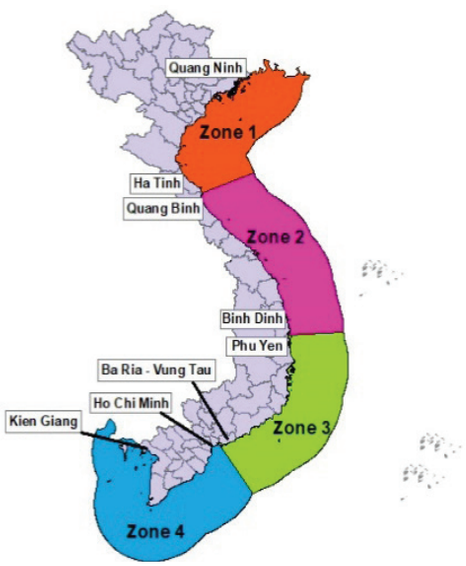

Fig. 7. Proposed four zones of Vietnam's offshore wind resources.

Second, the offshore wind resource zones classified above were assessed by using criteria (c) - (e) listed above. Fig. 8 reveals the existing synchronous power sources and major transmission lines in Vietnam [52] as required by criterion (c). The region in the north of the country is a large area containing diverse sources of electricity. The provinces along the northern border import some of their electricity from China. Additionally, there are major coal-fired power plants in the north eastern provinces. The major hydropower plants are located the north western provinces: Son La, Tuyen Quang, and Hoa Binh.

The continental shape of the northern central region is long and narrow. The electricity supply in this area comes from two main sources, hydropower and imported electricity from Lao, and is carried by 500 kV lines along this area. The source of electricity for the mainland along southern central region is mainly supplied by hydropower plants. In order to enhance the transmission of electricity to this area, 220 kV and 500 kV lines have been installed. Gas/oil-fired power plants are the main supply of electricity in the southern region where some of the electricity is exported to Cambodia. The spatiality of the power sources and transmission systems are displayed in Fig. 8 as required by criterion (c) as previously discussed [34]. It is worth noting that the country's major demand centres are the southern and northern regions [34].

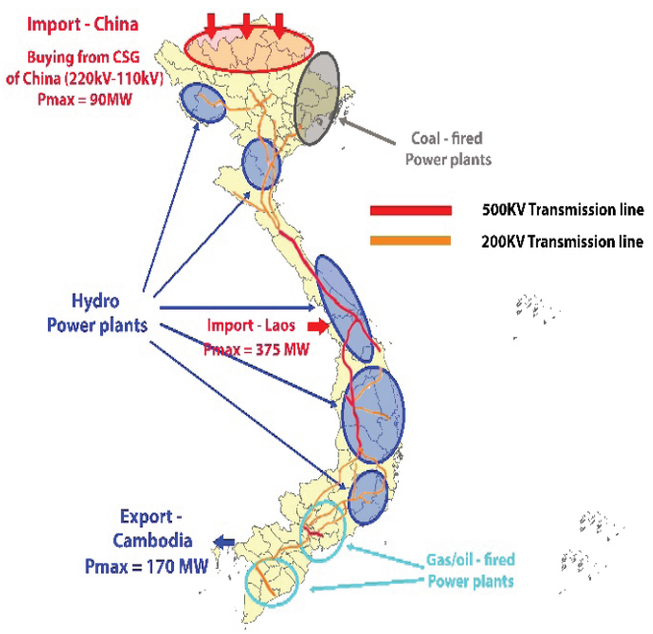

Fig. 8. Major synchronous power sources and power transmission lines in Vietnam [52].

The major seaports and container terminals are mapped in Fig. 9 and listed in Table 3 as required by criterion (d). Major ports with channel depths greater than 10 m and maximum acceptable vessel size of 30,000 dead weight tonnage (DWT) can be found in Zone 1, the southern part of Zone 2, Zone 3, and Zone 4. The following three container ports in Vietnam: Hai Phong and Dinh Vu in Zone 1 and Tan Cang Sai Gon in Zone 4, are among the top 20 container of Southeast Asia [53]. Especially, the Van Phong International Transhipment Terminal under development in Van Phong Bay, Khanh Hoa province of Zone 3, which has a depth range of 15-20 m, a large area, and anticipates a maximum vessel size of 9,000 TEUs (twenty-foot equivalent units) or approximately 120,000 DWT. Considering the important characteristics of a seaport, including draft/ channel depth, size of vessels accepted, and the available area, the port facilities in Zone 3 are the most favourable for offshore wind farm development. Those in Zone 1 and 4 are also of good capacity.

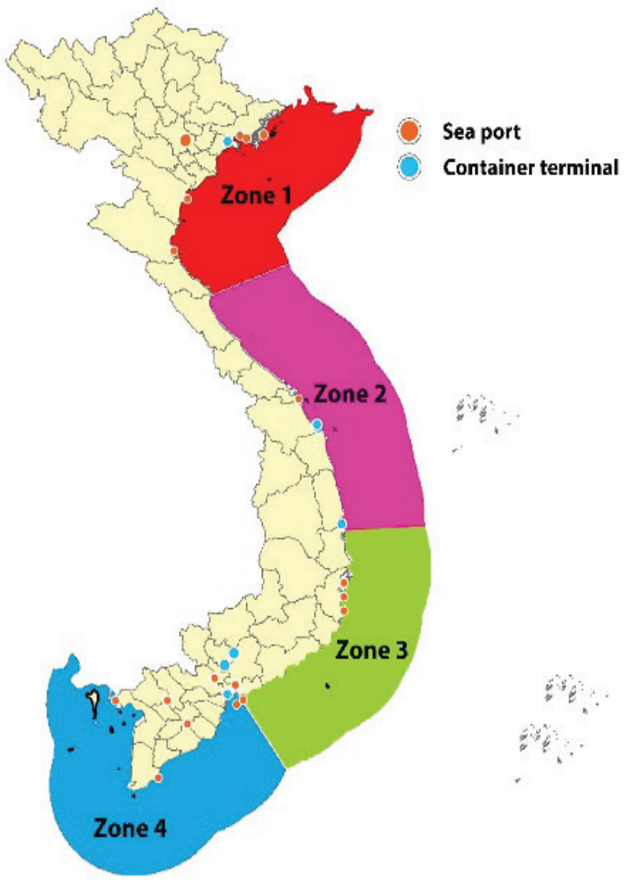

Fig. 9. Location of major ports, container terminals, and in-land river ports accessible to large vessels (data source: [54, 55]).

Table 3. Characteristics of major ports in Vietnam.

No.	Berth Length	Berth draft zero tide	Channel draft zero tide	Vessel accepted	Area
	(m)	(m)	(m)	(DWT)	(ha)
Zone 1					
1	3×680	13.0	13 - 20	50,000	15 [55]
	Quang Ninh [55]				
2	3×594	13.0	10.0	50,000	18.1
	Cai Lan International [55]				
3	5×848	8.5	5.5	40,000	29 [55]
	Hai Phong - Chua Ve [55]				
4	2×427	8.9	7.3	40,000	24 [55]
	Dinh Vu - Hai Phong [55]				
5	5×956	9.1	9.4		51
	Hai Phong - Tan Vu [55]				
Zone 2					
1		8.5	8.5	20,000	11.0
	Nghi Son, Thanh Hoa [55]				
2		12.0	11.0	30,000	8.2
	Chan May, Hue [55]				
3		12.0	10 -17	45,000	30
	Da Nang [55]				
4		12.0	10.5	30,000	36
	Quy Nhon, Binh Dinh [55]				
Zone 3					
1		11.8	11.1	20,000	8.0
	Nha Trang, Khanh Hoa [55]				
2		9.7	10.2	30,000	89
	Cam Ranh, Khanh Hoa [55]				
3	12,000 (total)	15~20		120,000 [56]	740
	Van Phong [57] (Potential)				
4		14	9.3	60,000	13.0
	Phu My, Baria - Vung Tau [55]				
Zone 4					
1	5×706	11.5	8.5	30,000	38 [55]
	Tan Cang [57]				
2	2,667 (total)	10.5	8.5	50,000 [55]	30.0
	Sai Gon [57]				
3	816 (total)	11.0	8.5	36,000 [55]	28.0
	Ben Nghe [57]				

Evaluation of wind energy potential and variation for each zone

In order to evaluate the wind energy potential and its variation, information regarding how the varying wind speed would be converted by the wind turbines to wind power is necessary. Such information is often revealed from the power curves of wind turbines. Given that offshore wind could enable the deployment of larger turbines and that three-bladed horizontal axis wind turbines (HAWTs) are mature and commercial, two large HAWTs with a power rating of 8 MW and with publicly available power curves, Vestas V164-8.0 [58, 59] and LEANWIND (LW) [41], are considered in this study. The parameters of the two turbines are listed in Table 4. The Vestas V164-8.0 is in use by several offshore wind farms such as Burbo Bank Offshore, the United Kingdom, and Norther N.V., Belgium [60]. However, it would be more difficult to design a support structure for the Vestas V164 [41]. Additionally, the rated wind speed of the Vestas V164-8.0 is 13.0 m/s and higher than that of the LW turbines (12.5 m/s) as shown in Table 4. The LW turbine is therefore cost-saving, able to meet the short to medium-term requirements of the offshore wind industry [41], and more suitable for the wind conditions in Vietnam. Accordingly, the LW 8 MW is chosen for the estimation of wind energy potential in this paper. Fig. 10 presents the power curve of the LW turbine used to estimate the energy production from wind speed. The reasonable distance of wind turbines chosen to minimise the wake effects in the prevailing wind direction is $10D_r$, and in the crosswind direction is $4D_r$ [61]. However, the wake effects due to adjacent turbines in the wind farms are not considered in this study [61].

Table 4. Information of Vestas V164-8.0 and LW 8 MW reference turbines.

Parameter	Vestas V164-8.0 [58]	LEANWIND 8 MW [41]
Rating power, P_r (kW)	8000	8000
Cut-in wind speed, v_i (m/s)	4	4
Rated wind speed, v_r (m/s)	13.0	12.5
Cut-out wind speed, v_o (m/s)	25	25
Rotor diameter, D_r (m)	164	164
Rotor speed range (rpm)	4.8-12.1 [59]	6.3-10.5
Rotor swept area, A_r (m^2)	21,124	21,113.36
Hub height, H_{hub} (m)	105	110

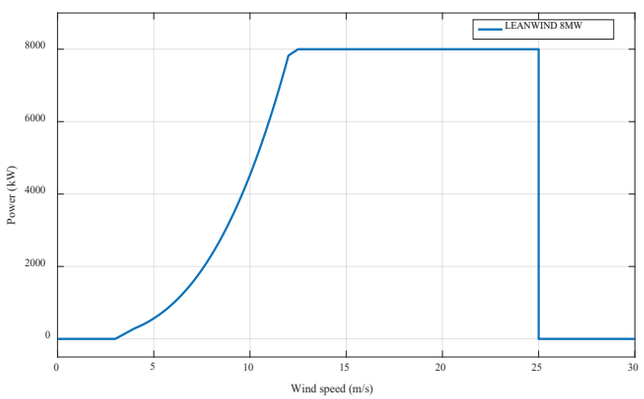

Fig. 10. Power curve of LEANWIND 8 MW turbine. Plotted from data in [41].

The seasonal accumulated wind energy density of the four zones from 2007 to 2011 is illustrated in Fig. 11, where the highest density of energy among the four zones is seen to occur during the winter months. Meanwhile, the second largest wind energy density occurs during autumn. On the other hand, the lowest power density occurs during the spring and the summer. It is apparent from Fig. 11 that Zone 3 contains the highest wind energy potential during the four seasons in Vietnam.

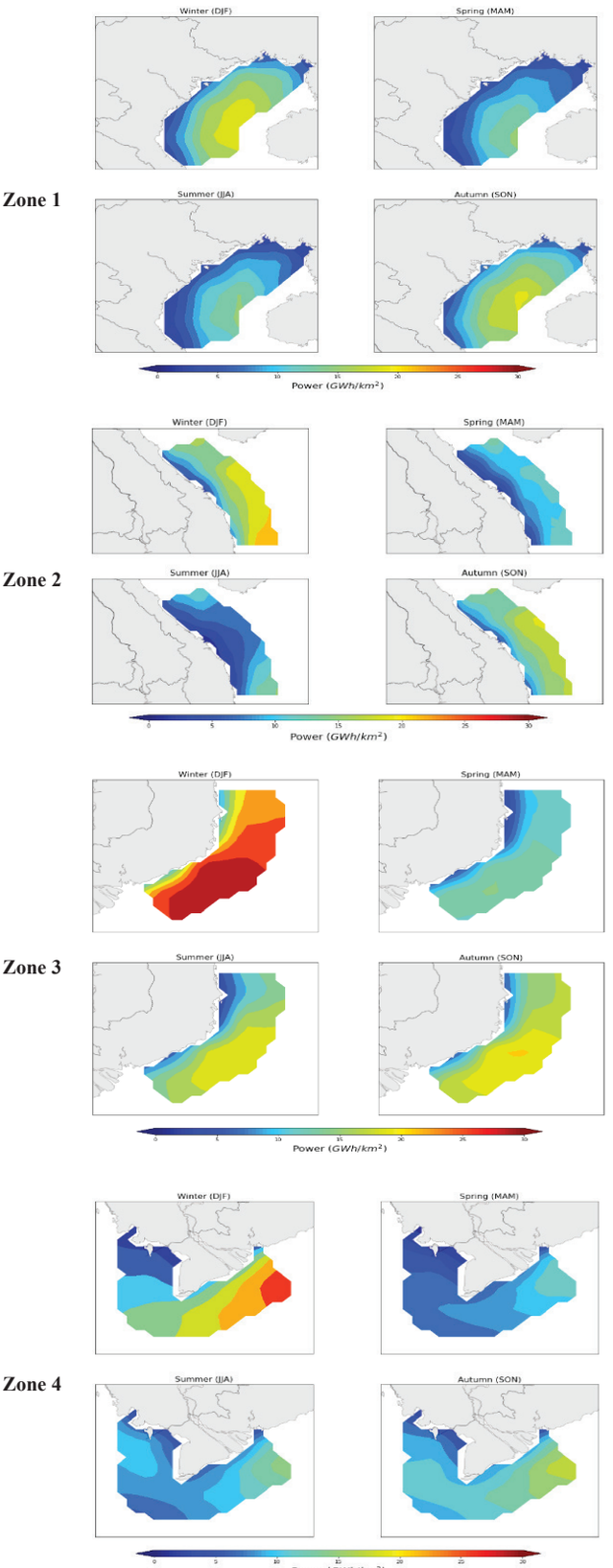

Fig. 11. Seasonal accumulated wind energy in four offshore zones in Vietnam.

Table 5 summarises the maximum seasonal accumulated wind power in the four zones. The highest value is that of Zone 3, during winter, with a value of 28.95 GWh/km^2. The season with the least wind energy potential occurred during spring and had the smallest value of 11.87 GWh/km^2 in Zone 4. Fig. 12 compares the annual accumulated wind density of the four zones between 2007 and 2011. It can be clearly seen that the annual accumulated wind energy density is about 80 GWh/km^2 at Zone 3, which is larger than in the other areas. The areas in Zone 2 and Zone 4 had wind energy densities similar to Zone 3. In Zone 1, the area around the latitude and longitude of 19.8 and 108, respectively, had the largest offshore wind energy potential. Bach Long Vi island is closest to that location.

Table 5. Maximum of seasonal wind energy in offshore wind zones (GWh/km^2).

Season	Zone 1	Zone 2	Zone 3	Zone 4
Winter	19.28	22.17	28.95	26.69
Spring	14.79	12.97	13.63	11.87
Summer	14.63	14.22	19.73	14.63
Autumn	18.33	18.49	20.15	17.34

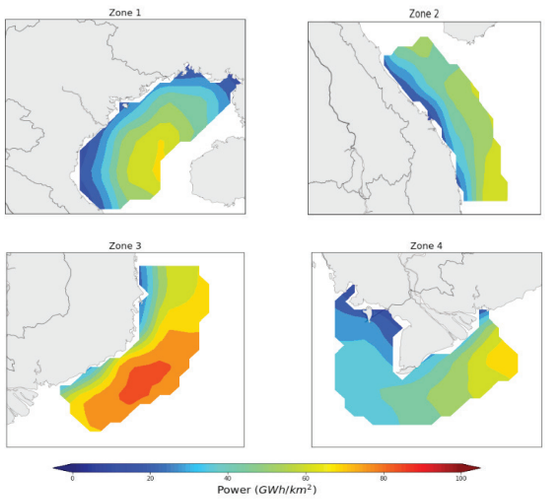

Fig. 12. Annual accumulated wind energy in four zones.

Capacity factor

The seasonal and annual CFs of the four zones using the LW 8 MW turbine power curves are shown in Figs. 13 and 14, respectively, where only the areas with a capacity factor greater or equal to 25% are shown. The north eastern monsoon enables CFs to reach their highest value. As a result, the transformation of wind energy into electricity by turbines is at its highest. Particularly, the area far from Phan Thiet city, about 120 km to the northwest, has a maximum capacity greater than 80%. Moreover, the annual average capacity factor in this area also had the highest value (about 60%) compared with the other zones. In contrast, the offshore area from Quang Binh to Quang Nam in Zone 2 is not effective for the operation of wind turbines in the summer.

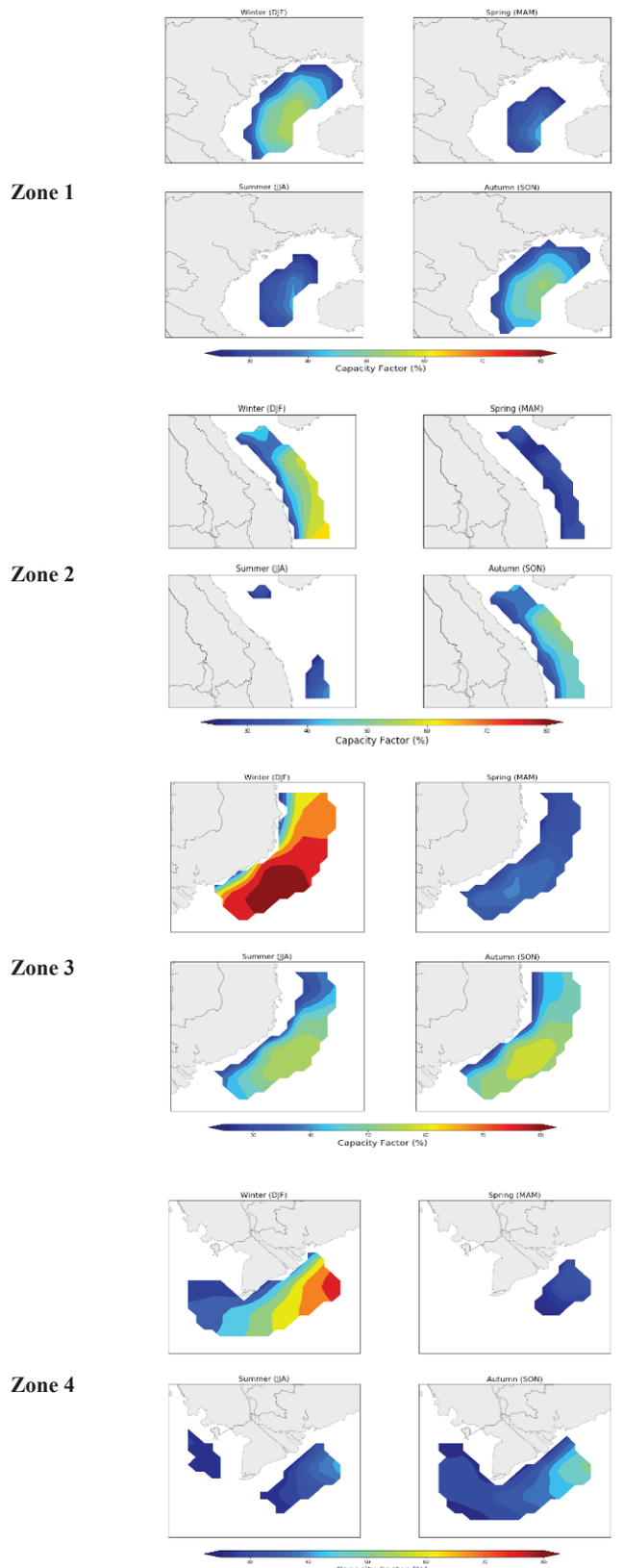

Fig. 13. Seasonal average capacity factor in four offshore wind zones using LW 8 MW turbines, only areas with CF≥25%.

Figure 15 showed the inter-annual CFs at four islands during the period 2007-2011. The authors selected four islands (Bach Long Vi, Ly Son, Phu Quy, and Phu Quoc) from four different zones (Zone 1, Zone 2, Zone 3 and Zone 4, respectively) to investigate. One particularly interesting fact highlighted by Fig. 15 is the offshore wind potential is very high around Phu Quy island. The CF in this area during the year 2011 reached 68% and the average over the 2007-2011 was 54.4%. There was a considerably high CF around Bach Long Vi island where the average figure during 2007-2011 reached 40.4%. In contrast, the CF was the lowest at Phu Quoc island, where the maximum figure was only 24.4% in the year 2011 and the five-year average was 17.7%. The inter-annual temporal variations in CF was also observed for the four islands, where the figure for Bach Long Vi in 2009 was 34.3%, compared to its highest value of 44.1% in 2010. The CF for Phu Quy island had the highest potential area in 2010 with 42.8% and only 67.7% in 2011. Such inter-annual temporal variations are important input to planning and designing energy storage systems, grid and synchronous power sources, as well as for energy demand management.

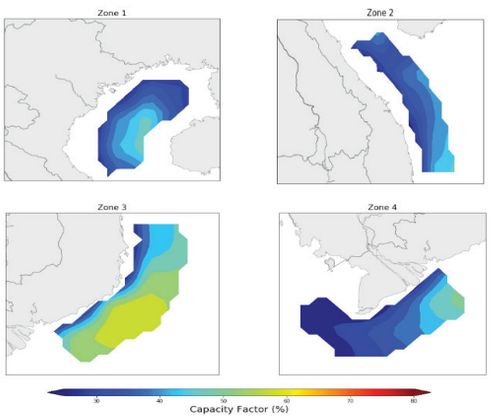

Fig. 14. Annual average capacity factor in four offshore wind zones using LW 8 MW turbines.

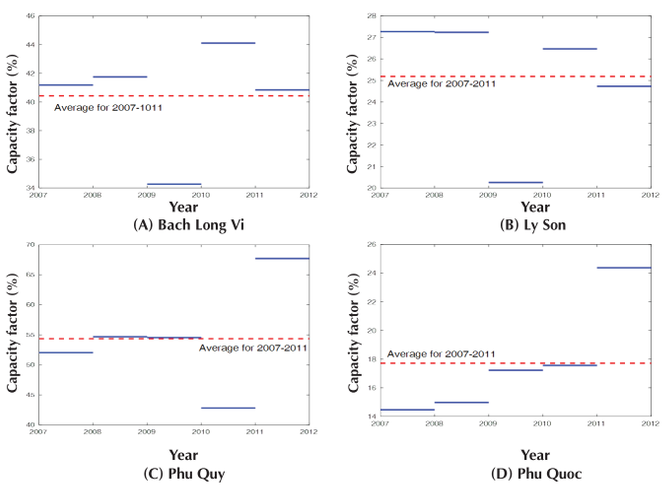

Fig. 15. Inter-annual capacity factor in four islands in the period 2007-2011. (A) Bach Long Vi (Zone 1), **(B)** Ly Son (Zone 2), **(C)** Phu Quy (Zone 3), and **(D)** Phu Quoc (Zone 4).

Wind power density distribution

Information about wind power distribution is shown in Figs. 16 and 17 and is important to assessing project feasibility, designing energy storage systems, and power transmission networks [33]. Based on the recommended layout of offshore wind farms [61], up to two LW turbines (8 MW) per one square kilometre can be installed. Therefore, the maximum power distribution for one square kilometre is 16 MW. In the Tonkin Gulf (Zone 1), the power distribution increased gradually to 100 NM (about 185 km) from the coastline of Vietnam. As similarly observed in the two previous sections, Zone 3 had the highest potential for offshore wind energy in relation to the other three zones. The maximum annual average power distribution in Zone 3 was about 9.3 MW/km^2. The area around Phu Quoc island had the lowest potential for wind energy in Zone 4. Fig. 18 provides the time histories of the inter-annual wind power density at the four islands between 2007 and 2011. Clearly, Phu Quy island had a higher wind power density than any other island. The maximum value of wind power density was 15.42 MW/km^2, which was higher than other regions. In Bach Long Vi, Ly Son, and Phu Quy, wind power density did not change much over the years. Meanwhile, there was a large changed over the years in Phu Quoc. There was a big gap in the maximum value of wind power density between 2008 and 2011 with 4.081 MW/km^2 and 8.001 MW/km^2, respectively. From Fig. 18 it can also be seen that the wind power density rose during the winter at all islands.

Based on the above sections, the evaluation of each zone using criteria (b) - (e) is summarised in Table 6. Zone 3, the southern part of Zone 2, and Ba Ria-Vung Tau in Zone 4 were found to be the most suitable for offshore wind energy development, especially considering their high capacity factors and moderate variation of power density, the fact that the resource is not far from shore, and its excellent port facility. Given the high demand in energy and good port capacity, but the potential resource is further offshore, Zone 1 and Zone 4 are recommended for future development when far offshore wind farms become more cost-effective.

This study, however, focused on natural aspects such as wind speed and direction, and physical aspects including reference turbines, synchronous power sources, transmission lines, and ports. Environmental, biological, governance, political, and management factors that can influence the evaluation of offshore wind zones were not considered.

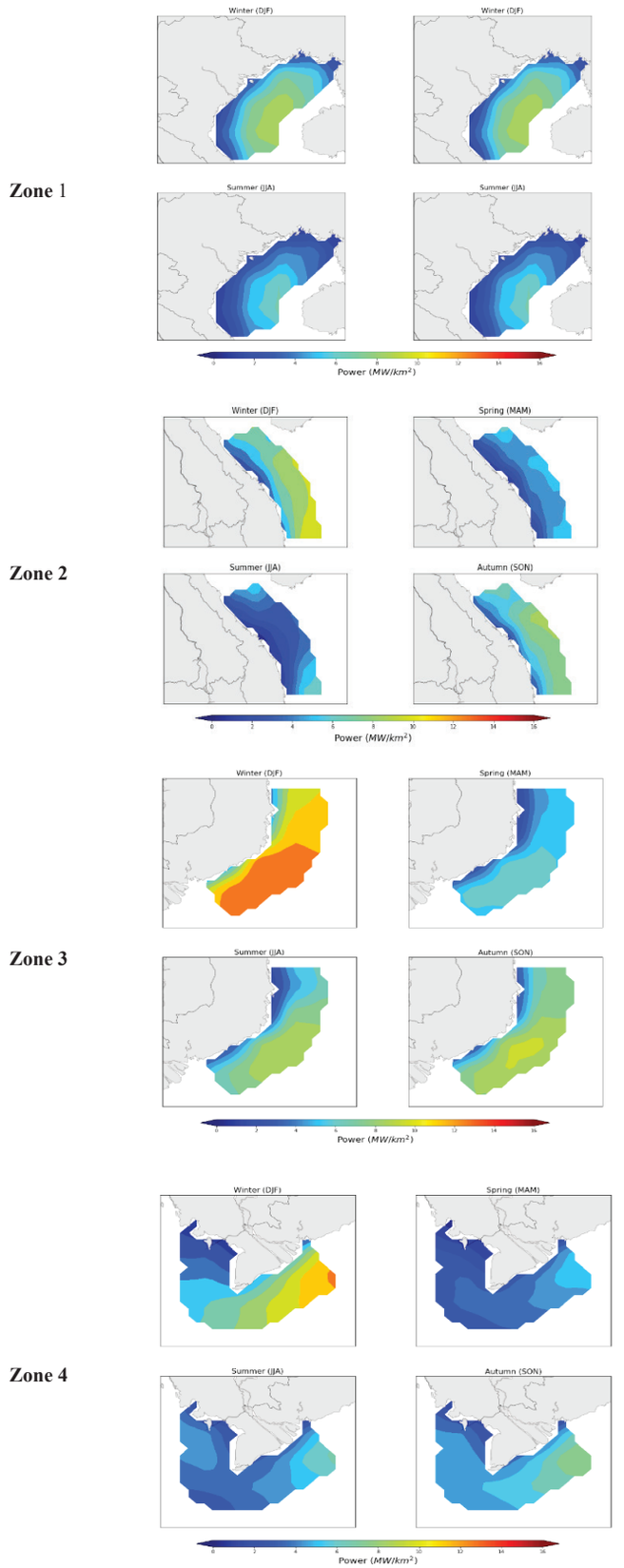

Fig. 16. Seasonal average power distribution in four zones.

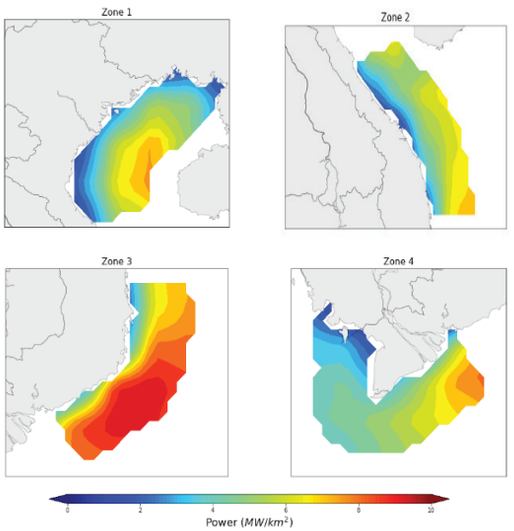

Fig. 17. Annual average power distribution in four zones.

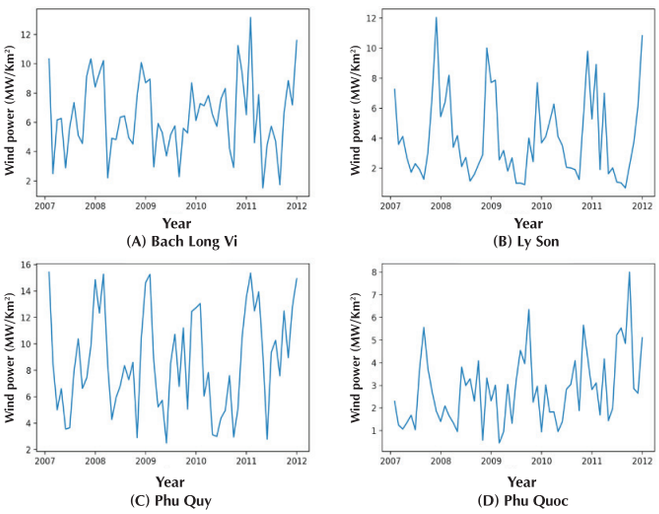

Fig. 18. Inter-annual wind power density in four islands period 2007-2011. (A) Bach Long Vi (Zone 1), **(B)** Ly Son (Zone 2), **(C)** Phu Quy (Zone 3), and **(D)** Phu Quoc (Zone 4).

Table 6. Summary of zone evaluation for offshore wind energy.

Criteria	Zone 1	Zone 2	Zone 3	Zone 4
Temperature variation	Very strong, 4 seasons, coldest winter	Strong, 4 seasons, moderate cold winter	Moderate, 2 seasons, less affected by monsoon	Weak, 2 seasons, least affected by winter
Synchronous power sources & transmissions	Hydropower, coal-fired	No major SPS. Main transmission lines available	Hydropower, Main transmission lines available	Gas/oil-fired
Ports	Very good (Cai Lan, Dinh Vu), larger areas needed	Poor in northern. Good in southern end close to Zone 3 (Chan May, Quy Nhon)	Excellent, large area available (Cam Ranh, Van Phong, Phu My)	Good (Tan Cang, Sai Gon), larger area needed
Wind energy potential (energy & power density, 5-year CF)	14-19 GWh/km^2; CF 30-45% (Bach Long Vi 40%); 4-7 MW/km^2	12-22 GWh/km^2; (large in southern); CF 25-40% (Ly Son 25.2%); 5-6.5 MW/km^2	14-29 GWh/km^2; CF 40-65% (Phu Quy 54.5%); 8-10 MW/km^2	12-27 GWh/km^2; strong near zone 3; CF 25-50% (Phu Quoc 17.8%), 4-8 MW/km^2
Wind temporal variation	Moderate, peak in winter	Moderate, peak in winter	Moderate	Strong, peak in winter
Wind spatial variation	Strong, centred zone far offshore	Strong, long zone very far offshore	Moderate, large zone closer to shore	Centred zone to northeast (Zone 3)

Conclusions

The shortage of reliable datasets, lack of comprehensive assessment of offshore wind resources and infrastructures, wind temporal and spatial variations, and integration of offshore wind development and operation into other marine strategies and activities have been highlighted as the major domestic challenges to offshore wind policymakers and developers in Vietnam. Addressing these challenges has been strategically presented, in which the CCMP data over the five year span 2007-2011, were validated with measurement data from seven meteorological stations. The offshore wind power resource was initially assessed by using temporal and spatial variations of offshore wind speed and directions. Based on expert consultations, temporal variation of temperature, the offshore wind resource in Vietnam was classified into four sea zones extending up to 100 NM from the coastline: (1) Quang Ninh to Ha Tinh, (2) Quang Binh to Binh Dinh, (3) Phu Yen to Ba Ria - Vung Tau, and (4) Ho Chi Minh city to Kien Giang. The LEANWIND 8 MW was chosen as the reference turbine for estimating wind energy potential. An assessment of offshore wind power resource and infrastructures was presented based on the following set of criteria: temporal variation in temperature, synchronous power sources and power transmission, major sea ports, and the spatial and temporal variation of offshore wind power and density. The following conclusions were drawn:

- The CCMP dataset is reliable as their wind speed probability distribution was in good agreement with that of the measurement data.

- The largest and average wind speeds were about 12 and 11 m/s at Phu Quy island (Zone 3) in January. The ranges of wind speed in Bach Long Vi (Zone 1) and Ly Son (Zone 2) were from 3.578- 9.682 m/s and 2.91-9.275 m/s, respectively. The wind speed/during this period in Phu Quoc (Zone 4) was the lowest, ranging from 2.765 to 7.347 m/s.

- The major ports with channel depths greater than 10 m and capable of accepting vessels up to 30,000 DWT are located in Zone 1, the southern part of Zone 2, Zone 3, and Zone 4. Especially, the Van Phong port in Zone 3 has a depth range of

15-20 m and expects to accept a vessel of up to 120,000 DWT.

- The highest density of energy occurred during the winter months and autumn was the second largest. Zone 3 contained the highest wind energy potential during the four seasons, where the annual accumulated wind energy density was about 80 GWh/km^2.

- The CFs over the five-year span 2007-2011 at Phu Quy, Bach Long Vi, Ly Son, and Phu Quoc were 54.5, 40.4, 25.2, and 17.8%, respectively. The considerable temporal variations inter-annually are important input to designing energy storage systems, grids, and synchronous power sources, as well as for energy demand management.

- Zone 3 (particularly Binh Thuan and Ninh Thuan sea), the southern part of Zone 2, and Ba Ria - Vung Tau in Zone 4 were the most suitable to offshore wind energy development, owing to high capacity factors and a power density with moderate variation, the fact that the resource was not far from shore, and their excellent port facilities.

- Given the high demand for energy and good port capacity, but the potential resource is further offshore, Zone 1 and Zone 4 are recommended for future development when far offshore wind farms become more cost-effective.

- Future studies to obtain measurement data for wind profiles at turbine hub heights, and to consider biology, metocean, and seabed topography and geology, are recommended before planning such marine spaces.

ACKNOWLEDGEMENTS

The first author (Vu Dinh Quang) and the fourth author (Nguyen Dinh Duc) have been supported by Vietnam National University, Hanoi; Vietnam Japan University and University of Engineering and Technology. The author Van Nguyen Dinh has been funded by Science Foundation Ireland (SFI) Research Centre: MaREI - 266 Centre for Marine and Renewable Energy (12/RC/2302). The authors are grateful to the support.

The authors declare that there is no conflict of interest regarding the publication of this article.

REFERENCES

[1] I. Dincer (2000), "Renewable energy and sustainable development: a crucial review", *Renewable and Sustainable Energy Reviews*, **4(2)**, pp.157-175.

[2] V.N. Dinh and E. McKeogh (2018), "Offshore wind energy: technology opportunities and challenges", *Lecture Notes in Civil Engineering, Proceedings of the Vietnam Symposium on Advances in Offshore Engineering*, **18**, pp.3-22.

[3] V.N. Dinh and B. Basu (2013), "On the modeling of spar-type floating offshore wind turbines", *Key Engineering Materials*, **569-570**, pp.636-643.

[4] C.-W. Zheng, Z.-N. Xiao, Y.-H. Peng, C.-Y. Li, Z.-B. Du (2018), "Rezoning global offshore wind energy resources", *Renewable Energy*, **129**, pp.1-11.

[5] Danish Energy Agency (2017), *Vietnam Energy Outlook Report*.

[6] P.H. Ty (2015), *Dilemmas of Hydropower Development in Vietnam: Between Dam-induced Displacement and Sustainable Development*, Delft: PhD Thesis, Utrecht University, The Netherlands.

[7] GIZ (2016), *Vietnam Power Development Plan for the Period 2011-2020: Highlights of the PDP 7 Revised*, GIZ Energy Support Programme in Viet Nam, available from: http://gizenergy.org.vn, Hanoi.

[8] M. Ha-Duong and H.A. Nguyen-Trinh (2018), "Two scenarios for carbon capture and storage in Vietnam", *Energy Policy*, **110**, pp.559-569.

[9] N.D. Luong (2015), "A critical review on potential and current status of wind energy in Vietnam", *Renewable and Sustainable Energy Reviews*, **43**, pp.440-448.

[10] GWEC (2018), *Global Wind Statistics 2017*, Global Wind Energy Council, available from: www.gwec.net.

[11] K.Q. Nguyen (2007), "Wind energy in Vietnam: resource assessment, development status and future implications", *Energy Policy*, **35(2)**, pp.1405-1413.

[12] V.Q. Doan, H. Kusaka, T.V. Du, N.D. Duc, T. Cong (2018), "Numerical approach for studying offshore wind power potential along the southern coast of Vietnam", *Lecture Notes in Civil Engineering, Proceedings of the Vietnam Symposium on Advances in Offshore Engineering*, **18**, pp.245-249.

[13] V.Q. Doan, V.N. Dinh, H. Kusaka, T. Cong, A. Khan, T.V. Du, N.D. Duc (2019), "Usability and challenges of offshore wind energy in Vietnam 1 revealed by the regional climate model simulation", *Scientific Online Letters on the Atmosphere*, Doi: 10.2151/sola. 2019-021.

[14] V.Q Doan and P.L.D. Anh (2018), "The zoning of offshore wind energy resources in the Vietnam sea", *Vietnam Symposium on Advances in Offshore Engineering*, pp.250-256.

[15] G. Gualtieri (2019), "A comprehensive review on wind resource extrapolation models applied in wind energy", *Renewable and Sustainable Energy Reviews*, **102**, pp.215-233.

[16] M. Gökçek, A. Bayülken, Ş. Bekdemir (2007), "Investigation of wind characteristics and wind energy potential in Kirklareli, Turkey", *Renewable Energy*, **32(10)**, pp.1739-1752.

[17] C. İlkiliç (2012), "Wind energy and assessment of wind energy potential in Turkey", *Renewable and Sustainable Energy Reviews*, **16(2)**, pp.1165-1173.

[18] A. Keyhani, M. Ghasemi-Varnamkhasti, M. Khanali, R. Abbaszadeh (2010), "An assessment of wind energy potential as a power generation source in the capital of Iran, Tehran", *Energy*, **35(1)**, pp.188-201.

[19] K. Sopian, M.Y.H. Othman, A. Wirsat (1995), "The wind energy potential of Malaysia", *Renewable Energy*, **6(8)**, pp.1005-1016.

[20] A.B. Mayhoub and A. Azzam (1997), "A survey on the assessment of wind energy potential in Egypt", *Renewable Energy*, **11(2)**, pp.235-247.

[21] A.S. Ahmed (2010), "Wind energy as a potential generation source at Ras Benas, Egypt", *Renewable and Sustainable Energy Reviews*, **14(8)**, pp.2167-2173.

[22] A.-Y. Sultan, Y. Charabi, A. Gastli, S. Al-Alawi (2010), "Assessment of wind energy potential locations in Oman using data from existing weather stations", *Renewable and Sustainable Energy Reviews*, **14(5)**, pp.1428-1436.

[23] H. Nfaoui, J. Buret, A.A.M. Sayigh (1998), "Wind characteristics and wind energy potential in Morocco", *Solar Energy*, **63(1)**, pp.51-60.

[24] A. Allouhi, O. Zamzoum, M.R. Islam, R. Saidur, T. Kousksou, A. Jamil, A. Derouich (2017), "Evaluation of wind energy potential in Morocco's coastal regions", *Renewable and Sustainable Energy Reviews*, **72**, pp.311-324.

[25] K.M. Bataineh, and D. Dalalah (2013), "Assessment of wind energy potential for selected areas in Jordan", *Renewable Energy*, **59**, pp.75-81.

[26] R.O. Fagbenle, J. Katende, O.O. Ajayi, J.O. Okeniyi (2011), "Assessment of wind energy potential of two sites in North-East, Nigeria", *Renewable Energy*, **36(4)**, pp.1277-1283.

[27] S.J. Lang and E.J. McKeogh (2009), "Forecasting wind generation, uncertainty and reserve requirement on the Irish power system using an ensemble prediction system", *Wind Engineering*, **33(5)**, pp.433-448.

[28] K.-Y. Oh, J.-Y. Kim, J.-K. Lee, M.-S. Ryu, J.-S. Lee (2012), "An assessment of wind energy potential at the demonstration offshore wind farm in Korea", *Energy*, **46(1)**, pp.555-563.

[29] T. Remmers, F. Cawkwell, C. Desmond, J. Murphy, E. Politi (2019), "The potential of advanced scatterometer (ASCAT) 12.5 km coastal observations for offshore wind farm site selection in Irish waters", *Energies*, **12(2)**, Doi:10.3390/en12020206.

[30] PO.DAAC (2018), *Cross-calibrated Multi-platform Ocean Surface Wind Vector L3.5A Monthly First-look Analyses*, Doi:10.5067/CCF35-01AM1.

[31] V.Q. Doan, H. Kusaka, M. Matsueda, R. Ikeda (2019), "Application of mesoscale ensemble forecast method for prediction of wind speed ramps", *Wind Energy*, **22(4)**, pp.499-508.

[32] A.M. Foley, P.G. Leahy, A. Marvuglia, E.J. McKeogh (2012), "Current methods and advances in forecasting of wind power generation", *Renewable Energy*, **37(1)**, pp.1-8.

[33] P.G. Leahy and E.J. McKeogh (2013), "Persistence of low wind speed conditions and implications for wind power variability", *Wind Energy*, **16(4)**, pp.575-586.

[34] AlexanderKies, B. Schysk, T.V. Dinh, L. Bremen, D. Heinemann, S. Schramm (2017), "Large-scale integration of renewable power sources into the Vietnamese power system", *Energy Procedia*, **125**, pp.207-213.

[35] A. Malvaldi, S. Weiss, D. Infield, J. Browell, P. Leahy, A.M. Foley (2017), "A spatial and temporal correlation analysis of aggregate wind power in an ideally interconnected Europe", *Wind Energy*, **20(8)**, pp.1315-1329.

[36] P. Elsner (2019), "Continental-scale assessment of the African offshore wind energy potential: spatial analysis of an under-appreciated renewable energy resource", *Renewable and Sustainable Energy Reviews*, **104**, pp.394-407.

[37] D. Kitsiou, M. Karydis, A.M. O'Hagan, E.P.J.O.A.S.K. Paterson, M.L. Tissier (2017), *Marine Spatial Planning: Methodologies, Environmental Issues and Current Trends*, New York: Nova Science.

[38] C. Ehler, J. Zaucha, K. Gee (2019), "Maritime/marine spatial planning at the interface of research and practice", *Maritime Spatial Planning*, pp.1-21, Doi:10.1007/978-3-319-98696-8_1.

[39] C. White, B.S. Halpern, C.V. Kappel (2012), "Ecosystem service tradeoff analysis reveals the value of marine spatial planning for multiple ocean uses", *Proceedings of the National Academy of Sciences*, **109(12)**, pp.4696-4701.

[40] J.C. Day (2002), "Zoning - lessons from the Great Barrier Reef Marine Park", *Ocean & Coastal Management*, **45**, pp.139-156.

[41] C. Desmond, J. Murphy, L. Blonk, W. Haans (2016), "Description of an 8 MW reference wind turbine", *Journal of Physics: Conference Series*, **753**, Doi:10.1088/1742-6596/753/9/092013.

[42] R. Atlas, R.N. Hoffman, J. Ardizzone, S.M. Leidner, J.C. Jusem, D.K. Smith, D. Gombos (2011), "A cross-calibrated, multiplatform ocean surface wind velocity product for meteorological and oceanographic applications", *Bulletin of the American Meteorological Society*, **92**, pp.157-174.

[43] P.W. Gaiser, K.M.S. Germain, E.M. Twarog, G.A. Poe, W. Purdy, D. Richardson, W. Grossman, W.L. Jones, D. Spencer, G. Golba, J. Cleveland, L. Choy, R.M. Bevilacqua, P.S. Chang (2004), "The windsat spaceborne polarimetric microwave radiometer: sensor description and early orbit performance", *IEEE Transactions on Geoscience and Remote Sensing*, **42(11)**, pp.2347-2361.

[44] A. Dabbaghiyan, F. Fazelpour, M.D. Abnavi, M.A. Rosen (2016), "Evaluation of wind energy potential in province of Bushehr, Iran", *Renewable and Sustainable Energy Reviews*, **55**, pp.455-466.

[45] M.H. Soulouknga, S.Y. Doka, N. Revanna, N. Djongyang, T.C. Kofane (2018), "Analysis of wind speed data and wind energy potential in Faya-Largeau, Chad, using Weibull distribution", *Renewable Energy*, **121**, pp.1-8.

[46] A.F. Davenport (1965), "The relationship of wind structure to wind loading", *Proc. Conf. on Wind Effects on Buildings & Structures*, HMSO.

[47] S.A. Hsu (1992), "An overwater stability criterion for the offshore and coastal dispersion model", *Boundary-Layer Meteorology*, **60(4)**, pp.397-402.

[48] A.A. Teyabeen, F.R. Akkari, A.E. Jwaid (2017), "Power curve modelling for wind turbines", *2017 UKSim-AMSS 19th International Conference on Computer Modelling & Simulation* (UKSim).

[49] C. Carrillo, A.F.O. Montaño, J. Cidrás, E. Díaz-Dorado (2013), "Review of power curve modelling for wind turbines", *Renewable and Sustainable Energy Reviews*, **21**, pp.572-581.

[50] https://www.leanwind.eu/results.

[51] C. Elkinton, A. Blatiak, H. Ameen (2014), *Assessment of Ports for Offshore Wind Development in the United States*, GL Garrad Hassan, America.

[52] EREA (2019), "Wind power development in Vietnam, presentation at the meeting on offshore wind development - Dutch experience and implication to Vietnam", *Electricity and Renewable Energy Authority of Vietnam*, Hanoi.

[53] V.L. Dang and G.T. Yeo (2017), "A competitive strategic position analysis of major container ports in Southeast Asia", *The Asian Journal of Shipping and Logistics*, **33(1)**, pp.19-25.

[54] https://www.searates.com/maritime/vietnam.html, [accessed 02 05 2019].

[55] http://www.vpa.org.vn/capacties/, [accessed 10 05 2019].

[56] http://open_jicareport.jica.go.jp/pdf/11999976_02.pdf.

[57] http://www.pul.ynu.ac.jp/files/s2-2_HoChiMinh.pdf, [accessed 10 05 2019].

[58] https://en.wind-turbine-models.com/turbines/318-vestas-v164-8.0.

[59] http://pdf.directindustry.com/pdf/vestas/offshore-v164-80-mw-v112-33-mw/20680310439.html [accessed 08 05 2019].

[60] http://www.mhivestasoffshore.com/norther-foi/.

[61] V.N. Dinh and H.X. Nguyen (2018), "Design of an offshore wind farm layout", *Lecture Notes in Civil Engineering, Proceedings of the Vietnam Symposium on Advances in Offshore Engineering*, **18**, pp.233-238.

Doi: 10.31276/VJSTE.62(1).17-22

Characteristics and antifungal activity of CuO-ZnO nanocomposites synthesised by the sol-gel technique

Vo N.L. Uyen[1, 2], Nguyen P. Anh[3, 4], Nguyen T.T. Van[3, 4], Nguyen Tri[3], Nguyen V. Minh[5], Nguyen N. Huy[1, 2], Tran V. Linh[1, 2], Pag-Asa Gaspillo[6], and Huynh K.P. Ha[1, 2*]

[1]Vietnam National University, Ho Chi Minh city, Vietnam
[2]University of Technology, Vietnam National University, Ho Chi Minh city, Vietnam
[3]Institute of Chemical Technology, Vietnam Academy of Science and Technology, Vietnam
[4]Graduate University of Science and Technology, Vietnam Academy of Science and Technology, Vietnam
[5]Biotechnology Department, Open University Ho Chi Minh city, Vietnam
[6]Department of Chemical Engineering, De La Salle University, Manila, Philippines

Received 16 January 2020; accepted 6 March 2020

Abstract:

CuO-ZnO nanoparticles were successfully synthesized by the sol-gel method. Characteristic properties of the synthesized nanoparticles were investigated using X-ray diffraction (XRD), field emission scanning electron microscopy (SEM), transmission electron microscopy (TEM), Fourier-transform infrared spectroscopy (FT-IR), N_2 adsorption/desorption isotherms, and BJH pore diameter distributions. The formation of highly crystalline CuO and ZnO was confirmed by XRD. FT-IR confirmed that Zn-O and Cu-O bonds were formed in the material. SEM and TEM images showed that the obtained CuO-ZnO nanoparticles were nearly spherical in shape and had a uniform size distribution with sizes ranging between 5-20 nm for the CuO-containing phase and 50-100 nm for the ZnO-containing phase. The CuO-ZnO sample showed effective antifungal activities against four strains. *Aspergillus* and *Penicillium* were completely inhibited with a concentration of 5 mg/ml of CuO-ZnO. For the *Magnaporthe* and *Neoscytalidium* strains, the minimum inhibitory concentration was 10 mg/ml.

Keywords: **antifungal activity, CuO, nanocomposite, sol-gel, ZnO.**

Classification number: **2.2**

Introduction

In recent years, the frequency of fungal infections and fungal contamination in daily life has rapidly grown due to the serious threats of environmental pollution and climate change. The progression of fungal infections and contamination not only increases the chances of human illness, but is also one of the leading causes of economic loss during the harvest and storage of agricultural products [1, 2]. Many varieties of harmful fungi such as *Pathogenic fungi, Magnaporthe oryzae*, *Penicillium,* and *Aspergillus niger* can cause disease in agronomic, horticulture, ornamental, and forest plants [3]. Among these fungi, *Magnaporthe oryzae* is a fungus that causes blast in rice and can also infect many other cereal crops such as barley, oats, and rye grass [4]. *Neoscytalidium dimidiatum* is another fungus that causes disease in many host plants found in tropical and subtropical regions such as South America, the Caribbean, Asia, and Africa [5]. Post-harvest fruits can be exposed to serious diseases by *Penicillium expansum*, including grey and blue mould, even when the most advanced post-harvest technologies were applied [6]. Meanwhile, high moisture products such as cakes, cheese, and cereal flour can be damaged by *Aspergillus niger* even when they are well preserved [7]. While many antifungal agents have been studied and applied to situations such as these, it remains difficult to prevent the growth of these fungi [1, 8].

Currently, many new and highly effective antifungal materials have been investigated to replace longstanding antifungals. In recent years, several types of nanomaterials have been synthesized and demonstrated to be resistant to fungi, along with superior physical and chemical properties

*Corresponding author: Email: hkpha@hcmut.edu.vn

compared to previous antifungal materials [8, 9].

There are many kinds of inorganic nanomaterials that possess superior properties such as high mechanical and chemical stability, low toxicity, and good strength even under extreme environmental conditions. Synthesized from silver [10-12], copper [3, 7, 13], titanium dioxide [14, 15], and zinc oxide [1, 13, 16, 17], these inorganic nanomaterials have been shown to have antibacterial properties, even in low concentrations and in the absence of light [18]. Because of the unique and superior physical and chemical properties of nanoparticles compared to their bulk counterparts, nanoparticles (NPs) have a high potential for use as fungicides in plants [16].

Among these inorganic materials, ZnO has great potential not only in the field of electronic materials but, more recently, as an effective antibacterial and anti-mould agent in low-light environments [19, 20]. ZnO exhibits excellent antibacterial properties in the pH range of 7 to 8 and has been used in many biomedical, antifungal, and cosmetic applications such as toothpaste, plaster, creams, and ointments. Further, ZnO has shown the ability to prevent bacterial penetration and reduce infections [19-21]. An increasing number of studies focusing on the antibacterial ability of ZnO have been published. These studies focus on controlling the properties of ZnO particles through synthesis methods, doping of other constituents into its structure, and by adjusting the particle size and shape of ZnO powders. Studies of the structure and related properties of ZnO, aimed at improving its application potential by doping with other metals or metal oxides, is of great significance and has stimulated extensive development. The properties of ZnO change when it is doped with metal ions such as Cu [22-26], Al [27], Ni [18], Mn [28], and Cr [29], and the resulting products have been applied to sensors, solar cells, photocatalysts, antibacterial activity, and dilute magnetic semiconductors. Among the transition metals, Cu is the preferred doping agent for ZnO because it easily forms a valence bond with ZnO through the overlap of its d-orbital [30]. Some previous studies have proven that ZnO nanoparticles doped with Cu have enhanced antibacterial activity [22-26].

While there are several previous studies of ZnO's antibacterial activity, its antifungal activity has been seldom studied. Specifically, the antifungal activity of a CuO/ZnO material against *Magnaporthe oryzae*, *Penicillium*, and *Aspergillus niger* has not yet been reported. Therefore, in this study, a ZnO-CuO nanoparticle material is synthesized and its antifungal activities against four fungi, including *Pathogenic fungi, Magnaporthe oryzae*, *Penicillium,* and *Aspergillus niger,* is investigated and compared.

Materials and methods

The nanopowder composite of CuO-ZnO was synthesized by dissolving 23.76 grams of $Zn(NO_3)_2.6H_2O$ (Xilong, purity >99%) into 50 ml of distilled water. The mixture was vigorously mixed using a magnetic stirrer and heated up to 80^oC for 2 h until the solution became transparent. After that, a solution of 11 ml of ethylene glycol (Xilong, purity >99.8%) and 4.84 grams of $Cu(NO_3)_2.3H_2O$ (Xilong, purity >99%) was added dropwise into the previous solution. Then distilled water was added to the combined solution to reach 100 ml, during continuous stirring, until a solution with a light blue colour was obtained. After 2 h under 80°C conditions, the solution turned into a gel and then the temperature was increased further until it reached a paste state. The gel mixture was dried at 200°C within 2 h and then calcined at 500°C for 2 h under airflow with a flow rate of 3 $l.h^{-1}$ and a heating rate of 10°C.min^{-1} to obtain a composite powder of CuO-ZnO with a CuO/ZnO weight ratio of 1/4. This powder was ball ground for 12 h and the nanocomposite powder of the product was obtained for antifungal activity testing and other characteristic physicochemical analyses. In this synthesis, oxalic acid was used to form the medium complex compounds with Zn^{2+} and Cu^{2+}, where ethylene glycol was used as a dispersing agent. Then, after drying at 200^oC to remove all the free water and ethylene glycol from the mixture, the powder that consisted of metallic organic compounds will have much lower calcination temperature (500°C) to form CuO-ZnO as compared to other methods [31, 32].

The structure and other characteristics of the CuO-ZnO composite nanopowder was investigated using X-ray diffraction (Bruker D2 Pharser), Brunauer-Emmett-Teller nitrogen adsorption isotherms (N_2-BET, Nova 2200e instrument), field emission scanning electron microscopy (Hitachi S4800), and transmission electron microscopy (Jeol Jem 1400). The point of zero charges (PZC) of the samples was determined by the salt addition method [33]. UV-Vis diffuse reflectance spectroscopy (DRS) was used to examine the bandgap of the samples and was recorded on a Varian Cary 5000 UV-Vis-NIR spectrophotometer with an integrating sphere in the range of 200-800 nm.

The minimum inhibitory concentration of the antifungal activity of the samples were evaluated according to the Clinical and Laboratory Standards Institute (CLSI) [34] (CLSI, 2010). The obtained Zn/Cu samples have been tested for antifungal activity against *Aspergillus* sp., *Pencillium* sp., *Neoscytalidium dimidiatum,* and *Maganaporthe oryzae*. To examine the minimum inhibitory concentration of Zn/Cu against the four fungi, different concentrations of Zn/Cu (N/2, N/4, N/8, N/16, N/32, N/64 and N/128 with N being

the initial concentration of the Zn/Cu solution in deionized water, N=20 mg/ml) were prepared with sterile, deionized water. Subsequently, the diluted samples were mixed with sterile Sabouraud Dextrose agar (SDA). By using sterile sticks, the standardized inoculum of each selected fungi with 1-2×10^6 spores/ml were inoculated on agar plates mixed with the Zn/Cu samples from low to high concentration. A plate of the sterile SDA, not mixed with Zn/Cu, was used as the control. Each strain of fungi was inoculated at the same location on each of the disks. Finally, the plates were incubated at 30-35°C for 2-3 days. The lowest concentration of Zn/Cu that inhibited the growth of tested bacteria was considered as the minimum inhibitory concentration (MIC) [35].

Results and discussion

Characteristics of samples

The result of the XRD analysis showed diffraction peaks of ZnO at 2θ=31.47°, 34.12°, 35.96°, 36.2°, 47.5°, 56.5°, 62.8°, 67.9°, and 69.05° (JCPDS card No. 36-1451) and CuO at 2θ=35.10°, 38.34° and 48.36° (JCPDS card No. 05-0661). No unknown peaks were observed from XRD, indicating that pure single oxides of ZnO and CuO were obtained. The average particle size of the CuO and ZnO in the CuO-ZnO nanocomposite was calculated by Scherrer's equation to be 20 nm and 40 nm, respectively (Fig. 1).

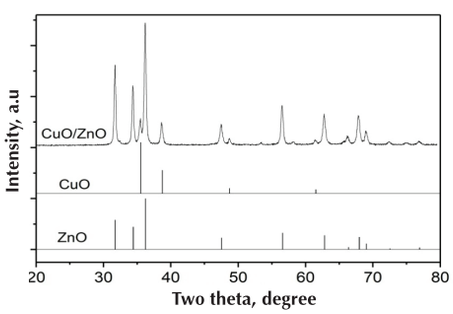

Fig. 1. XRD parttern of CuO-ZnO nanocomposite.

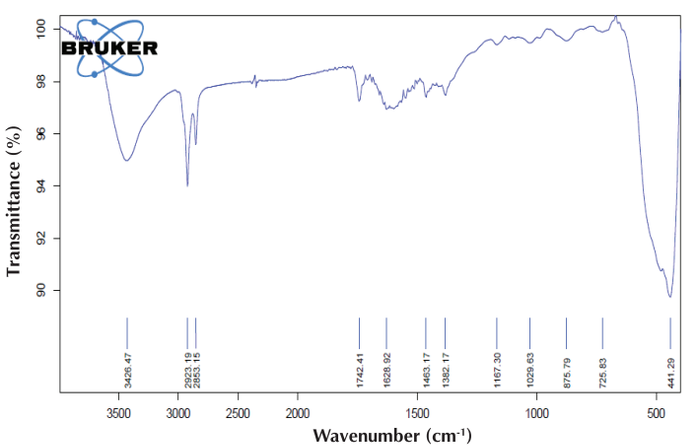

Fig. 2. FT-IR spectra of CuO-ZnO nanocomposite.

The functional groups of the CuO-ZnO nanocomposite provided by FT-IR can be seen in Fig. 2. The -OH functional groups were observed at 3426 cm^{-1} [36]. The C=O functional group was observed at a wavenumber of 1628 cm^{-1}. The weak peak at 2320 cm^{-1} corresponds to symmetric C-H bond vibrations. The peak at 441 cm^{-1} is assigned to the Zn-O bond, and the peak at 480 and 725 cm^{-1} are assigned to the Cu-O bond [37]. These results show that the CuO-ZnO composite material was successfully synthesized by the sol-gel technique.

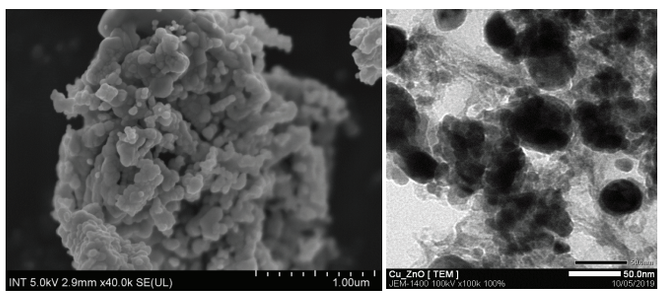

Fig. 3. SEM (A) and TEM (B) images of CuO-ZnO nanocomposite.

The surface morphology of the CuO-ZnO nanocomposite synthesized by sol-gel can be seen in Fig. 3A. The nanocomposites have a uniform particle shape and size with a low level of agglomeration. The particles were of spherical shape and the size of the prepared nanoparticles reached a range of 50-100 nm. Fig. 3B shows the TEM images of the prepared CuO-ZnO sample's morphology. The TEM image of the sample also indicated that the nanoparticles were highly dispersed with a spherical shape. A crystallite of spheroidal shape with an internal diameter of approximately 5-20 nm is mainly the CuO-containing phase. This result was consistent with the XRD pattern of the sample.

The textural properties of the as-synthesized materials were investigated using nitrogen adsorption/desorption isotherms. The N_2 adsorption/desorption isotherm curve of the CuO/ZnO nanomaterials is shown in Fig. 4A. The isotherms of the sample showed a type IV profile. Two steps of capillary condensation can be observed from the N_2 adsorption/desorption isotherms of the sample, with the first step at P/P^o=0.3 due to mesopores inside the ZnO and the second at a higher partial pressure (P/P^o=0.9) due to the capillary condensation of N_2 in interparticle pores with a smaller particle size [38]. Clearly, the CuO/ZnO nanomaterials show the characteristics of a mesoporous material [39], which is favourable for mass transfer of bacteria, as well as fungal attachment [40]. As observed in Fig. 4B, the pore size distribution for the sample was monomodal with a peak pore diameter of 24 Å.

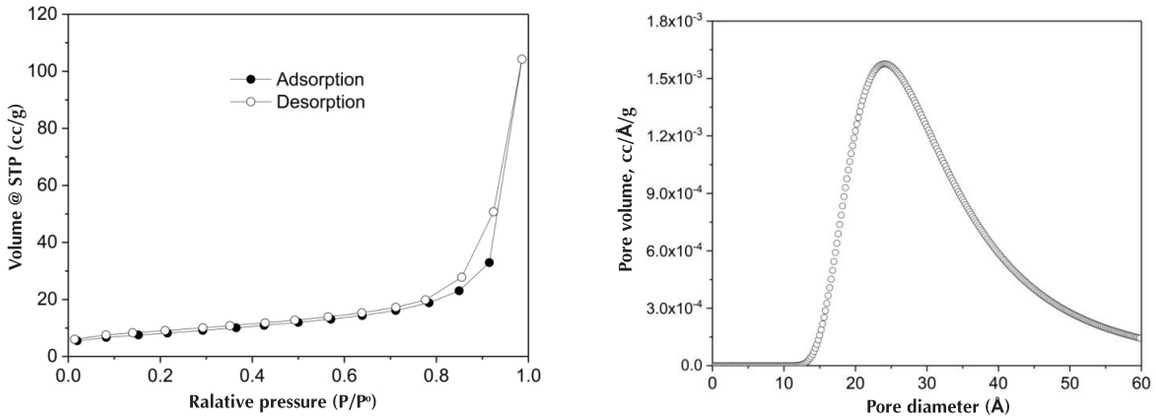

Fig. 4. (A) N_2 adsorption/desorption isotherms and (B) the BJH pore diameter distribution of the CuO-ZnO nanocomposite.

Table 1. Antifulgal activities of CuO-ZnO nanocomposite on four kinds of fungi.

Fungi	Concentrations of sample					
	Control	*N/2*	*N/4*	*N/8*	*N/16*	*N/32*
Magnaporthe oryzae (N=20 mg/ml)	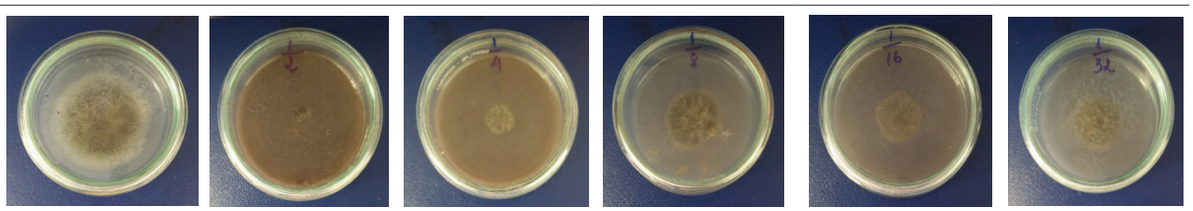					
	(+)	(-)	(+)	(+)	(+)	(+)
Neoscytalidium dimidiatum (N=20 mg/ml)	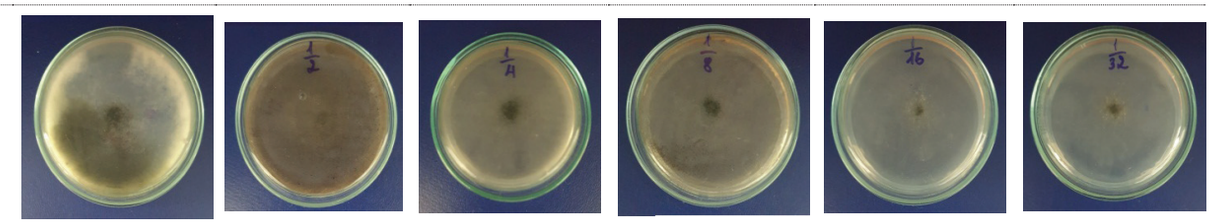					
	(+)	(-)	(+)	(+)	(+)	(+)
Penicillium (N=20 mg/ml)	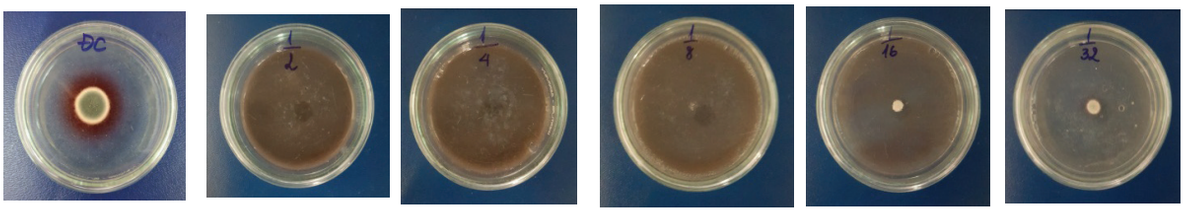					
	(+)	(-)	(-)	(+)	(+)	(+)
Aspergillus (N=50 mg/ml)	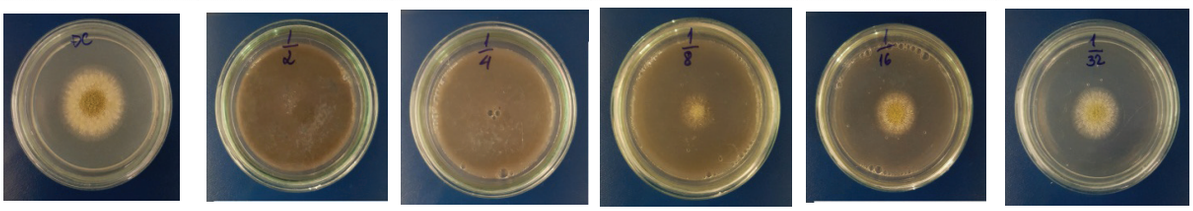					
	(+)	(-)	(-)	(+)	(+)	(+)

(-): no growth of fungus; (+): growth of fungus.

Antifungal activities

The results in Table 1 show that the CuO-ZnO material has a significant inhibitory effect on the growth of the fungi *Magnaporthe oryzae*, *Neoscytalidium dimidiatum*, *Aspergillus,* and *Penicillium*. It was demonstrated that the diameter of the colonies in all samples supplemented with CuO-ZnO was smaller than that of the control sample. The results also showed that when the concentration of CuO-ZnO increased, the inhibitory level also increased. According to these results, *Aspergillus* and *Penicillium* were completely inhibited with a concentration of 5 mg/ml of CuO-ZnO. For the remaining two kinds of fungi, the minimum inhibitory concentration was 10 mg/ml. Using CuO-ZnO as an agent for *Penicillium* and *Aspergillus* antifungal had better results than that of *Magnaporthe* and *Neoscytalidium*. This result can be explained by the distinct growth morphology of the fungi. Another reason for the difference in antifungal activities of CuO-ZnO among fungi may be the constitutive tolerant of each fungus [6].

Conclusions

A CuO-ZnO nanocomposite with small particle size was successfully prepared via the sol-gel method. The XRD, SEM, and TEM of the nanocomposite confirmed the formation of highly crystalline particles possessing a spherical shape with sizes in a range of 5-20 nm for the CuO-containing phase and 50-100 nm for the ZnO-containing phase. The N_2 adsorption/desorption isotherm curve of the CuO-ZnO nanomaterials showed a type IV profile, which is favourable for fungal attachment. Therefore, the CuO-ZnO nanocomposite showed efficient antifungal activities against *Magnaporthe oryzae*, *Neoscytalidium dimidiatum*, *Aspergillus,* and *Penicillium* with the MIC being 10 mg/ml. Hence, the properties of CuO-ZnO prepared via the sol-gel method can establish new pathways in the development of new antifungal agents.

ACKNOWLEDGEMENTS

This research was supported by Department of Science and Technology of Ho Chi Minh city under the contract number 30/2019/HD-QKHCN.

The authors declare that there is no conflict of interest regarding the publication of this article.

REFERENCES

[1] He Lili, Liu Yang, Mustapha Azlin, Lin Mengshi (2011), "Antifungal activity of zinc oxide nanoparticles against Botrytis cinerea and Penicillium expansum", *Microbiological Research*, **166**, pp.207-215.

[2] Spadaro Davide, Garibaldi Angelo, Gullino Maria Lodovica (2004), "Control of Penicillium expansum and Botrytis cinerea on apple combining a biocontrol agent with hot water dipping and acibenzolar-S-methyl, baking soda, or ethanol application", *Postharvest Biology and Technology*, **33**, pp.141-151.

[3] Pariona Nicolaza, I. Mtz-Enriquez Arturo, D. Sánchez-Rangel, Carrión Gloria, F. Paraguay-Delgado, Rosas-Saito Greta (2019), "Green-synthesized copper nanoparticles as a potential antifungal against plant pathogens", *RSC Advances*, **9**, pp.18835-18843.

[4] Wang Jiaoyu, Li Ling, Yin Yeshi, Gu Zhuokan, Chai Rongyao, Wang Yanli, Sun Guochang (2017), "Equol, a clinically important metabolite, inhibits the development and pathogenicity of *Magnaporthe* oryzae, the causal agent of rice blast disease", *Molecules*, **22(10)**, pii: E1799, Doi: 10.3390/molecules22101799.

[5] Madrid Hugo, Ruíz-Cendoya Mery, Cano Josep, Stchigel Alberto, Orofino Rosane, Guarro Josep (2009), "Genotyping and in vitro antifungal susceptibility of Neoscytalidium dimidiatum isolates from different origins", *International Journal of Antimicrobial Agents*, **34**, pp.351-354.

[6] S. Yehia Ramy, F. Ahmed Osama (2013), "In vitro study of the antifungal efficacy of zinc oxide nanoparticles against Fusarium oxysporum and Penicilium expansum", *African Journal of Microbiology Research*, **7**, pp.1917-1923.

[7] Bouson Supaporn, Krittayavathananon Atiweena, Phattharasupakun Nutthaphon, Siwayaprahm Patcharaporn, Sawangphruk Montree (2017), "Antifungal activity of water-stable copper-containing metal-organic frameworks", *Royal Society Open Science*, **4**, Doi: 10.1098/rsos.170654.

[8] Jasim Neeran Obied (2015), "Antifungal activity of Zinc oxide nanoparticles on Aspergillus fumigatus fungus & Candida albicans yeast", *J. Nat. Sci. Res.*, **5**, pp.23-27.

[9] K. Stoimenov Peter, L. Klinger Rosalyn, L. Marchin George, J. Klabunde Kenneth (2002), "Metal oxide nanoparticles as bactericidal agents", *Langmuir*, **18**, pp.6679-6686.

[10] Kim Keuk-Jun, Sung Woo Sang, Moon Seok-Ki, Choi Jong-Soo, Kim Jong Guk, Lee Dong Gun (2008), "Antifungal effect of silver nanoparticles on dermatophytes", *J. Microbiol. Biotechnol.*, **18**, pp.1482-1484.

[11] J. Klabunde Kenneth, Stark Jane, Koper Olga, Mohs Cathy, G. Park Dong, Decker Shawn, Jiang Yan, Lagadic Isabelle, Zhang Dajie (1996), "Nanocrystals as stoichiometric reagents with unique surface chemistry", *The Journal of Physical Chemistry*, **100**, pp.12142-12153.

[12] Guzman Maribel, Dille Jean, Godet Stéphane (2012), "Synthesis and antibacterial activity of silver nanoparticles against gram-positive and gram-negative bacteria", *Nanomedicine: Nanotechnology, Biology and Medicine*, **8**, pp.37-45.

[13] Phiwdang Kankanit, Phensaijai Mongkol, Pecharapa Wisanu (2013), "Study of antifungal activities of CuO/ZnO nanocomposites synthesized by co-precipitation method", *Advanced Materials Research*, pp.89-93.

[14] Maneerat Chamorn, Hayata Yasuyoshi (2006), "Antifungal activity of TiO_2 photocatalysis against Penicillium expansum in vitro and in fruit tests", *International Journal of Food Microbiology*, **107**, pp.99-103.

[15] Othman Siti Hajar, Salam Abd, Raudhah Nurul, Zainal Norhazlizam, Kadir Basha Roseliza, A. Talib Rosnita (2014), "Antimicrobial activity of TiO_2 nanoparticle-coated film for potential

food packaging applications", *International Journal of Photoenergy*, **2014**, 6pp.

[16] La Rosa-García De, C. Susana, Martínez-Torres Pablo, Gómez-Cornelio Sergio, Corral-Aguado Mario Alberto, Quintana Patricia, M. Gómez-Ortíz Nikte (2018), "Antifungal activity of ZnO and MgO nanomaterials and their mixtures against colletotrichum gloeosporioides strains from tropical fruit", *Journal of Nanomaterials*, **2018**, Doi: 10.1155/2018/3498527.

[17] P.A. Arciniegas-Grijalba, M.C. Patiño-Portela, L.P. Mosquera-Sánchez, J.A. Guerrero-Vargas, J.E. Rodríguez-Páez (2017), "ZnO nanoparticles (ZnO-NPs) and their antifungal activity against coffee fungus Erythricium salmonicolor", *Applied Nanoscience*, **7**, pp.225-241.

[18] Kumar R. Saravana, S.H.S. Dananjaya, De Zoysa Mahanama, Yang Minyang (2016), "Enhanced antifungal activity of Ni-doped ZnO nanostructures under dark conditions", *RSC Advances*, **6**, pp.108468-108476.

[19] Jin Jin, Fang Ling Jie, Tang Lian, Ji Peng, Wang Chao Sheng, Wang Hua Ping (2017), "Preparation of Nano Cu-ZnO/PET fiber for antibacterial application", *Materials Science Forum*, **898**, pp.2272-2278.

[20] Ma Ge, Liang Xiaoxi, Li Liangchao, Qiao Ru, Jiang Donghua, Ding Yan, Chen Haifeng (2014), "Cu-doped zinc oxide and its polythiophene composites: preparation and antibacterial properties", *Chemosphere*, **100**, pp.146-151.

[21] Tankhiwale Rasika, S.K. Bajpai (2012), "Preparation, characterization and antibacterial applications of ZnO-nanoparticles coated polyethylene films for food packaging", *Colloids and Surfaces B: Biointerfaces*, **90**, pp.16-20.

[22] Chatterjee Arijit Kumar, Chakraborty Ruchira, Basu Tarakdas (2014), "Mechanism of antibacterial activity of copper nanoparticles", *Nanotechnology*, **25(13)**, Doi: 10.1088/0957-4484/25/13/135101.

[23] A. Hassan Iman, P. Parkin Ivan, P. Nair Sean, J. Carmalt Claire (2014), "Antimicrobial activity of copper and copper (I) oxide thin films deposited via aerosol-assisted CVD", *Journal of Materials Chemistry B*, **2**, pp.2855-2860.

[24] P. Ruparelia Jayesh, Chatterjee Arup Kumar, P. Duttagupta Siddhartha, Mukherji Suparna (2008), "Strain specificity in antimicrobial activity of silver and copper nanoparticles", *Acta Biomaterialia*, **4**, pp.707-716.

[25] Santo Christophe Espírito, Morais Paula Vasconcelos, Grass Gregor (2010), "Isolation and characterization of bacteria resistant to metallic copper surfaces", *Appl. Environ. Microbiol.*, **76**, pp.1341-1348.

[26] M. Ferhat, Zaoui Ali, R. Ahuja (2009), "Magnetism and band gap narrowing in Cu-doped ZnO", *Applied Physics Letters*, **94(14)**, Doi: 10.1063/1.3112603.

[27] Bhargav Prashant Kumar, K.S.R. Murthy, Kaur Kamalpreet, M.S. Goyat, K. Pandey Jitendra, Dubey Santosh, Sharma Sudesh, Pant Charu (2019), "Influence of Al and Al-Cu dual doping on structural, optical, wetting and anti-fungal properties of ZnO nanoparticles", *Materials Research Innovations*, Doi: 10.1080/14328917.2019.1686560.

[28] Y. Abdollahi, A.H. Abdullah, Z. Zainal, N.A. Yusof (2011), "Synthesis and characterization of manganese doped ZnO nanoparticles", *International Journal of Basic & Applied Sciences*, **11**, pp.62-69.

[29] K. Vijayalakshmi, D. Sivaraj (2015), "Enhanced antibacterial activity of Cr doped ZnO nanorods synthesized using microwave processing", *RSC Advances*, **5**, pp.68461-68469.

[30] Khan Shakeel Ahmad, Noreen Farah, Kanwal Sadia, Iqbal Ahsan, Hussain Ghulam (2018), "Green synthesis of ZnO and Cu-doped ZnO nanoparticles from leaf extracts of Abutilon indicum, Clerodendrum infortunatum, Clerodendrum inerme and investigation of their biological and photocatalytic activities", *Materials Science and Engineering: C*, **82**, pp.46-59.

[31] Azimi Salameh (2013), "Sol-gel synthesis and structural characterization of nano-thiamine hydrochloride structure", *ISRN Nanotechnology*, **2013**, Doi: 10.1155/2013/815071.

[32] M. Allaf Rula, J. Hope-Weeks Louisa (2014), "Synthesis of ZnO-CuO nanocomposite aerogels by the sol-gel route", *Journal of Nanomaterials*, **2014**, Doi: 10.1155/2014/491817.

[33] Bakatula Elisee Nsimba, Richard Dominique, Neculita Carmen Mihaela, J. Zagury Gerald (2018), "Determination of point of zero charge of natural organic materials", *Environmental Science and Pollution Research*, **25**, pp.7823-7833.

[34] H. Rex John (2009), *Method for Antifungal Disk Diffusion Susceptibility Testing of Yeasts: Approved Guideline*, Clinical and Laboratory Standards Institute.

[35] Xia Zhi-Kuan, Ma Qiu-Hua, Li Shu-Yi, Zhang De-Quan, Cong Lin, Tian Yan-Li, Yang Rong-Ya (2016), "The antifungal effect of silver nanoparticles on Trichosporon asahii", *Journal of Microbiology, Immunology and Infection*, **49**, pp.182-188.

[36] Liu Zi-Ling, Deng Jian-Cheng, Deng Jing-Jing, Li Fei-Fei (2008), "Fabrication and photocatalysis of CuO/ZnO nano-composites via a new method", *Materials Science and Engineering: B*, **150**, pp.99-104.

[37] Habibi Mohammad Hossein, Karimi Bahareh (2014), "Application of impregnation combustion method for fabrication of nanostructure CuO/ZnO composite oxide: XRD, FESEM, DRS and FT-IR study", *Journal of Industrial and Engineering Chemistry*, **20**, pp.1566-1570.

[38] Kim Hyun You, Lee Hyuck Mo, Park Jung-Nam (2010), "Bifunctional mechanism of CO_2 methanation on Pd-MgO/SiO_2 catalyst: independent roles of MgO and Pd on CO_2 methanation", *The Journal of Physical Chemistry C*, **114**, pp.7128-7131.

[39] C.M. Janet, S. Navaladian, B. Viswanathan, T.K. Varadarajan, R.P. Viswanath (2010), "Heterogeneous wet chemical synthesis of superlattice-type hierarchical ZnO architectures for concurrent H_2 production and N_2 reduction", *The Journal of Physical Chemistry C*, **114**, pp.2622-2632.

[40] Oveisi Hamid, Rahighi Simin, Jiang Xiangfen, Nemoto Yoshihiro, Beitollahi Ali, Wakatsuki Soichi, Yamauchi Yusuke (2010), "Unusual antibacterial property of mesoporous titania films: drastic improvement by controlling surface area and crystallinity", *Chemistry-An Asian Journal*, **5**, pp.1978-1983.

Doi: 10.31276/VJSTE.62(1).23-27

Synthesis of novel organocatalysed phenoxazine for atom transfer radical polymerization of methyl methacrylate monomer

Thu Vo Hoang[1], Huong Thi Le[1], Nhung Thanh Thi Truong[1], Michał Michalak[2], Ha Tran Nguyen[1, 3*]

[1]Vietnam National University, Ho Chi Minh city, Vietnam
[2]Centre of Polymer and Carbon Materials, Polish Academy of Sciences, Poland
[3]Faculty of Materials Technology, University of Technology, Vietnam National University, Ho Chi Minh city, Vietnam

Received 8 January 2020; accepted 11 March 2020

Abstract:

In this research, a novel organic photocatalyst of 10-(perylene-3-yl-10H-phenoxazine (PHP) has been successfully synthesized from perylene and phenoxazine via Buchwald-Hartwig C-N coupling. The chemical structure of catalyst was determined via FT-IR, proton nuclear magnetic resonance (^{1}H-NMR) spectrum and optical properties were investigated through UV-Vis spectroscopy. The PHP has been used as the reducing photoredox catalyst for organocatalyzed atom transfer radical polymerrization (O-ATRP) under UV irradiation. The well controlled molecular weight of the methyl methacrylate polymers have been obtained nearly 80% with a low polydispersity index under 1.5.

Keywords: **atom transfer radical polymerization, methacrylate monomer, organic photocatalyst, phenoxazine.**

Classification number: **2.2**

Introduction

The polymerization of synthetic polymers through metal catalysts by ATRP is considered the state-of-the-art in the polymer industry [1-3]. The use of transition metals during ATRP provides many advantages including effective control of the molecular weight and polydispersity as well as control of the end-groups of the obtained polymers. However, traces of transition metals always remains in the obtained polymeric products [4, 5]. The presence of metals has limited the subsequent use of polymer products in bio-medicine and opto-electronic applications. To overcome this issue, an organic photocatalyst (O-ATRP/metal-free ATRP) has been developed for synthesis of metal-free polymers via controlled radical polymerization, which will gradually replace the traditional ATRP-based transition metal catalysts [6-8]. There have been many studies of O-ATRP polymerization using organic photocatalysts [9, 10]. Pintauer, et al. [11] have used phenoxazine and phenothiazine as organic photocatalysts for the controlled polymerization of acrylonitrile. Dadashi-Silab, et al. [12] used organic catalysts (perylene, diaryl dihydrophenazines) for ATRP of the MMA monomer under visible light. Further, Corrigan, et al. [13] used fluorescein as an organic catalyst to control the polymerization of MMA. In addition, metal-free ATRP has been applied to the modification/ functionalization of polymer surfaces, which enhanced the reactivity of the polymer [14].

In this research, the novel organic photocatalyst PHP was synthesized and applied to the polymerization of an MMA monomer for the first time [15, 16]. The structure of PHP was characterized via FT-IR and ^{1}H-NMR spectroscopy. In addition, the optical properties of the PHP catalyst were evaluated via UV-Vis spectroscopy. We also investigated the efficiency of the PHP organic photocatalyst for the O-ATRP process.

Experimental

Materials

Perylene (99%), phenoxazine (99%), $Pd(OAc)_2$ (99%) were purchased by Sigma Aldrich. NBS (99%), $P(t\text{-}Bu)_3$

*Corresponding author: Email: nguyentranha@hcmut.edu.vn

(98%), NaOt-Bu (97%), and MMA (99%) were purchased by Merck. Phenyl 2-bromo-2-methylpropanoate ($C_{10}H_{11}BrO_2$) was synthesized at our lab. All the solvents were purchased from Fisher Chemicals.

Characterization

^{1}H-NMR spectra were recorded in deuterated chloroform ($CDCl_3$), with tetramethylsilane as the internal reference, on a Bruker Avance 500 MHz. The UV-Vis spectrum of the polymer samples was recorded at the Key Laboratory, Faculty of Materials Technology, University of Technology, Vietnam National University, Ho Chi Minh city on a Shimadzu UV-Vis 2450 from Shimadzu Scientific at room temperature (25°C) over the range of 300 nm to 800 nm and scanning speed of 200 nm/min. The spectra from gel permeation chromatography (GPC) were recorded at the Key Laboratory, Faculty of Materials Technology, University of Technology, Vietnam National University, Ho Chi Minh city on a Polymer PL-GPC 50.

Synthesis of 1-bromoperylene

Perylene (500 mg, 1.98 mmol) and anhydrous dimethyl formamide (DMF) (6 ml) were added to a 100 ml 3-necked flask at 0°C. Aluminium foil was thoroughly wrapped around to cover the reaction vial and block out light. In the dark, *N*-bromosuccinimide (NBS) (388 mg, 2.18 mmol) in 4 ml of anhydrous DMF was slowly added to this solution using a dropping funnel. It was stirred for 1 h at 0°C and for 23 h at room temperature. Then, the reaction was terminated with 2 M HCl, extracted with $CHCl_3$, and dried with anhydrous Na_2SO_4. The product was a brown yellow solid with a yield = 95%.

Synthesis of PHP [17, 18]

A procedure from the literature was adapted for this synthesis. A 50 ml storage flask was fit with magnetic stirring bar, flamed under vacuum, and back-filled with nitrogen three times. The flask was then charged with phenoxazine (183.21 mg), NaOtBu (144.15 mg), $Pd(OAc)_2$ catalyst (4.49 mg), $P(tBu)_3$ (8.09 mg), and dry toluene (45 ml). The flask was evacuated and back-filled three times with nitrogen before 1-bromoperylene (331.21 mg) was added. The flask was then placed in an oil bath at 110°C while stirring for 24 h. The flask was then cooled to room temperature, diluted with $CHCl_3$, washed with water and brine, dried with K_2CO_3, and purified using column chromatography (3.3% EtOAc/hexane). The product was dried under reduced pressure to yield 78% of a red-orange solid.

Synthesis of polymers [6, 19]

The polymerization of PMA was performed by O-ATRP using PhBMP as the initiator and PHP as the photocatalyst. To start, a 25 ml storage flask was fit with a magnetic stir bar, flamed under vacuum, and backfilled with nitrogen three times. The MMA monomer (0.25 ml, 2.35 mmol) was dissolved in 0.5 ml of THF and placed in a flask. Then, 5.71 mg (23.5 µmol) of PhBMP initiator and PHP (1.02 mg, 2.35 µmol) were added separately. The mixture was stirred for 15 min. Then, three freeze-pump-thaw cycles were performed to remove the gas in the mixture. The mixture of the reaction solution was stirred until homogeneous. After that, the reaction solution was placed in a UV-box and irradiated with a wavelength of 365 nm for 24 h at room temperature. After the reaction process, the flask was removed from the UV-box and placed in the dark to stabilize. Finally, the polymer product was collected by precipitating the solution after reaction in cold methanol. Then it was dried and vacuumed to provide the cleaned polymer products.

Results and discussion

The PHP organic photocatalyst was successfully synthesized via Buchwald-Hartwig C-N coupling. Scheme 1 shows the synthesis process of the PHP organic photocatalyst. To synthesize 1-bromo perylene, the bromination of the electrophilic substitution was performed. The reaction took place in the presence of N-bromosuccinimide (NBS) in dimethylformamide (DMF) solvent. The yield of the reaction was 95% and the Buchwald-Hartwig C-N coupling reaction between 1-bromo perylene and phenoxazine was carried out. $Pd(OAc)_2$ and $P(t\text{-}Bu)_3$ as the catalyst and ligand, respectively, were used for this reaction process. The yield of the reaction was 78%.

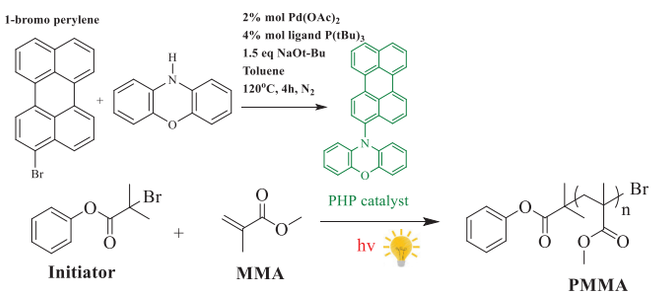

Scheme 1. Synthesis of the PHP organic photocatalyst and general O-ATRP of methyl methacrylate monomer.

After purification by silica column chromatography and vacuum for 24 hours, PHP predictive product was analyzed FT-IR to identify functional groups (Fig. 1). FT-IR results showed that the product had no fluctuations of N-H bond in phenoxazine at 3500 cm^{-1}. Specially, obtained product had the absorption peak at 3051 cm^{-1}, 1589 cm^{-1}, 1272 cm^{-1}, 1044 cm^{-1} that corresponds to Ar-H, C=C, C-N and C-O bond. This indicates that the predictive product PHP has specific links appropriate to its structure.

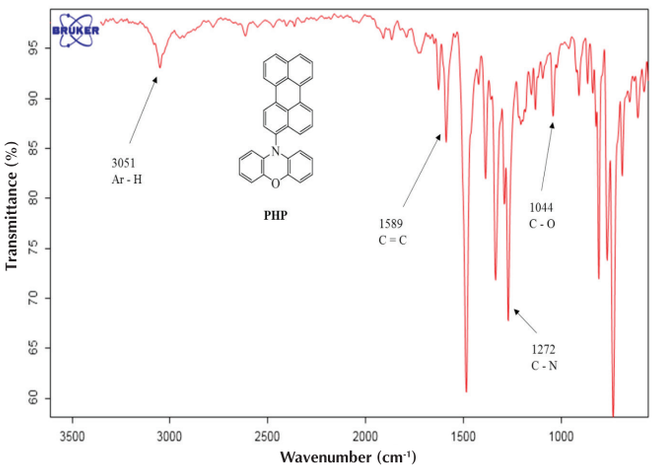

Fig. 1. Result of the FT-IR spectrum of the PHP product.

The chemical structure of PHP was analyzed via ^{1}H-NMR spectrum in Fig. 2 and the ^{1}H-NMR spectrum of phenoxazine showed in the Fig. 3. Comparing the ^{1}H-NMR spectrum of the phenoxazine precursor, the ^{1}H-NMR spectrum of the obtained product disappeared the peak at 4 ppm correspond to the proton of N-H bond in phenoxazine. The data in Fig. 2 showed that ^{1}H-NMR spectrum of PHP exhibited fully characteristic peaks of PHP including peaks of phenoxazine and perylene. The peaks from 7.48 ppm to 8.34 ppm corresponded to the protons of perylene. The peaks from 5.89 ppm to 6.73 ppm which assigned to the protons of phenoxazine ring. Based on the characteristics peaks, the reasonable their integration and the disappearance of N-H bonds in ^{1}H-NMR spectrum of PHP, the obtained product has been concluded that PHP catalyst was synthesized successfully.

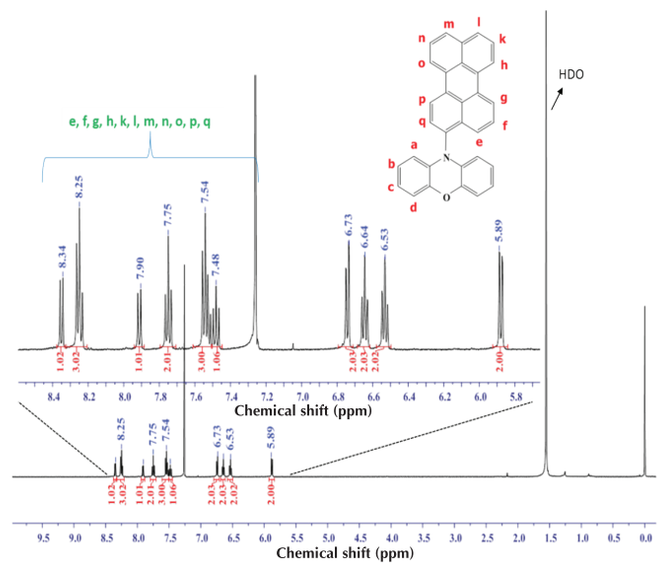

Fig. 2. The ^{1}H-NMR of PHP catalyst.

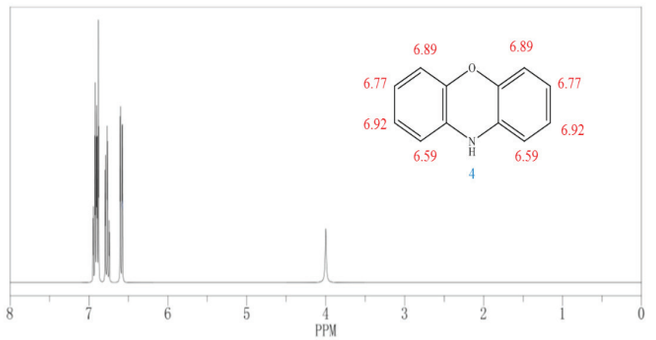

Fig. 3. The ^{1}H-NMR of phenoxazine.

From the results of FT-IR and ^{1}H-NMR analyzed above, it could be said that PHP catalyst has been successfully synthesized. Next, PHP and perylene were analyzed by UV-Vis to compare the spectral absorption in soluble form in THF solvent (Fig. 4). Perylene and PHP were dissolved in THF at different concentrations of 50, 40, 30, 20, 10 (μM) as measured by Shimadzu UV-Vis 2450 at room temperature range of 200 nm to 800 nm, 50 nm/min. Based on the UV-Vis spectrum of PHP catalyst, we recognized that the PHP absorbs the wavelength from 200-500 nm while the pyrene absorbs the wavelength from 200-450 nm. The UV-Vis spectrum of PHP curves exhibited two distinct absorption peaks at 250 and 450 nm which corresponding to the absorption of phenoxazine moieties and perylene, respectively. Moreover, the spectra showed a linear correlation between concentration and absorbance, and the molar extinction coefficient was determined through the Lambert - Beer law. In addition, the PHP exhibited the high intensity UV absorption at wavelength λ_{max1}=441 nm, λ_{max2}=417 nm with coefficient is ε_1=40870 ($M^{-1}.cm^{-1}$), ε_2=36980 ($M^{-1}.cm^{-1}$). This results confirmed that the PHP catalyst can activate in UV light.

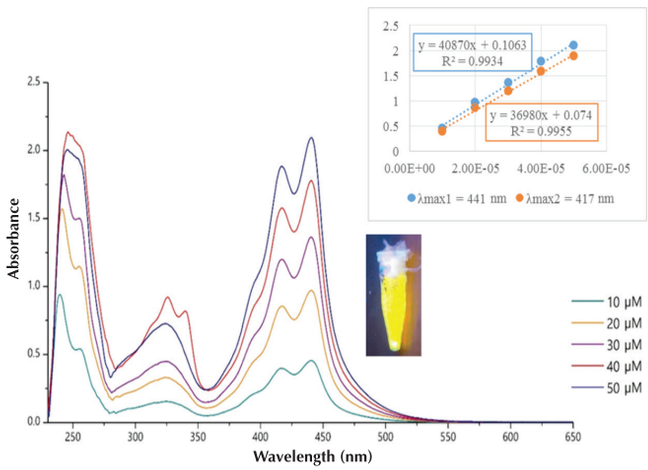

Fig. 4. The UV-Vis spectrum of PHP.

For a clearer picture, we consider the same concentration of the perylene precursor and PHP at 50 µM, shown in Fig. 5.

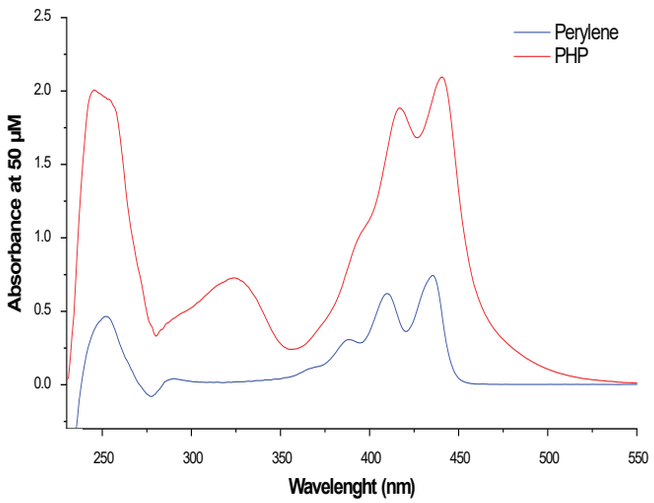

Fig. 5. The UV-Vis spectrum of PHP and perylene at 50 µM.

The spectrum shows that PHP has a higher absorbance than perylene at any wavelength. For example, at a wavelength of λ=440 nm, the absorbance of perylene was 0.536 while that of PHP was 2.093 (4 times higher). It can be said that PHP has a superior absorption capacity when compared to the commercial catalyst perylene.

According the studies of Hawker, Matyjaszewski, and Miyake, PHP was used as the organic photocatalyst for O-ATRP of an MMA monomer. The O-ATRP of the MMA monomer involves photoexcitation of the PHP catalyst to an excited state, PHP*, when under UV irradiation. This PHP* was capable of reducing the PhBMP initiator to generate an active radical for polymerization propagation. Efficient deactivation was considered to be the most important aspect of the production of a controlled polymer. Deactivation of the propagating radical regenerates the alkyl bromide and the ground state PHP. Here, we report PHP as a novel class of photocatalysts for O-ATRP and thus we surveyed several molar ratios of the PHP catalyst to the initiator and monomers to consider the effects of PHP toward polymerization.

The polymerization process was performed in the presence of the PHP catalyst following the O-ATRP procedure. The content of the catalyst at 0.5, 0.1, 0.05, and 0.02 were investigated for the polymerization of methyl methacrylate. The reactions were carried out in a THF solvent under 365 nm UV irradiation for 24 h. The results of O-ATRP for MMA polymerization using the PHP catalyst are presented in Table 1.

Table 1. Macromolecular Characteristic Features of PMMA Synthesized by O-ATRP Using PHP Catalyst.

[MMA]:[I]:[PHP]	Conv(%)	M_n (gmol^{-1})	M_w (gmol^{-1})	Dispersity (Đ)
[100]:[1]:[0.5]	62.69	21670	31160	1.44
[100]:[1]:[0.1]	60	17969	25742	1.43
[100]:[1]:[0.05]*	77.61	30457	38880	1.28
[100]:[1]:[0.02]	56.42	24913	33677	1.35

The results show that about 5% molar ratio of PHP to initiator has the highest monomer conversion of 77.61%. On the other hand, the conversion of monomers during the polymerization decreased when the amount of PHP catalyst increased. It should be noted that the resulting polymethyl methacrylate (PMMA) exhibited a M_n of 30457 gmol^{-1}, with a polydispersity index (Đ) of 1.28, which is reasonable for controlled polymerization (normally Đ is required to be below 1.5). This result demonstrated that the MMA monomer has been successfully polymerized via O-ATRP using PHP as an organic photocatalyst. Furthermore, it should be noted that 365 nm UV light was used for polymerization of the MMA monomer. Fig. 4 showed the lowest absorption range of PHP to be around 360-365 nm wavelength, but the efficiency of polymerization was over 50% at different catalytic concentrations. To promote the polymerization reaction, higher absorbance wavelengths should be used for monomer polymerization with the appropriate catalyst content. In addition, PHP can be used as a solar-driven photocatalyst for the ATRP process because of its ability to absorb photons over the corresponding wavelength range.

Several experiments of the [MMA]:[I]:[PHP]* system were also performed to investigate the change of the monomer with respect to reaction time.

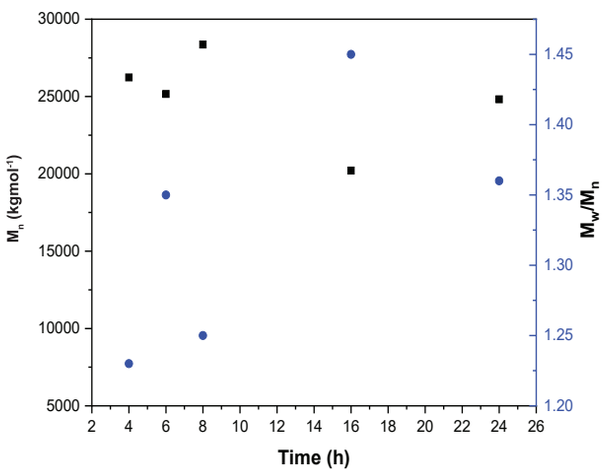

Fig. 6. Results for the polymerization of MMA using the PHP vs. time.

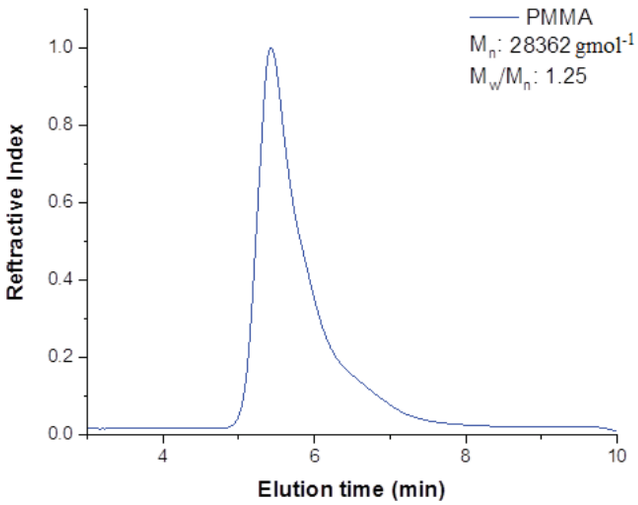

Fig. 7. The GPC of MMA polymer after an 8 hours reaction.

From these experimental results, it was shown that the MMA polymer with M_n molecular mass between 20000-30000 (gmol^{-1}) had a low Đ, under 1.5, when using PHP as a catalyst for the O-ATRP process (shown in Figs. 6 & 7). Clearly, the MMA polymer has a high M_n=28362 (gmol^{-1}) and low Đ=1.25 after 8 h of reaction time. This result shows that the obtained MMA polymer has a well-controlled molecular weight and a low Đ with short reaction time compared to other catalysts.

Conclusions

The PHP catalyst has been successfully synthesized based on phenoxazine and has been shown to be an effective non-metallic catalyst for O-ATRP. We have also demonstrated the successful metal-free organocatalyzed atom transfer radical polymerization using PHP as a photoredox catalyst. PHP leads to a controlled, photo-mediated process that bears many characteristics including accurate control over molecular weight, low polydispersity, and high retention of chain end groups. Specifically, PHP was used to produce polymethacrylate with a controlled molecular weight of 28362 gmol^{-1} as well as a narrow polydispersity of 1.25 after 8 h reaction with the MMA monomer. The organic photocatalyst PHP has shown its advantages over previous catalyst generations in ATRP. Further, this research enables a synthesis procedure for potential bio/electronic applications that required metal-free polymeric materials.

ACKNOWLEDGEMENTS

This research is funded by Vietnam National University, Ho Chi Minh city under grant number NV2019-20-03.

The authors declare that there is no conflict of interest regarding the publication of this article.

REFERENCES

[1] P.B. Zetterlund, Y. Kagawa, M. Okubo (2008), "Controlled/living radical polymerization in dispersed systems", *Chemical Reviews*, **108(9)**, pp.3747-3794.

[2] G. Moad, E. Rizzardo, S.H. Thang (2008), "Radical addition-fragmentation chemistry in polymer synthesis", *Polymer*, **49(5)**, pp.1079-1131.

[3] D.J. Keddie, et al. (2011), "Switchable reversible addition-fragmentation chain transfer (RAFT) polymerization in aqueous solution, N, N-dimethylacrylamide", *Macromolecules*, **44(17)**, pp.6738-6745.

[4] K. Matyjaszewski, J. Xia (2001), "Atom transfer radical polymerization", *Chemical Reviews*, **101(9)**, pp.2921-2990.

[5] K. Matyjaszewski (2012), "Atom transfer radical polymerization (ATRP): current status and future perspectives", *Macromolecules*, **45(10)**, pp.4015-4039.

[6] N.J. Treat, et al. (2014), "Metal-free atom transfer radical polymerization", *Journal of the American Chemical Society*, **136(45)**, pp.16096-16101.

[7] B. Mao, L. Gan, Y. Gan (2006), "Ultra high molar mass poly [2-(dimethylamino) ethyl methacrylate] via atom transfer radical polymerization", *Polymer*, **47(9)**, pp.3017-3020.

[8] K. Matyjaszewski (1996), "The importance of exchange reactions in controlled/living radical polymerization in the presence of alkoxyamines and transition metals", *Macromolecular Symposia*, **29(24)**, pp.7661-7670.

[9] G.M. Miyake, J.C. Theriot (2014), "Perylene as an organic photocatalyst for the radical polymerization of functionalized vinyl monomers through oxidative quenching with alkyl bromides and visible light", *Macromolecules*, **47(23)**, pp.8255-8261.

[10] J.C. Theriot, et al. (2016), "Organocatalyzed atom transfer radical polymerization driven by visible light", *Science*, **352(6289)**, pp.1082-1086.

[11] T. Pintauer, P. Zhou, K. Matyjaszewski (2002), "General method for determination of the activation, deactivation, and initiation rate constants in transition metal-catalyzed atom transfer radical processes", *Journal of the American Chemical Society*, **124(28)**, pp.8196-8197.

[12] S. Dadashi-Silab, X. Pan, K. Matyjaszewski (2017), "Phenyl benzo [b] phenothiazine as a visible light photoredox catalyst for metal-free atom transfer radical polymerization", *Chemistry-A European Journal*, **23(25)**, pp.5972-5977.

[13] N. Corrigan, et al. (2016), "Photocatalysis in organic and polymer synthesis", *Chemical Society Reviews*, **45(22)**, pp.6165-6212.

[14] K. Matyjaszewski, N.V. Tsarevsky (2009), "Nanostructured functional materials prepared by atom transfer radical polymerization", *Nature Chemistry*, **1(4)**, pp.276-288.

[15] R.M. Pearson, G.M. Miyake, et al. (2016), "Organocatalyzed atom transfer radical polymerization using N-aryl phenoxazines as photoredox catalysts", *Journal of the American Chemical Society*, **138(35)**, pp.11399-11407.

[16] B.G. McCarthy, et al. (2018), "Structure-property relationships for tailoring phenoxazines as reducing photoredox catalysts", *Journal of the American Chemical Society*, **140(15)**, pp.5088-5101.

[17] M.M. Heravi, et al. (2018), "Buchwald-Hartwig reaction: an overview", *Journal of Organometallic Chemistry*, **861**, pp.17-104.

[18] C.H. Lim, M.D. Ryan, G.M. Miyake, et al. (2017), "Intramolecular charge transfer and ion pairing in N, N-diaryl dihydrophenazine photoredox catalysts for efficient organocatalyzed atom transfer radical polymerization", *Journal of the American Chemical Society*, **139(1)**, pp.348-355.

[19] J.C. Theriot, et al. (2017), "Organocatalyzed atom transfer radical polymerization: perspectives on catalyst design and performance", *Macromolecular Rapid Communications*, **38(13)**, Doi: 10.1002/marc.201700040.

Doi: 10.31276/VJSTE.62(1).28-31

Synthesis of random copolymers of 4-vinylpyridine with *n*-octadecyl acrylate/*n*-octadecyl methacrylate by metal-free ATRP

Loc Tan Nguyen[1, 2], Duc-Anh Song Nguyen[1], Thuy Thu Truong[2], Le-Thu Thi Nguyen[2*]

[1]National Key Laboratory of Polymer and Composite Materials, University of Technology, Vietnam National University, Ho Chi Minh city
[2]Faculty of Materials Technology, University of Technology, Vietnam National University, Ho Chi Minh city

Received 20 January 2020; accepted 3 March 2020

Abstract:

Poly(4-vinylpyridine-*r*-*n*-octadecyl acrylate) and poly(4-vinylpyridine-*r*-*n*-octadecyl methacrylate) were successfully synthesised via atom transfer radical polymerization (ATRP) using 10-phenylphenothiazine as the photo-induced catalyst. The resulting copolymers were structurally characterised by proton nuclear magnetic resonance (^{1}H NMR) and the interactions were analysed by Fourier-transform infrared (FTIR) spectroscopy.

Keywords: **ATRP, metal-free, *n*-octadecyl, pyridine.**

Classification number: **2.2**

Introduction

Controlled radical polymerization (CRPs) has emerged as one of the most far reaching developments in polymer synthesis and has contributed fundamental techniques to prepare polymers with well-defined structure and architecture [1, 2]. Concerning CRP techniques, atom transfer radical polymerization (ATRP) is arguably the most utilized method as it is applicable to the polymer synthesis of a variety of monomers. One limitation of using ATRP is metal contamination of the products. Although metal loadings in a catalyst can be limited to parts per million (ppm), the residual metal in the products may cause difficulties in many sensitive applications such as biomaterials, microelectronics, etc [3]. However, recently developed photocatalysts for ATRP have been introduced as a potential method to synthesise polymers with complete elimination of transition metal residue and thus be less affected by reaction media [4].

N-octadecyl is a hydrocarbon chain (18C) that possesses highly hydrophobic properties. These long alkyl chains may crystalline when present in a polymer as side functional groups, even in the amorphous polymer backbone. Due to these properties, polymers consisting of *n*-octadecyl groups may be used for applications in self-assembling amphiphilic polymers [5] or self-healing materials [6].

Pyridine is also an interesting chemical structure. It possesses one lone pair of electrons excluded from the aromaticity such that they can bind with protons. Therefore, pyridine is alkaline and could also coordinate with transition metal ions or hydrogen to form complexes or hydrogen bonding interactions [7, 8]. This work focuses on combining

*Corresponding author: Email: nguyenthilethu@hcmut.edu.vn

the special properties of the two functional groups stated above into one copolymer with the expectation of compatible polymerization as well as interaction formation between polymer chains.

In this study, 10-phenylphenothiazine was used as a commercial photo-induced catalyst. We report the synthesis and characterisation of two copolymers of 4-vinylpyridine and *n*-octadecyl acrylate (or *n*-octadecyl methacrylate) as a first step toward applying metal-free ATRP to the synthesis of those potential copolymers. We expect the hydrophilicity of 4-vinylpyridine, as well as hydrophobicity of the *n*-octadecyl long chains, to contribute interesting properties, such as self-assembly or micelle formation, to the resulting copolymers.

Experimental section

Materials

4-vinylpyridine (4VP, 95%), *n*-octadecyl acrylate (OA, 97%), *n*-octadecyl methacrylate (OMA, 97%) were purchased from Sigma Aldrich and passed through an alumina column to remove the inhibitor. 10-phenylphenothiazine (P, Sigma Aldrich, >95%), ethyl 2-bromo-2-methylpropionate (I, Sigma Aldrich, 98%), tetrahydrofuran (THF, 99.8%, no stabilizer) were purchased from Acros Organics. Methanol and other solvents (Fisher, >98%) were also used.

Instrumentation

The ^{1}H NMR spectra were recorded in deuterated chloroform ($CDCl_3$), with TMS as the internal reference, on a Bruker Avance 500 MHz spectrometer. Gel permeation chromatography (GPC) measurements were performed on a PL-GPC 50 gel permeation chromatograph system equipped with a refractive index (RI) detector. THF was used as the eluent at a flow rate of 1.0 ml/min and the molecular weights and molecular weight distributions were calculated with reference to polystyrene standards. The FTIR spectra collected from the average of 252 scans with a resolution of 4 cm^{-1}, were recorded from a KBr disk on an FTIR Bruker Tensor 27.

Synthesis of copolymers

Poly (4-vinylpyridine-*r*-*n*-octadecyl acrylate) - P(4VP-*r*-OA) and poly (4-vinylpyridine-*r*-*n*-octadecyl methacrylate) - P(4VP-*r*-OMA) were prepared in two-neck flasks (Scheme 1). The reaction systems were flamed three times and filled with nitrogen before any chemicals were added. 4-vinylpyridine, *n*-octadecyl acrylate (or *n*-octadecyl methacrylate), THF, 10-phenylphenothiazine, and ethyl 2-bromo-2-methylpropionate ([4VP]/[OA]/[I]/[P] and [4VP]/[OMA]/[I]/[P]=100/50/1/1) were, respectively, added into the flask under nitrogen. The mixture was stirred at RT for 15 min and then degassed with three freeze-pump-thaw cycles. Then, polymerization was carried out in a UV box while the mixture was continuously stirred. After 48 h of reaction time, the UV light was turned off and the mixtures were stirred in the dark for 30 min for stabilisation. Finally, the copolymers were precipitated twice in cold methanol and dried under vacuum until the weight was unchanged.

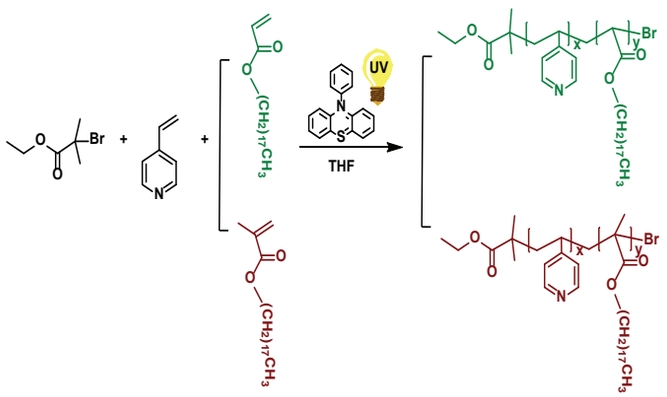

Scheme 1. Synthesis of P(4VP-*r*-OA) and P(4VP-*r*-OMA).

Results and discussion

After a 48 h reaction time, P(4VP-*r*-OA) and P(4VP-*r*-OMA) were received, giving gravimetric yields of 75 and 80%, respectively. From the GPC analysis (Fig. 1), the average molecular weight (Mw) of P(4VP-*r*-OA) was 12032 (PDI=1.77) whereas that of (4VP-r-OMA) was 18556 (PDI=1.59). The large distribution of molecular weights may result from poor compatibility between the monomers present in reaction mixtures during the period of co-polymerization [9].

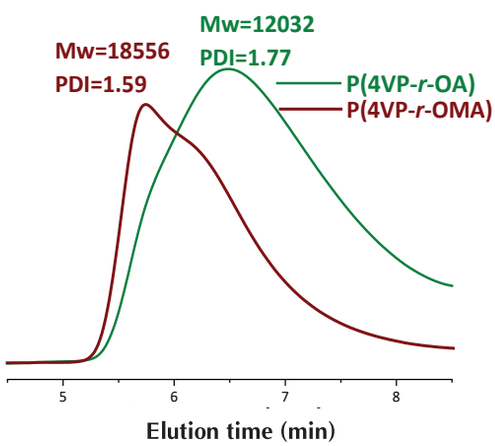

Fig. 1. GPC chromatograms of P(4VP-r-OA) and P(4VP-r-OMA).

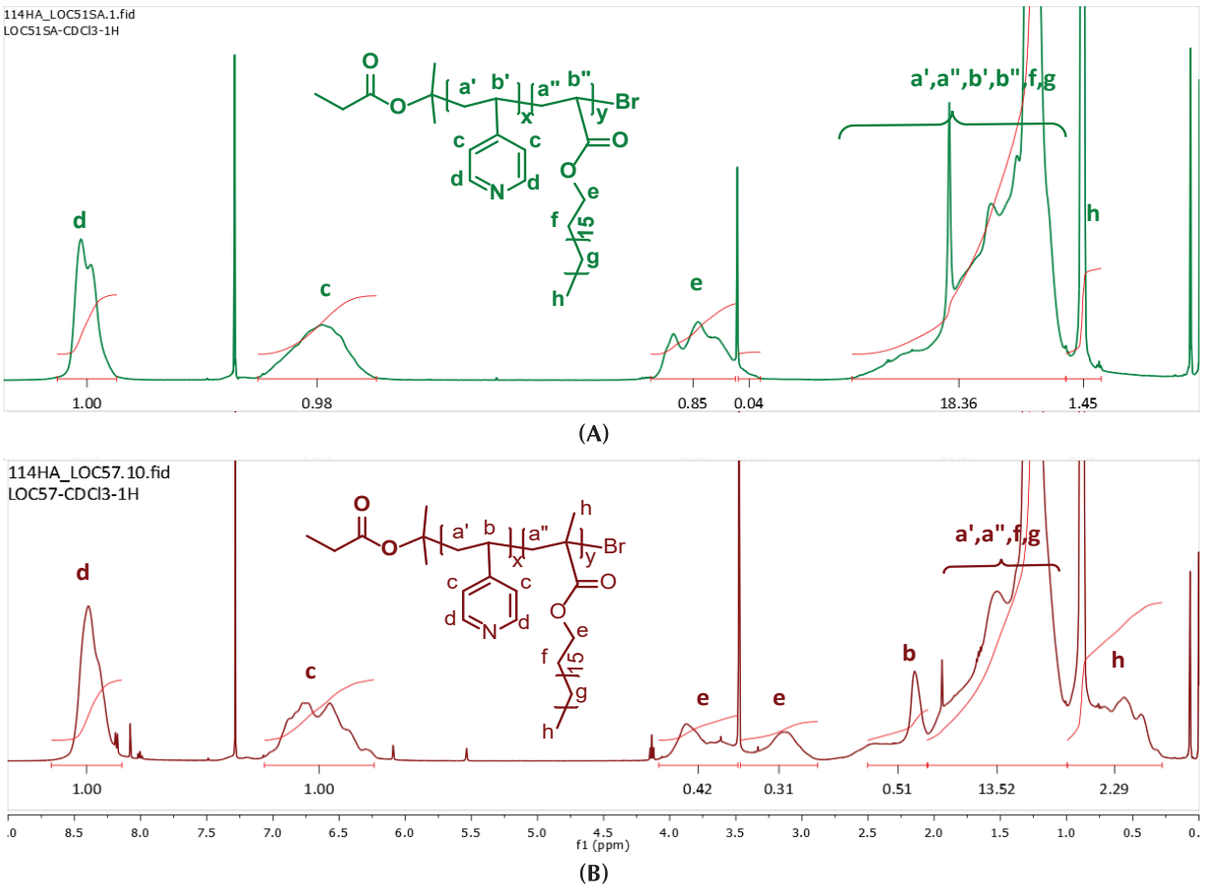

Fig. 2. ^{1}H-NMR spectra of P(4VP-r-OA) (A) and P(4VP-r-OMA) (B).

Study of copolymer structures

The structure of P(4VP-r-OA) and P(4VP-r-OMA) was characterised by proton nuclear magnetic resonance spectroscopy. The results are shown in Fig. 2. For P(4VP-r-OA), the chemical shifts (δ) were 8.20-8.56 ppm (d, 2H, meta-protons from pyridine ring), 6.27-7.07 ppm (c, 2H, ortho-protons from pyridine ring), 3.30-4.08 ppm (e, 2H, -O-CH_2- from *n*-octadecyl group), 0.99-2.61 ppm [a', a", b', b", f, g, 38H, protons from vinyl group (6H) and -CH_2-[CH_2]$_{15}$- from *n*-octadecyl group (32H)], and 0.71-0.99 ppm (h, 3H, methyl protons (CH_3) from *n*-octadecyl group). For P(4VP-r-OMA), the δ = 8.15-8.60 ppm (d, 2H, meta-protons from pyridine ring), 6.34-7.0 ppm (c, 2H, ortho-protons from pyridine ring), 2.87-4.00 ppm (e, 2H, -O-CH_2- from *n*-octadecyl group), 2.04-2.26 ppm (b, 1H, -CH- from vinyl group), 1.00-2.04 ppm (a", a", f, g, 36H, -CH_2- from vinyl and methacrylate groups (4H) and -CH_2-[CH_2]$_{15}$- from *n*-octadecyl group (32H)), and 0.28 -1.00 ppm (h, 6H, methyl protons (CH_3) from *n*-octadecyl and methacrylate groups). The different ratios, as well as interaction between the two units in the two copolymer chains, may be the cause of the atypical of chemical shifts at 2.125 and 3.125 ppm.

In addition, by measuring the relative intensities of the meta-protons from the pyridine ring (d, 2H) and the methylene protons (e, 2H) from the *n*-octadecyl group, the molar ratio of the two units in the copolymers can be calculated. Particularly, the fraction of 4VP/OA in P(4VP-*r*-OA) was 1.03 and the value of 4VP/OMA in P(4VP-*r*-OMA) was 1.31, whereas the feeding ratio of 4VP over OA (or OMA) was 2/1.

Study of interaction in copolymers

Both P(4VP-*r*-OMA) and P(4VP-*r*-OA) were analysed by FTIR, which illustrated the characteristic vibrations of the pyridine ring evidenced by the absorption bands at 1596.99 cm^{-1} (Fig. 3). The absorption bands at 1068.52 and 993.30 cm^{-1} are observed to confirm the in-plane and out-of-plane rings C-H bending, respectively [10].

The absorption band of C=O at 1730 cm^{-1} in poly (*n*-octadecyl acrylate) and poly (*n*-octadecyl methacrylate) were slightly broadened at the lower wavenumber may be caused by the hydrogen bonding of C=O and pyridine in the copolymer. Moreover, the formation of hydrogen bonding also slightly shifts the deformation band of pyridine at 1068.52 cm^{-1} to 1070.45 cm^{-1}.

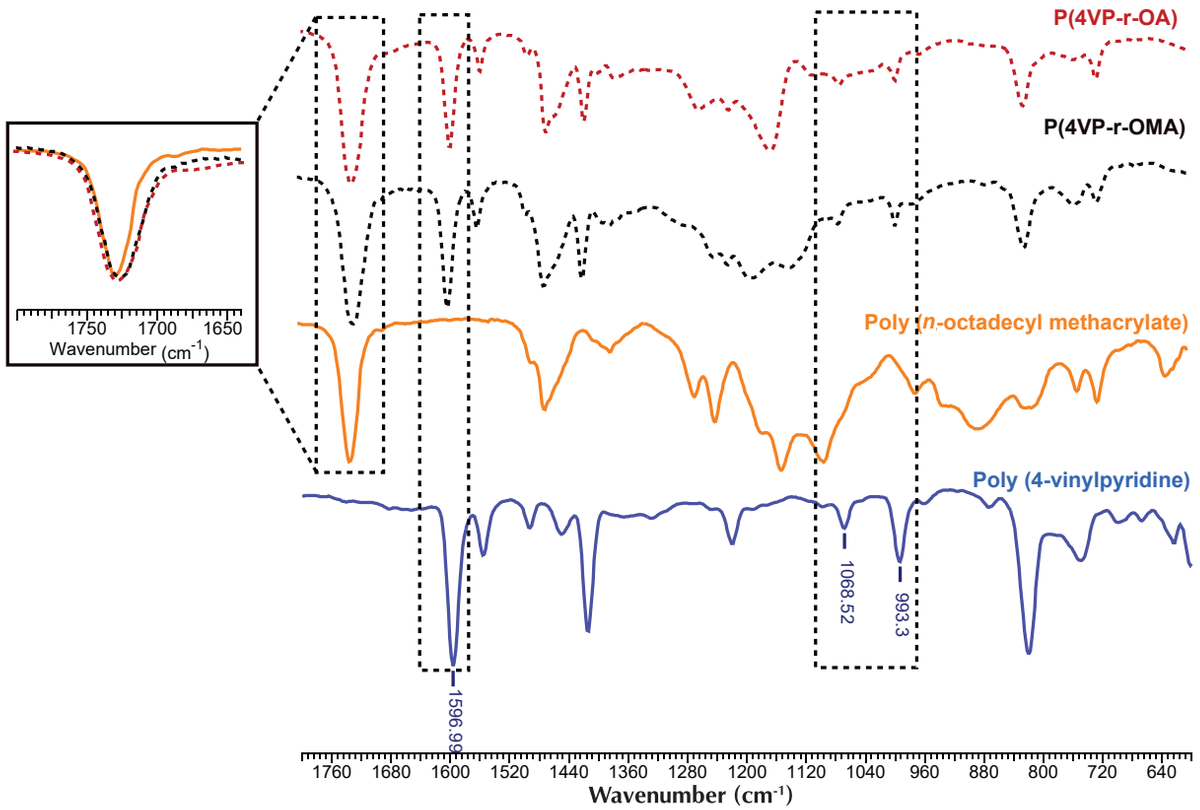

Fig. 3. FTIR spectrum of P4VP (blue line), POMA (orange line), P(4VP-*r*-OMA) (black line) and P(4VP-*r*-OA) (red line).

Conclusions

In conclusion, P(4VP-*r*-OMA) and P(4VP-*r*-OA) were successfully prepared via ATRP using 10-phenylphenothiazine as the photocatalyst with the feeding ratio of [4VP]/[OA or OMA]/[I]/[P] = 100/50/1/1), which gave high yields. More importantly, the use of an organic catalyst generated products with no metal contamination. When the feeding ratio of 4VP/OA (or OMA) was 2/1 (mol/mol), the unit fraction of 4VP/OA in P(4VP-*r*-OA) was 1.03 and that of 4VP/OMA in P(4VP-*r*-OMA) was 1.31.

ACKNOWLEDGEMENTS

This research is funded by Vietnam National Foundation for Science and Technology Development (NAFOSTED) under grant number 03/2019/TN.

The authors declare that there is no conflict of interest regarding the publication of this article.

REFERENCES

[1] M. Ouchi, T. Terashima, M. Sawamoto (2009), "Transition metal-catalyzed living radical polymerization: toward perfection in catalysis and precision polymer synthesis", *Chem. Rev.*, **109(11)**, pp.4963-5050.

[2] N.J. Treat, H. Sprafke, J.W. Kramer, P.G. Clark, B.E. Barton, J. Read de Alaniz, B.P. Fors, C.J. Hawker (2014), "Metal-free atom transfer radical polymerization", *J. Am. Chem. Soc.*, **136(45)**, pp.16096-16101.

[3] K. Matyjaszewski, N.V. Tsarevsky (2014), "Macromolecular engineering by atom transfer radical polymerization", *J. Am. Chem. Soc.*, **136(18)**, pp.6513-6533.

[4] T.H. Nguyen, L.-T.T. Nguyen, V.Q. Nguyen, L.N.T. Phan, G. Zhang, T. Yokozawa, D.T.T. Phung, H.T. Nguyen (2018), "Synthesis of poly (3-hexylthiophene) based rod-coil conjugated block copolymers via photoinduced metal-free atom transfer radical polymerization", *Polymer Chemistry*, **9(18)**, pp.2484-2493.

[5] J. Zhou, L. Wang, X. Dong, Q. Yang, J. Wang, H. Yu, X. Chen (2007), "Preparation of organic/inorganic hybrid nanomaterials using aggregates of poly (stearyl methacrylate)-b-poly (3-(trimethoxysilyl) propyl methacrylate) as precursor", *Eur. Polym. J.*, **43(5)**, pp.1736-1743.

[6] H. Jiang, L. Duan, X. Ren, G. Gao (2019), "Hydrophobic association hydrogels with excellent mechanical and self-healing properties", *Eur. Polym. J.*, **112**, pp.660-669.

[7] Y. Chen, W. Zhao, J. Zhang (2017), "Preparation of 4-vinylpyridine (4VP) resin and its adsorption performance for heavy metal ions", *RSC Advances*, **7(8)**, pp.4226-4236.

[8] J. Xia, X. Zhang, K. Matyjaszewski (1999), "Atom transfer radical polymerization of 4-vinylpyridine", *Macromolecules*, **32(10)**, pp.3531-3533.

[9] B. Reining, H. Keul, H. Höcker (1999), "Chloro-telechelic poly(ethylene oxide)s as initiators for the atom transfer radical polymerization (ATRP) of styrene and methyl methacrylate: structural features that affect the initiation efficiency", *Polymer*, **40(12)**, pp.3555-3563.

[10] K. Wu, Y. Wang, W. Hwu (2003), "FTIR and TGA studies of poly (4-vinylpyridine-co-divinylbenzene)-Cu(II) complex", *Polym. Degrad. Stab.*, **79(2)**, pp.195-200.

Doi: 10.31276/VJSTE.62(1).32-37

Pectin and cellulose extraction from passion fruit peel waste

Thi Tuyet Mai Phan*, Thi Sen Ngo

Department of Chemistry, University of Science, Vietnam National University, Hanoi

Received 26 August 2019; accepted 27 December 2019

Abstract:

Pectin and cellulose were successfully extracted from passion fruit peel waste. The maximum pectin yield of the process was 12.60% at pH=2 for 1.5 h. The pure cellulose obtained from the passion fruit peel waste was prepared by refluxing of the passion fruit peel powder with 1 M NaOH and 1.25 M HNO_3 solutions at 90°C for 1 h and 1.5 h, respectively. The passion fruit peel cellulose was converted to carboxymethyl cellulose (CMC) by etherification. The pure cellulose was soaked in a mixed solution of isopropyl alcohol and NaOH for 1.5 h. After that, it was reacted with cholroacetic acid at 70°C for 1.5 h. The optimum conditions for carboxymethylation were 5 g cellulose, 2.0 g cholroacetic acid, and 15 ml 20%w/v NaOH. The optimised product had a degree of substitution (DS) of 0.78 and was used as constituent in a biopolymer.

Keywords: **carboxymethyl cellulose, cellulose, passion fruit peel waste, pectin.**

Classification number: **2.2**

Introduction

Vietnam is one of the world's largest producers, consumers, and exporters of fresh and produced passion fruit. Passion fruit peel accounts for 80% of the fruit's weight, resulting in a very large amount of waste. Instead of recovering the waste, most companies choose to throw them away, causing environment pollution that subsequently has an adverse effect on human health. Passion fruit peels contain about 42% dry weight of cellulose and 18% pectin [1, 2]. Therefore, the potential of cellulose and pectin recovery from this waste is very high and quite feasible. Recovering value from fruit processing waste provides an alternative way to reduce the cost of biological waste disposal whilst creating added value for the fruit juice processing industry. However, only a few works have been found that mention the problem of pectin recovery [3-6] from passion fruit by-products. Furthermore, to the best knowledge of the authors of this work, no research on the simultaneous extraction of pectin and cellulose from passion fruit peel has been published. Therefore, studies on the recovery of cellulose and pectin from this waste is essential and important. The purpose of this work is to confirm the potential of Vietnamese passion fruit peels as a raw material for industrial pectin extraction and CMC production.

Experimental

Materials and passion fruit peel source

The main chemicals used in this study include monochloroacetic (MCA) (UK), acetic acid, nitric acid, and sodium hydroxyl (Merck). The solvents include methanol, ethanol, isopropanol, and acetone (Merck).

Preparation methods

Pectin extraction from passion fruit peels:

The extraction procedure was done according to the Kulkarni method [7] with a slight modification. Ten grams of dried passion fruit peel powder were mixed with 150 ml of diluted HNO_3 at 70°C. The dark slurry obtained was filtered by using a centrifuge machine. The residual solid part was put into a clean Erlenmeyer flask (volume of 250 ml) for the separation of the cellulose. The resulting slurries were cooled to 4°C and centrifuged for 30 min at 5000 rpm. The supernatant was precipitated with ethanol under an ethanol/concentrate ratio (v/v) of 1.5 at 4°C for 30 min in order to achieve pectin flotation. The floating pectin was separated by filter paper and rinsed with 96% ethanol. At the end of the process, the pectin precipitate was washed with acetone and dried in an oven at 65°C for 24 h. The

*Corresponding author: Email: maimophong@gmail.com

dried pectin was ground into a fine powder. The yield of the pectin was gravimetrically determined and expressed as a weight of the extracted dried pectin to 100 g of the dried peel used for extraction. This process was carried out at different pH values (pH = 1, 2, 3, 4) and different periods of time (t = 10, 30, 60, 90, 120 min). The treatments were carried out in duplicate.

The yield of the pectin was determined by using the below equation:

$$H_P(\%) = \frac{m_P}{m_0} x100$$

where H_p is the yield of pectin, m_p is the weight of obtained pectin, and m_0 is the weight of initial dried passion fruit peel powder.

Cellulose recovery from passion fruit peels:

Determination of optimum NaOH concentration: the solid residual part from the above process was treated with 50 ml of x M NaOH (x = 0.25 M, 0.50 M, 1.00 M, 1.25 M, 1.50 M) and cooked at 90°C for 60 min under continuous stirring. The dark slurry obtained was filtered and washed with 1 l of distilled water to the recover solid part. After that, this solid was treated with 50 ml of 1.25 M HNO_3 and cooked at 90°C for 90 min. This mixture was then filtered and washed with cold distilled water until the indicator paper did not change colour. The residue was dried in an oven at 60°C overnight until constant weight. Finally, the dried cellulose was ground and kept in a polyethylene bag for the cellulose modification in the next process.

Determination of optimum HNO_3 concentration: the solid residual part from the above process was treated with 50 ml of 1.0 M NaOH and cooked at 90°C for 60 min under continuous stirring. After that, this solid was treated with 50 ml of y M HNO_3 (y = 0.3 M, 0.75 M, 1.25 M, 1.75 M) and cooked at 90°C for 90 min. Then, the cellulose recovery procedure was repeated as above.

The yield of the cellulose extraction was determined by using the below equation:

$$H_C(\%) = \frac{m_C}{m_0} x100$$

where H_C is the yield of the cellulose extraction, m_c is the weight of the obtained cellulose, and m_0 is the weight of the initial dried passion fruit peel powder.

Synthesis of CMC:

Five grams of cellulose extraction obtained from passion fruit peel powder was added to 50 ml of isopropanol under continuous stirring for 30 min. Then, 15 ml of (10%, 15%, 20%, 25% w/v) NaOH was added dropwise into the mixture and further stirred for 1 h at room temperature. The carboxymethylation was started when y gram of MCA (y = 1.0 g, 1.5 g, 2.0 g, 2.5 g) was added under continuous stirring for another 90 min at 70°C. The solid part was neutralized with acetic acid to pH=7 and washed three times by soaking in 20 ml of ethanol for 10 min to remove undesirable by-products. The obtained CMC was filtered and dried at 60°C until constant weight and kept in a dry place.

The yield of the CMC was determined by using the below equation:

$$H_{CMC} = \frac{m_{CMC} - m_C}{m_C} x100$$

where H_{CMC} is the yield of the CMC, m_{CMC} is the weight of the obtained CMC, and m_C is the weight of the cellulose used to synthesis CMC.

Solubility of CMC: m_0 g of CMC were dissolved in 100 ml H_2O, at 50°C, for 30 min. After that, these were filtrated by filter paper. The solubility of the CMC was determined by using the below equation:

$$S = m_0 - m$$

where m_0 is the initial CMC weight and m is the excess CMC weight.

Research methods

Infrared spectroscopy (FTIR):

FTIR spectra were recorded on a FT/IR-6300 spectrometer, 32 times of scan, with a resolution of 4 cm^{-1}, in the wavenumber range of 600-4000 cm^{-1}.

The degree of substitution, DS_{rel}, of the carboxyl group in CMC can be determined by FTIR spectra by means of taking the ratio of the absorption spectra, as shown in the below equation [8]:

$$DS_{rel} = \frac{A_{1614}}{A_{2912}} - B$$

where is A_{1614} is the absorbance at 1614 cm^{-1}, which is assigned to the stretching vibration of the carboxyl group (COO^-), A_{2912} is the absorbance at 2912 cm^{-1}, which is assigned to the stretching vibration of methine (C-H), and B is a numerical constant correspondent to the A_{1614}/A_{2912} ratio of the cellulose, which was found to be zero. A linear relationship between the absolute and relative value of the degree of substitution was proved by Pushpamalar [9] as shown in the below equation:

$DS_{abs} = 0.4523 DS_{rel}$

Viscosity measurement method:

The average molecular weight (M) of the polymers was determined by viscometry according to the Mark and Houwink-Sakurada equation:

$[\eta] = K.M^{\alpha}$

where $[\eta]$ ($dl.g^{-1}$) is the intrinsic viscosity, M is the average molecular weight of the polymers, K and α are the characteristic constants for the used polymer-solvent systems. At room temperature (25°C) for pectin, K and α are $1.4x10^{-6}$ and 1.43 [10], respectively. At room temperature (25°C) for CMC (CMC was dissolved in 0.1 M NaCl solution), K and α are $7.3x10^{-3}$ and 0.93, respectively [8].

Intrinsic viscosity measurements were carried out using an Ubbelohde capillary viscometer having an internal diameter of 0.5 mm and a length of 10 cm. The flow times were recorded using a stopwatch.

Results and discussion

Pectin extraction

Effect of pH on the yield of pectin extraction:

The results presented in Fig. 1A indicated that the pH of the diluted HNO_3 solution had a significant impact on the pectin yield from passion fruit peel waste. The maximum yield of pectin was obtained at an extraction pH of 2.0. This is in agreement with the findings of other researchers who found that the highest yield of pectin was achieved from passion fruit peel at pH 2 [3, 7, 10-12]. This may be due to increasing acid strength (pH<2) that could hydrolyse and degrade pectin to uncollected small pectin particles resulting in an increased pectin-particle solubility and, consequently, pectin precipitation with alcohol is hindered [13]. On the other hand, at lower acid strength (pH>2), pectin molecules can be partially solubilized without degradation leading to difficulty in extraction of some pectin fractions due to attachment to other cell wall components [14].

Effect of treatment time on the yield of pectin extraction:

The yield of pectin extraction at different extraction times is shown in Fig. 1B. The extraction time was maintained at 10, 30, 60, 90 and 120 min for each extraction. The other extraction conditions, such as the ratio of water to peels, extraction temperature, and pH of the extracting medium were maintained at 15:1, 70°C, and 2, respectively. The results shown that the yield of pectin increased with extraction time up until 90 min. However, after further increase of the extraction time to 120 min, the pectin yield reduced. This could be due to the partial degradation of pectin. These results are in agreement with Xue [15]. It can be seen that, when reaction time was increased from 60 to 90 min, the pectin yield showed no significant increase, with pectin yield of 12.3 and 12.6%, respectively. Thus, the optimum time of extraction for the maximum yield of pectin was found to be 90 min. But, in case of prioritizing economic efficiency, a reaction time of 60 min is reasonable.

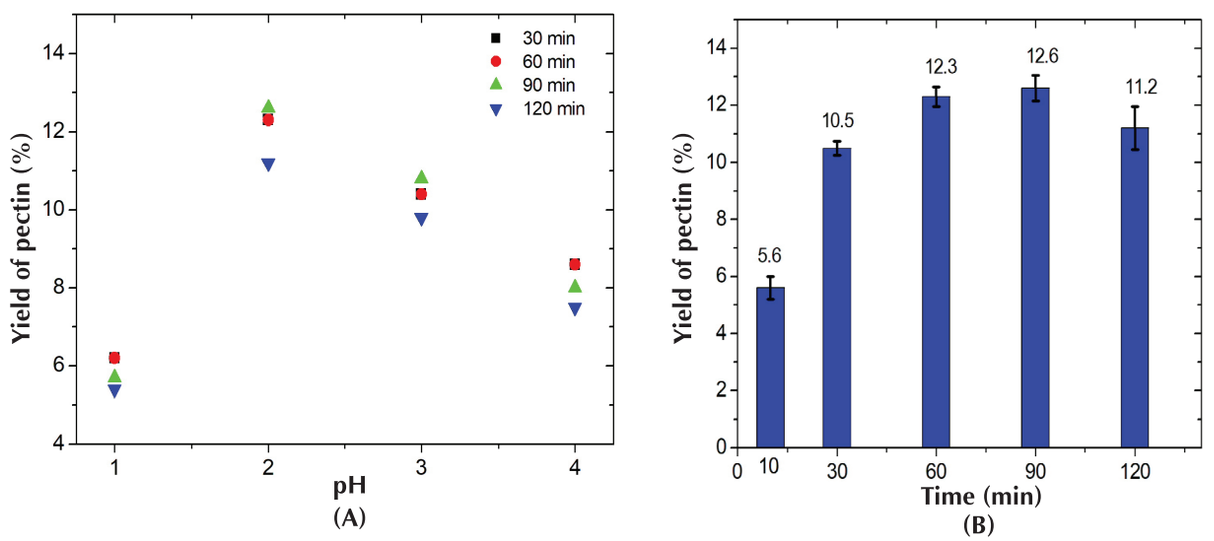

Fig. 1. Effect of (A) pH and (B) treatment time at pH 2 on yield of pectin extraction.

Characterization of obtained pectin:

The average molecular weight of pectin is M = 12532.82 (g/mol). The obtained pectin was characterized by FTIR spectroscopy and the result is shown in Fig. 2.

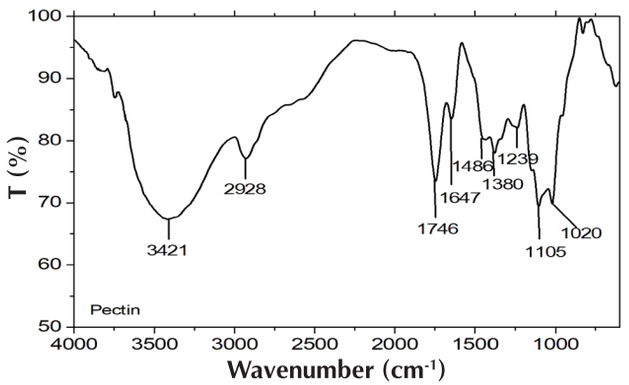

Fig. 2. FTIR spectroscopy of pectin.

The band at 3421 cm^{-1} can be assigned to the OH stretching mode, while the signal observed at 2928 cm^{-1} is attributed to the stretching vibrations of the C-H groups. The distinct band registered at 1746 cm^{-1} corresponds to asymmetric C=O stretching vibrations present in carboxyl or $COOCH_3$ groups. The band at 1647 and 1486 cm^{-1} may be assigned to COO-symmetrical and asymmetrical stretching vibrations of polygalacturonic acid, respectively. The occurrence of the band at 1380 cm^{-1} likely comes from the bending vibrations of C-H or O-H groups, while the presence of distinct bands observed together in the range of 1239-1020 cm^{-1} are associated with C-O-C stretching vibrations. The signal at 1105 cm^{-1} implies overlapping of the bands coming from C-O stretching and OH bending vibrations found in CH-OH groups. The band centered at 1746 cm^{-1} has been utilized to probe the degree of esterification (DE) in pectin. The FTIR spectroscopy results are entirely similar to other authors' results [16]. Therefore, the pectin extracted from passion fruit peel waste is of high purity.

Cellulose extraction

The process of cellulose recovery was conducted at various concentrations of NaOH and HNO_3 to determine the optimum treatment conditions. The results are listed in Table 1.

Table 1. Cellulose yield with various NaOH concentrations and HNO_3 concentrations.

Yield of cellulose	C_{NaOH} M, (HNO_3 1.25 M)				
	0.25	0.50	1.00	1.25	1.50
H_c(%)	21.70	28.50	32.13	29.60	26.8
Yield of cellulose	C_{HNO3} %, (NaOH 1 M)				
	0.30	0.75	1.25	1.75	
H_c(%)	23.50	28.50	32.13	26.20	

From Table 1 we see that the yield of cellulose varies depending on the change of NaOH concentration. The maximum yield of cellulose extraction was obtained at NaOH 1 M, and upon further increasing the NaOH concentration, the cellulose yield reduced.

In this experiment, HNO_3 was used to treat excess hemicellulose in the previous stage and the yield of cellulose reached the best result at HNO_3 1.25 M. After that, when the concentration of HNO_3 increases, the yield of pectin decreases (as shown in Table 1). This might be due to the destruction of the cellulose structure at high concentrations of HNO_3. In brief, the highest yield of the cellulose extraction is 32.13% at a NaOH concentration of 1.00 M and HNO_3 of 1.25 M.

Characterizations of cellulose by FTIR spectroscopy: FTIR spectroscopy of cellulose is displayed in Fig. 3. The band at 3350 cm^{-1} can be assigned to the OH stretching mode, while the signal observed at 2912 cm^{-1} is attributed to the stretching vibrations of the C-H groups of molecular cellulose. The C-C ring breathing band appeared at 1159 cm^{-1}. Besides, the vibration peaks at 1365 cm^{-1} and 1425 cm^{-1} are assigned to the CH and C-O bending vibration in the polysaccharide aromatic rings, respectively. Lastly, the wavenumber range of about 895-1053 cm^{-1} is associated with the β-(4, 17)-glycosidic linkages between the glucose units in cellulose [8]. FTIR spectroscopy of the cellulose extracted from passion fruit peel waste is similar to the result of Hong who recovered cellulose from sugarcane bagasse [8]. In addition, the absence of peaks at 1600-1800 cm^{-1}, characterized for the functional groups C=O and the aromatic ring of hemicellulose and lignin molecules [17, 18], proved that hemicellulose and lignin were completely removed. This means that the recovered cellulose is of high purity. This pure cellulose was then used for CMC synthesis.

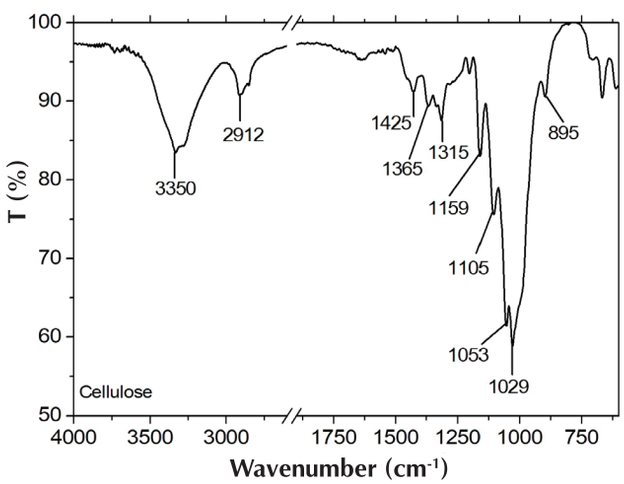

Fig. 3. FTIR spectroscopy of extracted cellulose.

CMC synthesis

Effect of NaOH concentration on DS and yield of CMC:

NaOH was used as an alkaline reagent to swell cellulose chains, which provides the ability of substitution by sodium carboxymethyl groups in cellulose units. The DS of the CMC obtained with different concentrations of sodium hydroxide are shown in Table 2.

Table 2. The yield and DS of synthesized CMC with various NaOH concentrations.

	NaOH, %wt			
	10	*15*	*20*	*25*
H_{CMC}, %	32.1	52.3	63.8	56.6
DS	0.48	0.57	0.78	0.61

As shown in Table 2, the DS of the CMC increased with NaOH concentration and attained the highest DS of 0.78 at a NaOH concentration of 20% (w/v). However, upon further increase of the NaOH concentration, a reduction in DS value was observed. This can be explained by the degradation effect of high concentrations of alkali reagent on CMC polymer chains. These results are similar to that of Hong [8] and Sunardi [12]. Table 2 also shows the CMC yields from different experiments, which had similar trends as the DS results.

Effect of MCA weight on DS and yield of CMC:

The effect of MCA weight on the DS value was determined by changing the amount of MCA from 1.0 g to 2.5 g. The result is shown as in Table 3, where the DS of the CMC increased with an increasing amount of MCA in a range of 1.0-2.0 g and then decreased slightly with further increase of the MCA amount. The highest DS value was observed at MCA weight of 2.0 g. The reason for this observation is that an undesired side reaction occurred that dominated CMC production with the greater availability of the MCA molecules. This range of DS value (from 0.48-0.78) is similar to another author's report [8] for bassage waste. Table 3 also shows that the trend in the change of CMC yield is similar to that of the DS.

Table 3. The yield and DS of CMC synthesized with various amount of MCA.

	Amount of MCA			
	1.0	*1.5*	*2.0*	*2.5*
H_{CMC}, %	43.7	63.8	79.5	72.2
DS	0.58	0.71	0.78	0.77

The optimum condition for carboxymethylation was 5 g cellulose, 2.0 g chloroacetic acid, and 15 ml of 20% w/v NaOH solution. The obtained CMC had a DS of 0.78 and yield of 79.5%.

Solubility of CMC

Solubility of CMC in water is one of the important properties that determine CMC applications, and depend on the DS of CMC. The relationship between DS and solubility can be plotted as a linear equation, and this result shows that the solubility of CMC in water increases linearly with the increasing DS. Surely, this was due to the greater substitution of carboxymethyl groups for the hydroxyl groups of the cellulose polymers. These carboxymethyl groups act as hydrophilic groups, so the increase of the DS will improve the CMC's ability to immobilize water in the system (Fig. 4).

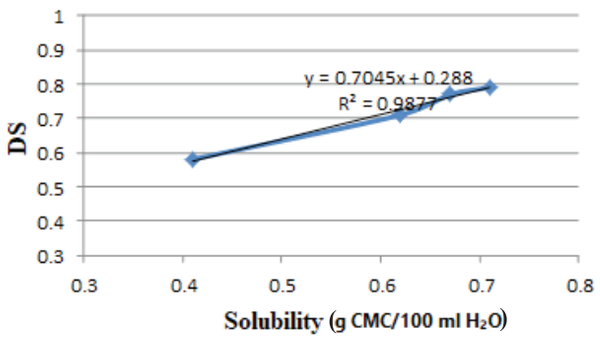

Fig. 4. The relationship between DS and solubility of CMC.

Thus, it can be concluded that the solubility of CMC depends on DS. The solubility of CMC with a given DS can be extrapolated from the linear equation.

Characterizations of CMC by FTIR spectroscopy: the FTIR spectroscopy of the synthesized CMC is shown in Fig. 5.

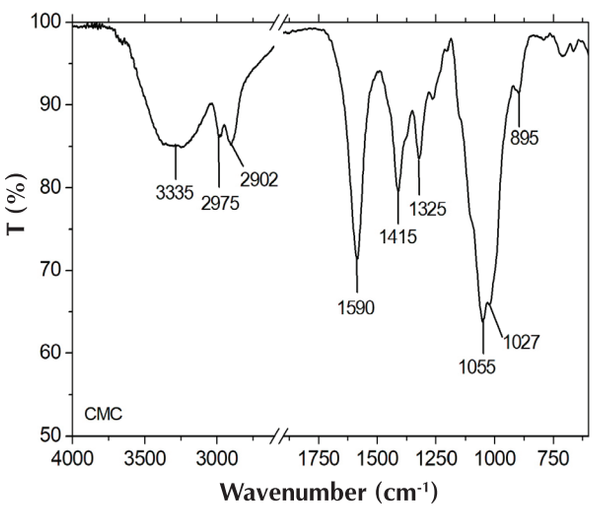

Fig. 5. FTIR spectroscopy of CMC from passion fruit peel.

The absorption peak at 3335 cm^{-1} appearing in the spectra indicates the free OH stretching vibration as well as inter-and intramolecular hydrogen bonds in the cellulose molecules. The bands at 2902 cm^{-1} and 1415 cm^{-1} are attributed to the stretching and scissoring vibrations of the C-H groups. The bands at 1055 cm^{-1} and 1027 cm^{-1} are relevant to the β-(4, 17)-glycosidic linkages between the glucose units in cellulose [8, 9, 19]. The presence of a strong absorption band at 1590 cm^{-1} was attributed to C=O stretching, confirming the presence of the -COO and -COONa groups, indicating the successful etherification of cellulose. This peak does not exist in the FTIR spectroscopy of cellulose (Fig. 2). The above analysis results are similar to those of earlier publications of Hong [8] for bassage waste and Sunardi [12] for purun tikus.

Conclusions

Pectin was successfully extracted from passion fruit peel waste with a maximum pectin extraction yield of 12.60 % at pH=2 for 90 min in a diluted HNO_3 solution. The obtained pectin was confirmed by FTIR spectra with the appearance of peaks at 1746 cm^{-1} and 1647 cm^{-1} related to methoxylated and free carboxyl groups, respectively. Cellulose was successfully recovered from passion fruit peel waste with yield of 32.13% at NaOH concentration of 1 M and HNO_3 of 1.25 M. CMC has been obtained by etherifying cellulose with monochloroacetic acid. The optimal condition for carboxymethylation was 5 g cellulose, 2.0 g cholroacetic acid, and 15 ml of 20% w/v NaOH solution. The optimised CMC products have a DS of 0.78 and yield of 79.5%. The chemical structure of the CMC was confirmed by FTIR spectra, indicating the C=O group at 1590 cm^{-1}. These results show that the separation of cellulose and pectin from passion fruit peel waste has great potential and feasibility.

The authors declare that there is no conflict of interest regarding the publication of this article.

REFERENCES

[1] J.C.C. Esquivel1, C.N. Aguilar, J.C. Montanez, A. Brandelli, J.D. Espinoza-Perez, C.M.G.C. Renard (2010), "Pectin from passion fruit fiber and its modification by pectinmethylesterase ", *J. Food Sci. Nutr.*, **15**, pp.57-66.

[2] M.H. Canteri, A. Sheer, C. Petkowicz, C. Ginies, C. Renard, G. Wosiacki (2010), "Physicochemical composition of the yellow passion fruit pericarp fractions and respective pectic substances", *J. Food Nutr. Res.*, **49(3)**, pp.113-122.

[3] S.Q. Liew, N.L. Chin, Y.A. Yusof (2014), "Extraction and characterization of pectin from passion fruit peels", *Agriculture and Agricultural Science Procedia*, **Vol.2**, pp.231-236.

[4] B.R. Sharma, et al. (2006), "An overview on pectins", *Times Food Processing Journal*, **(6-7)**, pp.44-51.

[5] Thi Xuan Sam Nguyen, Thi Huyen Le (2017), "Extraction of pectin from passion fruit peel for production of pectic oligosaccharides (POS)", *Vietnam Journal of Science and Technology*, **55(5A)**, pp.195-201.

[6] G.O. Locatelli, L. Finkler, L.L.C. Finkler (2019), "Orange and passion fruit wastes characterization, substrate hydrolysis and cell growth of cupriavidus necator, as proposal to converting of residues in high value added product, *An. Acad. Bras. Cienc.*, **91(1)**, pp.1-9.

[7] S.V. Kulkarni (2010), "Effect of extraction conditions on the quality characteristics of pectin from passion fruit peel", *Passiflora. F. Sci. Techno.*, **43**, pp.1026-1031.

[8] K.M. Hong (2013), *Preparation and Characterization of Carboxylmethyl Cellulose from Surgacane Bagasse*, Thesis of B.Sc. Chemistry, Faculty of Science Universiti Tunku Abdul Rahman, pp.30-33.

[9] V.L. Pushpamalar, et al. (2006), "Optimization of reaction conditions for preparing carboxymethyl cellulose from sago waste", *Carbohydrate polymers*, **64**, pp.312-318.

[10] M.Y. Sayah, R. Chabir, H. Benyahia, Y.R. Kandri, F.O. Chahdi, H. Touzani, F. Errachidi, (2016), "Yield, esterification degree and molecular weight evaluation of pectins isolated from orange and grapefruit peels under different conditions", *PLOS ONE*, **11(9)**, Doi: 10.1371/journal.pone.0161751.

[11] S. Rungrodnimitchai (2011), "Novel source of pectin from young sugar palm by microwave assisted extraction", *Procedia Food Science*, **1**, pp.1553-1559.

[12] N.M. Sunardi (2017), "Preparation of carboxymethyl cellulose produced from purun tikus (Eleocharis dulcis)", *The 4th International Conference on Research, Implementation, and Education of Mathematics and Science*, Doi: 10.1063/1.4995094.

[13] E. Kliemann, K.N.D. Simas, E.R. Amante, R. Amboni (2009), "Optimisation of pectin acid extraction from passion fruit peel (Passiflora edulis flavicarpa) using response surface methodology", *Inter. J. F. Sci. Techno.*, **44(3)**, pp.476-483.

[14] A.G.J. Voragen, G.J. Coenen, R.P. Verhoef (2009), "Pectin, a versatile polysaccharide present in plant cell walls", *Structural Chemistry*, **20(2)**, pp.263-275.

[15] Z.Z. Xue (2011), "Optimization of pectin extraction from citrus peel", *F. Sci.*, **18**, pp.128-132.

[16] C. Acikgoz (2011), "Extraction and characterization of pectin obtained from quince fruits (Cydonia vulgaris pers) grown in Turkey", *Asian J. Chem.*, **23(1)**, pp.149-152.

[17] J. Chumee, D. Seeburin (2014), "Cellulose extraction from pomelo peel: synthesis of carboxymethyl cellulose", *Inter. J. Mater. Metallurgical Eng.*, **8(5)**, pp.435-437.

[18] W. Xu, N. Reddy, Y. Yang (2009), "Extraction, characterization and potential applications of cellulose in corn kernels and distillers' dried grains with solubles (DDGS)", *Carbohydr. Polym.*, **76**, pp.521-527.

[19] S.A. Asl, M. Mousavi, M. Labbafi (2017), "Synthesis and characterization of carboxymethyl cellulose from sugarcane bagasse", *J. F. Process. Technol.*, **8(8)**, Doi: 10.4172/2157-7110.1000687.

Doi: 10.31276/VJSTE.62(1).38-42

Effect of UV filtering on dye-sensitised solar cells

Thai Hoang Nguyen[1, 2], Le Thanh Nguyen Huynh[1, 2], Thi Phuong Linh Tran[1], Viet Hai Le[1*]

[1]University of Science, Vietnam National University, Ho Chi Minh city
[2]Applied Physical Chemistry Laboratory, Vietnam National University, Ho Chi Minh city

Received 3 July 2019; accepted 15 November 2019

Abstract:

This work aimed to investigate the effect of commercial UV filter films (PS65, SEC04) on the performance and long-term outdoor stability of dye-sensitised solar cells (DSCs). The application of UV filter films to the DSCs lead to a slight decrease in cell performance. However, the cell performance remained constant after 2,000 h of outdoor exposure. Electrochemical impedance analysis showed a small transfer resistance in the TiO_2 photo-anode, which corresponded to the low recombination process of the electrons in TiO_2. The low electron recombination process supports the stable performance of the DSCs with the SEC04 film under outdoor conditions.

Keywords: **dye-sensitized solar cells performance, electrochemical impedance spectroscopy, outdoor testing, UV filter films.**

Classification number: **2.2**

Introduction

During the past half-century, the excessive consumption of fossil energy, together with the uneven distribution of fossil energy resources in the world, has pushed humanity to face serious environmental problems such as the greenhouse effect and lack of renewable energy resources. To overcome these problems, the development of clean and renewable energy sources must be a mandatory requirement at present and in the future. Among existing renewable energy sources, solar energy is considered to be the cleanest and safest choice. Solar cells are considered to be the most convenient method to turn solar energy into electricity and may even be an alternative to other energy sources since the invention of single-crystal solar cells in 1954. However, the issue of high cost is the biggest obstacle to be overcome in order for Si crystalline solar cells to be used by the masses [1, 2].

Dye-sensitized solar cells are progressively more developed to meet today's needs. The combination of photosensitizers with broad spectroscopic absorption and nanocrystalline oxide membranes allows for improved photo-multiplier tube (PMT) transformation efficiency, which has resulted in a significant transformation of light into electrical energy under a broad spectrum from UV to near-IR. Efficient solar energy-to-electricity conversion of 7.1% (AM 1.5, 750 W/m^2) was reached by Grätzel and O'Regan of the Swiss Federal Institute of Technology Lausanne, Switzerland (EPFL) in 1991 as an effective and eco-friendly replacement for crystal solar cells [1, 3]. EPFL recently achieved a record photovoltaic conversion efficiency of 15% [4]. DSCs has garnered full attention over the past decade due to low production costs and the ability to convert sunlight into electricity in an environmentally friendly manner. Hence, DSCs open up excellent prospects for the production of solar cells at a lower price than traditional technologies.

UV filters are flexible films that are applied to a glass surface to block UV and visible light at different levels. Over the past decade, there has been an increase in the number of manufacturers producing these filters. Most current filters can eliminate 95-99% UV radiation from in the wavelength range of 200 to 380 nm. UV filters are usually made of tightly pressed polyester layers that have many effects such as absorbing, scattering, or reflecting UV and visible light. Most of these membranes are soaked in dye or carbon particles or coated with a metal layer by a sputter. The metal coating is usually aluminium, which reflects the incident light, thus reducing UV transmission and visible light. Non-metallic layers contain organic compounds that absorb UV

*Corresponding author: Email: lvhai@hcmus.edu.vn

rays, preventing the UV rays from penetrating through the membrane. The four most prestigious compounds used for UV absorption include benzotriazoles hydroxyphenyl, hydroxyphenyl-triazines-s, oxalanilides, and 2-hydroxy benzophenones. Because the specific compounds used are often considered proprietary information, it is difficult to determine which compounds are present in current products.

DSCs utilize a TiO_2 photoanode, which is a semi-conductor that is photo-active in the UV range. Under UV lights, TiO_2 is activated and produces electrons and holes that bombard the dye in the electrolyte. As a result, UV filters are required to restrict the photo-catalytic properties of TiO_2 when the DSCs undergo outdoor exposure tests.

In this study, two types of UV filters were collected from several commercial products. Those with UV transmittance below 1% were used to protect the DSCs from the effects of UV radiation under outdoor conditions.

Experimental

Material

Ruthenium dye (N719), high stability electrolyte (HSE), thermal plastic sealant (surlyn), platinum paste (PT1), reflector titania paste (WER2-O), transparent titania paste (18NR-T), and FTO conducting glass (TEC15) were purchased from Dyesol (Australia). HCl, Ethanol, $TiCl_4$, DMF, and acetonitrile were purchased from Sigma-Aldrich (Germany). The commercial UV filters were supplied by an automobile shop.

Fabrication of DSCs

Anode preparation: the TEC15s glass substrates (as current collectors) were sonicated in a detergent solution for 15 min, then in 0.1 M HCl/ethanol for 30 min, and finally washed with distilled water. The substrate was soaked in a 40 mM $TiCl_4$ solution at 70°C for 30 min and then washed with distilled water and ethanol. The TiO_2 paste with a thickness of 12-14 µm was coated onto the conductive side of the substrate using the screen-printing method. Then, the TiO_2 coated electrodes were heated to 500°C under airflow for 30 min to obtain the TiO_2 photoanode.

Cathode preparation: the cathodes of the DSCs were fabricated via the screen-printing method using a PT1 platinum paste. The prepared cathodes were annealed at 450°C for 30 min.

DSCs assembly: the DSCs were assembled by placing a 25 µm Surlyn gasket between the photoanode and counter electrode and pressed with heat press at 170°C for 15 s. The N719 dye solution (10 mM in DMF) was injected into the space cells through a hole in the back of the cathode and remained for 4 min to ensure the dye was fully adsorbed in the TiO_2 film. Excess dye and DMF solvent were removed from the cell. Then, the space was cleaned with acetonitrile three times. HSE as the electrolyte solution was successively injected into the cells through a hole in the back of cathode. The dye soaking and electrolyte filling were carried out in a nitrogen-filled glove box to avoid oxygen and water. The cells were capped with a thin glass cover with a thermal sealant by heat press at 170°C for 15 s.

Characterization of DSCs performance: the photovoltaic performance was measured using a Keithley model 2400 multisource meter and an Oriel Sol1A (94061A, Newport, USA) solar simulator. A monocrystalline silicon reference solar cell (91150V - Oriel-Newport-USA) verified at NREL (USA) was used to adjust the solar simulator to the standard light intensity of one sun (100 mW/cm^2). Electrochemical impedance spectroscopy (EIS) on the fabricated DSCs was collected using an Autolab 302N (Ecochimie, Netherlands). The EIS measurement was carried out at open-circuit voltage under illumination. The frequency range is 0.01-100 kHz, and the alternating voltage amplitude was set at 10 mV.

Outdoor testing: the UV filter was applied on the photoanode side of the DSCs before aging testing. The outdoor test was carried out on the roof of a building at the University of Science, VNU-HCM. The tilt angle of the DSCs was 45° and faced due south [5]. The I-V curve and EIS were measured offline every seven days for two months.

Results and discussion

Filters

The filters from four commercial UV filter films were used to protect the DSCs. The optical properties of the four types of UV filters were assessed through optical transmission in the UV-Vis region. The UV-Vis spectra of the UV filters (Fig. 1) were measured between wavelengths of 200-900 nm, and the optical parameters of these UV filters are summarized in Table 1.

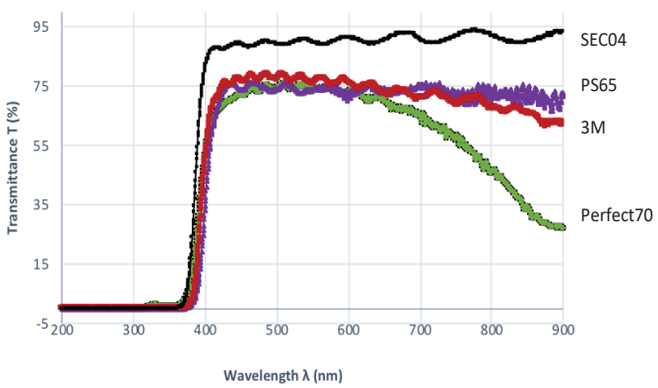

Fig. 1. The UV-Vis transmittance spectra of UV filters.

Table 1. Optical properties of UV filters.

UV filters name	Mean %T (500-800 nm)	λ at 50% T (nm)	λ at T<1% (nm)
SEC04	92	387	368
PS65	74	401	379
3M	74	397	379
Perfect70	67	392	357

In comparison with other commercial UV filters, the SEC04 filter has the highest mean percent transmittance (T%), and the PS65 filters have a better UV cut-off wavelength. Therefore, the SEC04 and PS65 filters were selected to protect for DSCs for the outdoor testing.

The effect of filtering upon the performance of DSCs

Figure 2 shows the I-V curve of an unfiltered and filtered DSC using the SEC04 UV filter. The short circuit current density (J_{sc}) and open-circuit voltage (V_{oc}) of filtered DSC are lower, in comparison with their unfiltered DSC. The effect of filtering upon the performance parameter of the DSCs is presented in Table 2. In both cases where the filter was applied, the efficiency (% η) was reduced due to a loss of light transmission through the UV filter. The reduction in % η is due to the overall transmission losses and increased UV cut-off to device [6]. From the UV-Vis data, the efficiency loss (% Δη) is larger in the DSC filtered with PS65 than it was with the DSC filtered with SEC04. This is an essential factor to consider when using a UV filter because a filter can prevent the effect of UV rays but also significantly reduces the DSCs' performance.

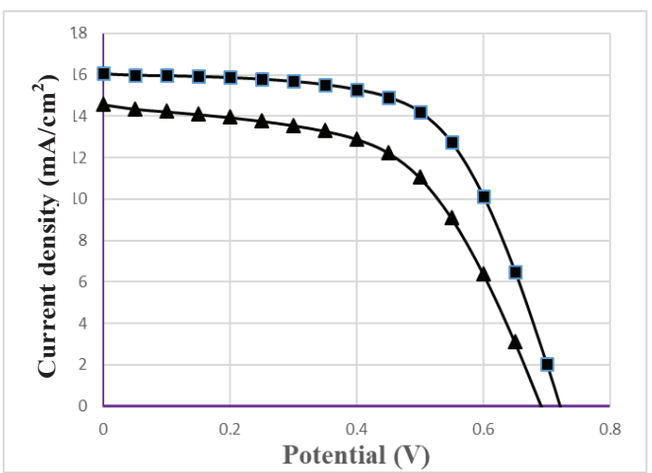

Fig. 2. Comparison of a typical I-V curve of unfiltered and filtered DSCs.

Table 2. The performance parameters of unfiltered and filtered DSCs.

UV filters		J_{sc}(mA/cm²)	Voc (V)	Fill factor	%η	%Δη
PS65	unfiltered	14.10	0.730	0.63	6.50	20
	filtered	10.80	0.721	0.64	5.00	
SEC04	unfiltered	1620	0.735	0.64	7.60	1.2
	filtered	14.40	0.739	0.65	6.70	

The effects of filtering on long - term stability of DSCs under outdoor testing

Outdoor testing results of DSCs filtered with PS65 and SEC04 are shown in Table 3.

Table 3. The I-V parameter of unfiltered DSC and filtered DSCs.

Type of DSCs	Exposure time (h)	J_{sc} (mA/cm²)	Voc (V)	Fill factor	η%
unfiltered DSC	0	17.20	0.737	0.641	8.13
	168	19.06	0.737	0.651	9.15
	336	19.46	0.720	0.660	9.17
	504	19.53	0.710	0.650	8.93
	1,152	16.82	0.647	0.649	7.06
	1,248	17.03	0.642	0.615	6.72
	1,992	0.04	0.294	0.086	0.00
DSC-PS65	0	10.86	0.712	0.611	4.73
	168	12.28	0.756	0.615	5.71
	336	13.81	0.758	0.631	6.61
	504	14.41	0.748	0.562	6.06
	1,488	15.35	0.723	0.549	6.09
	2,328	15.51	0.717	0.498	5.54
	3,120	14.45	0.621	0.336	3.02
DSC-SEC04	0	14.39	0.739	0.646	6.86
	168	16.23	0.784	0.678	8.64
	336	17.51	0.781	0.680	9.30
	504	16.93	0.787	0.691	9.20
	1,488	16.85	0.765	0.690	8.90
	2,328	16.30	0.770	0.677	8.50
	3,120	15.44	0.728	0.596	6.70

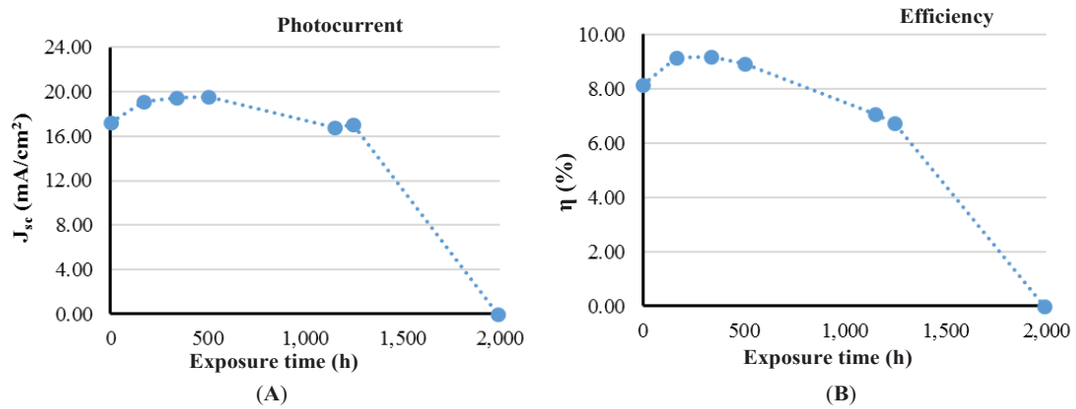

Fig. 3. Stability data of unfiltered DSCs depending on outdoor testing time. (A) Photocurrent, **(B)** Efficiency.

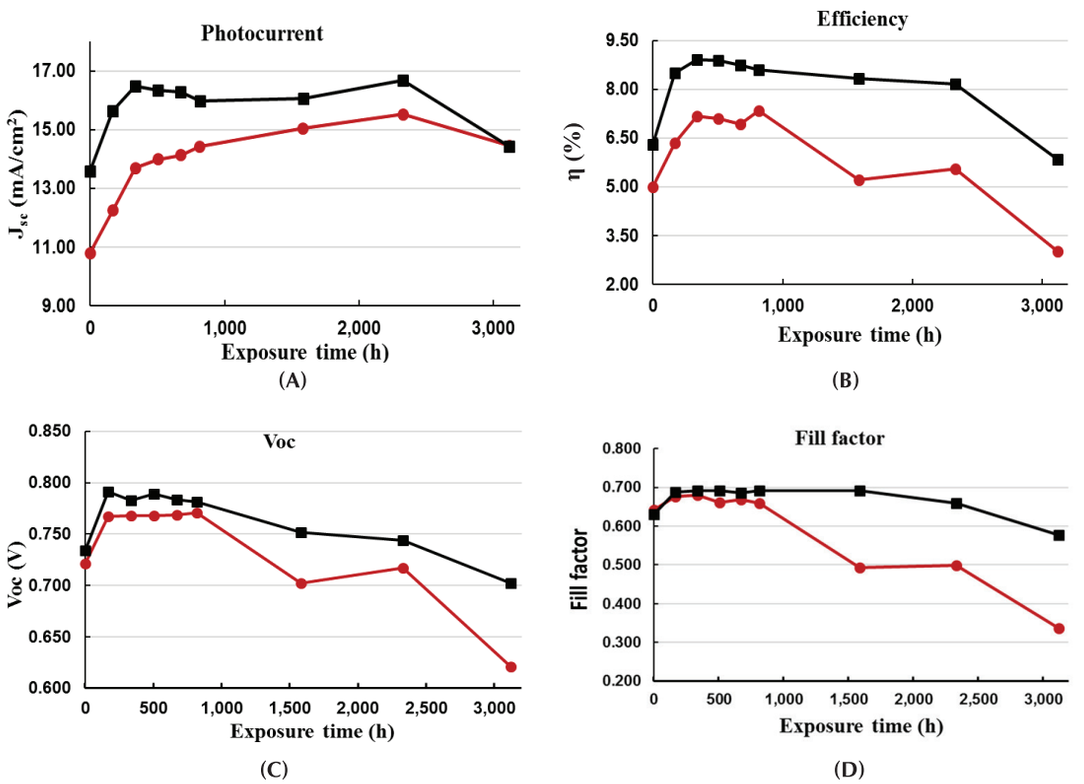

Fig. 4. Stability data of filtered DSCs with SEC04 (-■-), PS65 (-●-) depending on outdoor testing time.

Figures 3 and 4 show changes in the performance parameter of the unfiltered DSCs and those filtered with PS65 and SEC04 under outdoor testing conditions. Over the first 336 h, the cells increased in J_{sc}, V_{oc}, fill factor, and efficiency. The efficiencies were increased to 12% and 30% of the initial value for unfiltered cell and filtered cell, respectively. From 500 h to 1,000 h, a reduction of the cell efficiency occurred with unfiltered DSC, while during the same time interval the filtered DSC showed no changes in efficiency. The performance of the unfiltered DSCs suffered a dramatic drop after 1,000 h of testing. Meanwhile, no major changes in cell performance occurred during 2000 h of testing the filtered DSC. Degradation of the filtered DSCs began after 2,500 h of outdoor testing. Less significant degradation of the SEC04 filtered DSCs was found in comparison with the PS65 UV filter.

The electrochemical impedance spectroscopy of the unfiltered DSCs, PS65 filtered DSC, and SEC04 filtered DSC is shown in Fig. 5. The equivalent circuit was fitted as [$R(R_{ce}C_{ce})(R_tC_\mu)(R_dC_d)$], and the value of these components are detailed in Table 4 [7-9]. A significant decrease in the charge-transfer resistance (R_{ce}) of the counter electrode, as well as electron

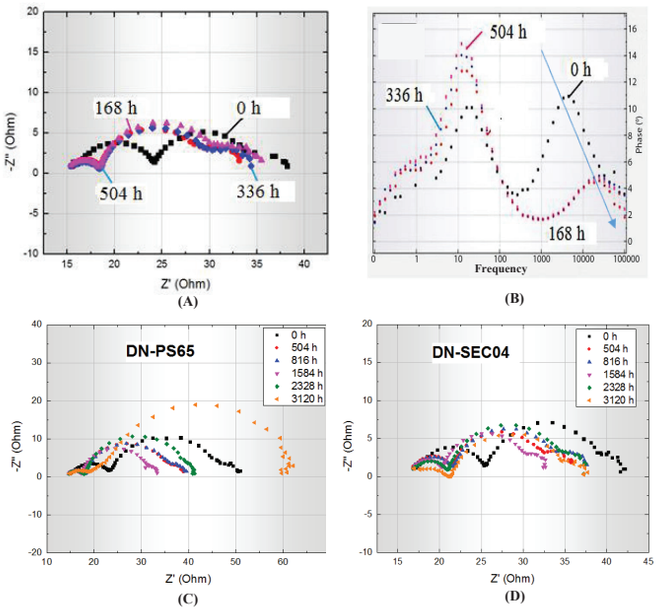

Fig. 5 The impedance spectra of unfiltered DSC (A, B) and filtered DSCs with PS65 (C), SEC04 (D).

transfer resistance (R_t) in the photoanode, after 186 h testing was observed. These phenomena can explain the increase in DSC performance during the first 336 h of testing time. The R_{ce} decreased due to the activation of the Pt cathode under illumination. For the first 186 h, the electron lifetime τ_e of the unfiltered DSC increased, indicating that the recombination rate of the DSCs decreased. Moreover, further decrease of the initial value occurred after an extra 336 h of testing.

The Nyquist plot of the DSC filtered with the SEC04 and PS65 UV filters showed the effect of stabilizing the DSCs over 2,000 h of outdoor testing. This means that the UV filter not only protected the DSC but did not impair the functionality of the DSC.

Table 4. Electrochemical impedance parameter of DSC with and without UV filter.

Type of DSCs	Exposure day	R_{ce} (Ω)	R_t (Ω)	τ_e (ms)
DSC	0	7.42	9.91	9.9
	168	2.86	10.2	13.2
	336	2.70	10.8	13.2
	504	2.91	11.5	13.2
DSC-PS65	0	8.00	21.2	9.9
	168	1.29	21.2	17.5
	336	3.07	14.8	9.9
	504	2.92	16.4	13.2
DSC-SEC04	0	7.52	13.2	9.9
	168	5.77	13.6	13.2
	336	4.12	9.93	9.95
	504	4.42	10.2	9.95

Conclusions

The UV filters SEC04 and PS65 applied to protect the DSC led to a reduction in cell efficiency. However, the stability of the cell was prolonged under extensive outdoor condition testing. The SEC04 filtered-DSC had a lower reduction in efficiency in comparison to the PS65 filtered-DSC because the SEC04 film has a higher average transmission of light than the PS65 filter. Thus, UV filter films are considered an effective, simple, and inexpensive solution to increase the performance of DSCs.

ACKNOWLEDGEMENTS

This research work was supported by Vietnam National University, Ho Chi Minh city through grant number HS2015-18-01.

The authors declare that there is no conflict of interest regarding the publication of this article.

REFERENCES

[1] B. O'Regan, M. Grätzel (1991), "A low-cost, high-efficiency solar cell based on dye-sensitized colloidal TiO_2 films", *Nature*, **353**, pp.737-740, Doi:10.1038/353737a0.

[2] J. Gong, J. Liang, K. Sumathy (2012), "Review on dye-sensitized solar cells (DSCs): fundamental concepts and novel materials", *Renewable and Sustainable Energy Reviews*, **16**, pp.5848-5860, Doi:10.1016/j.rser.2012.04.044.

[3] M. Grätzel (2003), "Dye-sensitized solar cells", *Journal of Photochemistry and Photobiology C: Photochemistry Reviews*, **4**, pp.145-153, Doi:10.1016/S1389-5567(03)00026-1.

[4] J. Burschka, N. Pellet, S.-J. Moon, R. Humphry-Baker, P. Gao, M.K. Nazeeruddin, M. Grätzel (2013), "Sequential deposition as a route to high-performance perovskite-sensitized solar cells", *Nature*, **499**, pp.316-319, Doi:10.1038/nature12340.

[5] A. Asghar, M. Emziane, H.K. Pak, S.Y. Oh (2014), "Outdoor testing and degradation of dye-sensitized solar cells in Abu Dhabi", *Solar Energy Materials and Solar Cells*, **128**, pp.335-342, Doi:10.1016/j.solmat.2014.05.048.

[6] Matthew Carnie, Trystan Watson, David Worsley (2012), "UV Filtering of dye-sensitized solar cells: the effects of varying the UV cut-off upon cell performance and tncident photon-to-electron conversion efficiency", *International Journal of Photoenergy*, Doi: 10.1155/2012/506132.

[7] S. Sarker, A.J.S. Ahammad, H.W. Seo, D.M. Kim (2014), "Electrochemical impedance dpectra of dye-sensitized solar cells: fundamentals and spreadsheet calculation", *International Journal of Photoenergy*, **2014**, Doi:10.1155/2014/851705.

[8] Q. Wang, J.-E. Moser, M. Grätzel (2005), "Electrochemical impedance spectroscopic analysis of dye-sensitized solar cells", *J. Phys. Chem. B.*, **109**, pp.14945-14953, Doi:10.1021/jp052768h.

[9] T.H. Nguyen, H.M. Tran, T.P.T. Nguyen (2013), "Application of electrochemical impedance spectroscopy in characterization of mass- and charge transfer processes in dye-sensitized solar cells", *ECS Trans*, **50**, pp.49-58, Doi:10.1149/05051.0049ecst.

Doi: 10.31276/VJSTE.62(1).43-49

Effect of preparation conditions on arsenic rejection performance of polyamide-based thin film composite membranes

Pham Minh Xuan[1, 2*], Le Hai Tran[1*], Huynh Ky Phuong Ha[1], Mai Thanh Phong[1], Van-Huy Nguyen[3], Chao-Wei Huang[4]

[1]*Faculty of Chemical Engineering, University of Technology, Vietnam National University, Ho Chi Minh city, Vietnam*
[2]*Department of Chemical Engineering, Dong Thap University, Vietnam*
[3]*Key Laboratory of Advanced Materials for Energy and Environmental Applications, Lac Hong University, Vietnam*
[4]*Department of Chemical and Materials Engineering, National Kaohsiung University of Science and Technology, Taiwan*

Received 10 January 2020; accepted 10 March 2020

Abstract:

Herein, a polyamide-based thin film composite (TFC) membrane was fabricated for the removal of arsenic (As) from water. The polyamide thin film was synthesized through interfacial polymerization (IP) onto a polysulfone porous substrate. A Box-Behnken design of response surface methodology was used to investigate the effect of preparation conditions, including piperazine (PIP) concentration, trimesoyl chloride (TMC) concentration, and reaction time on the As rejection and permeate flux of the synthesized membrane. The separation performance of the prepared membranes from 15 designed experiments was conducted with an arsenate (Na_2AsHSO_4) solution of 150 ppm at a pressure of 400 psi and a temperature of 25°C. The analysis of variance revealed the regression models to be adequate. From the regression analysis, the flux and As rejection were expressed by quadratic equations as a function of PIP concentration, TMC concentration, and reaction time. It was observed that the PIP concentration, TMC concentration, and reaction time had a significant effect on the flux and As rejection of the polyamide membrane. Moreover, a strong impact from the interaction of PIP and TMC was also observed on rejection of the resulting membrane. Using the desirability function approach to analyse the regression model, the optimal preparation conditions of the polyamide membrane were a PIP concentration of 2.5 wt.%, TMC concentration of 0.11 wt.%, and reaction time of 40 sec. The membrane exhibited a good As rejection of 95%.

Keywords: **arsenic, composite, membrane, polyamide, thin film.**

Classification numbers: **2.2, 2.3**

Introduction

Inorganic arsenic is a well-known carcinogen and one of the most harmful chemical contaminants found in drinking water around the world. Long-term ingestion of arsenic from water and food can cause cancer and skin lesions. According to the WHO, approximately 50 countries have As content in their drinking water at a value higher than 10 µg/l, which is the recommended safety limit set by the WHO [1]. Water pollution by As in Vietnam is a serious concern with the As content in groundwater ranging from 0.1 to higher than 0.5 mg/l, which exceeds the WHO standard by 10 to 50-fold. There are numerous methods employed to reduce As from water, such as co-precipitation [2], adsorption [3], and membrane filtration i.e. reverse osmosis RO [4] and nanofiltration (NF) [5]. Among these, the NF membrane process has emerged as an efficient approach for As removal from water due to its high permeate flux, good quality freshwater, and low operating cost [6].

The modern NF membranes have a TFC structure that consists of an ultra-thin polyamide film over a microporous substrate. The separation performance of TFC NF membranes, in terms of permeability and selectivity, are directly correlated with the structural and physicochemical properties of the ultra-thin polyamide film [7]. The selective polyamide active layer is synthesized by the IP process at the interface of two insoluble solvents. In this IP technique,

*Corresponding authors: Email: phamminhxuan1988@gmail.com; tranlehai@hcmut.edu.vn

many parameters, such as the monomer concentrations, types of monomers, and reaction time, could affect the physicochemical properties and separation performance of the membrane [8-14]. To the best of our knowledge, previous investigations were conducted using only one factor at a time, where only one variable was changed at each experimental trial. Consequently, no correlation between parameters were observed and thus could not indicate the optimum condition.

In this work, a polyamide thin film was synthesized through interfacial polymerization onto a polysulfone porous substrate. The Box-Behnken design of response surface methodology was used to investigate the effect of influential preparation conditions, including PIP concentration, TMC concentration, and reaction time, on the As rejection and permeate flux of the synthesized membrane. The result of this study is expected to contribute to a deeper understanding of the influence of preparation conditions on the As rejection of the membrane and to provide valuable data for preparing PA-based NF membranes for As removal from water.

Materials and methods

Materials

Polysulfone porous support substrates (PS20) were provided by Dow-Filmtec (USA). Piperazine and trimesoyl chloride with a purity of 99% were received from Sigma-Aldrich (USA). Deionized (DI) water and hexane (99%) were used as solvents for the synthesis of the polyamide membranes. Arsenate (Na_2AsHSO_4) was purchased from Guangzhou Zio Chemical (China).

Methods

The polyamide thin film was hand-cast on the PS20 substrate through IP [12]. The polyamide-based TFC membrane was formed by immersing the PS20 support membrane in a PIP aqueous solution for 2 min. Excess PIP solution was removed from the support membrane surface using an air knife (Exair Corporation) at about 4-6 psi. The PIP saturated support membrane was then immersed into the TMC-hexane solution for 20-70 s. The derived membrane was held vertically for 2 min before it was immersed in 200 ppm NaClO for 2 min and then dipped in 1,000 ppm $Na_2S_2O_5$ solution for 30 s. Finally, tthe membrane was dipped in DI water for 2 min. Before the obtained membrane could be used for the experiments, it was immersed in a DI water container with the water regularly replaced.

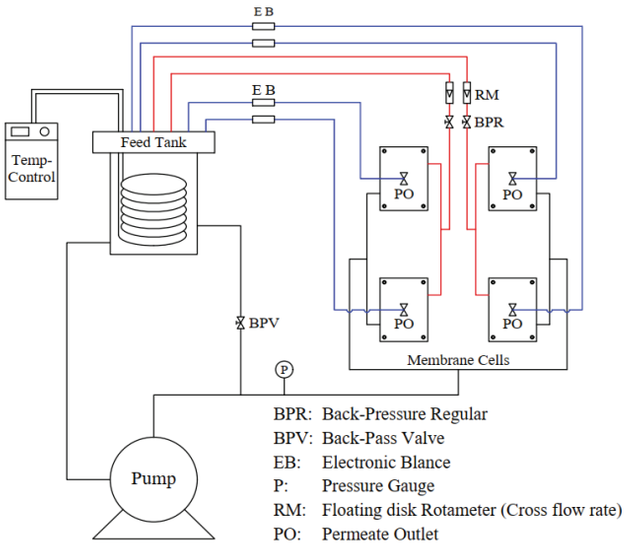

Fig. 1. Schematic illustration of the crossflow membrane process simulator.

The permeability of the synthesized membrane was evaluated for pure water and 150 ppb arsenate (Na_2AsHSO_4) aqueous solution using a custom fabricated bench-scale crossflow membrane process simulator (Fig. 1). The experiments were comprised of steps of compaction, equilibration, and cleaning under a fixed temperature of 25°C. First, DI water was filtered through the membranes at 450 psi for at least 6 h. After achieving a stable flux, the permeability of the membrane was determined by measuring the water flux under an applied pressure of 400 psi. Next, an arsenate solution with a fixed concentration of 150 ppb was filtered through the membrane at 400 psi. The flux was measured after the system performance was stable for at least 30 min. The concentration of As(V) in the feed and permeate solutions were determined via inductively coupled plasma atomic emission spectroscopy analysis (ICP-AES, Horriba). The data of flux and arsenate rejection reported in this work were based on the average of three experimental runs that have an error lower than 5%. Water flux can be determined from permeate water flow rate as follows:

$$J(lm^{-2}h^{-1}) = \frac{Q_P}{A_m \times t} \quad (1)$$

where Q_P is the permeate water flow rate, A_m is the effective membrane area (0.0024 m^2), and t is the filtration time. The As(V) concentrations in the feed and permeate solutions were used to calculate the observed As rejection as shown below:

$$R_S(\%) = \left(1 - \frac{C_{permeate}}{C_{Feed}}\right) \times 100 \quad (2)$$

where $C_{Permeate}$ and C_{Feed} are the As concentration in feed and permeate sides, respectively.

Table 1. Actual and coded levels of independent variables.

Variables	Factor	Level		
	X_i	*Low (-1)*	*Middle (0)*	*High (+1)*
PIP concentration (wt.%)	X_1	1.0	2.5	4.0
TMC concentration (wt.%)	X_2	0.05	0.10	0.15
Reaction time (s)	X_3	20	45	70

Based on preliminary experiments, three preparation conditions including PIP concentration, TMC concentration, and reaction time were determined as the most essential parameters. Therefore, the PIP and TMC concentrations and reaction times were chosen as independent variables and designated as X_1, X_2, and X_3, respectively. Table 1 describes the actual values and coded levels of the preparation conditions, which were varied over three levels as high level (+1), middle level (0), and low level (-1), respectively.

Table 2. The Box-Behnken design and corresponding flux and As rejection.

Run number	PIP conc., X_1 (wt.%)	TMC conc., X_2 (wt.%)	Reaction time, X_3 (sec.)	Flux, Y_1 ($lm^{-2}h^{-1}$)	Rejection, Y_2 (%)
1	1.0	0.05	45	56.70	26.4
2	1.0	0.15	45	5.35	91.1
3	4.0	0.05	45	0.90	96.0
4	4.0	0.10	70	0.85	92.3
5	2.5	0.05	20	28.85	60.9
6	1.0	0.10	20	44.35	35.3
7	2.5	0.05	70	7.30	87.0
8	1.0	0.10	70	13.95	82.8
9	4.0	0.10	20	8.50	95.9
10	2.5	0.10	45	6.95	96.6
11	2.5	0.10	45	9.80	96.5
12	2.5	0.10	45	12.75	94.0
13	2.5	0.15	20	9.35	95.4
14	4.0	0.15	45	5.15	96.8
15	2.5	0.15	70	5.40	96.7

The Box-Behnken statistical design (BBD) was employed to establish a mathematical model representing the correlation between individual factors and the predicted responses (i.e. permeation flux and As rejection). According to the BBD, 15 experimental runs were required to investigate the three variables. The experimental plan is shown in Table 2. A second-order model is generally used for describing the mathematical relationship between the variables (x_i) and responses (y_i), as shown in Eq. 3:

$$Y = b_o + \sum_{i=1}^{n} b_i X_i + \sum_{i\neq 1}^{n} b_{ij} X_i X_j + \sum_{i=1}^{n} b_{ii} X_i^2 + \varepsilon \quad (3)$$

where, Y is the predicted responses of flux or As rejection; X_i and X_j are independent factors in coded levels; b_i, b_{ii}, and b_{ij} are the coefficients of the linear, quadratic, and interaction terms of the model, respectively; b_o, n, and ε are the constant coefficient, number of studied factors, and random error of the model, respectively.

The response surface methodology (RSM) and statistical analysis of variance (ANOVA) were performed via Design-Expert software 8.0. The significance of variables, fitness, and adequacy of the developed models were judged statistically using R^2, adjusted R^2, F-value, and p-value. The terms of the models were retained or removed based on the probability value with a limit of 95 % confidence. Finally, the response surfaces obtained from the regression models were generated to visualize the individual and interactive effects of the influential factors.

Table 3. ANOVA response surface model of permeation flux and As rejection.

	Permeation Flux					As rejection				
	DF	*Sum of square*	*Mean square*	*F-value*	*p-value*	*DF*	*Sum of square*	*Mean square*	*F-value*	*p-value*
Model	6	3,447.8	574.6	18.3	0.0003	9	7,392.1	821.3	42.20	0.0003
X_1	1	1,376.8	1,376.8	43.7	0.0002	1	2,638.7	2,638.7	135.6	< 0.0001
X_2	1	586.5	586.5	18.6	0.0026	1	1,505.0	1,505.0	77.3	0.0003
X_3	1	504.8	504.8	16.0	0.0039	1	635.9	635.9	32.7	0.0023
X_1X_2	1	772.8	772.8	24.6	0.0011	1	1,022.2	1,022.2	52.5	0.0008
X_1X_3	1	129.4	129.4	4.1	0.0772	1	652.3	652.3	33.5	0.0022
X_2X_3	1	77.4	77.4	2.5	0.1554	1	153.6	153.62	7.9	0.0376
X_1^2	-	-	-	-	-	1	653.1	653.1	33.6	0.0022
X_2^2	-	-	-	-	-	1	86.8	86.8	4.5	0.0884
X_3^2	-	-	-	-	-	1	126.3	126.3	6.5	0.0514
Residual	8	251.9	31.5	-	-	5	97.3	19.5	-	-
Lack of fit	6	235.5	39.2	4.7	0.1873	3	93.1	31.0	14.7	0.1643
Pure error	2	16.8	8.4	-	-	2	4.2	2.1	-	-
Model summary										
SD	5.61					4.41				
R^2(%)	93.19					98.70				
Adj. R^2 (%)	88.09					96.36				

Results and discussion

Model fitting and statistical analysis

The observed flux (Y_1) and As rejection (Y_2) recorded through the designed experiments in RSM are reported in Table 2. The F-value tests were conducted with ANOVA for calculating the significance of the mathematical models. The results showed that the two-factor interaction model was proposed for the flux response (y_1), as shown in Eq. 4. Meanwhile, the quadratic model expressed in Eq. 5 was obtained for predicting the As rejection response (y_2):

$$y_1 = +14.41 - 13.12x_1 - 8.56x_2 - 7.94x_3 + 13.90x_1x_2 + 5.69x_1x_3 + 4.40x_2x_3 \quad (4)$$

$$y_2 = +95.72 + 18.16x_1 + 13.72x_2 + 8.91x_3 - 15.99x_1x_2 - 12.77x_1x_3 - 6.20x_2x_3 - 13.30x_1^2 - 4.85x_2^2 - 5.85x_3^2 \quad (5)$$

where x_1, x_2, and x_3 are the code values of PIP, TMC concentrations, and reaction time, respectively. The effect of each variable of the developed model on the responses are specified with a negative or positive symbol before the term.

The adequacy of the obtained models and the significance of the model terms and their interactions was validated using ANOVA. As can be seen in Table 3, the F-value of the model for flux is 18.25 and the p-value is lower than 0.05, which implies that the regression model is significant. The R^2 value for the predicted flux model is 93.19 %, indicating that only 6.81% of the experimental variations cannot be explained by the model. Moreover, the adjusted R^2 of 88.09% is in reasonable agreement with the R^2 value. For the developed model for As rejection, the F-value is 42.2 and the p-value is lower than 0.05, which shows the high significance of the model. The R^2 value of 93.19 % indicates that more than 90 % of the variation in the data is explained by the model, whereas, the adjusted R^2 of 96.36 % shows a good agreement with the R^2 value. These results illustrate the statistical validity of the predicted models. Thus, the developed models can be used to navigate the separation performance of the prepared membrane within the range of studied variables.

According to ANOVA analysis, the p-value of PIP and TMC concentrations, reaction time, and interaction between PIP and TMC concentrations are less than 0.05, which indicates the significance of these factors on the permeation flux of the prepared membrane. On the contrary, the other factors are insignificant or less significant in the developed model. For the As rejection, according to the analysis, it was found that the PIP concentration, TMC concentration, reaction time, interactions effects of PIP-TMC concentration, PIP concentration-reaction time, and TMC concentration-reaction time are the most effective parameters. However, the rest of the factors show an insignificant influence due to a p-value higher than 0.05.

Based on the ANOVA results, the non-significant or less significant factors were eliminated from the models for flux and As rejection. Thereby, the final models in terms of actual factors are expressed in Eq. (6) and Eq. (7):

$$Y_1 = +146.9 - 34.1X_1 - 792.9X_2 - 1.0X_3 + 185.3X_1X_2 \quad (6)$$

$$Y_2 = -167.2 + 78.3X_1 + 1{,}418.2X_2 + 2.5X_3 - 213.1X_1X_2 - 0.3X_1X_3 - 5.0X_2X_3 - 5.9X_1^2 \quad (7)$$

Evaluation of model factors on permeation flux and As rejection

Equation (6) illustrates the influence of the preparation conditions on permeation flux of the prepared membrane. It can be seen that the reaction time affects the flux less significantly than the PIP and TMC concentrations. Particularly, the PIP concentration is the most significant parameter on the flux and the interaction effect between the PIP concentration and TMC concentration plays an important role in controlling the flux of the membrane.

Figure 2 shows the response surface and contour plots that demonstrate the interactive influence of PIP and TMC concentration on the flux at a constant reaction time of 45 s. The flux was observed to decrease considerably when increasing the PIP or TMC concentration, but the decrement of the flux by the increase of PIP concentration is more significant than that of TMC concentration. This reduction in flux can be related to the growth of the membrane thickness [13]. The polymerization occurs at the interface between the TMC/hexane and PIP/water phases towards the organic phase due to the low solubility of TMC in water [14]. Thereby, PIP, with a concentration in great excess over TMC, is commonly utilized to accelerate the diffusion of the diamine monomer into the organic phase. Park, et al. [15] reported that with high TMC concentration (>0.1 wt.%), the kinetics of IP is dominantly governed by the PIP concentration and the increase in PIP concentration induces the creation of a thicker polyamide membrane.

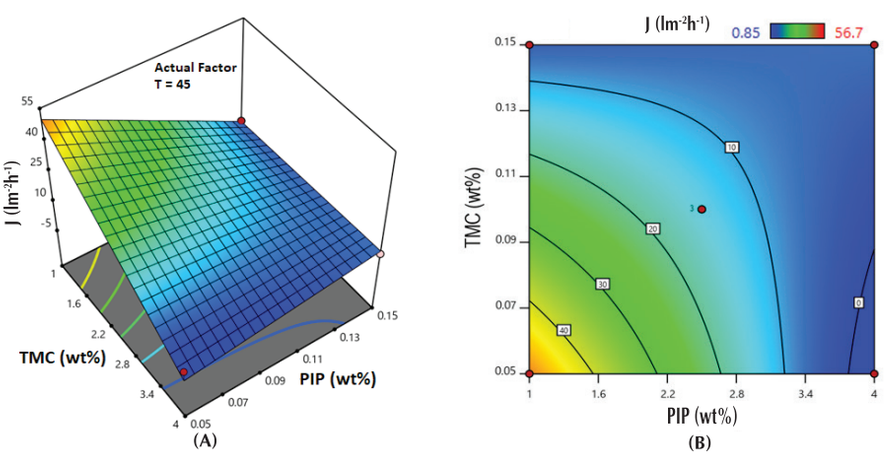

Fig. 2. (A) Response surface and (B) contour plots of PIP and TMC concentration effects on the permeation flux of the fabricated membrane.

The flux depends on not only the thickness but also on the hydrophilicity of the membrane. The higher hydrophilicity of the membrane surface, the stronger the affinity between the membrane and water molecules, and thus the flux of the membrane improves. The number of carboxylic groups related to the hydrophilicity of the membrane is generated by the hydrolysis of unreacted acyl halide groups in the TMC monomer [12]. Saha and Joshi found that an increasing TMC concentration can cause a rise in both the thickness and hydrophilicity of the membrane [14]. In this present work, the increase in thickness dominates the hydrophilicity of the membrane when increasing the TMC concentration. However, the decline in flux by increasing PIP concentration is more considerable than that caused by increasing TMC concentration.

Evaluation of model factors on As rejection

The response surface and contour plots showing the interaction impacts of PIP-TMC concentration, PIP concentration-reaction time, and TMC concentration-reaction time on the As rejection of the prepared membrane are illustrated in Fig. 3. It is apparent that the As rejection improves with an increase in PIP concentration, TMC concentration, and reaction time. Regarding Fig. 3(A, B), the As rejection strongly depends on the PIP concentration, while the TMC concentration shows a weaker factor.

It can be explained by the "self-limiting" mechanism of IP that the faster diffusion of the PIP monomers to the organic phase to bond with the TMC monomers forms an initial thin film with high crosslinking [16]. This dense thin film is regarded as a barrier that hinders the diffusion of PIP monomers to the reaction zone. As a result, the reaction is limited and then terminates. Over a variety of TMC concentrations from 0.05 to 0.15 wt.%, the As rejection increases sharply with an increase in m-phenylenediamine (MPD) concentration due to the formation of amide crosslinking in the prepared membrane. However, when the PIP concentration is much greater than the TMC concentration, the As rejection and permeant flux show a decreasing trend due to the expansion of the reaction zone that causes a thicker and looser structure membrane [14-16].

As shown in Fig. 3 (C, D, E, F), the increase in TMC concentration is demonstrated to extend the crosslinking

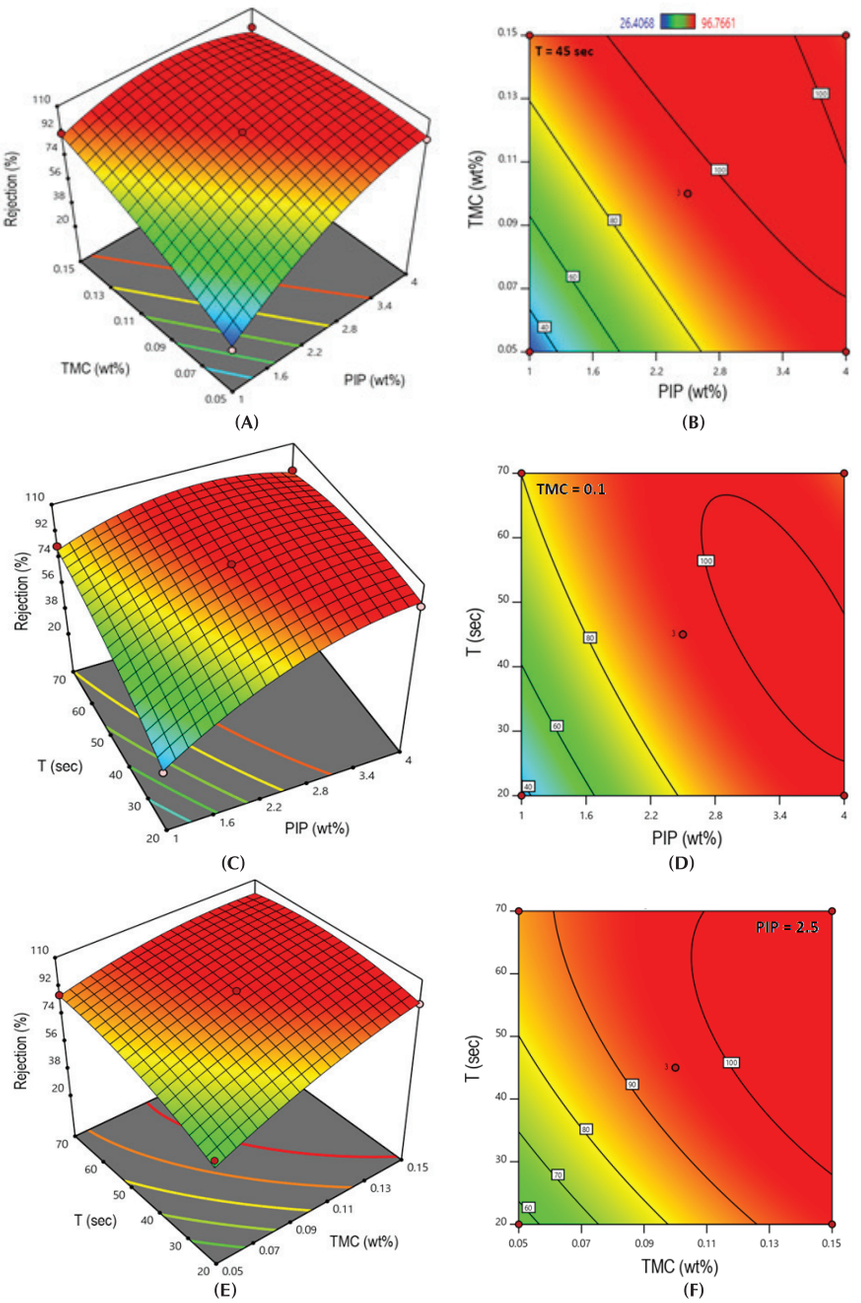

Fig. 3. Response surface (A) and contour plots (B) of the PIP - TMC concentration, (C,D) PIP concentration - reaction time, and (E,F) TMC concentration - reaction time effects on As rejection of the prepared membrane.

and thus enhance the As rejection of the resulting membrane. On the other hand, prolonging the reaction time can facilitate crosslinking to form a membrane with high As rejection. This result is in agreement with previous studies [11-16]. Saha and Joshi [14] suggested that increasing the TMC concentration could reduce the amine/acyl chloride ratio to form a thinner and denser membrane. Furthermore, Kadhom, et al. [16] observed that the polyamide membrane prepared via interfacial polymerization with short reaction time (within 15 s) exhibited a high flux and low ion rejection because the unreacted TMC monomers were hydrolysed to form linear amide moiety with carboxylic acid groups instead of a crosslinking structure.

Optimization

The results indicate a trade-off between the permeation flux and As rejection of the polyamide membrane. Thus, the increase of permeation flux is accompanied by the sacrifice of As rejection. Therefore, it could be suggested that the determination of the optimal ratio of PIP/TMC concentration and corresponding reaction time is required to achieve a membrane with high flux for As removal from water. Response surface optimization, combined with desirability function approach, was applied to maximize the permeation flux and As rejection. In order to obtain the optimum preparation conditions for a high-separation performance membrane, the desired goals in terms of flux and As rejection were defined as maxima. Fig. 4 illustrated the desirability, predicted flux, and As rejection as a function of preparation conditions. The results showed that the maximum permeation flux and As rejection of 13.9 $lm^{-2}h^{-1}$ and 96.7%, respectively, were achieved with a PIP concentration of 2.5 wt.%, TMC concentration of 0.11 wt.%, and reaction time of 40 s. An experiment with the optimized conditions was performed and the flux and As rejection of the prepared membrane were recorded to validate the optimization result as well as the regression models. The obtained flux and As rejection were 14.2±0.8 $lm^{-2}h^{-1}$ and 95.01±0.13% respectively, which demonstrates the validity of the statistical models to optimize the preparation conditions of the polyamide membrane for removing As from water.

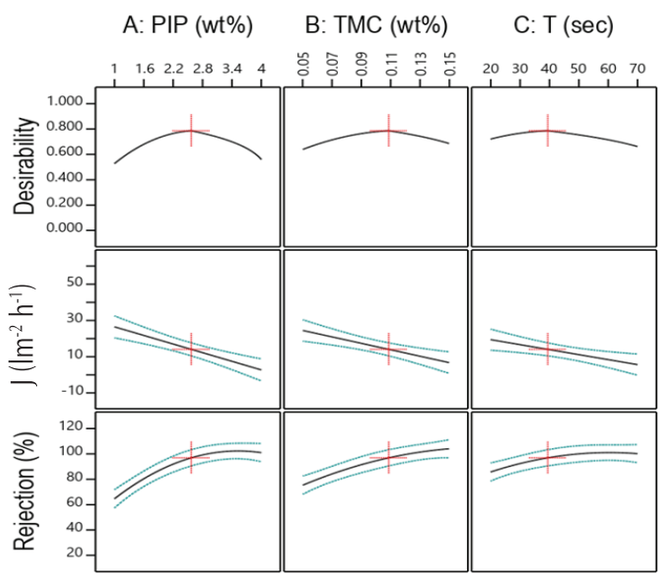

Fig. 4. The desirability, predicted flux, and As rejection as a function of preparation conditions.

Conclusions

A polyamide-based TFC membrane was fabricated for As removal from water. The polyamide membrane was synthesized through IP onto a polysulfone porous substrate. RSM, using Box-Behnken design, was applied to determine the effects of three important preparation conditions, including PIP concentration, TMC concentration, and reaction time, on the As rejection and permeate flux of the synthesized membrane. The study revealed that the PIP concentration was the most significant factor that influenced the flux and As rejection of the resulting membrane, while the reaction time was the least significant parameter. Furthermore, the small deviation between the predicted and actual results indicated the accuracy and validity of the regression models. According to the RSM, the optimal conditions to fabricate the polyamide membrane are PIP concentration of 2.5 wt.%, TMC concentration of 0.11 wt.%, and reaction time of 40 s.

ACKNOWLEDGEMENTS

The authors wish to thank the Ministry of Education and Training of Vietnam, B2019.SPD.05 Project, for their financial support of this work.

The authors declare that there is no conflict of interest regarding the publication of this article.

REFERENCES

[1] Sato, Y. Kang, M.Kamei, T. Magara, Yakasumako (2002), "Performance of nanofiltration for arsenic removal", *Water Research*, **36(13)**, pp.3371-3377.

[2] S.R. Wickramasinghe, Binbing Han, J. Zimbron, Z. Shen, M.N. Karim (2004), "Arsenic removal by coagulation and filtration: comparison of groundwaters from the United States and Bangladesh", *Desalination*, **169(3)**, pp.231-244.

[3] Gupta, Saini, Jain (2005), "Adsorption of As(III) from aqueous solutions by iron oxide-coated sand", *Journal of Colloid and Interface Science*, **288(1)**, pp.55-60.

[4] Košutić, et al. (2005), "Removal of arsenic and pesticides from drinking water by nanofiltration membranes", *Separation and Purification Technology*, **42(2)**, pp.137-144.

[5] Ming - Cheng Shih (2005) "An overview of arsenic removal by pressure-drivenmembrane processes", *Desalination*, **172(1)**, pp.85-97.

[6] Figoli, A. Casano, A. Criscuoli, et al. (2010), "Influence of operating parameters on the arsenic removal by nanofiltration", *Water Research*, **44(1)**, pp.97-104.

[7] H. Saitúa, M. Campderros, S. Cerutti, A.P. Padila (2005), "Effect of operating conditions in removal of arsenic from water by nanofiltration membrane", *Desalination*, **172(2)**, pp.173-180.

[8] S. Verissimo, K.V. Peinemann, J. Bordado (2006), "Influence of the diamine structure on the nanofiltration performance, surface morphology and surface charge of the composite polyamide membranes", *Journal of Membrane Science*, **279(1)**, pp.266-275.

[9] M.R. Teixeira, et al. (2005), "The role of membrane charge on nanofiltration performance", *Journal of Membrane Science*, **265(1-2)**, pp.160-166.

[10] N. Misdan, W.J. Lau, A.F. Ismail, et al. (2014), "Study on the thin film composite poly (piperazine-amide) nanofiltration membrane: impacts of physicochemical properties of substrate on interfacial polymerization formation", *Desalination*, **344,** pp.198-205.

[11] L. Meihong, Y. Sanchuan, Z. Yong, Gao Congjie (2008), "Study on the thin-film composite nanofiltration membrane for the removal of sulfate from concentrated salt aqueous: preparation and performance", *Journal of Membrane Science*, **310(1-2)**, pp.289-295.

[12] A.K. Ghosh, B.H. Jeong, X. Huang, Erik M.V. Hoek (2008), "Impacts of reaction and curing conditions on polyamide composite reverse osmosis membrane properties", *Journal of Membrane Science*, **311(1-2)**, pp.34-45.

[13] Ying Jin, Zhaohui Su (2009), "Effects of polymerization conditions on hydrophilic groups in aromatic polyamide thin films", *Journal of Membrane Science*, **330(1-2)**, pp.175-179.

[14] N. Saha, S.V. Joshi (2009), "Performance evaluation of thin film composite polyamide nanofiltration membrane with variation in monomer type", *Journal of Membrane Science*, **342(1-2)**, pp.60-69.

[15] Seong-Jik Park, Hye-Kyung An (2015), "Optimization of fabrication parameters for nanofibrous composite membrane using response surface methodology", *Desalination and Water Treatment*, **57(43)**, pp.1-11.

[16] Mohammed Kadhom, Baolin Deng (2019), "Synthesis of high-performance thin film composite (TFC) membranes by controlling the preparation conditions: technical notes", *Journal of Water Process Engineering*, **30**, Doi: 10.1016/J.JWPE.2017.12.011.

Doi: 10.31276/VJSTE.62(1).50-54

Evaluating the membrane fouling control ability of a reciprocation membrane bioreactor (rMBR) system

P.T. Nguyen[1], B.T. Dang[2], H.D. Pham[1], Q.T. Huynh[1], X.D. Nguyen[1], H.H. Nguyen[1], K.J. Lee[3], X.T. Bui[1*]

[1]University of Technology, Vietnam National University, Ho Chi Minh city, Vietnam
[2]Nagasaki University, Japan
[3]KOLON Industries, INC, Republic of Korea

Received 14 October 2019; accepted 26 December 2019

Abstract:

Membrane bioreactors (MBRs) are being increasingly applied to many full-scale plants around the world to treat both municipal and industrial wastewater. However, membrane fouling and energy consumption are significant challenges to broader applications of MBRs. By using a new MBR configuration, this research aims to compare the performance between a conventional MBR and a reciprocation MBR (rMBR) that uses inertial forces without air scouring for fouling reduction. The results show that there was no difference in chemical oxygen demand (COD) (92-98%) or total nitrogen (TN) (71-77%) after 280 d of operation under the same influent constraints. However, by using the inertial force, the fouling rates were 0.35 mbar/d for the rMBR, resulting in a significantly lower fouling rate in comparison with a conventional MBR and other literature reports. Thus, the lower energy consumption over long-term operation of a rMBR could be a promising solution to overcome the drawbacks of a MBR.

Keywords: **energy consumption, fouling, reciprocation membrane bioreactor.**

Classification numbers: **2.3, 3.5**

Introduction

With rapid population growth, the demand for water in daily life has increased, which poses many challenges to water supply efforts [1] leading to water shortage and water pollution. Therefore, strict standards and regulations have been proclaimed to force all industries to use appropriate treatment technologies to reduce pollution before discharging to receiving sources. Nowadays, many wastewater treatments plants have applied technologies such as conventional activated sludge, biological filters, and wastewater stabilisation ponds. However, these technologies have a limited scope of application due to their low energy recovery and high footprint, and improving effluent wastewater to meet a higher level of quality standards is needed. The use of traditional treatments faces many difficulties, namely fluctuations in flow rate and the composition of wastewater, which affects the quality of the effluent as well as increases suspended solids due to the sludge drift phenomenon. Moreover, in the situation of increasingly scarce land funds, simple technologies that save space and have high treatment efficiency are often considered for wastewater treatment.

MBR technology is a compact process that combines biodegradation by activated sludge with a membrane filtration process, and it is an advancement over the conventional activated sludge (CAS) technology [2, 3]. These features make it more natural to increase the capacity of an MBR system. For example, by increasing the membrane area, the MBR system can meet treatment efficiency standards as well as minimise the space used for the wastewater treatment system. The combination of an anoxic zone with MBR (i.e., AO-MBR technology)

*Corresponding author: Email: bxthanh@hcmut.edu.vn

could enhance performance in terms of nutrient removal. However, during operation, the accumulation of colloids, suspended solids, and microorganisms on the membrane surface has contributed to reducing permeate flux and reducing the lifetime of the filter. As a result, MBR requires strict and intense air scouring and chemical cleaning for flux recovery, which results in a significant increase of total operating costs [4]. Air scouring and chemical cleaning also contributes to diminishing the lifetime of the membrane over long-term operation. Therefore, the idea of this work is to remove the air scouring system within an MBR module and replace it with a reciprocating mechanism for fouling reduction. This reciprocating movement is made by a motor with a rotation axis that pulls the membrane's support with varying amplitude and frequency. This study aims to evaluate the performance of the rMBR in comparison to a conventional MBR in terms of organic and nutrient removal, membrane fouling reduction, and energy consumption to satisfy the requirements for practical application.

Materials and methods

Pilot set-up

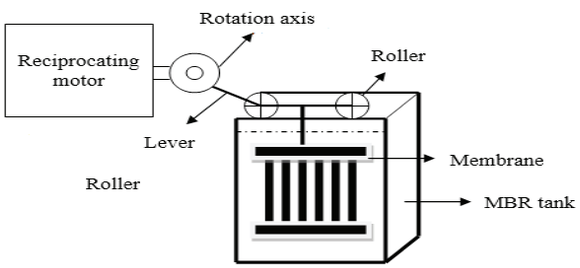

Fig. 1. Schematic diagram of the reciprocating module membrane.

The rMBR works similarly to the conventional MBR except air scouring is no longer used to minimise membrane fouling at the membrane tank. A detailed schematic of the reciprocating module membrane is shown in Fig. 1. The total system was designed with a group of treatment tanks, including an anoxic-oxic membrane tank. Other facilities such as a clean water tank, grease separating tank, equalization tank, and sludge storage tank were also investigated in this study. As shown in Fig. 1, a motor is attached to a rotation axis, which is controlled by a magnetometer that adjusts the rotational speed of the motor. The system was operated with a flux of 20 LMH, under a solids retention time (SRT) of 30 d, and organic loading rate (OLR) from 0.8 to 1.2 kg COD/m^3.d. The amplitude of the motor of the rMBR was set to 60 mm, the frequency at 0.46 Hz and 0.3 Hz, and the average movement speeds of the membrane module were 2.76 cm/s. This study uses a polyvinylidene fluoride (PVDF) hollow fibre membrane module (Kolon, Korea) with a pore size of 0.1 µm and a total surface area of 2.2 m^2. The membrane was attached to the rotation axis of the motor through the transmission bar. When the rotation axis moved circularly due to the transmission bar, the membrane was pushed, and the reciprocal movement created an inertial force on the fibres. This caused vibrations and inertial forces to facilitate the removal the pollutants on the surface and minimised fouling.

Wastewater and seed sludge

Wastewater in this study was taken from the manholes of canteen B4 of University of Technology, Vietnam National University, Ho Chi Minh city. Influent COD ranged between 400-900 mg/l, TN was between 18-38 mg/l, and total phosphorus (TP) was between 2-5 mg/l. Seed sludge used in the experiment was taken at the aerobic tank of the domestic wastewater treatment system of Coopmart Ly Thuong Kiet with a concentration of 1,955 mg/l with a sludge value index (SVI) equal to 153 ml/g. The seed sludge was acclimatised with domestic wastewater within 30 d for microorganisms' adaption and development with the new environment factor.

Analytical methods

Analytical methods for mixed liquor suspended solids (MLSS), COD, NH_4^+, NO_2^-, NO_3^-, TN, and TP are referenced in the Standard Methods for Examination of Wastewater [5]. The operation filtration of the membrane was automatically set up for 9 min of filtration, 0.5 min of backwashing, and 0.5 min of idle time for both the MBR and rMBR systems. To observe the membrane fouling, the trans-membrane pressure (TMP) was recorded daily, and the fouling rate (dTMP/dt) was determined by the slope between the TMP and operating time. The fouling membrane was washed with a NaOCl solution with a concentration of 250 ppm.

Results and discussion

Pollutant removal ability of pilot-scale system

After 280 d of operation, the quality of the treated water was assessed according to the following parameters: COD, NH_4^+, NO_2^-, NO_3^-, TN, and TP. The pollutant treatment ability of the MBR and rMBR systems at different operating conditions are shown in Fig. 2.

In the MBR stage, the COD treatment ability of the system was stable, which had an average treatment efficiency of 92-98%. This result was also found to be in line with other studies on MBR for domestic wastewater treatment [6, 7]. The COD concentration of the permeate reached an average value of 18±11.3 mg/l (mean ± standard deviation). The MBR system tended to stabilize very quickly after acclimatisation. Similarly, rMBR operation with a membrane movement speed of 2.76 cm/s saw the COD removal efficiency reach 92-99% concentration with 21±7 mg/l. It can be seen clearly that the new configuration did not affect the removal of organics, although the influent COD in the rMBR was significantly higher than in the MBR.

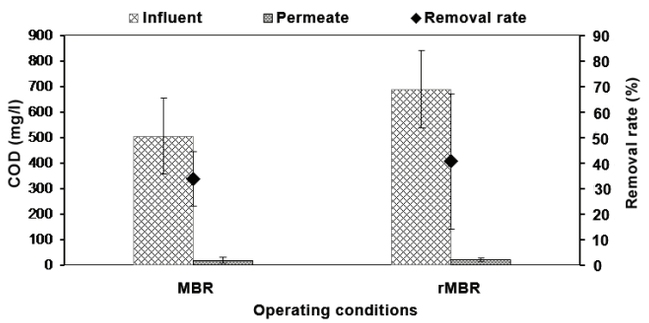

Fig. 2. COD treatment efficiency in different operating conditions.

The average specific substrate utilisation rate based on the MLSS of the COD in the MBR and rMBR were 0.33±0.1 and 0.4±0.1 kgCOD/kgMLSS.d, respectively. The average specific substrate utilisation rates did not affect the two MBRs. This is explained by the substrate consumption of microbials, which cause a decrease of COD. When using a membrane, it would act as a barrier to prevent the washing off of solids and biomass, which could contribute to improving the effluent [8, 9].

From Fig. 3, the TN treatment efficiency of conventional MBR in this period was 71±12%. Under rMBR conditions, the TN treatment efficiency was 77±11%, which was slightly higher than that of MBR. This implies that lacking air scouring, i.e. lowering dissolved oxygen (DO), could be induced to establish an anoxic zone rather than aerobic conditions for microorganisms in the membrane tank. Together with the anoxic tank, the rMBR supported the nitrification and denitrification processes much more effectively when compared with MBR. Overall, it can be seen that the nitrogen removal efficiencies were stable, with an average efficiency of 71-77%. This result was similar to the results from the previous studies of Ho, et al. (2015) and Liang, et al. (2014) [10, 11]. The process of treating nitrogen by biological methods in an AO-MBR system is quite complicated and done through the oxidation-reduction of nitrogen-containing compounds. For TN, the influent nitrogen was mainly ammonia and organic nitrogen, with an average ammonia concentration of about 40%.

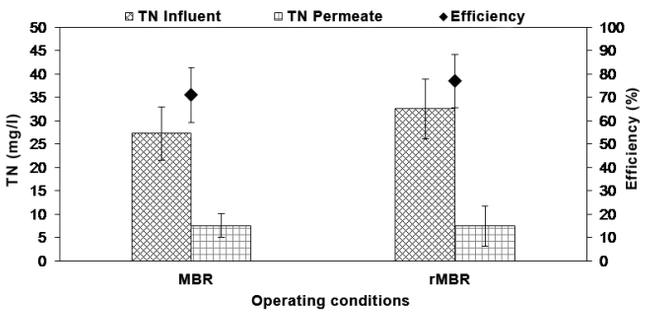

Fig. 3. TN concentration under different operating conditions.

The metabolism of ammonia and organic nitrogen in the MBR and rMBR achieved 82±14% and 96±4% average ammonia removal efficiency, respectively. Meanwhile, the average total Kjeldahl nitrogen (TKN) removal efficiency of each period was 74±9% and 83±13% for the MBR and rMBR, respectively. This demonstrates that the oxidation process occurred well enough to oxidise the ammonia in the wastewater and to reduce its concentration in the permeate. However, organic nitrogen was not as thoroughly treated, which is indicated by the TKN treatment efficiency. The average concentration of TKN in the permeate was still maintained and reached 6.6±2 mg/l and 5.5±2.5 mg/l for the MBR and rMBR, respectively. The average ammonia concentration in the permeate was 1.62±1.4 mg/l and 0.72±0.3 mg/l for the MBR and rMBR, respectively. Thus, the untreated organic nitrogen fraction during operation periods was 4.98 mg/l and 4.78 mg/l for the MBR and rMBR, respectively. The nitrate concentration in the oxic tank was almost higher than that of the anoxic tank. This can be explained by the circulation of nitrates from the oxic to anoxic zone had significantly reduced the amount of nitrate via the denitrification process. For the permeate, nitrite concentration was below 0.2 mg/l. Nitrites were still present in the system, but at low concentrations, which indicated that the metabolism was not complete.

Phosphorus was mainly absorbed into the biomass cell, which is then removed from the process through the sludge withdraw. This study had a SRT of 30 d, and the proper control of SRT could allow retention of high concentrations

of biomass for phosphorous removal [12]. Moreover, influent phosphorus was quite low so that the phosphorus treatment process always met the discharge standards with efficiencies of 63±22% and 57±19% for the MBR and rMBR, respectively (Fig. 4).

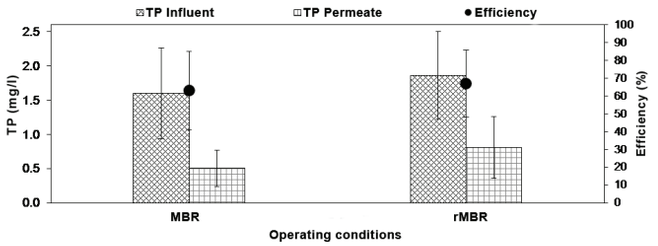

Fig. 4. TP concentration through each operating condition.

Fouling

Table 1. Fouling rates for the rMBR and MBR in comparison with literature reported using an MBR system.

System	SRT (d)	HRT (h)	OLR (kg COD/ m^3.d)	Flux (l/m^2.h)	Fouling rate (mbar/d)	References
FBMBR	48	36	0.9-1.1	12	2	[13]
Sponge-MBR	45	7.3	1.1	6	2.3	[14]
HF-MBR	45	7.3	0.4	6	8.7	[14]
AF-MBMBR	490	8	-	-	6.1	[15]
FS-MBR	30	15-25	-	16	0.31	[16]
FS-MBR	10	15-26	-	16	10.8	[16]
rMBR	30	8	0.8-1.2	20	0.35	This study
MBR	30	8	0.8-1.2	20	0.56	This study

The results show that the fouling control efficiencies of the rMBR were better and had a slower fouling rate than other MBR systems (Table 1). This demonstrates that the membrane fouling rate in rMBR, with an amplitude of 60 mm and frequency of 0.46 Hz (membrane movement speed of 2.76 cm/s), could potentially replace conventional MBR at a high flux range of 20 LMH and a low HRT of 8 h. This means that the rMBR could be used for treating a high capacity of wastewater while maintaining a significant reduction of fouling development, thereby holding promise to overcome the drawbacks of conventional MBR due to lower energy consumption over long term operation.

Conclusions

By using a pilot-scale rMBR system with different membrane movements, this research showed that the pollutant treatment efficiencies in wastewater were quite high, with average efficiencies were about 97% for COD, 75% for TN, and 62% for TP. In parallel, the fouling control ability of the MBR system combined with reciprocation was also shown, and the fouling rate was better controlled for the rMBR at a speed of 2.76 cm/s, amplitude of 60 mm, and frequency of 0.46 Hz.

ACKNOWLEDGEMENTS

This research was funded by University of Technology, Vietnam National University, Ho Chi Minh city under the grant number Tc-MTTN-2019-07.

The authors declare that there is no conflict of interest regarding the publication of this article.

REFERENCES

[1] F. Du, A.H. Hawari, B. Larbi, A. Ltaief, G.R. Pesch, M. Baune, J. Thöming (2018), "Fouling suppression in submerged membrane bioreactors by obstacle dielectrophoresis", *Journal of Membrane Science*, **549**, pp.466-473.

[2] S.I. Patsios, A.J. Karabelas (2011), "An investigation of the long-term filtration performance of a membrane bioreactor (MBR): the role of specific organic fractions", *Journal of Membrane Science*, **372(1)**, pp.102-115.

[3] T.T. Nguyen, X.T. Bui, B.T. Dang, H.H. Ngo, D. Jahng, T. Fujioka, S.S. Chen, Q.T. Dinh, C.N. Nguyen, P.T.V. Nguyen (2019), "Effect of ciprofloxacin dosages on the performance of sponge membrane bioreactor treating hospital wastewater", *Bioresour. Technol.*, **273**, pp.573-580.

[4] R. De Sotto, J. Ho, W. Lee, S. Bae (2018), "Discriminating activated sludge flocs from biofilm microbial communities in a novel pilot-scale reciprocation MBR using high-throughput 16S rRNA gene sequencing", *J. Environ. Manage.*, **217**, pp.268-277.

[5] APHA (2005), *Standard Methods for the Examination of Water and Wastewater*, 21st edition, Washington DC, USA.

[6] M. Ferraris, C. Innella, A. Spagni (2009), "Start-up of a pilot-scale membrane bioreactor to treat municipal wastewater", *Desalination*, **237(1-3)**, pp.190-200.

[7] Z. Fu, F. Yang, Y. An, Y. Xue (2009), "Simultaneous nitrification and denitrification coupled with phosphorus removal in an modified anoxic/oxic-membrane bioreactor (A/O-MBR)", *Biochem. Eng. J.*, **43(2)**, pp.191-196.

[8] K.G. Song, J. Cho, K.W. Cho, S.D. Kim, K.H. Ahn (2010), "Characteristics of simultaneous nitrogen and phosphorus removal in a pilot-scale sequencing anoxic/anaerobic membrane bioreactor at various conditions", *Desalination*, **250(2)**, pp.801-804.

[9] H. Falahti-Marvast, A. Karimi-Jashni (2015), "Performance of simultaneous organic and nutrient removal in a pilot scale anaerobic-anoxic-oxic membrane bioreactor system treating municipal wastewater with a high nutrient mass ratio", *Int. Biodeter. Biodegr.*, **104**, pp.363-370.

[10] J. Ho, S. Smith, J. Patamasank, P. Tontcheva, G.D. Kim,

H.K. Roh (2015), "Pilot demonstration of energy-efficient membrane bioreactor (MBR) using reciprocating submerged membrane", *Water Environ. Res.*, **87(3)**, pp.266-273.

[11] Z. Liang, A. Das, D. Beerman, Z. Hu (2014), "Biomass characteristics of two types of submerged membrane bioreactors for nitrogen removal from wastewater", *Water Res.*, **44(11)**, pp.3313-3320.

[12] B. Li, G. Wu (2014), "Effects of sludge retention times on nutrient removal and nitrous oxide emission in biological nutrient removal processes", *Int. J. Environ. Res. Public Health*, **11(4)**, pp.3553-3569.

[13] A. Izadi, M. Hosseini, G.N. Darzi, G.N. Bidhendi, F.P. Shariati (2019), "Performance of an integrated fixed bed membrane bioreactor (FBMBR) applied to pollutant removal from paper-recycling wastewater", *Water Resour. Ind.*, **21**, Doi: 10.1016/j.wri.2019.100111.

[14] T.T. Nguyen, X.T. Bui, T.D.H. Vo, D.D. Nguyen, P.D. Nguyen, H.L.C. Do, H.H. Ngo, W. Guo (2016), "Performance and membrane fouling of two types of laboratory-scale submerged membrane bioreactors for hospital wastewater treatment at low flux condition", *Sep. Purif. Technol.*, **165**, pp.123-129.

[15] W. Song, H. You, Z. Li, F. Liu, P. Qi, F. Wang, Y. Li (2017), "Membrane fouling mitigation in a moving bed membrane bioreactor combined with anoxic biofilter for treatment of saline wastewater from mariculture", *Bioresour. Technol.*, **243**, pp.1051-1058.

[16] R. Van den Broeck, J. Van Dierdonck, P. Nijskens, C. Dotremont, P. Krzeminski, J.H.J.M. van der Graaf, J.B. van Lier, J.F.M. Van Impe, I.Y. Smets (2012), "The influence of solids retention time on activated sludge bioflocculation and membrane fouling in a membrane bioreactor (MBR)", *Journal of Membrane Science*, **401**, pp.48-55.

Doi: 10.31276/VJSTE.62(1).55-61

Studies on applying SNP markers to breeding drought-tolerant maize hybrids

Nguyen Xuan Thang[1*], Bui Manh Cuong[1], Dang Ngoc Ha[1], Do Van Dung[1], Sudha Nair[2], M.T. Vinayan[2], Gajanan Saykhedkar[2], Raman Babu[3], Doan Thi Bich Thao[1], Tran Quang Dieu[1], Nguyen Chi Thanh[1], P.H. Zaidi[2]

[1]Maize Research Institute, Vietnam
[2]Asian Regional Maize Program, CIMMYT Int., India
[3]Pioneer Hi-Bred International Inc, USA

Received 21 May 2019; accepted 8 July 2019

Abstract:

The results of testing the International Maize and Wheat Improvement Center's (CIMMYT's) hybrid combinations, developed from hybrid 790 $F_{2:3}$ lines and 10 parental lines, using two testers (CML451 and CLO2450) under optimal and managed drought conditions in Ninh Thuan, Vietnam, show that the average grain yield of the biparental (BP) groups of heterosis groups A and B is, respectively, 2.58-3.65 tons/ha and 2.56-2.76 tons/ha in drought conditions, and 4.24-5.02 tons/ha and 5.41-5.93 tons/ha in well-watered conditions, respectively. By genotyping eight BP populations with 39,846 single nucleotide polymorphism (SNP) markers, CIMMYT experts identified 15 important gene regions that regulate grain yield associated with 15 SNP markers on chromosomes 3, 4, 5, 6, 7, 8, 9, and 10 which is useful for applying molecular markers in breeding drought-tolerant maize. On that basis, the Maize Research Institute of Vietnam studied and genotyped three populations, including 450 F_2 families, with 96 SNPs using the Kompetitive Allele Specific PCR (KASP) genotyping method. The result was that 57 SNP markers related to drought tolerance were found useful to these populations. In addition, 27 F_2 families demonstrating drought tolerance and high grain yield were selected as primary materials for breeding maize hybrids tolerant to stresses and adaptive to climate change.

Keywords: **drought, GWAS, KASP, maize, optimal conditions, SNP markers.**

Classification number: **3.1**

Introduction

Maize (*Zea mays* L.) is one of the three most important cereal crops after wheat and paddy rice. World maize production amounted to 1,075.6 million tons in the 2017/2018 crop year (USDA, 2019). However, climate change has become a considerable challenge for global maize production and led to a 3.8% reduction in yield from 1980 to 2008 [1].

Vietnam is one of the countries most affected by climate change, with a number of serious droughts occurring in the 2015-2017 period. With around 80% of the cultivated area under rainfed condition, drought is considered the biggest challenge for maize production in Vietnam [2]. Therefore, the research and selection of drought-tolerant maize varieties that have high grain yield and the ability to adapt to climate change are of great interest to maize breeders. However, drought tolerance is a low-heritability trait that is regulated by multiple genes; it requires substantial money and time to accomplish these daunting research and selection tasks. Fortunately, genomic selection (GS) by means of mapping quantitative trait loci (QTL) relating to drought tolerance using molecular markers is an efficient and time-saving tool in plant breeding. It results in the achievement of greater breeding value through selection at the early stages of the improvement cycle [3]. Currently, using single nucleotide polymorphisms (SNPs) is becoming more common in plant breeding through marker-assisted selection and is replacing simple sequence repeats (SSRs) for crops, such as maize, whose genomes have been completely sequenced [4].

Applying SNP markers using the Kompetitive Allele Specific PCR (KASP), a technique for genotyping, has been widely used in research because it is cheaper than BeadXpress and GoldenGate platforms, more effective and flexible in many applications, saves time, and produces fewer genotyping errors [4]. Currently, KASP is used by

*Corresponding author: Email: nxthangnmri@gmail.com

CIMMYT for the global maize improvement programme and in quality control QC analysis, QTL mapping, marker-assisted recurrent selection (MARS), genome-wide association studies (GWAS), allele mining [5].

Genetic selection based on SNP markers (KASP and Tagman) is more than 2-4 times effective than the traditional selection method that is based only on phenotype. In drought conditions, the genetic gains in grain yield per cycle using the GS method with KASP markers is 86 kg/ha, without changing the traits of maturity and plant height [6]. Furthermore, F. Bankole, et al. [7] indicate that, in each selection cycle using MARS with SNP markers, grain yield increased by 7% in drought conditions, and the frequency of favourable alleles increased from 0.510 at the original population (C_o) to 0.515 at the selection cycle C_2 of the MARS population.

In Vietnam, the application of SNP markers by means of the KASP method has been used to evaluate and select maize materials tolerant to stresses, especially drought. With the support and advice of CIMMYT's experts in cooperation programmes, the application of SNP markers in MRI's drought-tolerant maize breeding has been studied.

Materials and methods

CIMMYT's hybrid combinations

One thousand five hundred and eighty hybrid combinations developed by CIMMYT from 790 $F_{2:3}$ lines and two testers (tester 1: CML451; tester 2: CLO2450) and 20 hybrid combinations (of 10 parental lines with these testers) were evaluated for drought tolerance with five local checks of LVN10, LVN61, VN8960 (MRI, Vietnam), NK67 (Syngenta), and C919 (Monsanto) in the 2013/2014 dry season in Ninh Thuan.

Leaf samples

The 790 $F_{2:3}$ families developed by CIMMYT by crossing two drought tolerant maternal lines with eight elite ones (divided into two heterosis groups) were collected for genotyping with 1,250 SNP markers which were identified from 1,536 SNP markers, as per Yan, et al. [8].

MRI's three F_2 populations

These F_2 populations were developed from CML161 (one drought-tolerant female line) and the MRI's three male elite ones (TA6, P24 and G12). One hundred and fifty F_1 individuals of each population were selected based on the criteria of growth and development, drought tolerance, and pest resistance in order to self-pollinate and form F_2 seeds; the F_2 seeds of each population were planted in 150 rows (row length: 4.0 m; distance between hills: 0.7 m). The F_2 families of each population (150 F_2 families per population) were evaluated under managed drought conditions in Ninh Thuan. Leaf samples of three F_2 populations including 450 F_2 families (6-8 plants per family) grown at MRI were collected for genotyping with 96 SNP markers (*The physical positions of these SNP markers was determined on the maize genome chromosomes according to B73 RefGen_v2 at Maize GDB*) using the KASP method to select F_2 families capable of drought tolerance.

Methodologies of phenotyping

The experiments were conducted in field conditions designed using Latin squares (*Alpha lattices*). *For trials testing CIMMYT's hybrid combinations:* row length: 4.0 m; distance between rows: 0.75 m; distance between hills in the row: 0.25 m. The experiments were evaluated under managed drought and optimal conditions in Ninh Thuan according to CIMMYT's guidelines [9]. *For testing MRI's F_2 populations:* row length of 4.0 m at a spacing of 0.7 m by 0.2 m; evaluated under managed drought conditions in Ninh Thuan using CIMMYT's guidelines [10].

Methodologies of the GWAS

Genotypic and phenotypic data on grain yield were analysed using 55K models (56,110 SNP markers) and GBS v2.7 (954,179 SNP markers). Genotyping with 55K MaizeSNP50 from Illumina (*www.illumina.com*), while the SNP marker positions of GBS and 55K were sourced from Panzea_2.7GBS (*http://plants.ensembl.org/Zea_mays /Info/Index*). Based on standard requirements, a minimum allele frequency >0.05 for 55K and >0.02 for GBS; 39,846 SNP markers from 55K chips and 435,975 SNP markers from GBS were selected for genotying.

Methodologies of genotyping using the KASP method

KASP is a technique for genotyping with SNP markers [4] and consists of three components: the KASP assay mix, the KASP master mix, and DNA samples. The procedures were conducted according to the instructions of LGC Genomics Ltd (details at *http://www.lgcgroup.com*).

Phenotypic analysis

Analysis of variance of the genotype and phenotype (σ^2_g and σ^2_p) and heritability (h^2) were calculated using the formula suggested by Lush, et al. [11] with GenStat 12.0, METAR 2.1, and Fieldbook software (CIMMYT, 2010). The multivariate restricted maximum likelihood model and SAS ver. 9.2 software were used to calculate genetic variance and covariance.

Genotypic analysis

For GWAS with SNP markers, the multi-locus mixed

additive model was used [12]. The genotypic analysis was conducted with Variation Suite ver. 8.3.4 software.

Results

Testing of hybrid combinations developed from 790 $F_{2:3}$ families by CIMMYT in drought and optimal conditions in Ninh Thuan province, Vietnam

Phenotyping results: through testing, it was shown that the grain yield of hybrid combinations developed from crossing 790 $F_{2:3}$ families, parental lines of heterosis group A, and parental lines of heterosis group B with two testers in drought conditions decreased from 27.23 to 54.16%, from 16.2 to 100.0%, and from 5.88 to 83.3%, respectively, compared to well-watered conditions (Tables 1 and 2).

Table 1. Average grain yield of hybrid combinations (heterosis group A with two testers) in the 2013/2014 dry season under managed drought and optimal conditions in Ninh Thuan.

Heterosis group A	Conditions	Grain yields (tons/ha)			
		BP1 × testers	*BP2 × testers*	*BP3 × testers*	*BP4 × testers*
$F_{2:3}$ x CT±Std	Drought	3.65±1.87	2.86±1.77	3.18±1.68	2.58±1.53
	Optimal	5.02±1.53	4.24±1.71	4.66±1.82	4.58±1.79
	Reduction %	27.23	32.53	31.72	43.75
Variation	Drought	0.30÷6.89	0.00÷6.32	0.00÷6.54	0.00÷6.22
	Optimal	0.23÷8.29	0.23÷7.86	0.00÷7.6	0.00÷7.23
σ_ε^2	Drought	2.18	1.80	1.98	1.29
	Optimal	1.30	1.80	1.19	1.47
σ_g^2	Drought	0.45	0.41	0.46	0.78
	Optimal	0.77	0.72	1.20	0.95
h^2	Drought	0.29	0.31	0.32	0.55
	Optimal	0.54	0.44	0.67	0.56
P.e × testers±Std		P1 × testers	P2 × testers	P3 × testers	P4 × testers
P.e × tester 1 (CML415)	Drought	5.56±0.86	0.00±0.00	2.83±1.91	0.97±0.42
	Optimal	6.29±1.35	0.23±0.11	4.8±0.83	3.01±2.31
	Reduction %	11.61	100.00	41.04	67.77
P.e × tester 2 (CLO2450)	Drought	4.62±0.53	0.00±0.00	4.77±0.63	1.19±0.70
	Optimal	5.84±0.99	0.53±0.04	5.97±1.37	3.86±0.69
	Reduction %	20.89	100.00	20.10	69.17
P.dr × testers±Std		P9 × Testers			
P.dr × tester 1 (CML415)	Drought	2.17±1.23			
	Optimal	3.79±1.26			
	Reduction %	42.74			
P.dr × tester 2 (CLO2450)	Drought	4.08±1.22			
	Optimal	4.87±0.72			
	Reduction %	16.22			
$LSD_{0.05}$	Drought	2.90	2.60	2.80	2.20
	Optimal	2.20	2.60	2.10	2.40
CV (%)	Drought	40.90	47.10	43.20	43.40
	Optimal	22.80	31.60	23.60	26.40
Local checks	LVN10	LVN8960	NK67	C919	LVN61
Conditions	Drought Optimal	Drought Optimal	Drought Optimal	Drought Optimal	Drought Optimal
Grain yields (tons/ha)	3.15 4.79	4.25 5.26	5.00 6.12	4.47 7.01	4.76 7.36
Reduction %	8.02	12.15	13.05	35.62	20.35

Note: x: cross; ±Std: standard deviation; ÷: variation between minimum and maximum values; BP: Bi-parent; P: parental lines; P.e: elite lines (P1 to P8); P.dr: drought tolerant lines (P9 and P10); reduction %: the rate of reduction in grain yield in drought conditions compared with optimal conditions (%); σ_ε^2: error variation; σ_g^2: genotype variation; CV (%): coefficient of variation; $LSD_{0.05}$: least significant difference at a 95% confidence level.

Table 2. Average grain yield of hybrid combinations (heterosis group B with two testers) in the 2013/2014 dry season under managed drought and optimal conditions in Ninh Thuan.

Heterosis group B	Conditions	Grain yields (tons/ha)			
		BP5 × testers	*BP6 × testers*	*BP7 × testers*	*BP8 × testers*
$F_{2:3}$ × testers±Std	Drought	2.76±1.64	2.75±1.59	2.72±1.58	2.56±1.64
	Optimal	5.89±1.54	5.65±1.43	5.93±1.59	5.41±1.25
	Reduction %	53.14	51.40	54.16	52.72
Variation	Drought	0.00÷6.97	0.00÷7.18	0.00÷5.91	0.00÷6.39
	Optimal	0.20÷9.57	0.00÷8.57	0.53÷8.79	0.00÷8.67
σ_ε^2	Drought	2.17	0.34	1.80	1.79
	Optimal	1.48	0.57	1.49	0.95
σ_g^2	Drought	0.15	0.00	0.48	0.12
	Optimal	0.75	0.00	0.67	0.51
h^2	Drought	0.12	0.34	0.35	0.12
	Optimal	0.50	0.57	0.48	0.52
P.e × testers±Std		P5 × testers	P6 × testers	P7 × testers	P8 × testers
P.e × testers 1 (CML415)	Drought	2.99±1.38	0.75±0.76	2.73±1.18	1.43±1.27
	Optimal	4.84±0.43	4.49±0.74	6.27±0.74	5.01±0.52
	Reduction %	38.22	83.30	56.46	71.46
P.e × testers 2 (CLO2450)	Drought	3.42±1.04	2.68±0.93	0.83±0.71	3.17±1.18
	Optimal	3.60±0.79	5.45±0.18	4.32±0.23	6.36±1.06
	Reduction %	5.88	50.83	80.79	50.16
P.dr × testers±Std		P10 × testers			
P.dr × testers 1 (CML415)	Drought	1.12±0.63			
	Optimal	5.14±1.17			
	Reduction %	78.21			
P.dr × tester 2 (CLO2450)	Drought	3.17±2.09			
	Optimal	6.35±0.70			
	Reduction %	50.08			
$LSD_{0.05}$	Drought	2.90	2.60	2.60	2.60
	Optimal	2.40	2.00	2.40	1.90
CV (%)	Drought	53.50	47.90	48.50	51.90
	Optimal	20.70	18.30	20.80	18.00
Local checks	LVN10	LVN8960	NK67	C919	LVN61
Conditions	Drought Optimal	Drought Optimal	Drought Optimal	Drought Optimal	Drought Optimal
Grain yields (tons/ha)	3.15 4.79	4.25 5.26	5.00 6.12	4.47 7.01	4.76 7.36
Reduction %	8.02	12.15	13.05	35.62	20.35

Note: x: cross; ±Std: standard deviation; ÷: variation between minimum and maximum values; BP: Bi-parent; P: parental lines; P.e: elite lines (P1 to P8); P.dr: drought tolerant lines (P9 and P10); reduction %: the rate of reduction in grain yield in drought conditions compared to optimal conditions (%); σ_ε^2: error variation; σ_g^2: genotype variation; CV (%): coefficient of variation; $LSD_{0.05}$: least significant difference at a 95% confidence level.

In drought conditions, the average grain yield of hybrid combinations of BP groups of heterosis group A with testers reached 2.58-3.65 tons/ha, of which the combinations developed from BP1 had the highest yield (3.65 tons/ha) and the least reduction (27.23%) (Table 1). Hybrid combinations created from $F_{2:3}$ families of heterosis group B with these testers showed no differences in grain yield, with the range of 2.56 to 2.76 tons/ha (Table 2).

In optimal conditions, the average grain yield of hybrid combinations among BP groups of heterosis groups A and B with testers reached 4.24-5.02 tons/ha and 5.41-5.93 tons/ha, respectively. The yield of hybrid combinations of the two drought-tolerant lines (P9 and P10) with these testers in drought conditions decreased by 42.74-78.21% for tester 1 and by 16.22-50.08% for tester 2 compared to those in optimal conditions. The results indicate that hybrid combinations derived from P9 and P10 with tester 2 demonstrate better drought tolerance. In drought conditions, the yield of hybrid combinations developed from elite lines with two testers also decreased, by 27.23-43.75% for group A and by 51.40-54.16% for group B, compared to those in the optimal condition. Thus, the progenies of group A showed a smaller reduction in grain yield than did those of group B did in dehydrated conditions. In other words, the hybrid combinations that originated in group A had better tolerance to drought than did those that originated in group B (Tables 1 and 2).

Compared to the grain yield of five local checks, the highest yield of hybrid combinations developed from $F_{2:3}$ families with testers in drought and optimal conditions was, respectively, 6.89 tons/ha and 8.29 tons/ha (for group A), and 7.18 tons/ha and 9.57 tons/ha (for group B) - higher than these of local checks (3.15-5.00 tons/ha in drought conditions; and 4.79-7.36 tons/ha in optimal conditions, with a reduction in grain yield of 8.02-35.62%) (Tables 1 and 2).

This result is significant because it was found that among 790 $F_{2:3}$ families developed from eight BP lines, some showed better drought-tolerance ability, were higher in grain yield than their parental lines, and, especially, reached a yield equivalent to the five local checks. These families can potentially be selected as materials and germplasms for a drought-tolerant maize breeding programme in order to adapt to climate change.

Genome-wide association analysis for grain yield of eight progenic populations $F_{2:3}$

The MRI is a member of the project *"Abiotic stress tolerant maize for increasing income and food security among the poor in South and Southeast Asia"*. Experts from CIMMYT conducted GWAS with 39,846 SNP markers for 790 $F_{2:3}$ families of eight populations. As the result, 15 genomic regions controlling the trait of grain yield in drought conditions were identified. These regions associating with the SNPs markers include S3_151334181, S4_224910359, S5_208101878, S6_67260174, S7_40327099, S8_144372859, S9_88734345, S9_82359236, S9_154651413, S9_151662859, S9_100305550, S9_96774495, S9_11501850, S10_137460286, and S10_147354987 (from Panzea_2.7 GBS) on chromosomes 3, 4, 5, 6, 7, 8, 9, and 10 (Table 3) and can be significant for drought-tolerant maize breeding programmes.

Table 3. The list of 15 genomic regions controlling grain yield for BP populations of the $F_{2:3}$ generation through GWAS of each chromosome.

SNP markers	Chr	GWAS DD-dd	Marker location	Loci										Minor allele	Allele frequency	Major allele
				P1	*P2*	*P3*	*P4*	*P5*	*P6*	*P7*	*P8*	*BP/P9*	*BP/P10*			
S3_151334181	3	0.59	151.334.181	C/C	C/C	G/G	C/G	C/G	C/G	C/C	C/C	C/C	C/C	G	0.11	C
S4_224910359	4	8.50	224.910.359	C/C	T/T	T/T	T/T	C/T	T/T	C/C	C/C	C/C	C/C	T	0.30	C
S5_208101878	5	7.32	208.101.878	T/T	T/T	T/T	T/G	T/T	T/T	T/G	T/T	T/T	G/G	G	0.26	T
S6_67260174	6	0.53	67.260.174	C/C	C/C	C/C	C/A	C/A	C/A	A/A	A/A	C/C	C/C	A	0.25	C
S7_40327099	7	7.99	40.327.099	G/G	G/G	G/G	G/A	G/G	G/G	A/A	G/A	G/G	G/G	A	0.08	G
S8_144372859	8	1.99	144.372.859	T/T	C/C	C/C	C/C	C/C	C/C	T/T	T/T	C/C	C/T	T	0.31	C
S9_88734345	9	8.70	88.734.345	A/A	A/A	A/A	A/A	A/A	A/G	A/A	A/A	A/A	G/G	G	0.20	A
S9_82359236	9	7.84	82.359.236	C/C	C/C	C/C	C/A	C/C	C/C	C/C	C/C	C/C	A/A	A	0.19	C
S9_154651413	9	4.30	154.651.413	A/A	C/C	C/C	A/C	A/A	A/A	A/A	C/C	A/A	C/C	C	0.43	A
S9_151662859	9	-2.64	151.662.859	T/T	T/T	A/A	T/T	T/A	T/T	T/T	T/T	T/T	T/T	A	0.06	T
S9_100305550	9	-5.50	100.305.550	G/G	T/T	T/T	T/T	T/T	G/G	G/G	T/G	T/T	T/T	G	0.18	T
S9_96774495	9	-5.54	96.774.495	G/G	A/A	A/A	A/A	A/A	G/G	G/G	A/A	A/A	A/A	G	0.18	A
S9_11501850	9	-5.85	11.501.850	C/C	C/C	C/C	C/C	C/C	C/C	G/G	G/G	C/C	C/C	G	0.10	C
S10_137460286	10	0.02	137.460.286	G/G	C/C	G/G	C/G	G/G	C/G	C/C	C/G	C/C	C/C	G	0.26	C
S10_147354987	10	-1.87	147.354.987	T/C	T/T	C/C	T/C	T/T	C/C	T/T	T/C	T/T	C/C	C	0.46	T

Note: P: parental lines; BP/P: populations developed from parent pairs; DD-dd: homozygous.

Identifing materials tolerant to drought with SNP markers by means of KASP method

Based on the results of phenotyping and genotyping with SNP markers of the cooperation programme with CIMMYT, the MRI conducted initial research on identifying materials tolerant to drought with SNP markers by means of the KASP method and evaluated their drought tolerance in Ninh Thuan in the 2018/2019 dry season.

Results of phenotyping three populations including 450 F_2 families: it has been shown that the yield of three populations in drought conditions, in which had been selected 27 F_2 families with grain yields equivalent to local check DK7328 and higher than the yield of NK67,

Table 4. Results of evaluating the grain yield of three populations (including 450 F_2 families) under managed drought conditions in Ninh Thuan.

Statistical Indices	Grain yields (tons/ha)					
	CML161 x TA6		*CML161 x P24*		*CML161 x G12*	
F_2±Std	1.20±0.52		1.33±0.52		1.00±0.45	
Variation	0.01÷3.14		0.00÷3.25		0.66÷3.40	
σ_p^2	3.01		4.83		4.12	
σ_e^2	0.13		0.14		0.10	
σ_g^2	1.67		3.44		3.08	
h^2	0.56		0.71		0.75	
$LSD_{0,05}$	1.02		1.03		0.88	
CV (%)	42.91		39.64		45.41	
Parental lines	CML161	TA6	CMl161	P24	CML161	G12
Grain yields (tons/ha)	0.580	0.247	0.948	0.368	0.812	0.513
Local checks	NK7328	NK67	NK7328	NK67	NK7328	NK67
Grain yields (tons/ha)	2.455	2.327	2.801	2.618	3.041	2.803

Note: x: cross; ±Std: standard deviation; σ_p^2: phenotype variation; σ_e^2: error variation; σ_g^2: genotype variation; h^2: heritability; CV (%): coefficient of variation; $LSD_{0.05}$: least significant difference at a 95% confidence level.

varies from 1.00 to 1.33 tons/ha (Tables 4 and 5). The heritability (h^2), which was from 0.56 to 0.75, showed that the relationship between phenotype and genotype of these populations was positive. Genotypic variance (σ_g^2) on grain yield in drought conditions ranged from 1.67 to 3.44, leading to the conclusion that variation in grain yield was mainly affected by male lines (TA6, P24, and G12).

Results of genotyping three populations including 450 F_2 families and parental lines: through genotyping 450 F_2 families and four parental lines with 96 SNP markers using the KASP technique combined with CIMMYT's researched data, the initial results showed that there were 57 meaningful SNP markers in these populations of 450 F_2 families and that these markers could be related to yield in drought conditions (Table 6). The trait of grain yield is controlled by many genes and the interaction among major and minor loci that affect this trait in drought conditions. Hence, potential SNP markers identified through the KAPS method can be useful for breeding drought-tolerant maize.

Table 5. Selected families of three populations under managed drought conditions in Ninh Thuan.

F_2 families	Pedigree	GY (tons/ha)	F_2 families	Pedigree	GY (tons/ha)
Population 1: CML161xTA6			Population 2: CML161xP24		
BP1_110	(CML161xTA6)-110	3.14	BP2_188	(CML161xP24)-188	3.25
BP1_107	(CML161xTA6)-107	2.92	BP2_181	(CML161xP24)-181	3.10
BP1_101	(CML161xTA6)-101	2.91	BP2_239	(CML161xP24)-239	3.08
BP1_127	(CML161xTA6)-127	2.80	BP2_177	(CML161xP24)-177	3.06
BP1_102	(CML161xTA6)-102	2.80	BP2_226	(CML161xP24)-226	3.00
BP1_7	(CML161xTA6)-7	2.55	BP2_275	(CML161xP24)-275	2.99
BP1_93	(CML161xTA6)-93	2.45	BP2_196	(CML161xP24)-196	2.96
BP1_33	(CML161xTA6)-33	2.34	BP2_207	(CML161xP24)-207	2.94
NK7328	Local check 1	2.46	BP2_203	(CML161xP24)-203	2.91
NK67	Local check 2	2.33	BP2_281	(CML161xP24)-281	2.85
$LSD_{0,05}$		1.02	BP2_295	(CML161xP24)-295	2.79
CV (%)		42.91	BP2_227	(CML161xP24)-227	2.79
Population 3: CML161xG12			BP2_166	(CML161xP24)-166	2.76
BP3_344	(CML161xG12)-344	3.40	BP2_271	(CML161xP24)-271	2.71
BP3_335	(CML161xG12)-335	3.32	K7328	Local check 1	2.80
BP3_301	(CML161xG12)-301	3.27	NK67	Local check 2	2.62
BP3_307	(CML161xG12)-307	3.20	$LSD_{0,05}$		1.03
BP3_331	(CML161xG12)-331	3.12	CV (%)		39.64
K7328	Local check 1	3.04			
NK67	Local check 2	2.80			
$LSD_{0,05}$		0.88			
CV (%)		45.41			

Note: x: cross; GY: grain yield; CV (%): coefficient of variation; $LSD_{0.05}$: least significant difference at a 95% confidence level.

Table 6. The list of 57 SNP markers for drought tolerance useful to MRI's populations using KASP method.

SNP markers	Chr	Maker location	Alleles		SNP markers	Chr	Maker location	Alleles	
S10_10246089	10	10246089	A	G	S3_220896526	3	220896526	C	T
S10_122267546	10	122267546	G	C	S3_220901626	3	220901626	A	G
S10_136938361	10	136938361	A	T	S4_10217574	4	10217574	A	T
S10_139313697	10	139313697	G	A	S4_123979624	4	123979624	A	G
S10_139318575	10	139318575	C	T	S4_229316522	4	229316522	A	T
S10_139321312	10	139321312	G	A	S5_11882524	5	11882524	T	G
S10_139321315	10	139321315	T	G	S5_167585338	5	167585338	A	G
S10_145942320	10	145942320	A	G	S5_179010958	5	179010958	A	C
S10_19372348	10	19372348	G	A	S5_179024804	5	179024804	T	C
S10_19372355	10	19372355	C	T	S5_212872911	5	212872911	C	G
S1_182392227	1	182392227	A	G	S5_213035501	5	213035501	A	T
S1_182423684	1	182423684	C	T	S5_39454290	5	39454290	A	G
S1_182423923	1	182423923	T	C	S5_42746321	5	42746321	A	T
S1_183911148	1	183911148	A	G	S5_42746324	5	42746324	T	C
S1_188224557	1	188224557	C	G	S6_105833772	6	105833772	G	A
S1_21714481	1	21714481	T	G	S6_105833891	6	105833891	T	G
S1_288696288	1	288696288	A	C	S6_106407839	6	106407839	A	G
S2_118910398	2	118910398	A	G	S6_106736814	6	106736814	T	C
S2_15997107	2	15997107	T	C	S7_13851342	7	13851342	G	A
S2_213597045	2	213597045	C	G	S7_157204971	7	157204971	A	G
S2_51286162	2	51286162	G	A	S7_19272803	7	19272803	G	T
S3_1467367	3	1467367	G	C	S8_160298809	8	160298809	A	G
S3_1467368	3	1467368	G	A	S8_75390111	8	75390111	T	C
S3_156797754	3	156797754	A	C	S8_94438283	8	94438283	T	C
S3_169044562	3	169044562	A	G	S9_116356519	8	116356519	C	T
S3_187437395	3	187437395	A	C	S9_152528782	9	152528782	T	G
S3_187712524	3	187712524	A	G	S9_20311986	9	20311986	A	C
S3_187712599	3	187712599	C	G	S9_22106256	9	22106256	T	A
S3_220888091	3	220888091	T	C					

The identification of significant SNP markers will support and improve breeding drought-tolerant maize. Based on the application of these SNPs at major gene regions associated with drought tolerance, materials tolerant to drought can be found. Through genotyping with 96 SNP markers and phenotyping under managed drought conditions, it was initially shown that the drought tolerance of 450 F_2 families is inherited from the female line (CML161), twenty-seven F_2 familes with these SNP markers related to drought tolerance and the grain yield from 2.34 to 3.40 tons/ha, equivalent to the local checks of DK7328 (2.46 to 3.04 tons/ha) and NK67 (2.33 to 2.80 tons/ha) were found through testing in the field. These families could be primary materials for the MRI's drought-tolerant maize breeding in the future.

Discussion

Through cooperation programmes with CIMMYT, studies on applying SNP markers in drought-tolerant maize breeding were conducted with the participation of scientists from the MRI, which helped the institute gain access to modern research technologies.

A number of good materials with drought tolerance, that are adapted to climate change, and that moreover improve the research capacity of MRI scientists regarding the application of SNP markers in maize breeding and towards mastering maize breeding technology with SNP markers have initially been developed.

Based on CIMMYT's results pertaining to genotyping materials with SNP markers in the course of the Affordable, Accessible Asian Drought Tolerant Maize and Abiotic Stress-Tolerant Maize for Increasing Income and Food Security among the Poor in South and Southeast Asia projects, and with advice and support from CIMMYT experts, the MRI studied and genotyped 450 F_2 families with 96 SNP markers using the KASP method. Fifty-seven SNP markers related to drought tolerance were found useful in these populations. The research results also show that the allele call rate was 87%, which is equivalent to that in studies that currently apply SNP markers using the KASP method, which have found a rate of 50-97% [13, 14].

This research can be used as a guideline for the MRI

breeding maize tolerant to stresses by combining traditional and biotechnological methods in accordance with current conditions in Vietnam. At the same time, in order to develop drought-tolerant materials that are adapted to climate change in hybrid maize breeding programmes, it is necessary to continue research that applies SNP markers to the MRI's existing germplasm and to enhance cooperation with CIMMYT and other international institutes regarding the application of SNP markers in maize breeding.

Conclusions

Based on CIMMYT cooperation programmes involving phenotyping and genotyping with SNP markers by means of QTL mapping and GWAS, the MRI initially carried out genotying three populations including 450 F_2 families with 96 SNP markers by KASP method, it was shown that 57 SNP markers related to drought tolerance were found useful to these populations and, through testing them in drought conditions, 27 F_2 families with drought tolerance and high yield were selected as primary materials for breeding stress-tolerant maize hybrids that are adapted to climate change.

ACKNOWLEDGEMENTS

This work was funded by Vietnam Government through Fostering Innovation through Research, Science and Technology (FIRST) project under Grant Agreement No. 18/FIRST/2a/MRI and supported by a budget from the Deutsche Gessellschaft für Technische Zusammenarbeit (GTZ) under CIMMYT's project: Abiotic Stress Tolerant Maize for Increasing Income and food Security among the poor in South and Southeast Asia- ATMA. We would like to deeply thank Dr. P.H Zaidi, Dr. Sudha Nair, Dr. Raman Babu and CIMMYT, India scientists for their support and consultation.

The authors declare that there is no conflict of interest regarding the publication of this article.

REFERENCES

[1] D.B. Lobell, et al. (2011), "Climate trends and global crop production since 1980", *Science*, **333(6042)**, pp.616-620.

[2] Mai Xuan Trieu (2014), "Maize production in Vietnam: current status and future prospects", *12th Asian Maize Conference and Expert Consultation on Maize for Food, Feed, Nutrition and Environmental Security*, Bangkok, Thailand, CIMMYT, pp.332-338.

[3] K. Koehler (2014), *Application of Genomic Selection in Commercial Corn Breeding and Crop Improvement*, Dow AgroSciences.

[4] K. Semagn, R. Babu, S. Hearne, M. Olsen (2014), "Single nucleotide polymorphism genotyping using Kompetitive Allele Specific PCR (KASP): overview of the technology and its application in crop improvement", *Molecular Breeding*, **33(1)**, pp.1-14.

[5] R.J. Elshire, J.C. Glaubitz, Q. Sun, J.A. Poland, K. Kawamoto, E.S. Buckler, S.E. Mitchell (2011), "A robust, simple genotyping-by-sequencing (GBS) approach for high diversity species", *PLOS ONE*, **6(5)**, Doi: 10.1371/journal.pone.0019379.

[6] Y. Beyene, et al. (2015), "Genetic gains in grain yield through genomic selection in eight bi-parental maize populations under drought stress", *Crop Science*, **55**, pp.154-163.

[7] F. Bankole, et al. (2017), "Genetic gains in yield and yield related traits under drought stress and favorable environments in a maize population improved using marker assisted recurrent selection", *Frontiers in Plant Science*, **8(808)**, Doi: 10.3389/fpls.2017.00808.

[8] J. Yan, et al. (2010), "High-throughput SNP genotyping with the GoldenGate assay in maize", *Molecular Breeding*, **25(3)**, pp.441-451.

[9]. P.H. Zaidi (2002), *Drought Tolerance in Maize: Theoretical Considerations & Practical Implications*, CIMMYT, Int.

[10] M. Zaman Allah, et al. (2016), *Phenotyping for Abiotic Stress Tolerance in Maize: Drought Stress*, CIMMYT, Mexico.

[11] J.L. Lush, A.E. Mollin (1942), "Litter size and weight as permanent characteristics of sows", *Techical Bulletin*, **836**, pp.1-40.

[12] A. Korte, et al. (2012), "A mixed-model approach for genome-wide association studies of correlated traits in structured populations", *Nature Genetics*, **44(9)**, pp.1066-1071.

[13] D.L. Hyten, et al. (2010), "High-throughput SNP discovery through deep resequencing of a reduced representation library to anchor and orient scaffolds in the soybean whole genome sequence", *BMC Genomics*, **11**, Doi: 10.1186/1471-2164-11-38.

[14] U. Majeed, E. Darwish, S.U. Rehman, X. Zhang (2019), "Kompetitive Allele Specific PCR (KASP): a singleplex genotyping platform and its application", *Journal of Agricultural Science*, **11(1)**, pp.11-20.

Doi: 10.31276/VJSTE.62(1).62-68

Analysis of genetic diversity in Pa Co pine (*Pinus kwangtungensis* Chun ex Tsiang) using RAPD and ISSR markers

Mai Thi Phuong Thuy[1*], Tran Thi Thu Ha[1], Tran Ho Quang[2]

[1]*Institute of Forest Tree Improvement and Biotechnology, Vietnamese Academy of Forest Sciences*
[2]*Institute of Biotechnology, Vietnam Academy of Science and Technology*

Received 8 January 2019; accepted 28 May 2019

Abstract:

***Pinus kwangtungensis* (Pa Co pine) is one of three five-needle pine species in Vietnam, found on the slopes of limestone mountains at altitudes between 1200 and 1500 m. Global warming and long-term deforestation threaten the existence of the species in nature. The genetic diversity of plant populations provides a background for future conservation and improvement programmes. However, the genetic diversity of Pa Co pine is unknown. This study aimed to use inter-simple sequence repeat (ISSR) and random amplified polymorphic DNA (RAPD) genetic markers to evaluate the genetic-diversity parameters of *P. kwangtungensis* to understand the genetic effects of small and fragmented populations, as well as provide the genetic background for its conservation. Total genomic DNA was extracted from fresh needles of 40 trees in four different areas and amplified with 15 RAPD and 16 ISSR markers. Results indicated that the genetic diversity index (h) of *P. kwangtungensis* was 0.2530 with RAPD and 0.223 with ISSR. High genetic variation was found within populations (72% with RAPD and 87% with ISSR). Principal coordinates analysis based on RAPD analysis revealed that the presence of three groups was in accordance, whereas no clear cluster was formed according to ISSR analysis. The results from this study enhance the understanding of the genetic effects of small and fragmented populations of native species that are rare, vulnerable, and require conservation.**

Keywords: **conservation, genetic diversity, ISSR, *Pinus kwangtungensis*, RAPD.**

Classification number: **3.5**

Introduction

Pa Co pine (*Pinus kwangtungensis* Chun ex Tsiang) is one of three five-needle pines in Vietnam; the two others are Da Lat pine (*P. dalatensis* Ferre) and Xuan Nha pine (*P. armandii* subsp. *xuannhaensis* L.K.Phan). It grows naturally in the Northwest region on the slopes of limestone mountains at altitudes between 1200 and 1500 m [1]. This region has a type of tropical climate, but the winters are cold. The mean annual temperature is 14-20°C and the average rainfall exceeds 1200 mm [2]. Pa Co pine is found in northern Vietnam (including Cao Bang, Son La, Hoa Binh, and Thanh Hoa) provinces. Trees can reach 20 m in height and 70 cm in diameter at breast height. The two images in Fig. 1 show a *P. kwangtungensis* tree. It has scaly, brown, and rough bark, with leaves (needles) in bundles of 2-5 per fascicle. The needles are 3-7 cm long and 1-1.5 mm wide. Female cones are cylindrical or ovoid, up to 8 cm long, and 1.5-7 cm wide. The pendant has a short angled peduncle at maturity, either solitary or in pairs. Seed scales are obovate with rhombic apophysis, a thin apex, and umbo depressed. Seeds are ellipsoid- or ovoid-shaped, 0.8-1.2 cm in size, and with wings 2-3 cm long. When on the tree, the opening and release of seeds are not persistent. Furthermore, seed maturation occurs 2 years after pollination. The species has multiple uses. Its timber is useful for constructing houses and furniture as well as developing infrastructure. In addition, local people often use this tree for medicine [3] and to make bonsai trees [2] for ornamental purposes. However, this species is threatened by the rapid global population growth rate along with climate change. In the IUCN Red List of Threatened Species, *P. kwangtungensis* is listed as Near Threatened [4]. In Vietnam, Pa Co pine is listed as a vulnerable species (VU A1acd, B1+2bce). Pa Co

**Corresponding author: Email: phuongthuy284@gmail.com*

pine populations are small, fragmented, restricted habitat, and lack of the natural regeneration. These populations are also persistent logging while the number of mature trees is limited [5]. Therefore, the conservation of this vital species is essential to prevent it from going extinct.

Fig. 1. Pa Co pine tree (left) and branch with needles and cone (right). Photo: Trinh Ngoc Bon, Silvicuture Research Institute, Vietnamese Academy of Forest Sciences.

Studying the genetic diversity in a plant population provides basic information for future conservation and improvement programmes. The application of a molecular marker system is a quick and effective tool for studying genetic diversity. Several molecular marker systems, including random amplified polymorphic DNA (RAPD), inter-simple sequence repeat (ISSR), and restriction fragment length polymorphism have been used to study the genetic diversity of conifers [6-9]. Previous studies on the genetic variation of conifers such as *Cunninghamia lanceolata* var. *konishii* [10], *Fokienia hodginsii* [11], *Glyptostrobus pensilis* [12], and *Pinus kremfii* [9] in Vietnam have revealed low levels of genetic differentiation among populations. Genetic diversity studies have also been conducted for other crucial native species such as *Erythrophleum fordii* Oliv. [13], *Hopea cordata* Vidal [14], *Afzelia xylocarpa* Kurz [15], and *Dipterocarpus alatus* Roxb [16]. These studies have been significant for the conservation plans of these species. At present, knowledge on the genetic diversity of *P. kwantungensis* is lacking, which is a barrier to the development of a conservation strategy. Therefore, exploring the genetic diversity in *P. kwangtungensis* is critical for designing a future conservation plan for this species.

The objective of this study was to analyse the existing level of genetic variability in *P. kwangtungensis* populations using RAPD and ISSR markers. Compared with other molecular markers, RAPD and ISSR are easy, cost-effective, and fast tools for studying genetic diversity. Moreover, they do not require prior knowledge of the flanking sequence of the genome of the species concerned [17]. The results will provide the background for the conservation, management, and restoration of this species.

Methodology

Sample collection

Fresh leaves of 40 individual *P. kwangtungensis* trees were collected from four sites, and these are listed in Table 1. The sizes of the populations were 15, 3, 20, and 2 in Moc Chau town - Moc Chau - Son La, Muong Sang - Moc Chau - Son La, Hang Kia - Mai Chau - Hoa Binh, and Pa Co - Mai Chau - Hoa Binh, respectively. The samples were kept in plastic bags with silica gel in the field, transferred to Molecular Biology Laboratory (Institute of Forest Tree Improvement and Biotechnology), and stored at 4°C until DNA extraction.

Table 1. Sample collection locations of *P. kwangtungensis* and the trees' status.

No	Sample ID	Regions	Geographic location		Elevation (m)	Tree status
			Longitude	*Latitude*		
1	MC1	Moc Chau town - Moc Chau - Son La	20°53'18.9"	104°38'7.2"	1189	Old
2	MC2	Moc Chau town - Moc Chau - Son La	20°53'18.7"	104°38'7.2"	1196	Old
3	MC3	Moc Chau town - Moc Chau - Son La	20°53'18.9"	104°38'7.2"	1197	Old
4	MC4	Moc Chau town - Moc Chau - Son La	20°53'18.6"	104°38'7.2"	1204	Old
5	MC5	Moc Chau town - Moc Chau - Son La	20°53'18.5"	104°38'7.2"	1220	Old
6	MC6	Moc Chau town - Moc Chau - Son La	20°53'18.3"	104°38'7.2"	1222	Old
7	MC7	Moc Chau town - Moc Chau - Son La	20°53'18.2"	104°38'7.2"	1224	Old
8	MC8	Moc Chau town - Moc Chau - Son La	20°53'17.4"	104°38'7.2"	1226	Old
9	MC9	Moc Chau town - Moc Chau - Son La	20°53'17.0"	104°38'7.2"	1230	Old

10	MC10	Moc Chau town - Moc Chau - Son La	20°53'16.5"	104°38'7.2"	1225	Old
11	MC11	Moc Chau town - Moc Chau - Son La	20°53'16.6"	104°38'7.2"	1219	Young
12	MC12	Moc Chau town - Moc Chau - Son La	20°53'16.3"	104°38'7.2"	1222	Old
13	MC13	Moc Chau town - Moc Chau - Son La	20°53'16.9"	104°38'7.2"	1221	Young
14	MC14	Moc Chau town - Moc Chau - Son La	20°53'15.5"	104°38'7.2"	1219	Young
15	MC15	Moc Chau town - Moc Chau - Son La	20°53'12.6"	104°38'7.2"	1212	Old
16	MS1	Muong Sang - Moc Chau - Son La	20°53'36.6"	104°37'8.2"	1180	Young
17	MS2	Muong Sang - Moc Chau - Son La	20°53'39.4"	104°37'5.7"	1212	Old
18	MS3	Muong Sang - Moc Chau - Son La	20°53'39.7"	104°37'4.8"	1208	Old
19	HK1	Hang Kia - Mai Chau - Hoa Binh	20°44'0.8"	104°53'23.1"	1409	Young
20	HK2	Hang Kia - Mai Chau - Hoa Binh	20°44'0.9"	104°53'23"	1412	Young
21	HK3	Hang Kia - Mai Chau - Hoa Binh	20°44'1.5"	104°53'23.2"	1412	Old
22	HK4	Hang Kia - Mai Chau - Hoa Binh	20°44'1.9"	104°53'23.6"	1411	Old
23	HK5	Hang Kia - Mai Chau - Hoa Binh	20°44'2.5"	104°53'24.1"	1386	Tree regeneration
24	HK6	Hang Kia - Mai Chau - Hoa Binh	20°44'13.3"	104°53'25.0"	1398	Young
25	HK7	Hang Kia - Mai Chau - Hoa Binh	20°44'4.7"	104°53'25.4"	1398	Old
26	HK8	Hang Kia - Mai Chau - Hoa Binh	20°44'4.9"	104°53'25.3"	1394	Old
27	HK9	Hang Kia - Mai Chau - Hoa Binh	20°44'4.5"	104°53'25.6"	1393	Young
28	HK10	Hang Kia - Mai Chau - Hoa Binh	20°44'33.5"	104°53'46.8"	1411	Old
29	HK11	Hang Kia - Mai Chau - Hoa Binh	20°44'35.5"	104°53'44.6"	1411	Old
30	HK12	Hang Kia - Mai Chau - Hoa Binh	20°44'35.7"	104°53'44.3"	1410	Old
31	HK13	Hang Kia - Mai Chau - Hoa Binh	20°44'36.2"	104°53'43.6"	1407	Old
32	HK14	Hang Kia - Mai Chau - Hoa Binh	20°44'36"	104°53'44.2"	1400	Old
33	HK15	Hang Kia - Mai Chau - Hoa Binh	20°44'36.3"	104°53'43.8"	1406	Old
34	HK16	Hang Kia - Mai Chau - Hoa Binh	20°44'37.8"	104°53'43.2"	1389	Old
35	HK17	Hang Kia - Mai Chau - Hoa Binh	20°44'37.9"	104°53'43"	1384	Old
36	HK18	Hang Kia - Mai Chau - Hoa Binh	20°44'37.9"	104°53'42.9"	1382	Old
37	HK19	Hang Kia - Mai Chau - Hoa Binh	20°44'38.2"	104°53'42.7"	1366	Old
38	HK20	Hang Kia - Mai Chau - Hoa Binh	20°44'38.5"	104°53'42.6"	1357	Old
39	PC1	Pa Co - Mai Chau - Hoa Binh	20°44'38.2"	104°53'42.7"	1306	Young
40	PC2	Pa Co - Mai Chau - Hoa Binh	20°44'38.5"	104°53'42.6"	1326	Young

DNA extraction

Total genomic DNA was extracted from fresh needles. Approximately 100 mg of each sample was used. Leaves were ground into a fine powder in liquid nitrogen and DNA was extracted using the hexadecyltrimethylammonium bromide (CTAB) method [18]. DNA was run on 0.8% agarose gel in 1X TAE buffer through electrophoresis at 90V for 20 mins. DNA concentrations were measured using a the NanoDrop™ ND-1000 UV-Vis spectrophotometer (Thermo Scientific, USA) and then aliquoted to a concentration of 10 ng/µl.

Polymerase chain reaction (PCR) amplification

We used 15 RAPD and 16 ISSR primers (Integrated DNA Technologies, USA) for this study. Table 2 lists the primers and their sequences. PCR amplification was performed in a 20 µl volume containing 50 ng of DNA, 2X PCR MasterMix Buffer (Thermo Scientific, USA), and 1 µM primers. The RAPD-PCR steps were as follows: 3 min at 94°C, followed by 40 cycles of 1-min denaturing at 94°C, 1 min at 37°C, and 1.5 min of elongation at 72°C, before ending with 7 min at 72°C. The ISSR-PCR steps were as follows: 5 min at 94°C, followed by 40 cycles of 45 s at 94°C, 45 s at 56°C, and 1 min 30 s at 72°C, before ending with 7 min at 72°C.

The PCR products were run on 2% agarose gels in 1X TAE buffer to separate the bands; a 1 kb ladder (Thermo Scientific, USA) was used as the DNA standard. The gels were visualised and captured using the DigiDoc-It™ Imagine system (Analytik Jena Company, USA).

Table 2. List of RAPD and ISSR primers used for PCR amplification.

No	RAPD primer	Sequence (5'-3')	No	ISSR primer	Sequence (5'-3')
1	OPA4	AATCGGGCTG	1	UBC807	AGAGAGAGAGAGAGAGT
2	OPA6	GGTCCCTGAC	2	UBC818	CACACACACACA CACAG
3	OPC15	GACGGATCAG	3	UBC824	TCTCTCTCTCTCTCTCG
4	OPC19	GTTGCCAGCC	4	UBC834	AGAGAGAGAGAGAGAGYT
5	OPD12	CACCGTATCC	5	UBC835	AGAGAGAGAGAGAGAGYC
6	OPE3	CCAGATGCAC	6	UBC836	AGAGAGAGAGAGAGAGYA
7	OPE14	TGCGGCTGAG	7	UBC843	CTCTCTCTCTCTCTCTGA
8	OPF1	ACGGATCCTG	8	UBC851	GTGTGTGTGTGTGTGTCTG
9	OPL18	ACCACCCACC	9	UBC855	ACACACACACACACACT
10	OPP9	GTGGTCCGCA	10	UBC856	ACACACACACACACACYA
11	OPR3	ACACAGAGGG	11	UBC881	GGGTGGGGTGGGGTG
12	OPV15	CAGTGCCGGT	12	HB10	GAGAGAGAGAGACC
13	OPAB6	GTGGCTTGGA	13	HB12	CACCACCACGC
14	UBC210	GCACCGAGAG	14	HB15	GTGGTGGTGGC
15	UBC218	CTCAGCCCAG	15	ISCS14	AGTGAGTGAGTGAGTGAGTGA
			16	ISCS34	TGTGTGTGTGTGTGTGRC

Data analysis

The amplification fragments from using RAPD and ISSR were scored according to a binary matrix, where 0 and 1 were coded for the absence and presence of a band, respectively. The genetic diversity index was calculated using the software POPGENE v1.32 [19]. Analysis of molecular variance (AMOVA) and principal coordinate analysis (PCoA) were conducted using GenAlEx v6.502 software [20, 21].

Results

Amplification results of RAPD and ISSR

For the 40 samples from four populations of *P. kwangtungensis*, 15 RAPD primers generated 59 bands ranging in size from 250 to 2000 bp, in which 54 bands were polymorphic loci (91.53%). The 16 ISSR primers produced a total of 142 fragments ranging in size from 250 to 3000 bp, in which 134 bands were polymorphic loci (94.37%). Figs. 2 and 3 are examples of primer amplification results in agarose gel through electrophoresis.

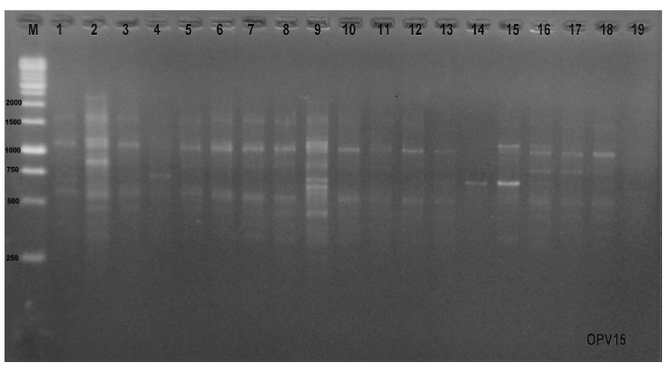

Fig. 2. RAPD amplification results using OPV15 primer. Lane 1-19: representative DNA samples. M: marker 1 kb.

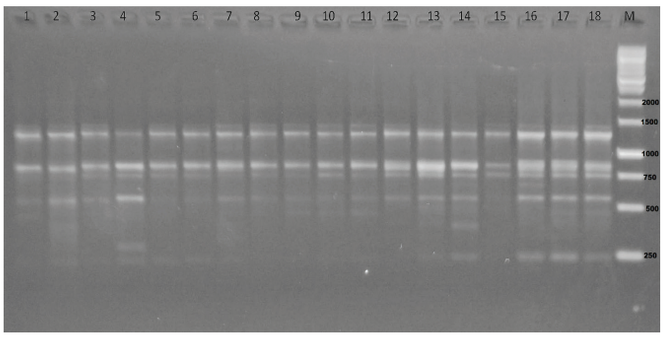

Fig. 3. ISSR amplification results using UBC807 primer. Lane 1-18: representative DNA samples. M: marker 1 kb.

Genetic diversity index

Table 3 shows the genetic diversity of the four populations. Based on RAPD analysis, the range of the mean number of alleles was 1.0508-1.7797, the effective number of alleles (*Ne*) was 1.0360-1.4037, the Shannon index (*I*) was 0.0307-0.3663, and Nei's genetic diversity (heterozygosity, *h*) was 0.0211-0.2404. Based on ISSR, the range of the mean number of alleles was 1.1338-1.7817, *Ne* = 1.0946-1.3363, *I* = 0.0809-0.3279, and *h* = 0.0554-0.2092. The Moc Chau population exhibited the highest genetic diversity based on RAPD, whereas the Hang Kia population exhibited the highest based on ISSR. The Pa Co population had the lowest variation in both analyses.

Table 3. Genetic diversity parameter of the four populations.

Marker	Index		Moc Chau	Muong Sang	Hang Kia	Pa Co	All
RAPD	N_a	Mean	1.7797	1.1356	1.6441	1.0508	1.1953
		SD	0.4180	0.3453	0.4829	0.2216	0.2809
	N_e	Mean	1.4037	1.1114	1.3344	1.0360	1.4216
		SD	0.3622	0.2961	0.3693	0.1567	0.3592
	h	Mean	0.2404	0.0598	0.1974	0.0211	0.2530
		SD	0.1886	0.1552	0.1978	0.0918	0.1783
	I	Mean	0.3663	0.0854	0.2993	0.0307	0.3904
		SD	0.2609	0.2200	0.2801	0.1340	0.2382
	Number of polymorphic loci		6	8	38	3	54
	PPB (%)		77.97	13.56	64.41	5.08	91.53
ISSR	N_a	Mean	1.7535	1.2746	1.7817	1.1338	1.9437
		SD	0.4325	0.4479	0.4146	0.3416	0.2314
	N_e	Mean	1.3190	1.1989	1.3363	1.0946	1.3467
		SD	0.3437	0.3521	0.3321	0.2416	0.3063
	h	Mean	0.1959	0.1115	0.2092	0.0554	0.2223
		SD	0.1802	0.1883	0.1753	0.1415	0.1582
	I	Mean	0.3076	0.1626	0.3279	0.0809	0.3561
		SD	0.2507	0.2705	0.2451	0.2066	0.2128
	Number of polymorphic loci		107	39	111	19	134
	PPB (%)		75.35	27.46	78.17	13.38	94.37

Note: N_a: number of observed alleles; N_e: number of effective alleles; *h*: Nei's (1973) gene diversity; *I*: Shannon index; PPB: percentage of polymorphic bands.

The results of the AMOVA (Table 4) in both the RAPD and ISSR analyses revealed that most of the variation was within populations (72% for RAPD and 87% for ISSR).

Table 4. Analysis of molecular variance of *P. kwangtungensis*.

	RAPD markers	ISSR markers
Among populations	28%	13%
Within populations	72%	87%
PhiPT	0.283, p≥0.001	0.126, p≥0.001

Genetic similarity and cluster analyses of genetic distances

Tables 5 and 6 show the Nei's [22] genetic identity and distance of populations based on RAPD and ISSR, respectively. For both markers, the largest genetic distance was found between Muong Sang and Pa Co (0.3042 with RAPD and 0.2470 with ISSR), and the smallest was found between Moc Chau and Hang Kia (0.0924 with RAPD and 0.0397 with ISSR). The genetic identity showed the same result when the largest identity was between populations of Moc Chau and Hang Kia, and the smallest was between Muong Sang and Pa Co.

Table 5. Nei's genetic identity (above diagonal) and genetic distance (below diagonal) using RAPD markers.

Population	Moc Chau	Muong Sang	Hang Kia	Pa Co
Moc Chau	-	0.8884	0.9117	0.8178
Muong Sang	0.1183	-	0.7928	0.7377
Hang Kia	0.0924	0.2321	-	0.8845
Pa Co	0.2011	0.3042	0.1227	-

Table 6. Nei's genetic identity (above diagonal) and genetic distance (below diagonal) by ISSR markers.

Population	Moc Chau	Muong Sang	Hang Kia	Pa Co
Moc Chau	-	0.9159	0.9611	0.8553
Muong Sang	0.0879	-	0.9066	0.7811
Hang Kia	0.0397	0.0981	-	0.8858
Pa Co	0.1563	0.2470	0.1213	-

A dendrogram-based Nei's genetic distance using UPGMA (Unweighted Pair Group Method with Arithmetic Mean), which was modified from the NEIGHBOR procedure of PHYLIP Version 3.5, is shown in Fig. 4 for RAPD and Fig. 5 for ISSR to reveal the genetic relationship among the four populations. These four populations were divided into three groups: Moc Chau and Hang Kia were in one group with low genetic distance, whereas Pa Co and Muong Sang were separated into two different groups.

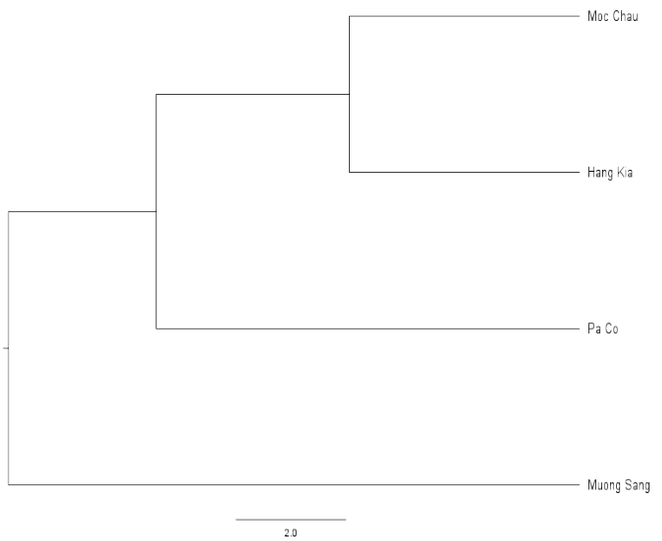

Fig. 4. Genetic distance dendrogram for populations of *P. kwangtungensis* using RAPD markers.

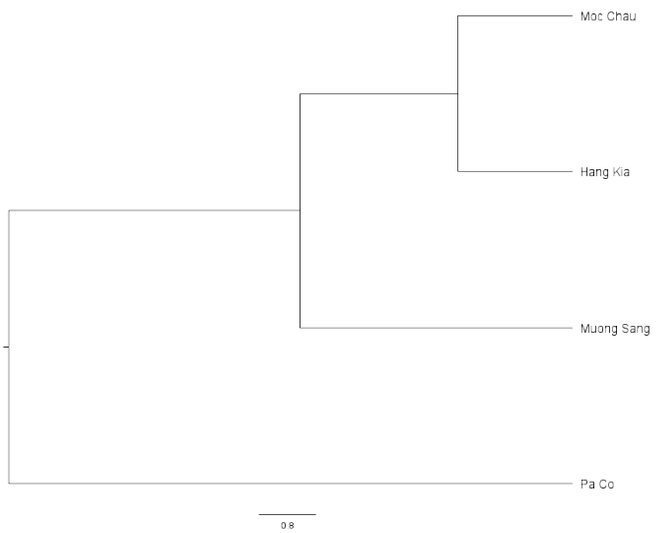

Fig. 5. Genetic distance dendrogram for populations of *P. kwangtungensis* using ISSR markers.

Figures 6 and 7 presents the results of the PCoA using RAPD and ISSR markers, respectively. The first two components of PCoA explained 37.54% of the variation in RAPD and 16.52% in ISSR markers. In the RAPD PCoA (Fig. 6), three clusters were generated. All Muong Sang population samples and most Moc Chau samples formed one group. The second group consisted of most individuals of the Hang Kia population. The Pa Co population formed the third group with some representative accessions of Hang Kia (HK1, HK2, HK4, HK5, HK6, and HK18) and Moc Chau populations (MC1, MC4, and MC14). No distinct cluster was identified in the ISSR PCoA analysis (Fig. 7).

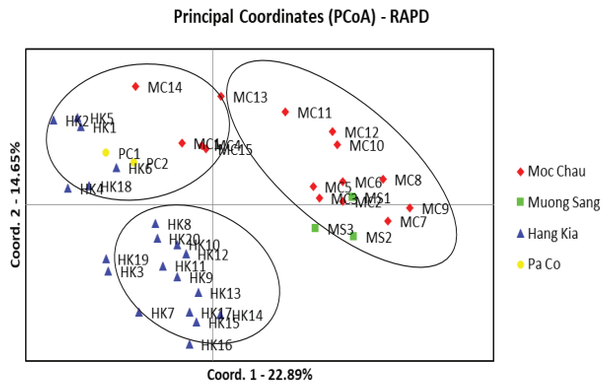

Fig. 6. PCoA revealing the genetic relationships among individuals using RAPD markers.

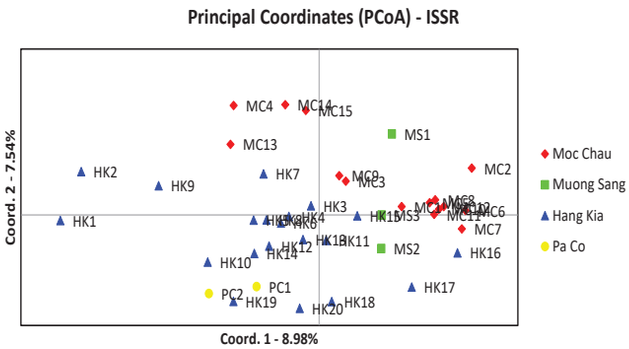

Fig. 7. PCoA revealing the genetic relationships among individuals using ISSR markers.

Discussion and conclusions

This is the first attempt to study the genetic diversity of *P. kwangtungensis* in Vietnam using molecular markers. Based on the RAPD analysis, the genetic parameters revealed the widest genetic diversity in the Moc Chau (Son La) populations and the narrowest in Pa Co (Hoa Binh). By contrast, the ISSR analysis showed the highest variation in the Hang Kia (Hoa Binh) populations and lowest in Pa Co. Moreover, the number of individuals in each population varied considerably. The sizes of the populations were 15 in Moc Chau and and 20 in Hang Kia. By contrast, the Muong Sang (Son La) and Pa Co populations only had three and two samples, respectively. Further analysis with the higher number of samples of these two populations should be conducted in the future to fully examine the genetic resources of *P. kwangtungenesis* in Vietnam.

Using ISSR markers, the mean of genetic diversity for *P. kwangtungensis* in this study (h = 0.2223) was slightly higher than two other fine-needle pines in Vietnam, namely *P. dalatensis* (h = 0.115) [23] and *P. armandii* subsp. *xuannhaensis* (h = 0.114) [24]. Furthermore, these results were consistent with other studies of genetic diversity in threatened conifer species in Vietnam, such as *Taxus chinensis* (I = 0.202) and *Taxus wallichiana* (I = 0.217) [25] as well as *Cunninghamia lanceolata* var. *konishii* (I = 0.2355) [10]. The AMOVA revealed that most of the genetic diversity resided within *P. kwangtungensis* populations (Table 5). These findings were similar to those of studies on other conifer species [12, 23, 25].

The high level of genetic variability within the species might mainly be caused by: (1) the size and fragmented distribution of natural populations; (2) changes in the original vegetation structure and/or the invasion of exotic species in small forest patches of the species; and (3) logging activities or human interference. The natural distributions of *P. kwangtungensis* occurred in Vietnam's Northwest region on the slopes of limestone mountains at altitudes between 1200 and 1500 m [1] and remain in such small patches. These small and fragmented habitats may prevent gene flow among the populations and result in breeding, thereby leading to a decrease in genetic diversity [24]. In addition, human activities such as timber exploitation and agricultural-land expansion contribute to the low number of observed individuals in the natural population.

In conclusion, the genetic diversity of species is crucial for the conservation of genetic resources. In this study, we found a wide range of variation among accessions. The Moc Chau population showed the highest level of genetic diversity and the Pa Co population showed the lowest. This study explored three distinct groups of populations from 40 collected samples of Pa Co pine. Strong genetic similarities were observed between the Moc Chau and Hang Kia populations. The large variability in the number of samples from different populations may have influenced the identification of actual variability within and among the populations. The low number of trees available in the natural habitat emphasised the urgency of developing and implementing a conservation strategy for this species. The long-term conservation of this species should involve in-situ conservation through strict protection from illegal logging, ex-situ conservation through propagating and replanting in new places, and extending genetic diversity by artificial crossing.

ACKNOWLEDGEMENTS

This research was funded by International Foundation for Sciences, Sweden (Project ID: D/5644-1). The authors gratefully thanks Institute of Forest Tree Improvement and Biotechnology (IFTIB), Vietnamese Academy of Forest Sciences (VAFS) for supporting on the facility and equipment for research. We also acknowledge to Mr. Bui Ngoc Quang, Ms. Do Thi Thuc, Ms. Do Thi Thu, Msc. Ngo Thi Minh Duyen (Department of Molecular Biology, IFTIB) for helping in lab work assistance. Thanks to Mr. Trinh Ngoc Bon and Mr. Nguyen Quang Hung (Silviculture Research

Institute, VAFS) for helping in samples collection.

The authors declare that there is no conflict of interest regarding the publication of this article.

REFERENCES

[1] P.V. Thang, et al. (2013), *Instruction on Pinus Species in Mountain Region at Mai Chau-Moc Chau, Hoa Binh and Son La Provinces*, Agriculture Publishing House, Hanoi, Vietnam.

[2] N.D.T. Luu, P.I. Thomas (2004), *Conifers of Vietnam*, The World Publishing House, Hanoi, Vietnam.

[3] N.V. Tap (2009), *Report on Results in Medicinal Plants at Hang Kia - Pa Co Nature Reserve, Mai Chau, Hoa Binh Province*, People and Nature Reconciliation (PanNature), Vietnam.

[4] A. Farjon (2013), *Pinus Fenzeliana*, IUCN Red List of Threatern Species.

[5] N.D.T. Luu, B.V. Thuc, P.V. Thang (2012), "Conservation status assessment and study of propagation techniques by seeds and cuttings for *Pinus kwantungensis* Chun ex Tsiang at Hang Kia - Pa Co nature reserve, Hoa Binh province", *Journal of Agriculture and Rural Development*, **8**, pp.106-110.

[6] X. Xue, et al. (2007), "Genetic diversity of *Picea asperata* populations based on RAPDs", *Plant Biology*, **9(1)**, pp.101-108.

[7] A. Rubio-Moraga, et al. (2012), "Genetic diversity of *Pinus nigra* Arn. populations in Southern Spain and Northern Morocco revealed by inter-simple sequence repeat profiles", *Int. J. Mol. Sci.*, **13(5)**, pp.5645-5658.

[8] L. Zhang, et al. (2013), "Analysis of genetic diversity in *Larix gmelinii* (Pinaceae) with RAPD and ISSR markers", *Genet. Mol. Res.*, **12(1)**, pp.196-207.

[9] X.R. Wang, et al. (2000), "The phylogenetic position of the endemic flat-needle pine *Pinus krempfii* (*Pinaceae*) from Vietnam based on PCR-RFLP analysis of chloroplast DNA", *Plant Systematics and Evolution*, **220(1-2)**, pp.21-36.

[10] N.M. Tam, et al. (2009), "Genetic variation in threatened conifer *Cunninghamia lanceolata* var. *konishii* using ISSR markers: implications for conservation", *Journal of Biology*, **31**, pp.66-72.

[11] N.M. Tam, et al. (2011), "Genetic diversity of an endangered species, *Fokienia hodginsii* (Cupressaceae)", *African Journal of Biotechnology*, **10(71)**, pp.15838-15844.

[12] N.M. Tam, et al. (2013), "Genetic variation and population structure in Chinese water pine (*Glyptostrobus pensilis*): a threatened species", *Indian Journal of Biotechnology*, **12(4)**, pp.499-503.

[13] Q.T. Lien, et al. (2004), "The use of RAPD and chloroplast DNA markers in the study of genetic relationship of *Erythrophleum fordii* Oliv. from different origins", *Basic Research Issues on Life Science*, Science and Technics Publishing House, pp.464-468.

[14] N.H. Nghia, et al. (2006), "Analysis of genetic diversity of *Hopea cordata* Vidal, a species of Dipterocarpaceae by DNA markers", *Journal of Agriculture and Rural Development*, **10**, pp.75-77.

[15] N.H. Nghia, et al. (2007), "Results on genetic diversity analysis of *Afzelia xylocarpa* (Kurz) Craib provenances by using RAPD markers", *Journal of Agriculture and Rural Development*, **14,** pp.44-48.

[16] N.T.H. Hong, et al. (2012), "Study of the genetic diversity of *Dipterocarpus alatus* Roxb. by using RAPD markers", *Vietnam Journal of Forest Sciences*, **3,** pp.2293-2301.

[17] E. Zietkiewicz, D. Labuda (1994), "Genome fingerprinting by simple sequence repeat (SSR)-anchored polymerase chain reaction amplification", *Genomics*, **20(2)**, pp.176-183.

[18] J.J. Doyle, J.L. Doyle (1990), "Isolation of plant DNA from fresh tissue", *Focus*, **12(1)**, pp.13-15.

[19] F.C. Yeh, et al. (1997), *Popgene, the User-friendly Shareware for Population Genetic Analysis*, Molecular Biology and Biotechnology Centre, University of Alberta, Canada.

[20] R. Peakall, et al. (2006), "Genalex 6: genetic analysis in excel. Population genetic software for teaching and research", *Molecular Ecology Notes*, **6**, pp.288-295.

[21] R. Peakall, et al. (2012), "GenAlEx 6.5: genetic analysis in excel. Population genetic software for teaching and research - an update", *Bioinformatics*, **28(19)**, pp.2537-2539.

[22] M. Nei (1973), "Analysis of gene diversity in subdivided populations", *Proc. Natl. Acad. Sci. USA*, **70(12)**, pp.3321-3323.

[23] D.T. Phong, et al. (2016), "Genetic variation of *Pinus dalatensis* Ferre' (Pinaceae) populations - endemic species in Vietnam revealed by ISSR markers", *Journal of Chemical, Biological and Physical Sciences*, **54(2)**, pp.1415-1425.

[24] N.M. Tam, et al. (2015), "Genetic diversity in Xuan Nha pine (*Pinus armandii* subsp.*xuannhaensis* L.K.Phan)", *Research Journal of Biotechnology*, **10**, pp.30-36.

[25] D. Vu, et al. (2017), "Genetic diversity in two threatened species in Vietnam: *Taxus chinensis* and *Taxus wallichiana*", *Journal of Forestry Research*, **28**, pp.265-272.

Doi: 10.31276/VJSTE.62(1).69-73

Responses of green algae and diatom upon exposure to chromium and cadmium

Minh-Tan Vo[1], Van-Tai Nguyen[1], Thi-My-Chi Vo[1], Thi-Nhu-Phuong Bui[2], Thanh-Son Dao[1*]

[1]University of Technology, Vietnam National University, Ho Chi Minh city
[2]Institute for Environment and Resources, Vietnam National University, Ho Chi Minh city

Received 5 June 2019; accepted 22 October 2019

Abstract:

In this study, the detrimental effects of trace metals on the growth of phytoplankton and the phytoremediation potential of microalgae from Vietnam are elucidated. Two green algae *Scenedesmus accuminatus var biseratus* and *Scenedesmus protuberans,* along with the diatom species *Cyclotella* sp., were exposed to chromium (Cr) and cadmium (Cd) at three distinct concentrations ranging from 5-761 µgl^{-1} and 18-667 µgl^{-1}, respectively, over a period of 14 days. The results indicated that *S. acuminatus var biseratus* and *Cyclotella* sp. were relatively tolerant to Cr, even at the highest test concentration, while the growth rate of S. *protuberans* was significantly inhibited when exposed to 660 µgl^{-1} of Cr. Only *Cyclotella* sp. showed a high Cd tolerance, whereas Cd at concentrations of 493 and 607 µgl^{-1} prohibited the growth rate of *S. acuminatus* and *S. protuberans*, respectively. Moreover, at the concentrations tested, all three algal species could remove 90-100% of the Cr out of the test medium. The diatom *Cyclotella* sp. could reduce up to 99% of Cd whereas the two green algae could only do not remove more than 13% of Cd from the test medium. We strongly recommend the *Cyclotella* sp. as a candidate for phytoremediation in metal-contaminated water. Our results contribute vital information toward solutions that environmental experts and managers are searching for to resolve pollution caused by trace metal contaminants.

Keywords: ***Cyclotella* sp., *Scenedesmus accuminatus var biseratus*, *Scenedesmus protuberans,* trace metals.**

Classification number: **5.1**

Introduction

Recently, an increase in the concentration of trace metals (e.g. chromium, zinc, copper) in bodies of water such as rivers, lakes, and reservoirs caused by anthropogenic activities has been a concern. Although trace metals (e.g. Cu, Ni, Zn) at low concentrations are essential to the life and growth of organisms, at critical concentrations these metals have been demonstrated to cause harmful effects on the ecosystem and human health [1, 2].

Among the trace metals, Cd and Cr are usually found in industrial wastewater. While Cd is chiefly sourced from mining activities, ceramics, and other industrial activities [3], Cr is derived from tanneries, industrial electroplating, and wood preservation [4]. Cr mainly exists in the environment as two types, hexavalent chromium and trivalent chromium. According to a previous study, chromium (VI) can cause mutation, DNA destruction, genetic modification, and cancer. In contrast, Cr (III) is essential for protein, fat, and carbohydrate metabolism and is an encouraged supplement to the daily diet [4]. On the other hand, the toxicity of Cd is very disturbing to organisms due to its unique properties such as being highly toxic even at low concentrations and its long digestion time [5].

In aquatic ecosystems, microalgae, including green algae and diatom, are primary producers and play an critical role in the food web [6]. Moreover, microalgae are very sensitive to small environmental changes [7]. Therefore, many studies on microalgae exposed to trace metals (e.g. Cd, Cr) at high concentrations have been conducted to evaluate the toxicity of these contaminants. Previous investigations indicated that both Cd and Cr are essential for algal development, however, at a particular concentration, these elements can interfere with biochemical and cellular processes that cause reduced growth or even death in microalgae [8-10].

In Vietnam, more and more attention has been focused on solutions to environmental challenges, especially trace metal pollution. Many studies demonstrated that there has been a

*Corresponding author: Email: dao.son@hcmut.edu.vn

sharp rise in trace metal concentration in the water bodies of Vietnam, mainly due to wastewater discharge [11-13]. Moreover, Vietnam is located in a tropical area that has a high diversity of species, including phytoplankton. However, to our knowledge, there are few studies on the negative effects of trace metals on microalgae strains originating from Vietnam [14, 15]. Therefore, this study aimed to investigate the development and the absorption capacity of two green algal strains, *Scenedemus acuminatus var biseratus* and *Scenedemus protuberans*, and the diatom species, *Cyclotella* sp., isolated from Vietnam after their exposure to two common trace metals, Cd and Cr, in laboratory conditions.

Materials and methods

The colonial freshwater green algae *Scenedesmus accuminatus var biseratus*, *Scenedesmus protuberans,* and the unicellular brackish water diatom species *Cyclotella* sp. (Figs. 1A, 1B, 1C, respectively) were isolated in several water bodies located in Ho Chi Minh city by pipetting and washing [16]. All algae were cultured in Z8 medium [17]. However, for the Z8 medium used to culture the diatom, the initial water solution was a combination of twice distilled water with a portion of microbial filtered sea water to achieve 3 ppt (‰) salinity and Na_2SiO_3 was added (F/2 medium) [18]. The algae were maintained and tested under a photoperiod of 12 h light (3,000 lux) and 12 dark at 27±1°C [19].

(A) (B) (C)

Fig. 1. The test organisms *Scenedemus acuminatus var biseratus* (A), *Scenedemus protuberans* (B), and *Cyclotella* sp. (C). Scale bars=20 µm.

The Cr^{3+} and Cd^{2+} (from $Cr(NO_3)_3$ and $Cd(NO_3)_2$, respectively) at a concentration of 1,000 mgl^{-1} (Merck, Germany) were used as stock solutions for the experiments. The metals Cr and Cd from stock solutions were combined with the algal medium to achieve the proposed concentrations for the experiment. The medium containing the metals was filtered through 0.2 µm filters (Whatman) prior to testing with microalgae. Each algal species was incubated in a 250 ml flask containing 150 ml of test solution and was exposed to either Cr or Cd at three distinct concentrations, ranging from 5-761 $µgl^{-1}$ and 18-667 $µgl^{-1}$ for Cr and Cd, respectively. A control experiment, in which the algae were not exposed to any trace metal, was also conducted. The physical parameters (e.g. pH and temperature) of each treatment, including the control, at the beginning and end of the test days ranged from 6.8-7.2 pH and 29.4-29.7°C, thus did not change significantly. The electrical conductivity (EC) of the test medium for green algae (Z8 solely) varied between 874-884 $µScm^{-1}$, whereas that of the medium for diatom (modified Z8 with a salinity of 3‰) ranged from 6.52-6.57 $mScm^{-1}$. Similarly, the hardness (characterized by titration [20]) of the Z8 medium ranged from 37-46 mg $CaCO_3$ l^{-1}, and that of the salty (3‰) Z8 medium ranged from 614-628 mg $CaCO_3$ l^{-1}. The large difference between the EC and hardness values of the two media is related to the amount of salt added into the Z8 medium for diatom cultivation. Sub-samples from each test medium, taken at start and end of the experiment, were filtered (with pore size of 0.45 µm - Sartorius, Germany) and acidified with saturated HNO_3 (Merck) prior to the determination of Cr or Cd concentration by electrothermal atomic absorption spectrometry [20]. Both control and treated samples were prepared in triplicates [21, 22]. Over the 14-day experimental period, sub-samples consisting of 2 ml of algal solution were taken from each flask on the starting day and every two days, and preserved with Lugol solution [23] for cell density enumeration.

The growth rate of microalgae (R) was calculated according to Lobban, et al. (1988) [24] with the equation of $R=(\ln X_2-\ln X_1)/(t_2-t_1)$; where X_1 and X_2 are algal density at time t_1 and t_2. Additionally, the following formula was used in order to calculate the metal uptake ratio $(U\%)=100x(M_1-M_2)/M_1$; where M_1 and M_2 are metal concentrations at the beginning and the end of the test. The Kruskal-Wallis test (Sigma Plot 12.0) was used to calculate the statistically significant difference of the growth rate between control and exposures.

Results and discussion

Influence of chromium on growth rate of microalgae

The growth rate of *S. accuminatus var. biseratus* in the control sample and in the samples exposed to 16 µg Cr l^{-1} was 0.27 folds day^{-1}, whereas the growth rate in the samples exposed to Cr at concentrations of 112 and 761 $µgl^{-1}$ was 0.29 and 0.24 folds day^{-1}, respectively. There was no statistically significant difference in the growth rate of this algal strain between the control and all exposures (Fig. 2A). In the experiment with *S. protuberans,* the growth rate in the control sample and exposures to 5 and 80 µg Cr l^{-1} were similar, approximately 0.10 folds day^{-1}. However, the growth rate in the exposure to 660 µg Cr l^{-1} was inhibited and reached only 0.05 folds day^{-1}. Moreover, there was a statistically significant difference in this parameter between

the control sample and the sample exposed to Cr at the highest concentration ($p<0.01$ by Tukey test) (Fig. 2B). Compared to *S. acuminatus var. biseratus*, the growth rate of *Cyclotella* sp. in all treatments, including the control, was lower, varying from 0.16-0.18 folds day^{-1}. Nevertheless, they had the same responses when exposed to Cr. Particularly, a statistically significant difference was not found between the control and all treatments (Fig. 2C).

Previous studies demonstrated that the inhibitory effects of Cr on the microalgal growth of *S. protuberans* depended on concentration in a similar manner as observed in this study. Wong and Chang (1991) [25] showed that the growth of *Chlorella vulgaris* was not inhibited when exposed to Cr at a concentration of 250 µgl^{-1}. On the other hand, when the Cr concentration exceeded 500 µgl^{-1}, there would be inhibition of photosynthesis. At concentration higher than 5,000 µgl^{-1}, Cr increased the cell permeability resulting in inhibition of the growth of *C. vulgaris*. Additionally, another study [26] also indicated that the growth of *Chlorella pyrenoidosa* was inhibited upon exposure to 1,000 µgl^{-1} of Cr for 72 hours. On the contrary, some green algae (*Scenedesmus acutus, S. obliquus, Chlorella fusca, C. vulgaris*) and the cyanobacterium *Pseudanabaena mucicola* could grow well at 1,000 µgl^{-1} of Cr [14, 27], which supports this current study. However, there is no compelling evidence to indicate that *S. acuminatus v. biseratus* and *Cyclotella* sp. are unaffected by Cr. These results could be due to the Cr concentrations in this study being below a threshold that would trigger growth inhibition phenomenon in these algae. Moreover, this study showed that *S. acuminatus var biseratus* and *Cyclotella* sp. were relatively tolerant to Cr that could be useful information for further researches on the treatment of Cr pollution in wastewater using these microalgae.

Influence of cadmium on growth rate of microalgae

In Cd exposures, the growth rate of two green algae strains *S. acuminatus var biseratus*, *S. protuberans* and diatoms species *Cyclotella* sp. ranged from 0.06-0.46, 0.02-0.1, and 0.15-0.18 folds day^{-1}, respectively. Interestingly, when compared to the control, there was a statistical decrease in the growth rate of all the green algae except the diatom *Cyclotella* sp. when Cd exposures were at the highest concentration (Fig. 3).

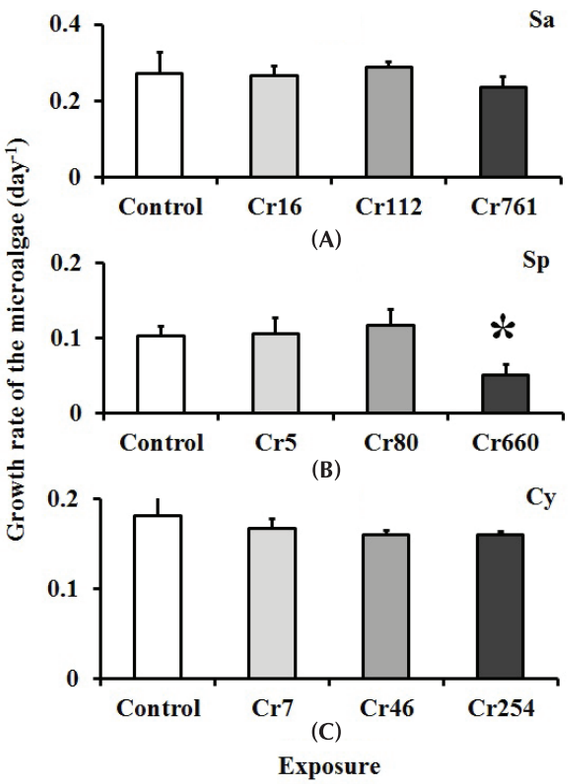

Fig. 2. Growth rate of *S. acuminatus var biseratus* (A), *S. protuberans* (B) and *Cyclotella* sp. (C) in Cr exposures. The asterisk indicates the significant difference ($p<0.05$) between control and Cr exposures by Kruskal-Wallis test.

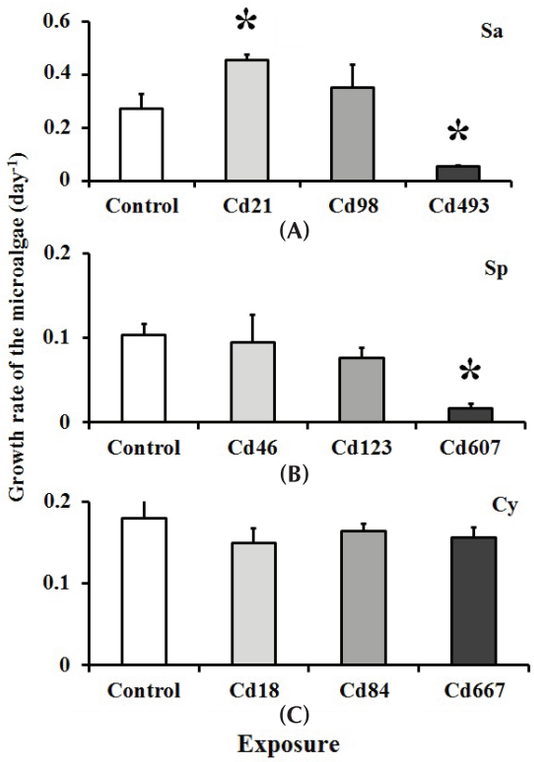

Fig. 3. Growth rate of *S. acuminatus var biseratus* (A), *S. protuberans* (B) and *Cyclotella* sp. (C) in Cd exposures. The asterisk indicates the significant difference ($p<0.05$) between control and Cd exposures by Kruskal-Wallis test.

This result is in total agreement with the findings of previous investigations that revealed the growth inhibition of microalgae could be caused by Cd exposure. For example, Hart and Scaife (1977) [28] showed that Cd at a concentration of 250 μgl^{-1} inhibited the growth rate of the green alga *C. pyrenoidosa*. Similarly, Letty, et al. (2009) [29] determined the detrimental effects of three distinct concentrations of Cd (5, 10, and 20 μgl^{-1}) on cellular viability in the microalgae *Scenedesmus* sp. and *Dunaliella viridis*. Additionally, at Cd concentrations up to 1,000 μgl^{-1} did not impact the growth of diatom *Phaeodactylum tricomutum* [30], which supports our observations of the high tolerance of the diatom *Cyclotella* sp. to Cd exposure (Fig. 3C).

On the other hand, at low concentrations, Cd was demonstrated to significantly stimulate the growth rate of *S. acuminatus var biseratus* (Fig. 3). Although there was no evidence that Cd can stimulate the growth of algae, according to Sbihi, et al. (2012) [10], Cd inhibited the photochemical activity in algae at the concentration of more than 100 μgl^{-1}. The current results show that the diatom species *Cyclotella* sp. was more tolerant to Cd than the other two strains of green algae *S. acuminatus var biseratus* and *S. protuberans*.

Cr and Cd uptake capacity of microalgae

Cyclotella sp. was demonstrated to have a high capacity for both Cr and Cd absorption, reaching 99-100%. This result was similar to the previous investigations of Morin, et al. (2007, 2008) [31, 32], in which diatom species were demonstrated to have a very high potential for metal absorption. On the other hand, a green microalga *Dunaliella* sp. could only uptake less than 10% of Cd in an artificial medium [33]. As it should be, species from different algal classes would have different cell characteristics, for example, diatoms have a frustule made of silicate while green algae does not have this property. Consequently, different species will have a diverse capacity for metal uptake, but this needs further investigations to clarify. Regarding Cr uptake, the capacity of *S. acuminatus var biseratus* and *S. protuberans* were very high, 96 and 90%, respectively. Our findings are strongly supported by a previous study in which *Scenedesmus* sp. removed more than 98% of Cr in a water environment [34]. On the other hand, these green algae showed a poor performance in Cd uptake, only 13% for *S. acuminatus var biseratus* and 6% for S. *protuberans* (Table 1). In contrast, when compared to the Cr uptake potential, *Scenedesmus acutus* and *Chlorella vulgaris* had a higher Cd uptake capacity [35]. This suggests that we can apply different microalgae in order to effectively remove metal contaminants in water bodies.

Table 1. Cr and Cd uptake ratio by the three test microalgae.

Metals	Algal species	Metal concentrations (μgl^{-1})		Uptake ratio (%)
		Initial test	*End test*	
Cr	S. *acuminatus var biseratus*	761	27	96
	S. *protuberans*	660	67	90
	Cyclotella sp.	254	0	100
Cd	S. *acuminatus var biseratus*	493	431	13
	S. *protuberans*	607	569	6
	Cyclotella sp.	667	10	99

Conclusions

This study indicated that *S. acuminatus var biseratus* and *Cyclotella* sp. were relatively tolerant to Cr concentrations up to 761 μgl^{-1} for *S. acuminatus var biseratus* and 254 μgl^{-1} for *Cyclotella* sp. The growth rate of S. *protuberans* was significantly inhibited when exposed to 660 μgl^{-1} of Cr. In the case of Cd exposures, only *Cyclotella* sp. showed to have a high tolerance at concentrations up to 667 μgl^{-1} whereas Cd at the concentrations of 493 μgl^{-1} and 607 μgl^{-1} decreased the growth rate of *S. acuminatus var biseratus* and *S. protuberans*, respectively. Besides, the three tested phytoplankton reduced 90-100% of dissolved Cr in medium. Although the two green algae had a low capacity for Cd absorption, the diatom species showed good performance in removing Cd. Therefore, these algae could be considered as potential candidates for removing metal contaminants in water bodies. Moreover, the mechanisms behind the effects of trace metals on algae and the metal tolerance in algae should be investigated in the future.

ACKNOWLEDGEMENTS

This study is funded by University of Technology, Vietnam National University, Ho Chi Minh city, under the grant project number SVOISP-2018-MT&TN-14.

The authors declare that there is no conflict of interest regarding the publication of this article.

REFERENCES

[1] J.C. Igwe, A.A. Abia (2003), "Maize cob and husk as ad-sorbents for removal of Cd, Pb and Zn ions from wastewater", *Physical Sciences*, **2**, pp.83-94.

[2] M.J. Horsfall, I.A. Spiff (2005), "Equilibrium sorption study of Al, Co, and Ag in aqueous solutions by fluted pumpkin (*Telfairia Occidentalis* Hook f) waste biomass", *Acta Chimica Slovenica*, **52**, pp.174-181.

[3] T.A. Davis, B. Volesky, R.H.S.F. Vieira (2000), "Sargassum seaweed as biosorbent for heavy metals", *Water Research*, **34(17)**, pp.4270-4278.

[4] D. Bagchi, S.J. Stohs, M. Downs, M. Bagchi, H.G. Preuss (2002), "Cytotoxicity and oxidative mechanisms of different forms of chromium", *Toxicology*, **180(1)**, pp.5-22.

[5] United States Department of Labor (2003), *Occupational Safety and Health Administration,* OSHA 3136-08R, https://www.osha.gov/Publications/3136-08R-2003-English.html#exposure.

[6] L.E. Graham, L.W. Wilcox (2000), *Algae*, Pearson Prentice Hall, Upper Saddle River, 700 pp.

[7] I. Juttner, S. Sharma, B. Dahal, S.J. Ormerod, P.J. Chimonides (2003), "Diatoms as indicators of stream quality in the Kathmandu valley and middle hills of Nepal and India", *Freshwater Biology*, **48**, pp.2065-2084.

[8] K. Anantharaj, C. Govindasamy, G. Natanamurugaraj, S. Jeyachandran (2011), "Effect of heavy metals on marine diatom *Amphora coffeaeformis* (Agardh. Kutz)", *Global Journal of Environmental Research*, **5(3)**, pp.112-117.

[9] S. Masmoudi, N.D. Nhung, A. Caruso, H. Ayadi, M.M. Annick, G. Tremblin, M. Bertrand, B. Schoefs (2013), "Cadmium, copper, sodium and zinc effects on diatoms: from heaven to hell - a review", *Cryptogamie, Algologie*, **34(2)**, pp.185-225.

[10] K. Sbihi, O. Cherifi, M. Bertrand (2012), "Toxicity and biosorption of chromium from aqueous solutions by the diatom *Planothidium lanceolatum* (Brébisson) Lange-Bertalot", *American Journal of Scientific and Industrial Research*, **3(1)**, pp.27-38.

[11] T.V. Quy, T.V. Son (2010), "A study of waste water impacts of main factories on water quality of To Lich river, Ha Noi", *VNU Journal of Science: Earth Sciences*, **26**, pp.174-178.

[12] E. Strady, V.B.H. Dang, J. Némery, S. Guédron, Q.T. Dinh, H. Denis, P.D. Nguyen (2016), "Baseline seasonal investigation of nutrients and trace metals in surface waters and sediments along the Saigon river basin impacted by the megacity of Ho Chi Minh city (Vietnam)", *Environmental Science and Pollution Research*, **24(4)**, pp.3226-3243.

[13] S. Costa-Böddeker, P. Hoelzmann, L.X. Thuyen, H.D. Huy, H.A. Nguyen, O. Richter, A. Schwalb (2016), "Ecological risk assessment of a coastal zone in Southern Vietnam: spatial distribution and content of heavy metals in water and surface sediments of the Thi Vai estuary and Can Gio mangrove forest", *Marine Pollution Bulletin*, **114(2)**, pp.1141-1151.

[14] T.S. Dao, N.H.S. Le, M.T. Vo, T.M.C Vo, T.H. Phan, T.N.P. Bui (2018), "Growth and metal uptake capacity of microalgae under exposure to chromium", *Journal of Vietnamese Environment*, **9(1)**, pp.38-43.

[15] T.L. Pham, T.S. Dao, H.N. Hiep, T.K.N. Pham, T.T.H. Ngo, H.M. Bui (2019), "Lipid production combined with removal and bioaccumulation of lead (Pb) by the green alga *Scenedesmus* sp.", *Polish Journal of Environmental Studies*, accepted manuscript, Doi: 10.15244/pjoes/109277.

[16] H. Belcher, E. Swale (1988), *Culturing Algae - A Guide for Schools and Colleges*, The Ferry House, UK.

[17] J. Kotai (1972), "Instructions for preparation of modified nutrient solution Z8 for algae", *Norwegian Institute for Water Research*, **Oslo B-11(69)**, pp.1-5.

[18] R.R. Guillard, J.H. Ryther (1962), "Studies on marine planktonic diatoms. *I. Cyclotella nana Hustedt* and *Detonula confervacaea* (Cleve) Gran", *Canadian Journal of Microbiology*, **8**, pp.229-239.

[19] T.S. Dao, G. Cronberg, J. Nimptsch, L.C. Do-Hong, C. Wiegand (2010), "Toxic cyanobacteria from Tri An reservoir, Vietnam", *Nova Hedwigia*, **90**, pp.433-448.

[20] APHA (2012), *Standard Methods for the Examination of Water and Wastewater*, 22nd Edition, American Public Health Association, American Water Works Association and Water Environment Federation, Washington, DC. 2340.

[21] M. Muhaemin (2004), "Toxicity and bioaccumulation of lead in *Chlorella* and *Dunaliella*", *Journal of Coastal Development*, **8**, pp.27-33.

[22] S. Ruangsomboon, L. Wongrat (2006), "Bioaccumulation of cadmium in an experimental aquatic food chain involving phytoplankton (*Chlorella vulgaris*), zooplankton (*Moina macrocopa*), and the predatory catfish *Clarias macrocephalus* × *C. gariepinus*", *Aquatic Toxicology*, **78**, pp.15-20.

[23] G.R. Hasle, G.A. Fryxell (1995), "Taxonomy of Diatoms", *Manual on Harmful Marine Microalgae*, Intergovernmental Oceanographic Commission, UNESCO, pp.339-364.

[24] C.S. Lobban, D.J. Chapman, B.P. Kremer (1988*), Experimental Phycology - A Laboratory Manual*, Cambridge University Press, U.K.

[25] P.K. Wong, L. Chang (1991), "Effects of copper, chromium and nickel on growth, photosynthesis and chlorophyll a synthesis of *Chlorella pyrenoidosa* 251", *Environmental Pollution*, **72(2)**, pp.127-139.

[26] Z.T. Horcsick, V. Olah, A. Balogh, I. Meszaros, L. Simon, G. Lakatos (2006), "Effect of Chromium (VI) on growth, element and photosynthetic pigment composition of *Chlorella pyrenoidosa*", *Acta Biological Szegediensis*, **50(1-2)**, pp.19-23.

[27] M.A.P. Dinis, V.J.P. Vilar, A.A.M.G. Monteiro, R.A.R. Boaventura (2012), "Effect of Cr(VI) in four Portuguese microalgae growth", *Environmental Engineering and Management Journal*, **11(11)**, pp.2013-2022.

[28] B.A. Hart, B.D. Scaife (1977), "Toxicity and bioaccumulation of cadmium in *Chlorella pyrenoidosa*", *Environmental Research*, **14**, pp.401-413.

[29] B.C.M. Letty, M.C. Ingrid, M.M. Xiomara, B.M. Carolina, M.S. Patricia (2009), "Effect of cadmium on cellular viability in two species of microalgae (*Scenedesmus* sp. and *Dunaliella viridis*)", *Biological Trace Element Research*, **130(1)**, pp.86-93.

[30] E. Torres, A. Cid, C. Herroro, J. Abalde (1997) "Effecof cadmium on growth, ATP content, carbon fixation and ultrastructure in the marine diatom *Phaeodactylum tricornutum* Bohlin", *Water, Air, and Soil Pollution*, **117**, pp.1-14.

[31] S. Morin, M. Vivas-Nogues, T.T. Duong, A. Boudou, M. Coste, F. Delmas (2007), "Dynamics of benthic diatom colonization in a cadmium/zinc-polluted river (Riou-Mort, France)", *Fundamental and Applied Limnology*, **168(2)**, pp.179-187.

[32] S. Morin, T.T. Duong, O. Herlory, A. Feurtet-Mazel, M. Coste (2008), "Cadmium toxicity and bioaccumulation in freshwater biofilms", *Archives of Environmental Contamination and Toxicology*, **54**, pp.173-186.

[33] B. Kutlu, E. Mutlu (2017), "Growth and bioaccumulation of cadmium, zinc, lead, copper in *Dunaliella* sp. isolated from Homa Lagoon, eastern Aegean sea", *Indian Journal of Geo Marine Science*, **46(6)**, pp.1162-1169.

[34] M. Ballen-Segura, L.H. Rodriguez, D.P. Ospina, A.V. Bolanos, K. Perz (2016), "Using *Scenedesmus* sp. for the phycoremediation of tannery wastewater", *Tecciencia*, **12(21),** pp.69-75.

[35] L. Travieso, R.O. Canizares, R. Borja, F. Bentez, A.R. Dominguez, R. Dupeyron (1999), "Heavy metal removal by microalgae", *Bulletin of Environmental Contamination and Toxicology*, **62**, pp.144-151.

Doi: 10.31276/VJSTE.62(1).74-84

Assessing the conversion between agricultural and built-up area in the Vu Gia - Thu Bon river basin

Van Tra Tran[1*], Xuan Thinh Nguyen[2], Stefan Greiving[2]

[1]*Vietnam Institute of Meteorology, Hydrology and Climate Change, Vietnam*

[2]*Faculty of Spatial Planning, TU Dortmund University, Germany*

Received 5 July 2019; accepted 30 September 2019

Abstract:

The conversion of agricultural land into developed infrastructure entails trade-offs. Therefore, studying the dynamics of change between agriculture and developed areas is essential. This study utilizes remote sensing technology to study this dynamic. In particular, satellite images were utilized to assess the current land use master plan for the period of 2011-2020 in the Vu Gia - Thu Bon river basin, Vietnam. Land cover before and after implementation of the land use master plan was classified using three indices of the Normalized Difference Water Index (NDWI), the Normalized Difference Vegetation Index (NDVI), and the Normalized Difference Built-up Index (NDBI). Two main land cover types of paddy rice cultivation area and developed area were compared for the two time periods. The land cover classification results revealed that the land use master plan in the river basin has achieved its conversion target four years ahead of schedule. Additionally, the changes were thoroughly assessed within the context of socioeconomic development in the river basin. Land cover changes in the river basin created five major implications for policymakers, including the need to reassess the land use master plan target, the need for regulatory measures in housing development, the true nature of the paddy rice conversion mechanism, the irreversible nature of agriculture land conversion, and market conditions for newer agricultural products.

Keywords: **agriculture, change detection, land cover, land use.**

Classification number: **5.1**

Introduction

Vietnam is currently undergoing radical economic transformation [1]. The economy, once heavily dependent on agricultural production, is now geared towards "industrialization and modernization" [1, 2]. As a result, an increasing amount of agricultural land is being converted into non-agricultural uses throughout the country [3-5].

Land use change, however, creates trade-offs that must be viewed cautiously at the policy level. Farmland and forest land converted to urban development provide better living standards and fuel economic growth in the urban area, however, the conversion creates problems related to the environment and society [3, 4, 6, 7-10]. Reduction in areas for food and timber production could reduce the livelihoods of those dependent on the sector while soil erosion, salinization, desertification, and soil degradation reduce soil quality [11].

Urbanization further presents many socioeconomic challenges in the form of conflicts between agricultural and non-agricultural land uses [12]. For example, local farmers may be forced to compensate for the negative impacts generated by agriculture on nearby residents. Furthermore, when the total amount of farmland falls below a certain threshold, the local agricultural economy may collapse as all agricultural-supporting sectors disappear [13]. Conflicts directly related to land appropriation and reallocation are also a hotly debated issue [3, 4].

Given the importance and relevance of agricultural land use conversion in Vietnam, there has been a great deal of research on the topic. The rich body of research in different areas suggested that land use in Vietnam has been highly dynamic and has changed significantly in the past. Additionally, there is a general consensus that these changes have major social, environmental, and economic implications. Binh, et al. (2005) [14], Hauser, et al. (2017) [7], and Hanh, Thuc, Kervyn (2015) [8] studied the land

*Corresponding author: Email: tvtra@monre.gov.vn

cover conversion within Ca Mau province in Southern Vietnam using remote sensing and concluded that the increase in built-up area has been significant at the cost of agricultural land. Disperati and Virdis (2015) [6] and Phuc, Van Westen, Zoomers (2014) [3] studied the land cover change dynamic in Thua Thien - Hue province in Central Vietnam and found that urban areas have encroached on peri-urban agriculture areas. While Disperati and Virdis (2015) attributed the changes to population increase and policies, Phuc, Van Westen, and Zoomers (2014) argued for a case of change due to policies and market forces. A more holistic research for entire Vietnam was conducted by To, Mahanty and Dressler (2015) [12] and Saksena, et al. (2014) [15]. These studies concurred that reduction in agricultural land is observed with an increase in built-up area.

This research provided a case study for the Vu Gia - Thu Bon river basin (VGTB) in Vietnam. The effectiveness of the ongoing land use master plan for the period of 2011-2020 is thoroughly studied using remote sensing technologies. The major objectives of the study include: 1) Identify and map the land cover in the VGTB river basin before and after the current land use plan; 2) Detect the changes of land cover between agricultural and non-agricultural land in the river basin; 3) Determine the total effectiveness of the plan in terms of the agricultural and the built-up area components; and 4) Critically review the changes as a result of the land use master plan and their implications for policies in the future. The study not only thoroughly assesses the effect of land use planning in the river basin but also provides information so that future policies could be better designed for sustainable development.

Materials and methodology

Study area

VGTB river basin is located in the Central coastal zone of Vietnam (Fig. 1). The total catchment area of VGTB is approximately 10,350 km^2 and covers Da Nang city and Quang Nam province. The total population in the river basin is approximately 2 million (2018 census).

Agricultural production remains one of the most important economic sectors in the river basin, with the agricultural sector employing roughly half of the population [16]. Paddy rice remains the dominant crop with approximately 70% of the irrigated agriculture area devoted to rice. Within the last several years, the river basin has seen rapid development. A large proportion of existing agricultural land has been converted into non-agricultural land as a result of both national and local policies.

National policies include the 7th Resolution in 1994 and the 15th Resolution in 2002 of the Vietnam Communist Party (the ruling party in Vietnam) [17, 18]. While the 7th Resolution promotes industrialization and modernization

Fig. 1. Location of the study area.

of the economic sector for the time period of 1994-2000, the 15th Resolution promotes the same process for the time period of 2001-2010. Later policies also hinted on the same direction for economic development for later time periods.

Local policies in the VGTB river basin therefore must fall into national policy lines and are aimed towards building a stronger industrial sector and reducing reliance on agriculture. One important piece of policy in the river basin includes the land use master plan for both Quang Nam and Da Nang for the time period of 2011-2020 [19, 20]. Agricultural area is expected to decrease while built-up area increases.

Data

Satellite images covering the entirety of the VGTB river basin are utilized for the study. A high-resolution SPOT image from AIRBUS and the widely used Landsat image from the United States Geological Survey are used. A SPOT 7 image was acquired for the area within Da Nang city while Landsat images include both the Landsat 5 and the more recent Landsat 8 data. A total of 10 Landsat scenes were used in the study, including five Landsat 8 scenes and five Landsat 5 scenes. Images for 2016 and 2017 were provided by Landsat 8 while images for 2010 and 2011 were provided by Landsat 5. The Landsat 5 data were used in place of the

Landsat 7 data due to a Landsat 7 mission sensor error (scan line error).

The Landsat scenes used in the study are listed in Table 1. The selection of the scenes is due to the level of cloud coverage and for multi-temporal NDVI assessment.

Table 1. LANDSAT satellite images used for the study.

Data	Date	Scene names
Landsat 8 OLI (30x30 m)	8th March 2016	LC81240492016068LGN00
	8th March 2016	LC81240502016068LGN00
	25th April 2016	LC81240492016116LGN00
	2nd May 2016	LC81250492016123LGN00
	11th March 2017	LC81240492017070LGN00
Landsat 5 TM (30x30 m)	7th February 2011	LT51240492011038BKT00
	7th February 2011	LT51240502011038BKT00
	5th July 2010	LT51250492010186BKT01
	11th May 2010	LT51240492010131BKT01
	12th June 2010	LT51240492010163BKT01

The land use master plan for Quang Nam province and Da Nang city for the period of 2011-2020 [19, 20] were further utilized. Two main land cover types are the focus, including the changes in agricultural area and the changes in built-up area. Changes in the agricultural and built-up areas are summarized in Table 2. Informal development is not considered within the scope of this study.

Table 2. Land use type changes in Quang Nam and Da Nang until 2020.

Land use type	Quang Nam (km^2)	Da Nang (km^2)	Total change (km^2)
Agriculture (rice)	- 33.12	- 13.48	- 44.6
Built-up	+ 242.03	+ 50.54	+ 292.57

Methodology

The effect of land use plans in the river basin is determined through a land cover change detection procedure. This includes classifying land cover based on Landsat images in two time periods prior to and after the land use master plan and comparing the classification. The changes could thus be analyzed.

Land cover classification:

This study classifies land cover largely based on the six cover types in the Intergovernmental Panel on Climate Change's (IPCC) recommendation [21]: grassland, agriculture, forest, water, built-up area, and others. However, this study utilized only five types of land cover, namely, water, vegetation, agriculture, empty land, and built-up area.

Grassland cover in the definition of IPCC does not exist in the study area. This includes the non-existence of rangelands and pasture lands. For this reason, the vegetation class used in the study is a combined class of forest, bushes, and other types of vegetation that do not fall into the category of agricultural land. It is true that combining the two land covers creates higher inaccuracy in general, however, the purpose of the study is the focus on assessing changes in agricultural area and built-up area. Therefore, this land cover type of vegetation does not impact the overall accuracy of the assessment.

A further assumption is made during the classification of agricultural area in the river basin. In particular, given that the majority of the agricultural area in the river basin is paddy rice, agricultural land cover would thus be assumed to be paddy rice. A detailed description of the various land cover classification is illustrated in Table 3.

Table 3. Description of land cover class classification.

Land use type	Description
Water (Wa)	Wetland class from IPCC's classification and includes permanent open water, lakes, reservoirs, and streams
Vegetation (Ve)	Lumping of forest and grassland from IPCC's classification. The land cover includes: production forest, natural forest, special use forest, protected forest, grassland, perennial crops, annual crops
Agriculture (Ag)	Paddy rice
Empty land (Em)	Similar to other land class from IPCC. Includes bare soil, and sandy beaches
Built-up (Bu)	Similar to settlement class from IPCC. This includes: residential, commercial, industrial, and other urban land

Land cover classification is based on indices, namely the NDVI, NDWI, and NDBI. ERDAS Imagine software package was used for the purpose of land cover classification.

The land cover classification procedure is based on thresholding of the indices. A three-level classification scheme is applied where thresholding indices provide the first level of classification of vegetation and agriculture, water, empty land, and built-up area. A second level of classification involves performing multi-temporal NDVI through the use of a number of Landsat images. This procedure separates vegetation and agriculture land cover classes. Thresholding was also performed to separate empty land and built-up area in the NDBI. A classification decision tree is illustrated in Fig. 2.

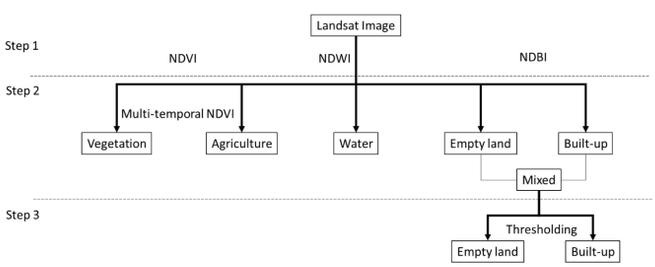

Fig. 2. Hierarchy classification scheme for land cover mapping.

Accuracy assessment:

An overall accuracy index and the Kappa coefficient are used to determine the accuracy of the classification scheme. Reference points for accuracy assessment are selected from Landsat images with the aid of high-resolution Google Earth images. This method has been attempted by other studies [22-24]. Both random points and points that could potentially be misclassified were selected. The minimum number of reference points followed the rule established by McCoy (2005) [25], where:

$$N=Z^2(p)(100-p)/E^2 \quad (1)$$

with N being the number of sample points, $Z = 2$ (standard normal deviate for a 95% confidence interval), p is expected accuracy, and E is allowable error (100- confidence interval). For this study, an accuracy of 85% is expected, therefore, a minimum of 204 samples would be required.

Additional ground truthing points were obtained to reassess and validate the choice of ground reference points selected for the classification scheme in 2016. This was carried out in early 2017. The reassessment of ground reference points in 2011 could not be carried out through ground truthing and, since there are no other available data, was not accomplished. The location of ground reference points for the classification of land cover is illustrated in Fig. 3.

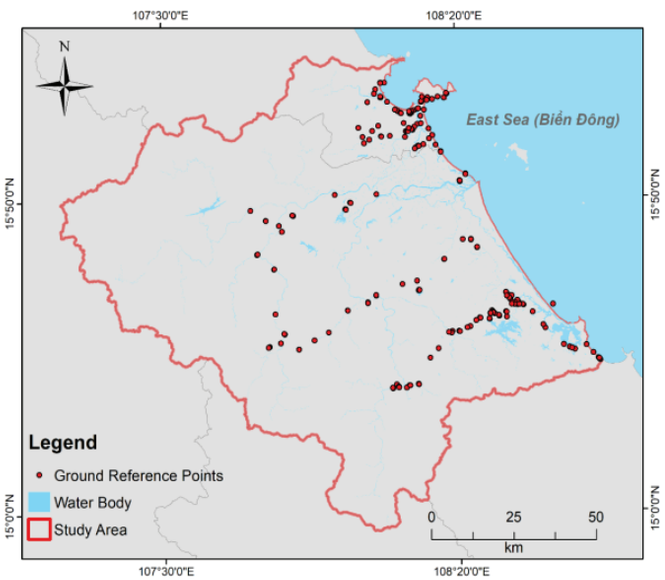

Fig. 3. Ground reference points for accuracy assessment.

The land cover classification results from the study are further compared with land use statistics. More specifically, the total land area of the different classes was compared with the land use inventories from the Vietnam Ministry of Natural Resources and Environment (MONRE) in 2010 and 2015. Through comparison of the land cover classification with the land use inventory data, the relative accuracy of the land cover classification scheme could be established, providing an additional level of assessment. It should be noted, however, that there is a mismatch of timescale between the land cover classification and the land use inventory. In particular, land cover classification was performed for 2011 and 2016 while the land use inventory was available for 2010 and 2015. Additionally, there also exists a slight difference between land cover and land use. Therefore, small discrepancies between the two could be found.

Results and discussions

Land cover classification results

Land cover classification for the years 2011 and 2016 are illustrated in Fig. 4. The corresponding accuracy assessments are listed in Table 4.

Table 4. Accuracy assessment of land cover classification using indices.

Accuracy measurement	2011	2016
Overall accuracy (%)	82	85
Kappa coefficient	0.77	0.81

Land cover classification for both 2011 and 2016 using indices is relatively successful. For land cover in 2016, the overall accuracy and Kappa coefficient are 85% and 0.81, respectively. Likewise, the overall accuracy and Kappa coefficient for the land cover classification scheme in 2011 are 82% and 0.77, respectively. The level of accuracy and Kappa coefficient are deemed sufficient compared to other studies [8, 26, 27], therefore, the results are accepted for further analysis.

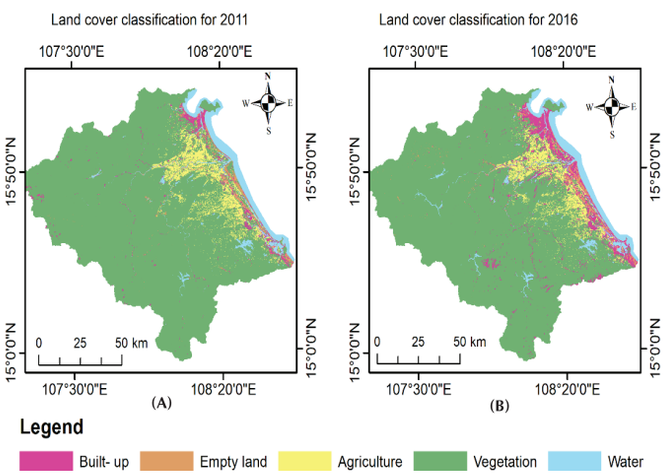

Fig. 4. Classification of land cover in VGTB river basin.

Table 5. Producer's and user's accuracy of land cover classification.

Class	2011		2016	
	Producer's	*User's*	*Producer's*	*User's*
Water (Wa)	74.5	100.0	86.3	100.0
Vegetation (Ve)	91.0	76.3	80.6	84.4
Agriculture (Ag)	86.8	100.0	91.4	97.0
Empty land (Em)	83.3	62.5	78.6	84.6
Built-up (Bu)	71.1	72.7	87.7	71.4

The user's and producer's accuracy for the classification are listed in Table 5. Producer's accuracy represents how well reference points are classified. On the other hand, user's accuracy represents the probability that a pixel classified into a given category actually represents that category on the ground.

The classification scheme in 2016 is more successful than the classification scheme in 2011 given the producer's and user's accuracy levels. For the classification scheme in 2011, a low producer's accuracy for water and built-up classes indicated that the classification of these pixels does not agree well with the ground reference points. For the classification scheme in 2016, a low user's accuracy level indicates a misclassification of built-up with other types of land cover.

A general case in the classified image is the domination of vegetation cover. This is mainly due to the vegetation growth even in sandy areas within the river basin (Fig. 5). As such, the reflectance of the satellite image reveals a highly green area (also mostly due to the coarse resolution) and the NDVI measure indicates these areas are covered by vegetation. This classification as a whole is not false.

Fig. 5. Example of empty land covered with vegetation.

The comparison of total land cover for the different classes was also compared with the land use inventory issued by the MONRE (Table 6). It should be noted that the area of only four out of the five land cover classes was compared. The total area of surface water is not compared given the limited information within the land use inventory.

From the comparison, land cover classification results and the land use inventory agree well with each other in the order of magnitude. However, notable differences are worth discussing. Without losing much accuracy and for the purpose of the discussion, an under-prediction of the land cover classification indicates that, for a particular land cover class, the area in the land cover classification scheme is smaller than the area in the land use inventory. Likewise, an over-prediction of the land cover classification implies that the area of a particular land cover in the classification scheme is greater than the area of the same land cover in the land use inventory.

Table 6. Comparing land cover results with land use data from MONRE (units: km^2).

		Vegetation	Agriculture	Empty land	Built-up
2011	Classification results	10,344.09	635.26	180.91	200.58
	Land use (MONRE)	10,316.29	607.84	156.05	280.60
	Difference	27.80	27.42	24.87	-80.03
	Difference (%)	0.27	4.32	13.74	39.90
2016	Classification results	10,036.95	581.39	181.92	543.03
	Land use (MONRE)	9,983.24	566.63	169.61	623.94
	Difference	53.71	14.76	12.31	-80.91
	Difference (%)	0.54	2.54	6.77	14.90

For 2011, there is a significant magnitude of mismatch of built-up area between the land cover classification scheme and the land use inventory. In particular, the land cover classification scheme provided approximately 80 km^2 less built-up area than the land use inventory data. Given that the total land area of all four classes must be the same in both the land cover classification and land use inventory, the under-prediction of built-up area is compensated for by the over-prediction of vegetation, agriculture, and empty land.

A similar over-prediction and under-prediction pattern is observed between the land cover classification scheme and the land use inventory in 2016. In other words, the land cover classification scheme consistently under-predicts the total area of built-up land while it over-predicts the total area of vegetation, agriculture, and empty land.

The lower-than-expected accuracy of the land cover classification when compared to the land use inventory is mostly attributed to the coarse resolution of the Landsat images. This is illustrated in Fig. 6. A Landsat 8 image of the Central Business district (CBD) of Da Nang city along the banks of the Han river is displayed side by side with a SPOT 7 image. Using the same two satellite scenes, the classification of the built-up area is also shown. The selected area has been highly developed. Therefore, there is little change between 2015 (the date of the SPOT 7-acquired data) and 2016 (the date of the Landsat 8-acquired data). Therefore, comparison of the two is meaningful.

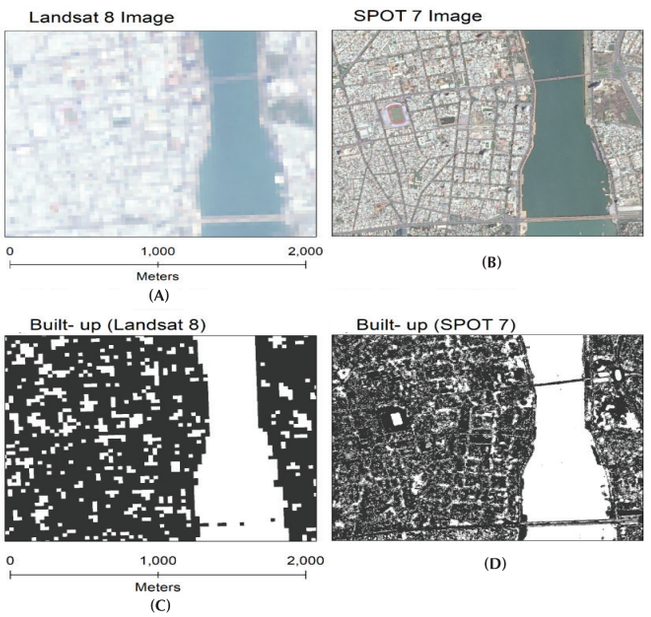

Fig. 6. Comparison of Landsat 8 and SPOT 7 images.

The SPOT image has a higher base resolution (1.5 mx1.5 m) when compared to the Landsat 8 image (30 mx30 m). Given the higher resolution, the SPOT image provided a better classification result of the built-up area within the CBD of Da Nang city within the river basin. This is also true when using the SPOT image to classify other land cover classes as compared to the Landsat image. The coarse resolution of the Landsat 8 image thus creates a major source of uncertainty and error in the classification of land cover in the study. An overall low accuracy of the classification scheme is therefore explained.

Land cover change detection

Land cover change detection was performed and a change matrix is illustrated in Table 7. The rows demonstrate the magnitude of changes that a particular type of land cover in 2011 underwent. The columns display the total area into which a particular land cover in 2011 was converted. For example, 580.13 km^2 of water in 2011 remained as water body in 2016. However, 2.32 km^2 of water in 2011 was converted into vegetation by 2016.

Table 7. Land cover change matrix between 2011 and 2016 (units: km^2).

		2016					
		Wa	*Ve*	*Ag*	*Em*	*Bu*	*Change*
2011	Water (Wa)	580.13	2.32	0.45	4.05	23.42	17.53
	Vegetation (Ve)	35.45	9,936.38	14.12	52.42	305.72	-307.13
	Agriculture (Ag)	1.91	53.81	566.37	3.06	10.11	-53.86
	Empty land (Em)	4.79	14.51	0.45	105.73	55.42	1.01
	Built-up (Bu)	5.63	29.93	0.00	16.65	148.36	342.45

The conversion of agriculture and vegetation is highly interesting. Approximately 53.81 km^2 agricultural land was converted into vegetation between 2011 and 2016. In the other direction, 14.12 km^2 of vegetation in 2011 was converted into agriculture by 2016. This could suggest an error in the classification scheme where a small amount of paddy rice area was not fully detected in the multi-temporal NDVI analysis. The error in classification leads to an agricultural area being falsely classified as vegetation in 2011.

Conversion of built-up area into other types of land cover should be viewed cautiously. This is mainly due to the fact that this conversion mechanism is not normally expected. Once an area has undergone development and is converted to built-up infrastructure, very rarely is this area converted back into vegetation, agriculture, or empty land.

The conversion of built-up area into water in the classification scheme could be attributed to several reasons. This includes the excavation of new artificial lakes in the city of Da Nang, the seasonal fluctuation of water in streams (flooding), and errors in classification. Water surface has a similar reflectance with built-up area when using the threshold of indices. Therefore, water surface in the 2011 scene was falsely classified as built-up area and correctly classified as water again in the 2016 scene, leading a change of built-up area into water surface.

The conversion of built-up area in 2011 into vegetation in 2016 is an error caused by cloud coverage. The scenes in 2011 exhibited dense cloud coverage towards the west of the river basin. Given that clouds have similar reflectance to built-up area, these pixels were incorrectly classified as built-up area in 2011. In the 2016 scene, the area with cloud coverage was not present, providing the true reflectance value of the underlying land cover, which is vegetation. This phenomenon created the conversion of built-up area into vegetation.

For the time period under consideration, built-up area

increased 342.45 km^2. This level of increase is approximately 117% of the target increase stated in the land use master plan of Quang Nam and Da Nang city, indicating that more built-up land has been created than planned. Paddy rice reduction for the time period under consideration is 53.86 km^2, a figure that is greater than the target reduction in the land use master plan. In particular, the level of reduction is 116% of the target reduction (Table 8).

Table 8. Land planning changes in Quang Nam and Da Nang until 2020.

	Planned (2011-2020) (km^2)	Status (2011-2016) (km^2)	Goal reached (%)
Agriculture (rice)	-46.60	-53.86	116
Urban area	+292.57	+342.45	117

The reduction of paddy rice cultivation area is fragmented rather than covering large areas. The spatial distribution of paddy rice conversion area is illustrated in Fig. 7. There appears to be no large-scale paddy rice area reduction but rather smaller-scale reductions at the household level.

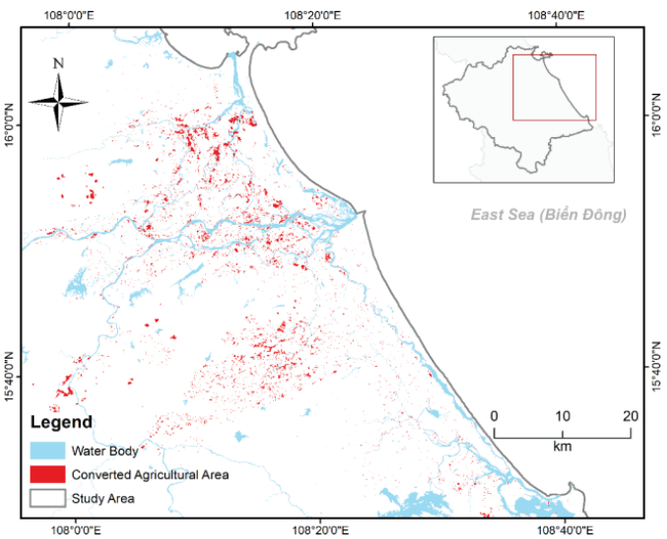

Fig. 7. Paddy rice area converted between 2011 and 2016.

Paddy rice area in 2011 was replaced by built-up infrastructure, water, vegetation, and empty land by 2016. Of the 68.89 km^2 of rice cultivation area converted, roughly 25% was converted into built-up area. A smaller proportion of the conversion of paddy rice land is into water. The remaining majority of paddy rice land conversion was into vegetation and empty land (Table 9).

Table 9. Conversion of agricultural land (units: km^2).

Converted into Built-up	Converted into Water	Converted into Vegetation	Converted into Empty land	Total conversion
10.10	19.12	53.81	30.60	68.89

The conversion of paddy rice into built-up areas took place in Da Nang city and along the Da Nang - Hoi An - Tam Ky connecting route (Fig. 8). Da Nang is growing rapidly, leading to a high demand for urban development. This demand forces agricultural area to be replaced by built-up area. In addition, the conversion of paddy rice along the Da Nang - Hoi An - Tam Ky connecting route is a direct result of urbanization.

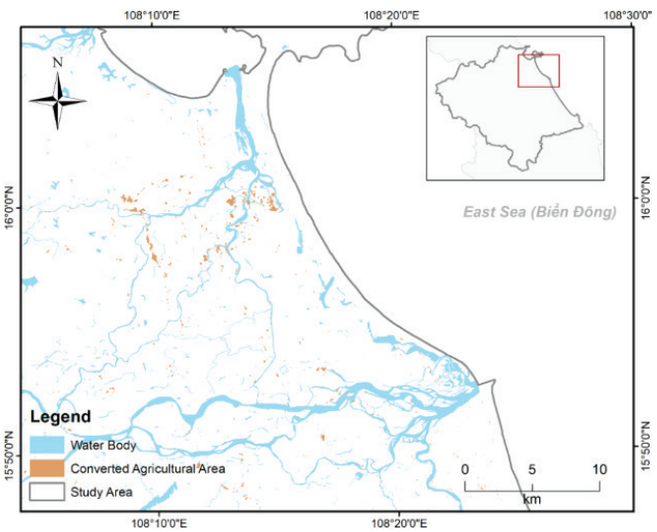

Fig. 8. Conversion of agricultural area into built-up area.

The conversion of agricultural land into built-up area could be assessed in relation to the socioeconomic development of the river basin in the same period. This study utilizes four socioeconomic indicators for the assessment, including: average monthly income (million Vietnam dong - VND), average population (inhabitants), gross output of economic sector (VND), and gross domestic product share by economic sector (%). The values of the indicators were taken from the Statistical Yearbook of Quang Nam in 2011 and 2015 [28, 29]. The selection of 2015 as the end period instead of 2016 is due to the nature of the statistical yearbook and land cover classification scheme. Land cover classification was performed for early 2016 while socioeconomic data in 2015 were compiled in early 2016, hence, the overlapping time period provides a better comparison basis.

From 2011 to 2015, average monthly income increased in both rural and urban areas in Quang Nam (Table 10). Average monthly income in the urban area nearly doubled while income in the rural area increased 1.5 times. Nonetheless, the increase in average monthly income of the urban area is slightly higher than in the rural area both in absolute terms (VND) and relative terms (percentage).

Table 10. Average monthly income per capita in Quang Nam province (unit: million VND).

	2011	2015	Change
Urban	1.413	2.585	82.9%
Rural	1.179	1.862	57.9%

Higher income in the urban area could boost an incentive for migration from rural areas to urban areas. In other words, people living in the rural area are attracted by the higher income increase in the urban area and migrated for better living standards. Assessment of migration is performed using population data in Quang Nam Province (Table 11).

Table 11. Population (inhabitants) and birth rate in the VGTB river basin.

	Population			Birth rate		
	2011	*2015*	*Change*	*2011*	*2015*	*Change*
Urban	273,072	356,845	30.7%	9.56%	9.92%	0.36%
Rural	1,161,928	1,123,945	- 3.3%	10.80%	10.79%	0.01%

For the time period under consideration, the urban population increased 30.7% while the rural population decreased 3.3%. This change in urban and rural population could be attributed to either natural increase in birth rate or migration.

It is clear from Table 11 that the birth rate in the urban area is positive while the birth rate in the rural area is nearly zero. Therefore, the increase in the urban population was surely affected by the increase in the natural birth rate. However, the contribution of the birth rate is not as significant as the overall increase in population (30.7% versus 0.36%). Therefore, migration of people into the urban area clearly was a more significant contributor. On the other hand, the reduction in population in the rural area could not be attributed to a stagnant birth rate; in fact, the rural birth rate neither increased nor decreased during the time period. Therefore, the decrease in rural population could only be a direct result of mass movement.

The migration pattern from rural to urban is fairly common in rapidly urbanizing areas. This migration pattern could trigger spikes in real estate prices due to the principle of supply and demand. A quick analysis of land prices in Da Nang city for the period of 2011-2015 revealed an increase of as much as 35% with an average price increase of approximately 18% [30, 31].

The gross product in agriculture and industry in Quang Nam province increased significantly for the time period of 2011-2015 (Table 12), more than doubling in both sectors with a slightly higher increase in industry. The measure of gross output is in VND.

Table 12. Gross output and contribution of agriculture and industry (unit: million VND).

	Gross output			Contribution		
	2011	*2015*	*Change (%)*	*2011 (%)*	*2015 (%)*	*Change (%)*
Agriculture	7,829,380	17,614,624	125.0	20.7	16.4	- 4.3
Industry	28,845,598	75,044,064	160.2	40.5	43.2	2.6

Although the gross output of agriculture more than doubled, its share within Quang Nam's economy decreased slightly (4.3%). This contradicts the increase in share of industry for the same period (2.6%). The values are illustrated in Table 12. Without being too presumptuous, a shift in the economic structure of Quang Nam from agriculture to industry could be deducted and could have implications for land use in the region.

By reviewing the socioeconomic indicators, a number of conclusions could be drawn regarding the conversion of agricultural land into built-up area. *Firstly*, there exists a migration pattern from the rural area to the urban area within the river basin. This is fuelled by better living standards and incomes in the urban area. This migration created a higher demand for urban housing, therefore, more built-up area has been developed to meet the increase in population. *Secondly*, there exists a shift in the economic structure of the river basin. An increase in the industrial share of the economy created higher demand for built-up infrastructure, and a decrease in the agriculture share of the economy reduced demand for agricultural area. Therefore, the conversion of agriculture into built-up area is explained.

The conversion of agricultural land into water bodies occurred only near river streams (Fig. 9). This can suggest two conversion mechanisms. Firstly, paddy rice cultivation land close to river streams has been totally abandoned due to erosion. However, this accounts for only a small proportion of the conversion. The other conversion mechanism is the conversion from cropland to aquaculture. The explanation is somewhat justifiable given that the market value for aquaculture products is higher than the market value for crops, providing incentives to farmers to change their produce. In particular, shrimp prices are approximately 40 times higher than rice (200,000 VND versus 5,000 VND/kilogram) [8]. In addition, the Vietnam Ministry of Agriculture and Rural Development has offered incentives to increase the country's agricultural export value. Thus, more cropland is being converted into fish or shrimp farms (aquaculture).

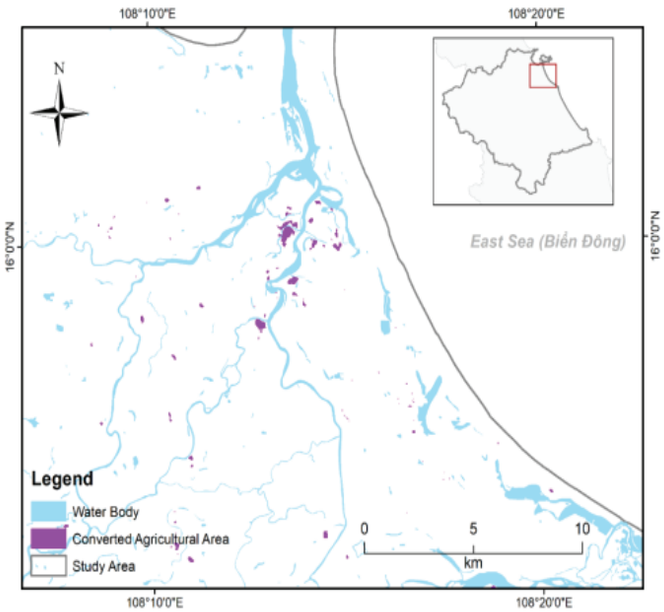

Fig. 9. Conversion of agricultural land into water bodies.

The conversion of agricultural land into vegetation accounts for the majority of agricultural land reduction within the period of 2011-2016. The classification scheme limits the ability to assess the exact type of vegetation into which paddy rice has been converted. One suggestion is that the type of crop cultivated changed from paddy rice to perennial crops. Using the classification method, these areas are green throughout the months used in the multi-temporal NDVI assessment, which would not be expected with paddy rice cultivation techniques. Therefore, these areas would have been occupied by another type of vegetation. The spatial distribution of the conversion of paddy rice into other types of vegetation is illustrated in Fig. 10.

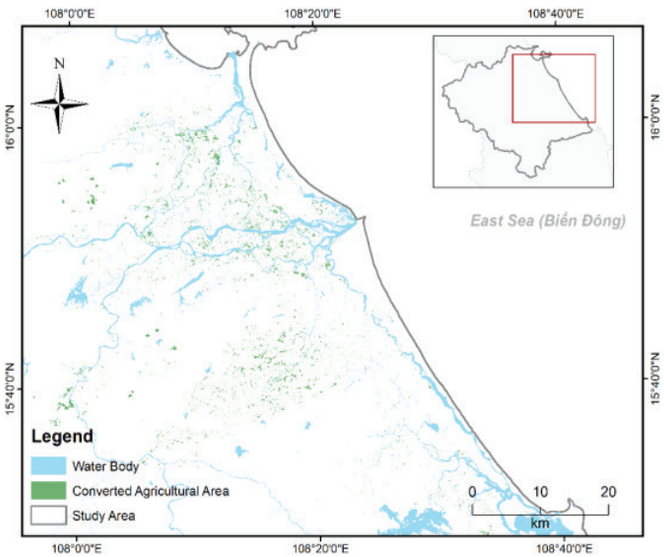

Fig. 10. Conversion of agricultural area into vegetation.

The remaining agricultural land conversion was into empty land. All conversions took place within the city area of Da Nang, which suggests that previously cultivated areas for paddy rice are now abandoned. Given the rapid urbanization pressure discussed earlier, these agricultural areas would have now been converted into built-up area, however, they were still in the process of being developed at the time of the satellite image. An example of the spatial distribution of such conversion is illustrated in Fig. 11.

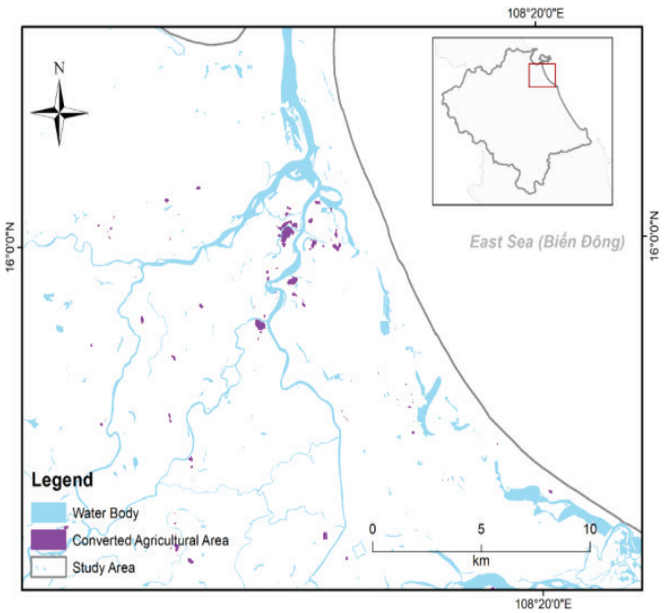

Fig. 11. Conversion of agricultural area into empty land.

Implications of the results

The implications of the land cover change dynamic between agricultural and non-agricultural uses in the VGTB river basin are manifold. They include reassessment of the land use master plan target, measures to regulate housing development, the nature of the mechanism of paddy rice conversion, assessment of aquaculture development in agriculture, and improved market conditions for newer agriculture crops.

Firstly, the increase in built-up area has reached its target four years ahead of schedule. Consequently, further development must be delayed to ensure that no additional increase in built-up area will take place over the coming years. Given that there are another three years until the end of the land use master plan period, there is a chance that further development would violate the target for the built-up area. That is to say, if the land use master plan is to be adhered to at all costs, no further land development would be allowed to take place in the following years. Therefore, policymakers are faced with two options: either strictly enforce the target for the increased built-up area or revise the target.

Secondly, the increase in built-up area, especially housing development, should be placed under scrutiny and regulation with the purpose of avoiding a housing market bubble. The increase in built-up area as evaluated earlier is due to better development opportunities as well as land use policies. Given the incentives both by policies and financial reward, the market would further create pressure to utilize undeveloped land and convert it into built-up areas. However, an overabundance of housing could backfire, creating a housing market bubble and speculation. The consequence of a bubble burst could be fatal to current and future development.

Thirdly, the paddy rice cultivation area decreased according to the master plan, however, it was not converted into built-up area but rather into other types of agricultural uses. This suggests another mechanism in play preserving paddy rice (agricultural) land from urbanization. Given the financial incentives of converting agricultural land into built-up area, one question arose: Why has only a small portion of paddy rice been converted into built-up area while the increased built-up area target has been met? The answer could be found in the Land Law of 2013 [32]. In particular, clause 57 maintained that conversion of agricultural land into built-up area must be approved by the local government, therefore, discouraging such conversion. Moreover, one could also view the question in terms of people's livelihood. Agriculture remains the backbone of the local economy, hence, people would rather keep their land and replace rice with higher-value products such as perennial crops and aquaculture rather than selling their land for urban development.

Fourthly, the conversion of paddy rice area into aquaculture could have a non-reversible effect on the use of land in the future. Aquaculture close to a coastal zone would normally be in the form of saline-adaptive species. Therefore, once paddy rice fields have been converted into fish or shrimp farms, reverting back to paddy rice would require much effort to remove soil salinity. Aquaculture near the coast in general, and fish and shrimp farms in particular, require the construction of ponds of sea water. Once sea water has been introduced, the soil eventually becomes saline due to evaporation. Therefore, reverting back to paddy rice fields from aquaculture can be challenging. This would require a large amount of effort to improve the soil quality and to reduce soil salinity levels to a threshold acceptable to a rice crop. Therefore, the conversion of paddy rice into aquaculture farms must be undertaken cautiously as it represents a non-robust conversion mechanism.

Finally, the conversion of land for paddy rice cultivation into land for other types of crops or aquaculture must be viewed with the overall economy in mind. The nature of rice allows the product to be stored for a long period of time and transported to easily accessible markets both domestically and internationally. The same is not true for other types of crops and aquaculture products. Fruits, for example, cannot be stored for periods longer than weeks. Hence, the market for newer agricultural products in the region has to be thoroughly assessed and accessibility must be improved. Failure to do so will result in an overabundance of products that are unable to reach consumers, creating socioeconomic problems in the river basin.

Conclusions

Land use policy has been evaluated in this study through the use of GIS and remote sensing technologies. Land cover maps for 2011 and 2016 were produced using an index-based classification approach. The 2011 map represented land cover prior to the current land use master plan while the 2016 map represented land cover after the master plan was adopted.

Land cover change detection between 2011 and 2016 revealed an increase in built-up area and a decrease in agricultural (rice) area. Built-up area in 2016 met its target four years ahead of schedule, indicating a rapid urbanization process. Agricultural area (rice area) also met its target in 2016. However, the conversion of agricultural area has largely been a conversion between types of crops and to aquaculture. To a smaller extent, there has also been conversion from agricultural area into built-up area.

The implication of these results could be used to better understand the impacts of land policies in the river basin. By understanding the resulting effect of the policies, adjustments could be made to the current land use policies and lessons could be learned to apply to future policies. This is especially important since not all policies worked out according to their intended purposes; socioeconomic factors may contribute to the deviation from the land use policies.

However, this study is not without limitations and room for further improvement. Land cover classification in the study could possibly be further improved in a number of ways. This includes utilizing other sources of data such as land use maps from the Vietnam Ministry of Natural Resources and Environment and higher-resolution satellite data such as those from SPOT.

The authors declare that there is no conflict of interest regarding the publication of this article.

REFERENCES

[1] Labbé, Danielle (2016), "Critical reflections on land appropriation and alternative urbanization trajectories in periurban Vietnam", *Cities*, **53**, pp.150-155.

[2] Khanh Toan Pham, Minh Bao Nguyen, Ha Dieu Nguyen (2011), "Energy supply, demand, and policy in Vietnam, with future projections", *Energy Policy*, **39(11)**, pp.6814-6826, Doi:10.1016/j.enpol.2010.03.021.

[3] Phuc Nguyen Q, A.C.M. Van Westen, Annelies Zoomers (2014), "Agricultural land for urban development: The process of land conversion in Central Vietnam", *Habitat International*, **41**, pp.1-7.

[4] Thi H.T. Nguyen, Tuan Van Tran, Quang T. Bui, Quang H. Man, Timo D.V. Walter (2016), "Socio-economic effects of agricultural land conversion for urban development: case study of Hanoi, Vietnam", *Land Use Policy*, **54**, pp.583-592.

[5] Van Cu Pham, Thi-Thanh-Hien Pham, Thi H.A. Tong, Thi T.H. Nguyen, Ngoc H. Pham (2013), "The conversion of agricultural land in the peri-urban areas of Hanoi (Vietnam): patterns in space and time", *Journal of Land Use Science*, **10(2)**, pp.224-242, Doi:10.1080/1747423X.2014.884643.

[6] Disperati, Leonardo, Salvatore G.P. Virdis (2015), "Assessment of land-use and land-cover changes from 1965 to 2014 in Tam Giang-Cau Hai lagoon, Central Vietnam", *Applied Geography*, **58**, pp.48-64.

[7] Hauser, T. Leon , Giang Nguyen Vu, Binh A. Nguyen, Emma Dade, Hieu M. Nguyen, Trang T.Q. Nguyen, Toan Q. Le, Long H. Vu, Ai T.H. Tong, Hoa V. Pham (2017), "Uncovering the spatio-temporal dynamics of land cover change and fragmentation of mangroves in the Ca Mau peninsula, Vietnam using multi-temporal SPOT satellite imagery (2004-2013)", *Applied Geography*, **86**, pp.197-207.

[8] Hanh Tran, Tran Thuc, Matthieu Kervyn (2015), "Dynamics of land cover/land use changes in the Mekong delta, 1973-2011: a remote sensing analysis of the Tran Van Thoi district, Ca Mau province, Vietnam", *Remote Sensing*, **7(3)**, pp.2899-2925, Doi:10.3390/rs70302899.

[9] S.J. Leisz (2017), "Land-cover and land-use transitions in Northern Vietnam from the early 1990s to 2012", *Redefining Diversity and Dynamics of Natural Resources Management in Asia*, pp.77-86, San Diego, Elsevier.

[10] Hoang H. Nguyen, Paul Dargusch, Patrick Moss, Ammar A. Aziz (2017), "Land-use change and socio-ecological drivers of wetland conversion in Ha Tien plain, Mekong delta, Vietnam", *Land Use Policy*, **64**, pp.101-113.

[11] Lubowski, N. Ruben, M. Vesterby, S. Bucholtz, M.J. Roberts (2006), "Major uses of land in the United States, 2002", *Economic Information Bulletin*, **EIB-14**, 54pp.

[12] Phuc X. To, Sango Mahanty, Wolfram H. Dressler (2015), "'A new landlord'? community, land conflict and State Forest Companies (SFCs) in Vietnam", *Forest Policy and Economics*, **58**, pp.21-28.

[13] Wu J. Jie (2008), "Land use changes: economics, social, and environmental impacts", *Choices*, **23(4)**, pp.6-10.

[14] T.N.K.D. Binh, Nico Vromant, T. Hung Nguyen, Luc Hens, E.K. Boon (2005), "Land cover changes between 1968 and 2003 in Cai Nuoc, Ca Mau peninsula, Vietnam", *Environ. Dev. Sustain.*, **7(4)**, pp.519-536, Doi:10.1007/s10668-004-6001-z.

[15] S. Saksena, J. Fox, J. Spencer, M. Castrence, M. DiGregorio, M. Epprecht, N. Sultana, M. Finucane, L. Nguyen, T.D. Vien (2014), "Classifying and mapping the urban transition in Vietnam", *Applied Geography*, **50**, pp.80-89.

[16] T.Q Viet (2014), *Methodology for Estimating the Impacts of Climate Change Induced Saltwater Intrusion on Agriculture in Estuaries. Testing for the Vu Gia - Thu Bon River Basin, Vietnam*, Ph.D., RUB University.

[17] Vietnam Communist Party (1994), *Resolution No. 07-NQ/HNTW*, http://dangcongsan.vn/tu-lieu-van-kien/tu-lieu-ve-dang/lich-su-dang/books 11520162411956/index-2152016246565625.html.

[18] Vietnam Communist Party (2002), *Resolution No. 15-NQ/TW*, https://thuvienphapluat.vn/van-ban/Linh-vuc-khac/Nghi-quyet-15-NQ-TW-nam-2002-day-nhanh-cong-nghiep-hoa-hien-dai-hoa-nong-nghiep/139273/noi-dung.aspx.

[19] Government of Vietnam (2013a), *Resolution No. 105/NQ-CP*.

[20] Government of Vietnam (2013b), *Resolution No. 74/NQ-CP.*

[21] IPCC (2003), *Good Practice Guidance for Land Use, Land-use Change and Forestry/The Intergovernmental Panel on Climate Change*, Ed. by J.Penman, M. Gytarsky, T. Hiraishi, T. Krug, D. Kruger, R. Pipatti, L. Buendia.

[22] Rwanga, S. Sophia, J.M. Ndambuki (2017), "Accuracy assessment of land use/land cover classification using remote sensing and GIS", *International Journal of Geosciences*, **8(4)**, pp.611-622, Doi:10.4236/ijg.2017.84033.

[23] Senf, Cornelius, Pedro J. Leitão, Dirk Pflugmacher, Sebastian van der Linden, Patrick Hostert (2015), "Mapping land cover in complex Mediterranean landscapes using Landsat: improved classification accuracies from integrating multi-seasonal and synthetic imagery", *Remote Sensing of Environment*, **156**, pp.527-536.

[24] Akinyemi, O. Felicia (2017), "Land change in the central Albertine rift: insights from analysis and mapping of land use-land cover change in north-western Rwanda", *Applied Geography*, **87**, pp.127-138.

[25] McCoy, M. Roger (2005), *Field Methods in Remote Sensing*, New York, NY: The Guilford Press.

[26] Li Cheng and Nguyen Xuan Thinh (2013), "Investigation and comparison of land-cover change patterns in Xuzhou city, China, and Dortmund city region, Germany, using multi-temporal Landsat images", *Journal of Applied Remote Sensing,* **7**, Doi: 10.1117/1.JRS.7.073458.

[27] Tilahun, Abineh, Bogale Teferie (2015), "Accuracy assessment of land use land cover classification using google earth", *AJEP*, **4(4)**, Doi:10.11648/j.ajep.20150404.14.

[28] Quang Nam Statistical Office (2012), *Quang Nam Statistical Yearbook 2011*, Hanoi, Statistical Publishing House.

[29] Quang Nam Statistical Office (2016), *Quang Nam Statistical Year Book 2015*, Hanoi, Statistical Publishing House.

[30] Da Nang People's Committee (2011), *Decision number 35/2011/QD-UBND.*

[31] Da Nang People's Committee (2014), *Decision number 50/2014/QD-UBND.*

[32] National Assembly of Vietnam (2013), *Land Law 2013- No. 45/2013/QH13.*

Doi: 10.31276/VJSTE.62(1).85-89

Treatment of ammonium in slaughterhouse wastewater by UASB technology combined with EGSB using anammox and PVA gel

Minh Nhat Phan[1], Nguyen Van Nhi Tran[2], Jimmy Yu[2], Tan Phong Nguyen[1*]

[1]Faculty of Environment and Natural Resources, University of Technology, Vietnam National University, Ho Chi Minh city
[2]Civil and Environmental Engineering, School of Engineering and Built Environment, Griffith University, Australia

Received 22 January 2020; accepted 10 March 2020

Abstract:

Slaughterhouse wastewater (SWW) possesses very high organic and nutrient concentrations and its residues are moderately solubilized, which leads to pollution affecting the environment and human health. The objective of this study was to investigate the effective removal of ammonium in slaughter wastewater by up flow anaerobic sludge blanket (UASB) technology combined with an expanded granular sludge bed (EGSB) using anammox and PVA gel as the biomass carrier. Ammonium loading rates (NLRs) increased from 0.25 kg N-NH_4^+/m^3.d to 0.75 kg N-NH_4^+/m^3.d with hydraulic retention times (HRTs) of 12, 6, and 4 h. The system was operated in 2 phases. In phase 1, the removal of ammonium by employing the combination of UASB technology and EGSB using anammox was examined. The removal efficiencies of nitrite were 52% (NLRs=0.25 kg N-NH_4^+/m^3.d), 69% (NLRs=0.5 kg N-NH_4^+/m^3.d) and 64% (NLRs=0.75 kg N-NH_4^+/m^3.d). On the other hand, the removal efficiencies of ammonium were about 37% (NLRs=0.25 kg N-NH_4^+/m^3.d), 64% (NLRs=0.5 kg N-NH_4^+/m^3.d) and 55% (NLRs=0.75 kg N-NH_4^+/m^3.d). In phase 2, a PVA gel was supplied to the EGSB as the biomass carrier for growing the anammox sludge. The result showed that the removal efficiencies of nitrite were about 55% (NLRs=0.25 kg N-NH_4^+/m^3.d), 77% (NLRs=0.5 kg N-NH_4^+/m^3.d), and 73% (NLRs=0.75 kg N-NH_4^+/m^3.d). In addition, the removal efficiencies of ammonium were about 56% (NLRs=0.25 kg N-NH_4^+/m^3.d), 68% (NLRs=0.5 kg N-NH_4^+/m^3.d), and 60% (NLRs=0.75 kg N-NH_4^+/m^3.d).

Keywords: **ammonium removal, anammox, EGSB, PVA gel.**

Classification number: **5.1**

Introduction

The main pollutant sources of wastewater from the slaughtering process are paunch, faeces, fat and lard, grease, undigested food, blood, suspended material, urine, loose meat, soluble proteins, excrement, manure, grit, and colloidal particles. SWW contains large amounts of biochemical oxygen demand (BOD), chemical oxygen demand (COD), total organic carbon (TOC), total nitrogen (TN), total phosphorus (TP), and total suspended solids (TSS). The treatment of SWW has been achieved by traditional methods such as aerobic and anaerobic biological systems.

Anammox (anaerobic ammonium oxidation) is a globally important microbial process of the nitrogen cycle that takes place in many natural processes. Anammox is a reaction that ammonium oxidation to dinitrogen gas using nitrite as the electron acceptor under anoxic conditions [1]. Since its discovery two decades of ago, anammox-related research and its applications have experienced strong growth. Researchers have considered the anammox process as a method of treating the high-nutrient concentrations of wastewater. Based on mass balance from culture experiments using a sequencing batch reactor (SBR) to take account of the biomass growth, the anammox reaction has the following scaling coefficients [2, 3].

$$NH_4^+ + 1.32NO_2^- + 0.066HCO_3^- + 0.13H^+ \rightarrow 1.02N_2 + 0.26NO_3^- + 0.066CH_2O_{0.5}N_{0.5} + 2.03H_2O \quad (1)$$

In comparison with traditional technologies, anammox has many advantages such as high nitrogen removal, low operational costs, and small space requirement [4]. Anammox has been successfully applied to treatment of wastewater on the laboratory scale, pilot scale, and full scale. Many types of wastewater have been surveyed with positive results. For example, the anammox process has been applied to the treatment of landfill leachate. This research

*Corresponding author: Email: ntphong@hcmut.edu.vn

showed that ammonium removal efficiency reached 88.1% and TN removal efficiency reached 80% [2]. However, in this study, the anammox process is applied in combination with PVA gel for the treatment of SWW. The purpose of the study is to assess slaughter wastewater treated by using UASB combined with EGSB technologies as well as to evaluate the factors that affect the treatment efficiency of these processes.

Material and methods

Feed SWW

SWW was taken from the VISSAN Company's wastewater treatment plant. The characteristic of the SWW is shown in Table 1.

Table 1. Characteristics of SWW.

Serial	Parameter	Unit	Value
1	pH		6.6-7.9
2	COD	mg/l	1,000-1,400
3	NH_4^+-N	mg/l	90-140
4	TKN	mg/l	130-170
5	NO_2^--N	mg/l	0-1.58
6	NO_3^--N	mg/l	0-2.50
7	Alkalinity	mg $CaCO_3$/l	600-1,200
8	TP	mg/l	15-35
9	Temperature	°C	28-31

Set-up of experiment and operational conditions

The lab-scale system has three reaction tanks including the UASB, partial nitrification (PN), and EGSB is shown in Fig. 1.

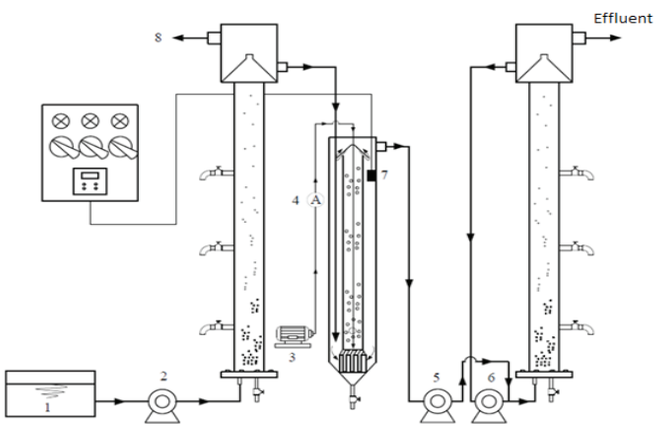

Fig. 1. Schematic diagram of the lab-scale system. (1) Influent tank, (2) Influent pump, (3) Air pump, (4) Air valve, (5) Pump, (6) Circulating pump, (7) pH probe, (8) Biogas collection.

The wastewater pumped to the UASB was stored in a tank with volume of 90 l. The UASB is an acrylic tube with a working volume of 10 l with a height of 1.2 and 0.09 m internal diameter. On the column, there are 3 inspection valves. Each of these are 30 cm apart to collect wastewater and sludge samples. The PN also an acrylic tube. The working volume is 12.4 l with 0.78 m height and 0.14 m diameter. The central pipe is made of PVC and is composed of a 40 cm long section of pipe connected to a cone with a chisel around it. Air flow was supplied from the bottom of the tank through an air pump and adjusted through a valve. After passing the UASB-PN, wastewater will be stored in tanks with volume of 90 l and pumped into the EGSB tank. The EGSB tank is an acrylic tube with a working volume of 10 l, 1.2 m high and 0.09 m internal diameter. Water circulation in the tank is done through a circulating pump. The treatment efficiency of the system is analysed and evaluated.

Enrichment of sludge and PVA gel

Enrichment of sludge: anaerobic sludge is taken from the anaerobic tankand ammonia-oxidizing bacteria (AOB) sludge is taken from the aeration tank of the VISSAN wastewater treatment system. The anammox sludge is taken from the Institute of Tropical Biology, Ho Chi Minh city.

PVA gel: the PVA gel was provided by KURARAY AQUA CO., LTD. The PVA (Polyvinyl alcohol) gel is comprised of 4 mm spherical beads having a specific gravity of 1.025. One PVA-gel bead can hold up to 1 billion microorganisms depending on operating conditions [5].

Operational conditions (Table 2)

Table 2. Operational conditions.

Input flow (l/h)	HRT (h)	Ammonium loading rate (kg NH_4^+-N/m^3.d)	DO PN (mg/l)	Operating time (d)
0.5	12	0.25	0.8-1.0	1-20
1	6	0.5	0.8-1.0	21-40
1.5	4	0.75	1-1.2	41-60

Wastewater was brought from the wastewater tank to the UASB through a pumping system. The reactor was operated in dark conditions by using a black plastic sheet fully covering the body to prevent the growth of algae. The mixed liquor suspended solids (MLSS) concentration of the reactor was maintained within 15,000 mg/l. The purpose of the UASB is to treat large quantities of organic matter in wastewater by converting organic nitrogen into ammonia to facilitate subsequent processing.

Water self-flowed from the UASB to the PN tank. The MLSS in the PN was kept in the range of 4,000-5,000 mg/l, the DO was adjusted from 0.8 to 1.2 mg O_2/l, and the pH

was adjusted automatically through a pH controller and chemical pump. $NaHCO_3$ salt was added to the PN tank to adjust the pH in the range of 7.5-8.5. The goal of the PN tank is to convert a part of NH_4^+ into NO_2^- to a NH_4^+/NO_2^- ratio of 1/1.32 and to prevent the formation of NO_3^-, creating the most favourable conditions for the anammox process in the EGSB tank to take place.

The EGSB tank contains the activity of anammox microorganisms in anaerobic conditions. In addition, there is a water circulation pump that create a disturbance in the tank to increase the contact between the wastewater and microorganisms. The biological processes that take place in the tank will reduce the nitrogen content in the wastewater. The model is split into two stages. During stage one, the UASB/EGSB-anammox alone treated the SWW. In stage 2, the PVA gel was introduced into the model as a biomass carrier.

Results and discussion

The UASB/EGSB-anammox

Partial nitritation (PN): Figs. 2 and 3 show the loading rate of ammonium to be 0.25 kg NH_4^+-N/m^3.d corresponding to an ammonium concentration of 120±7.5 mg/l. After the SWW passed through the UASB tank, the ammonium content increased to 134±7.5 mg/l. Nitrification process took place in the PN tank and the ammonium conversion efficiency was about 57%. The NO_2^--N/NH_4^+-N ratio was about 1.27±0.3 and the highest ratio was 1.53 on the 20th day with an ammonium conversion efficiency of 63%. The DO in the PN tank at this stage was only about 0.8-1.0 mg/l, and the pH was in the range of 7.4-8.2 after long retention times to create conditions for AOB growth. The NO_3^--N concentration of the effluent from the PN tank was very low (5±1.2 mg/l). This proved that the process in the PN tank was indeed the nitrification process, and the nitritation process was almost non-existent.

After the loading rate of ammonium was increased to 0.5 kg NH_4^+-N/m^3.d, the input wastewater had a relatively stable ammonium content (123±8.8 mg/l). The ammonium concentration after passing through UASB tank increased to 130±8 mg/l. During the first few days during the loading process, the ratio of NO_2^--N/NH_4^+-N was about 1.06 and the conversion rate was only about 51%. Because this value was quite low, the DO, pH and alkalinity parameters in the operation were adjusted to quickly improve the ratio. In the proceeding days, the ratio of NO_2^--N/NH_4^+-N increased gradually day by day until the ratio reached its highest value on the 27th day, with an of NO_2^--N/NH_4^+-N of 1.4 and conversion efficiency of nearly 57%. On the 30th day, the ratio of NO_2^--N/NH_4^+-N was 1.31, which is similar to the theoretical ratio, and the ammonium conversion efficiency reached 60%. In general, an average NO_2^--N/NH_4^+-N ratio in the range of 1.22±0.2 is suitable for the anammox process in the EGSB tank.

After the first 10 days the loading rate of ammonium was up to 0.75 kg NH_4^+-N/m^3.d, corresponding to HRT of 4 h, and the results showed that the conversion efficiency of ammonium decreased to 44%, the ratio of NO_2^--N/NH_4^+-N fluctuated in the range of 0.9-0.93, and the lowest ratio, 0.79, was found on the 44th day. This proves that changing the load has a great impact on the processes. Increased load makes AOB sludge not able to adapt to the new living environment and other biological processes also become unstable. The process gradually stabilized in the following days. Then 10 days later, the ratio of NO_2^--N/NH_4^+-N was 1.1±0.04 and relatively stable. On day 59, the ammonium conversion efficiency reached 59%.

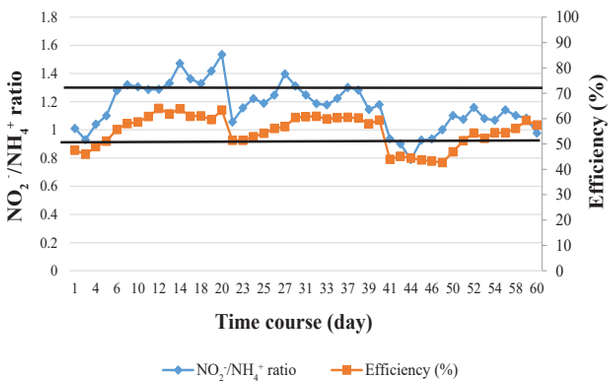

Fig. 2. NO_2^-/NH_4^+ ratio in the survey process.

Nitrogen removal efficiency: the concentration of input and output nitrogen compounds of the EGSB tank is shown in Fig. 3. Over the first 20 days, the model was operated at a low loading rate of 0.25 kg NH_4^+-N/m^3.d in order to allow the anammox bacteria to gradually adapt to SWW. The removal efficiency of NO_2^--N increased with operation time, from the first day the removal efficiency was 22% and on the 20th day the removal efficiency was 52% with 41.78 mg NO_2^--N/l removed. The average NH_4^+-N removal efficiency was 37% after 20 days of operation with 18 mg NH_4^+-N/l removed. At the same time, the amount of nitrate produced was 1.8 mg NO_3^--N. This shows that the anammox bacteria began to adapt to the wastewater.

When the loading rate of ammonium was increased 0.5 kg NH_4^+-N/m^3.d on the 21st day, the NH_4^+ removal efficiency was 25% and the NO_2^--N removal efficiency was 27%. This indicated that the anammox bacteria cannot adapt to new loads yet. After the loading rate increaset, the processing efficiency increased markedly in the following days shown by an adjustment of the NO_2^--N/NH_4^+-N ratio

in the range of 1.0-1.4 which created favourable conditions for the anammox bacteria. After 20 days of operation at an ammonium loading rate of 0.5 kg NH_4^+-N/m^3.d, the NH_4^+ removal efficiency was 64% and the NO_2^--N removal efficiency was 70%. The amount of NO_3^--N generated was about 8.8% compared to the amount of NH_4^+-N consumed, which proves that the nitrate reduction process coexisted with anammox process.

When the loading rate of ammonium was increased 0.75 kg NH_4^+-N/m^3.d, the treatment efficiency had a sharp decline over the first few days. The NH_4^+ removal efficiency was 39% and the NO_2^--N removal efficiency was 18%. The main cause of this situation is that the annamox bacteria could not adapt to the sudden change in load. In the following days, the operating conditions reached a steady state whereby the removal efficiency increased gradually. On the last day, the performance reached 57 and 69%, with 26 mg NH_4^+-N/l and 30.5 mg NO_2^--N/l removed. The average removal performance at this load was 55% (NH_4^+-N) and 64% (NO_2^--N). The amount of NO_3^--N generated was about 5% compared to the amount of NH_4^+-N consumed.

In general, the input NH_4^+-N concentration was 134±5, 130±8, and 110±10 mg/l for ammonium loading rate of 0.25, 0.5, and 0.75 kg NH_4^+-N/m^3.d, respectively, and the ammonium treatment efficiency of the model reached 37, 64, and 55% respectively.

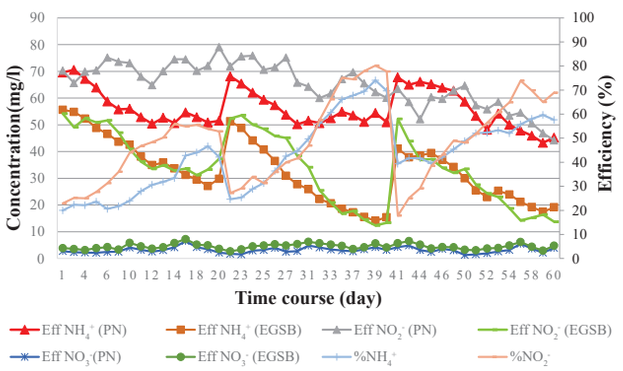

Fig. 3. Concentration of input and output nitrogen compounds of the EGSB tank.

The UASB/EGSB-anammox combined with PVA gel

PN: from Figs. 4 and 5 show that the 0.25 kg NH_4^+-N/m^3.d loading rate of ammonium, the input ammonium concentration was 126±10 mg/l. The ammonium conversion efficiency was about 58%, and the NO_2^--N/NH_4^+-N ratio was 1.16±0.29. On the 7th day, the NO_2^-/NH_4^+ ratio decreased to 0.75 because the system had problems during operation making the conversion rate from ammonium to nitrite lower than required. After fixing the problem, the NO_2^-/NH_4^+ ratio increased gradually, and on the 14th day the NO_2^-/NH_4^+ ratio was 1.32 with ammonium conversion efficiency of 64%.

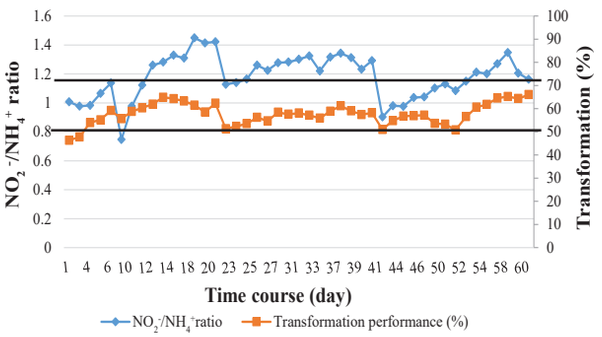

Fig. 4. NO_2^-/NH_4^+ ratio in the survey process.

After increasing the loading rate of ammonium up to 0.5 kg NH_4^+-N/m^3.d, the ammonium conversion efficiency decreased to 51%. The input ammonium was 133±6 mg/l and the average NO_2^-/NH_4^+ ratio was about 1.25±0.12. On the 32nd day, the ratio was 1.32. This ratio is the ideal theoretical ratio. While the ratio in this period was relatively unstable most of the ratios were in the range of 1.0-1.4 which meant they were still suitable for the next process.

On days 41 to 44, the loading rate of ammonium was increased to 0.75 kg NH_4^+-N/m^3.d corresponding to an HRT of 4 h. The results showed that the conversion efficiency of ammonium decreased to 51%. The ratio of NO_2^-/NH_4^+ decreased to 0.9±0.07 because the sludge did not adapt to the change in loading rate. In the following days, the ratio of NO_2^-/NH_4^+ increased gradually. On the 58th day, the highest ratio reached 1.34 with an ammonium conversion efficiency of 65%. The average ammonium conversion efficiency was 58%.

Nitrogen removal efficiency: the concentration of input and output nitrogen compounds from the EGSB tank is shown in Fig. 5. Over the first 20 days, the model was operated with a low loading rate of 0.25 kg NH_4^+-N/m^3.d, and the removal efficiency of NO_2^- and NH_4^+ increased with operation time. On the first day, the removal efficiency of NO_2^- was about 35% and the removal efficiency of NH_4^+ was about 42%. On the 6th day, the removal efficiency of NO_2^- increased to 51% and the removal efficiency of NH_4^+ increased to 56%. On the 7th day, the removal efficiency of NO_2^- unexpectedly dropped to 32.6% and the removal efficiency of NH_4^+ was about 35% because the NO_2^-/NH_4^+ ratio was 0.75. After fixing a problem in the PN tank, the NH_4^+ and NO_2^- treatment efficiency increased gradually and became relatively stable. The average processing efficiency was about 55% for NH_4^+ and 55% for NO_2^-. At the same time, the production of NO_3^- was about 6.4% of the influent NH_4^+.

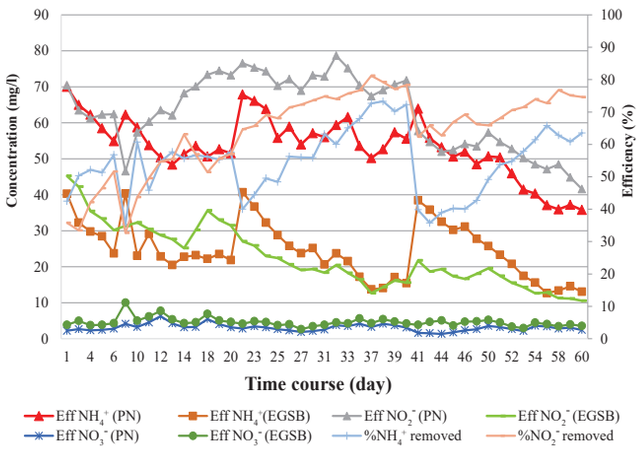

Fig. 5. Concentration of input and output nitrogen compounds of EGSB tank.

When increasing the loading rate of ammonium to 0.5 kg NH_4^+-N/m^3.d, the removal efficiency of NO_2^- and NH_4^+ was relatively stable. After 20 days of operation, the highest removal efficiency value was reached on day17, with 73% for NH_4^+-N removal and 81% for NO_2^--N removal. The average NH_4^+-N removal efficiency was about 68% and the average NO_2^--N removal efficiency was about 77%. Over the last 5 days of this period, the output of ammonium nitrogen was approximately 14±0.56 mg/l. The amount of NO_3^--N produced was about 5% of the influent NH_4^+.

The loading rate of ammonium was increased to 0.75 kg NH_4^+-N/m^3.d. On the first day, the removal efficiency of NO_2^- was 62% and the removal efficiency of NH_4^+ was 40%. Then, over the following days, the removal performance increased slowly. On the 54th day, the effect reached a steady state, and the NH_4^+-N removal efficiency was about 61% and the NO_2^--N removal efficiency was about 74%. On the last day, the performance reached 63% NH_4^+-N removal and 75% NO_2^--N removal, with 24.0 mg NH_4^+-N/l and 46 mg NO_2^--N/l removed.

Conclusion

The UASB/EGSB-anammox system was applied to treat SWW. HRTs were surveyed from 12, 6, and 4 h, and the ammonium removal efficiencies were 37, 64, and 55%, respectively. The nitrite removal efficiencies were 52, 69, and 64%, respectively. The PVA gel added during the second phase of the model showed an increase in pollution handling and model stability when operating at high loading rates. The ammonium removal efficiencies were 56, 68, and 60% for HRTs of 12, 6, and 4 h, respectively, and nitrite removal efficiencies were 55, 77, and 73%, respectively. This research model can be adapted to higher loads in order to assess its ability to handle critical conditions.

The authors declare that there is no conflict of interest regarding the publication of this article.

REFERENCES

[1] P.K. Lieu, et al. (2005), "Single-stage nitrogen removal using anammox and partial nitriteation (SNAP) for treatment of synthetic landfill leachate", *Japanese Journal of Water Treatment Biology*, **41(2)**, pp.103-112.

[2] M. Strous, et al. (1997), "Ammonium removal from concentrated waste steams with anaerobic ammonium oxidation (annamox) process in different reactor configurations", *Water Res*., **31(8)**, pp.1955-1962.

[3] M.C. Schmid, et al. (2007), "Anaerobic ammonium-oxidizing bacteria in marine environments: widespread occurrence but low diversity", *Environ. Microbiol*., **9(6)**, pp.1476-1484.

[4] A.O. Sliekers, et al. (2003), "Canon and anammox in a gas-lift reactor", *FEMS Microbiology Letters*, **218(2)**, pp.339-344.

[5] http://www.kuraray-aqua.co.jp/en/product/pvagel.html.

Doi: 10.31276/VJSTE.62(1).90-96

Climate change vulnerability indicators for agriculture in Ho Chi Minh city

Vu Thuy Linh[1, 2*], Ho Minh Dung[3, 4], Nguyen Kim Loi[2]

[1]Department of Natural Resources and Environment Ho Chi Minh city
[2]Insitute for Environment and Resources, Vietnam National University, Ho Chi Minh city
[3]Research Center for Climate Change, Nong Lam University, Ho Chi Minh city
[4]Institute for Computational Science and Technology (ICST)

Received 10 November 2019; accepted 6 February 2020

Abstract:

The term vulnerability has been used in a variety of contexts, including climate change impact assessment. This study aimed to set up and evaluate climate change vulnerability indicators (CCVI) of agricultural zones based on exposure, sensitivity, and adaptation capacity to climate change in Ho Chi Minh city. Data from consultations with 10 experts was collected and analysed by the analysis hierarchy process (AHP). The CCVI, which includes 3 primary indicators and 22 secondary indicators, was applied to the agricultural districts in Ho Chi Minh that have been demonstrated to be the most vulnerable to climate change under both current conditions and over a longer timescales under various climate change exposure scenarios. The CCVI was weighted to support the climate change vulnerability assessment and indicate comparatively low or high climate change vulnerability areas. Finally, the areas most needy of further adaptation activities for agriculture in Ho Chi Minh city were identified.

Keywords: **agriculture, AHP, climate change, vulnerability indicator.**

Classification number: **5.2**

Introduction

Climate change has clearly affected all areas of society and economy. In particular, Ho Chi Minh city is considered to be one of the 10 cities most affected by climate change [1]. Agricultural production in Vietnam, and in Ho Chi Minh city in particular, depends very much on the weather and faces several challenges such as changing water sources, rising temperatures, and droughts, among other extreme weather phenomena.

Ho Chi Minh city resides in the southeast region of Vietnam and has a total area of 2,095.01 km^2 [2]. The city is located in a transitional zone between the southeast and the Mekong delta. Ho Chi Minh city has lower elevations to the southeast. Located downstream of the Dong Nai river system, Ho Chi Minh city, also known as Saigon, has a very developed network of rivers and canals with a total length of 7,955 km (Fig. 1).

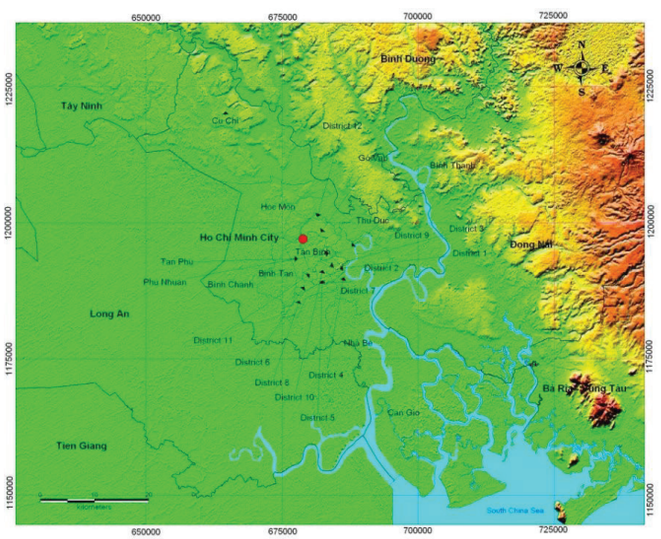

Fig. 1. Ho Chi Minh city, located within the Dong Nai river basin. Source: [3].

*Corresponding author: Email: vtlinh.uk@gmail.com

According to the Ho Chi Minh city Department of Agriculture and Rural Development (2015), 14 out of the 24 districts have agricultural activities with the 5 main agriculture districts being Cu Chi, Hoc Mon, Binh Chanh, Nha Be, and Can Gio. In total, the agricultural land area amounts to 104,000 hectares, accounting for nearly 50% of the total city area. Although the area of agricultural land has decreased gradually due to civilization, the average production value is still high. The average growth rate of agricultural production over the period of 2006-2010 reached 4.14%, and between 2011-2015 it was 6.01% [4].

Due to climate change, the agricultural production area has become mainly concentrated in suburban districts such as Cu Chi, Hoc Mon, and Binh Chanh, which are the most low-lying areas along the river, and thus, the most affected by climate change. According to the report of the Steering Committee for Climate Change Adaptation and Mitigation Action Plan [5], over the past 6 years (2005-2010), climate change events, especially tropical storms, high tides, and heavy rain causing prolonged flooding, has caused damage to the agricultural production of Ho Chi Minh city. Specifically, 1,520 ha of rice and 2,970 ha of sugarcane are affected by inundation, 1,770 ha of rice and 2,970 ha of sugarcane are affected by saline intrusion, and over 1,101 hectares of rice and 545 hectares of vegetables are affected by drought.

These effects threaten sustainable city development if immediate and appropriate adaptations to these impacts are not established. Thus, it is necessary to assess the extent of vulnerability under the impact of climate change on agricultural production. This study was carried out with the aim of determining the climate change factors that cause damage to agricultural production and to determine a weight for each indicator. These results are an important basis for conducting vulnerability assessments for the city's agricultural sector.

Literature review

Vulnerability is an implicit concept and has been addressed in many works. There are various ways to define the concept of vulnerability. Vulnerability is usually addressed with respect to specific types of risks such as flood, drought, and poverty. Dwyer, et al. (2004) [6] stated that there have been many concepts of vulnerability and each concept can be defined based on specific domains. Vulnerability assessments are investigated over diverse scales such as national, regional, local, or in a specific ecosystem. In its beginning stages, vulnerability assessments were concentrated on assessing physical risks [7-9]. Such an approach was also applied to many other aspects such as food security [10, 11] or socio-economic development [12].

In 1992, vulnerability was defined as the extent to which a system cannot cope with the effects of climate change and sea level rise [13]. From 1996 to 2007, the Intergovernmental Panel on Climate Change's (IPCC) second assessment report issued many definitions of climate change vulnerability. In general, vulnerability can be understood to be the degree to which "a system is susceptible to, and unable to cope with, adverse effects of climate change, including climate variability and extremes. Vulnerability is a function of the character, magnitude, and rate of climate change and variation to which a system is exposed, its sensitivity, and its adaptive capacity". According to these new concepts, vulnerability can decrease when more adaptation options are implemented.

According to the IPCC, vulnerability is a function of the character, magnitude, and rate of climate change and can vary depending on which system is exposed, its sensitivity, and its adaptive capacity. Vulnerability is dependent on the exposure to risks (E), sensitivity (S), and adaptive capacity (AC) of a system that deals with climatic impacts. In particular, the exposure component is made up of the factors reflecting the physical changes of climate such as weather condition, hydrology, etc. Sensitivity is the vulnerability magnitude of each system when no adaption options are implemented or is the extent to which each system depends on certain conditions. Adaptive capacity is the extent to which each system can ease the adverse impacts of climate change or utilize the opportunities from beneficial effects.

Vulnerability (V) can be described as follows:

$$V = f(E, S, AC)$$

where:

- E: exposure is the extent of a system that is exposed to significant changes in climate.

- S: sensitivity is the extent of a system affected both negatively and positively by climate change (including change of means, extremes, and climate variability).

- AC: adaptive capacity is the capacity of each organization or each system that can ease risks related to climate change or can utilize benefits from such changes.

The vulnerability assessment method uses an index or a set of indicators with weights or average weights for each indicator to assess vulnerability [14]. Vulnerability is a positive correlation to exposure and sensitivity of the exposed system. This means that an increase in exposure leads to an increase in vulnerability.

A wide range of research based on vulnerability assessment index has been conducted [8, 15-21]. This index is made up of many indicators that make a region vulnerable.

A set of indicators has been developed specifically for exposure, sensitivity, and adaptability, or for all three factors combined like in the studies by UNESCO-IHE [21]. However, developing an appropriate set of indicators remains an important challenge [17].

Recently, a group of authors conducted vulnerability assessments on residential, industrial, and agricultural services using GIS tools combined with AHP [22-24]. Factors of exposure, sensitivity, and adaptive capacity were weighted and used for building a vulnerability map. However, almost all research was concerned with the impact assessment of flood damage [22, 25, 26].

Therefore, in order to assess the overall impact of all the factors on agriculture in Ho Chi Minh city, research and development of suitable and measurable CCVI based on exposure, sensitivity, and adaptive capacity is crucial.

Methodology

CCVI

According to the objectives of vulnerability assessments to climate change, the first step is to synthesize necessary factors that can influence vulnerability in the study area. To achieve this task reliably and effectively, a literature review and file survey is used. In particular, the literature review approach enables the researcher to draw a general picture of vulnerability in the study area from the past to present day. Meanwhile, fieldwork makes it possible for the researcher to have insights into the real situation of climate change impacts, local livelihood and their relationships, and the potential effects of climate change in the future.

From the above literature review and field survey results, a list of influential factors in the zone vulnerable to climate change are developed. These factors are subdivided into four groups as follows: nature, economy, society, and infrastructure.

The process of developing CCVI for agriculture is done through a literature review process on climate change variability and its impacts on the agricultural sector in Ho Chi Minh city. In addition, economic and social factors are also considered to assess the system's sensitivity to climate change. Consultation with experts at a workshop facilitated the determination of the indicators important to the assessment of the vulnerability of the agriculture in Ho Chi Minh city. The selection of indicators was informed by a set of four factors provided by Gbetibouo, et al. (2010) [27], namely, relevance, adequacy, ease, and data availability.

The expert consultation method is commonly used in many fields and research directions, such as in studies on vulnerability assessment [28, 29], on climate change adaptation [30, 31], and in agricultural [32] and fishery studies [33]. The list of experts is based on the team's discussion. The team invited 9 experts with a variety of expertise such as economics, environmental resource management, water resource management, and hydrometeorology to consult about vulnerability indicators and their respective weights. The experts had general knowledge about climate change and over 5 years research experience on climate change. The review of Rowe and Wright (1999) [34] suggests that the number of experts can range from 3 to 98.

The literature review provided a list of climate exposure, sensitivity, and adaptive capacity indices typical in agriculture sectors. The consultation in vulnerability indicators was conducted over 3 steps including: (i) forming a list of experts to invite for consultation; (ii) sending questionnaires to the experts, and (iii) the expert consultation. Experts were requested to assess the degree of impact of climate change variabilities and indices. A Likert scale was used to assess impact degree from 1 (very light) to 5 (very serious) and the rating scale of certainty was from 1 (not sure) to 3 (very sure). The evaluation is described in more detail in Table 1. The weighted average score was used to measure the degree of impact.

Table 1. Description of the assessing scale of climate change degree of impact and scale of certainty.

Scale	Definition	Explanation
Scale of climate change impact degree		
1	Very light	... has very light impact to agriculture production
2	Light	... has light impact to agriculture production
3	Average	... has average impact to agriculture production
4	Seriously	... has serious impact to agriculture production
5	Very seriously	... has very serious impact to agriculture production
Scale of certainty		***Degree of certainty***
1	Not so sure	0-30%
2	Sure	>30-70%
3	Very sure	>70%

Weighting by Analytic Hierarchy Process (AHP)

The established CCVI are expressed through the integrated climate change risk index. In essence, each indicator and its components have a certain role in shaping the vulnerability level. Consequently, the weight of each CCVI factor is identified by the AHP [12, 35]. AHP descends from the theoretical measurement of priority and is based on mathematics and psychology. There are three prime

principles of AHP: analyzing, comparing, and synthesizing. When assessing vulnerability to climate change, there are multiple factors that contribute to each vulnerability level. In addition, the interconnection between these factors is complicated. However, the imperative question that needs to be clearly addressed is which factor could be considered as most influential to vulnerability in a certain area, and the other urgent question is how to estimate these factors quantitatively. Therefore, applying AHP is a suitable and effective approach. After consideration of how AHP was applied in previous studies, the procedure of AHP in this study is shown in Fig. 2.

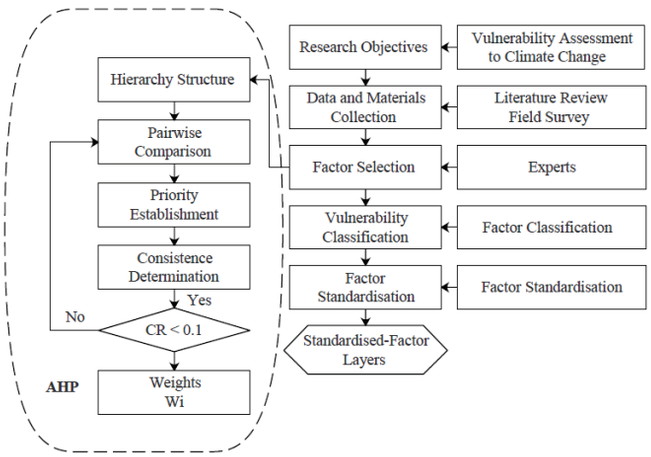

Fig. 2. The AHP procedure.

To determine the most influential factors, a questionnaire was sent to experts and the final pair-wise comparison values for each indicator was discussed and resolved by the experts. In the AHP procedure, the values of the pair-wise comparison matrix are qualitative, so these values must be converted into quantitative ones. Further, it is also necessary to check the consistency of each matrix through the consistency ratio (CR). Finally, in the case where the CR is less than 10%, the results of computing weights can be approved. If CR is greater than 10%, it will be necessary to return to the expert to check the answer.

Results and discussion

Vulnerability assessment indicators for Ho Chi Minh city agriculture

Exposure index is understood as a direct threat, including the nature and extent of changes in extremes of the region [27]. The National Target Program to Respond to Climate Change in Vietnam [15] has identified the impacts of climate change in areas that can be affected. In particular, the Southern delta (including Ho Chi Minh city) and the Mekong river are currently affected by the phenomena of saline water intrusion, flood, storm, and drought. According to the results of the expert consultations, it is believed that the agricultural sector in most severely damaged by the impacts of climate change. The weighted average of heavy rain exposure was 3.88, temperature rise was 3.50, and the flooding was 4.13. The expert was certain of his assessment with a weighted average of 2.38 points (Table 2).

Table 2. Score of the various climate change effects.

No	Climate change effects	Score	Certainty
1	Saline intrusion	3.63	2.38
2	Drought	3.50	2.38
3	Heavy rain	3.88	2.38
4	High temp.	3.50	2.38
5	Flooding	4.13	2.38
6	Sea level rise	2.38	2.38
7	Storm	1.96	2.38

Based on the climate change trend of Ho Chi Minh city and expert consultant results, this study selected 6 climatic indicators that often occur and affect agricultural production, high temperature, heavy rain, meteorological and hydrological drought, flood, and saline intrusion to determine exposure.

The sensitivity index describes human environmental conditions that can exacerbate the level of danger, improve hazards, or cause an impact [22, 24]. Researchers on climate change have pointed out the relationship between socio-economic factors, as well as infrastructure, that affect the impacts of climate change, such as income, poverty, and employment, among others [12, 16, 17]. Therefore, the study also classifies factors affecting climate change impacts into 3 economic, social, and infrastructure groups [36]. Based on the statistical yearbook and other vulnerability assessment studies, this study uses 12 indicators within the economic, social, and infrastructure groups to determine sensitivity.

Adaptative capacity index is the ability to implement adaptation measures that can prevent potential impacts [22, 24]. In order to assess resilience, this study had two focus directions: government support and citizen self-response [12]. This study used the following 4 indicators to assess resilience: awareness of urban climate change (flooding), experience of coping with flooding, heavy rain, and high temperature, government support, and accessibility to resources.

Table 3 presents all the CCVI for the agriculture in Ho Chi Minh city and their functional relationship with indicators.

Table 3. Climate change vulnerability assessment indicators for agriculture.

Indicator	Index	Sub_index	Description	Functional relationship with indicator
Exposure	High temperature	Trend of high temperature day	Day is over 35°C	+
	Heavy rain	Trend of heavy rain day	Rainfall day in 95 percentile	+
	Hydrological drought	Trend of hydrology drought	Drought day base on K/SDI index	+
	Meteorological drought	Trend of meteorology drought	Drought day base on SQI index	+
	Flood	Depth of flood	Depth of flood	+
	Saline intrusion	Salinity	Salinity	+
Sensitivity	Society	Worker in agriculture	Ratio per district	+
		Dependent inhabitant	Ratio per district	+
		Female	Ratio per district	+
		Poor household	Ratio per district	+
		Population density	Number people of km^2 per district	+
	Economy	Rice area	m^2 per district	+
		Plant area	m^2 per district	+
		Aquaculture area	m^2 per district	+
		Proportion of households with the main income from agriculture	Ratio per district	+
	Infrastructure	The rate of irrigation system is modernized	Ratio per district	-
		Road density is concreted	Ratio per district	-
		Rate of using electricity grid	Ratio per district	-
Adaptive capacity		Climate change awareness and urban flooding	Score per district	+
		Experience coping with floods, heavy rain, high temperatures	Score per district	+
		Government support	Score per district	+
		Access to support	Score per district	+

+: positive functional relationship; -: negative functional relationship.

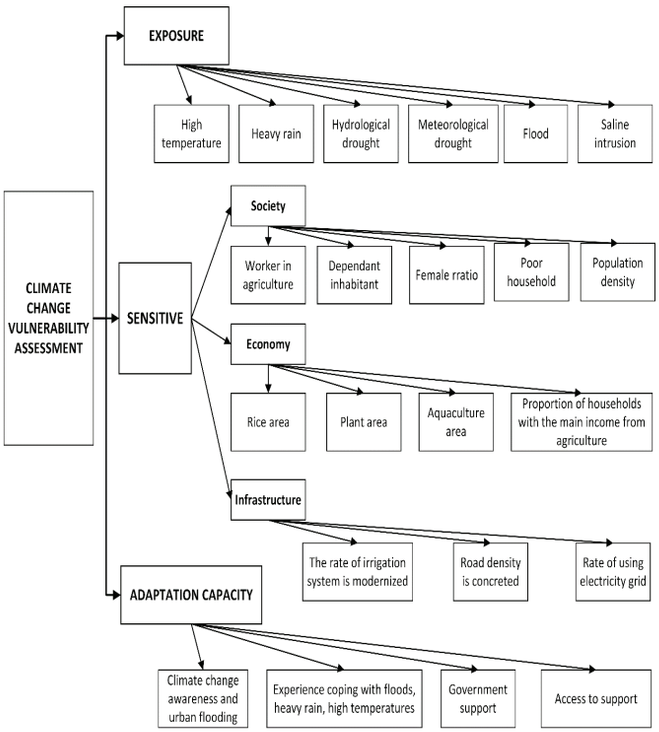

Fig. 3. Hierarchy structure of climate change vulnerability assessment.

Weighting by AHP

After building a comparison matrix pair with the main and secondary indices, the AHP algorithm calculates the weight for each of the abovementioned indicators as in Fig. 3. The result of the 9 questionnaires are synthesized and the consistency ratio is calculated for each table. The computed weights of the indicators with a consistency ratio less than 10% are presented in Tables 4 and 5.

Table 4. Weights for exposure indicators.

Exposure	Weight	
	In crop activities	*In aquaculture activities*
High temperature (E_1)	0.1532	0.1986
Heavy rain (E_2)	0.1149	0.1467
Meteorology drought (E_3)	0.1572	0.1436
Hydrology drought (E_4)	0.1668	0.145
Flood (E_5)	0.2210	0.1841
Saline intrusion (E_6)	0.1869	0.1819

Two sets of weights for exposure indicators that are formulated separately for Ho Chi Minh city's cultivation and aquaculture agricultural sectors. In particular, flooding was found to have the most impact on cultivation and hot weather had the greatest impact on aquaculture.

Table 5. Weights for sensitivity and adaptive capacity indicators.

Indicator	Index	Sub_index	Weight
	Society		***0.1794***
Sensitivity		Worker in agriculture	0.2118
		Dependent inhabitant	0.2167
		Female	0.1246
		Poor household	0.2898
		Population density	0.1571
	Economy		***0.3206***
		Rice area	0.3193
		Plant area	0.2151
		Aquaculture area	0.2131
		Proportion of households with the main income from agriculture	0.2525
	Infrastructure		***0.5000***
		The rate of irrigation system is modernized	0.3588
		Road density is concreted	0.3198
		Rate of using electricity grid	0.3214
Adaptive capacity		Climate change awareness and urban flooding	0.1833
		Experience coping with floods, heavy rain, high temperatures	0.3303
		Government support	0.2889
		Access to resources	0.1976

For Ho Chi Minh city's agriculture, the survey findings show that infrastructure investment on agriculture, including irrigation systems, power grids, and concrete roads, had the highest impact on vulnerability. Meanwhile, social factors also contributed to vulnerability but at a lower level.

Besides, weighting calculations also showed that experience with coping with floods, heavy rain, and high temperatures was the most important factor behind decreasing climate change vulnerability in agriculture.

After the E, S, and A indicators are defined, V is calculated by the formula as following:

$$V = \sum w_{Ei} \times E_i + \sum w_{Sn} \times S_n - \sum w_{Ae} \times A_e$$

where w: weight, i: number of E; n: number of S; e: number of A.

Then, the value of V will show Ho Chi Minh city's agricultural sector's vulnerability to climate change. The CCVI for agriculture is a method of vulnerability analysis through integrated aspects of a system.

Finally, the calculation results from the vulnerability index will be normalized from 0 to 1. The areas with avulnerability value near 1 are highly vulnerable to climate change and a value of V near zero indicates that the area is not vulnerable.

After the CCVI is calculated for each exposure, vulnerability can be assessed through synthesis or a separate analysis of each exposure for each specific area. From the set of vulnerability indicator assessments to climate change for agriculture, it is possible to establish thematic maps and digital data tables for managers and citizens to easily access.

Conclusions

There are many perspectives, concepts, and definitions of vulnerability, but on the basis of multiple perspectives and concepts, vulnerability is strongly dependent on exposure, sensitivity, and adaptive capacity. In particular, weights for each indicator were also established to assess the level of contribution to the overall system. By referring to prior literature on natural influences, socio-economic conditions, and climate change impacts on Ho Chi Minh city, the 22 vulnerability assessment indicators for Ho Chi Minh city's agriculture were established including 6 exposure, 12 sensitivity, and 4 adaptability indicators.

Applying CCVI to agriculture can make inhabitants and governments aware of vulnerability in Ho Chi Minh city's agricultural areas. With the CCVI, vulnerability assessment by index development is an effective method to convert qualitative factors into quantitative factors so that climate change impacts can be predicted in different scenarios. Additionally, CCVI and their weights are powerful tools for mapping vulnerable agricultural areas within the city. In this way, it will provide policymakers with a broad overview of the agriculture components affected and of possible adaptation options that should be taken.

ACKNOWLEDGEMENTS

This study is part of "Application GIS and modeling for climate change vulnerability assessment mapping in Ho Chi Minh city and proposing adaptation and mitigation plan to the period 2050" project under contract number 29/2017/HD-SKHCN with Institute for Computational Science and Technology. We want to send our sincere thank to Department of Science and Technology, Ho Chi Minh city and Insititute for Computational Science and Technology.

The authors declare that there is no conflict of interest regarding the publication of this article.

REFERENCES

[1] Asean Development Bank (2010), *Ho Chi Minh city Adaptation to Climate Change, Summary Report*, Mandaluyong city, Philippines.

[2] Natural conditions of Ho Chi Minh city (2011), Government Web Portal, accessed March 8, 2016, weblink http://tphcm.chinhphu.vn/dieu-kien-tu-nhien.

[3] VCAPS (2013), *Atlas Ho Chi Minh City Moving Toward the Sea,*

Adapting to Climate Change, Ho Chi Minh city (in Vietnamese).

[4] Department of Agriculture and Rural Development of Ho Chi Minh city (2015), *Report on the Results of Implementation of Direction and Administration of Agricultural Production and Rural Development in 2014 and Implementation of the 2015 Plan*, Ho Chi Minh city (in Vietnamese).

[5] DONRE (2010), *Climate Change Adaptation and Mitigation Action Plan Report,* Ho Chi Minh city (in Vietnamese).

[6] A. Dwyer, et al. (2004), *Quantifying Social Vulnerability: A Methodology for Identifying Those at Risk to Natural Hazards*, 92pp, Geoscience Australia Record. 14.

[7] P. Blaikie, et al. (2014), *At Risk: Natural Hazards, People's Vulnerability and Disasters*, 496pp, Routledge.

[8] S. Cutter, B. Boruff, W. Shirley (2003), "Social vulnerability to environmental hazards", *Social Science Quarterly*, **84(2)**, pp.242-261.

[9] P. Peduzzi, et al. (2009), "Assessing global exposure and vulnerability towards natural hazards: the disaster risk index", *Natural Hazards and Earth System Sciences*, **9(4)**, pp.1149-1159.

[10] S. Hughes, et al. (2012), "A framework to assess national level vulnerability from the perspective of food security: the case of coral reef fisheries", *Environmental Science & Policy*, **23**, pp.95-108.

[11] M. Ulrichs, et al. (2015), "Climate change & food security vulnerability assessment. Toolkit for assessing community-level potential for adaptation to climate change", *CCAFS Working Paper No.108*, Copenhagen, Denmark: CGIAR Research Program on Climate Change, Agriculture and Food Security (CCAFS).

[12] W.N. Adger, P.M. Kelly, Huu Ninh Nguyen (2012), *Living with Environmental Change: Social Vulnerability, Adaptation and Resilience in Vietnam*, 359pp, Routledge.

[13] United Nation (1992), *United Nations Framework Convention on Climate Change*.

[14] Ernest Nti Acheampong, Nicholas Ozor, Eric Sarpong Owusu (2014), "Vulnerability assessment of Northern Ghana to climate variability", *Climatic Change*, **126**, pp.31-44.

[15] Ngo Thi Van Anh, Nguyen Thanh Tuong, Le Ha Phuong (2013), "Assessing vulnerability to climate change of Can Tho city", *The 17th National Scientific Conference on Meteorology, Hydrology, Environment and Climate Change* (in Vietnamese).

[16] Tran Vinh Quang (2016), *Determining the Flood Vulnerability Assessment Indicators in Dak Rong District, Quang Tri Province*, Department of Meteorology, Hydrology and Oceanography, University of Science, VNU, Hanoi (in Vietnamese).

[17] T.E. Downing, et al. (2001), *Vulnerability Indices, Climate Change Impacts and Adaptation*, Nairobi, UNEP Division of Policy Development and Law.

[18] M.M. Friggens, et al. (2013), *Review and Recommendations for Climate Change Vulnerability Assessment Approaches with Examples from the Southwest*, U.S., 106pp, Department of Agriculture, Forest Service, Rocky Mountain Research Station.

[19] S.F. Balica, Nigel George Wright, Frank van der Meulen (2012), "A flood vulnerability index for coastal cities and its use in assessing climate change impacts", *Natural Hazards and Earth System Sciences*, **64(1)**, pp.73-105.

[20] Mai Trong Nhuan, et al. (2014), "An integrated and quantitative vulnerability assessment for proactive hazard response and sustainability: a case study on the Chan May-Lang Co Gulf area, Central Vietnam", *Sustainability Science*, **9(3)**, pp.399-409.

[21] UNESCO-IHE (2019), *Flood Vulnerability Factors*, cited date 5/11/2019, weblink http://unihefvi.free.fr/flood_vulnerability_factors.php.

[22] Can Thu Van, et al. (2014), "Developing flood vulnerability index using decentralized system analysis (AHP) - testing for several commune units in Quang Nam province in the lower basin of Thu Bon river", *Vietnam Meteorological and Hydrological Administration*, pp.10-18 (in Vietnamese).

[23] Can Thu Van and Nguyen Thanh Son (2015), "Developing a weighting method to determine flood vulnerability index of the Vu Gia - Thu Bon river basin", *VNU Journal of Science: Natural Science and Technology*, **31(1S)**, pp.93-102 (in Vietnamese).

[24] S. Tao, et al. (2011), "Research progress in agricultural vulnerability to climate change", *Advances in Climate Change Research*, **2(4)**, pp.203-210.

[25] N. Downes, et al. (2010), "Urban sustainability in times of changing climate: the case of Ho Chi Minh city, Vietnam", *46th ISOCARP Congress 2010*.

[26] Le Quang Dinh, Le Van Thang, Nguyen Huy Anh (2012), "Application of GIS for mapping the vulnerability of NBD for rice land in the coastal strip of Phu Yen province", *Hue University Journal of Science*, **5(8)**, pp.17-24.

[27] Glwadys A. Gbetibouo, Claudia Ringler, Rashid Hassan (2010), "Vulnerability of the South African farming sector to climate change and variability: an indicator approach", *Natural Resources Forum*, **34(3)**, pp.175-187.

[28] Bertil Forsber, et al. (2012), "An expert assessment on climate change and health - with a European focus on lungs and allergies", *Environmental Health*, **11(1)**, p.S4.

[29] Vitor Baccarin Zanetti, Wilson Cabral de Sousa Junior, Débora M. De Freitas (2016), "A climate change vulnerability index and case study in a Brazilian coastal city", *Sustainability Science*, **8(8)**, Doi: 10.3390/su8080811.

[30] B.K. Sovacool, et al. (2012), "Expert views of climate change adaptation in least developed Asia", *Journal of Environmental Management*, **97**, pp.78-88.

[31] Anna Alberini, Aline Chiabai, Lucija Muehlenbachs (2006), "Using expert judgment to assess adaptive capacity to climate change: evidence from a conjoint choice survey", *Global Environmental Change*, **16(2)**, pp.123-144.

[32] A. Hirpa, et al. (2010), "Analysis of seed potato systems in Ethiopia", *American Journal of Potato Research*, **87(6)**, pp.537-552.

[33] P.T.A. Ngoc, et al. (2016), "Economic feasibility of recirculating aquaculture systems in pangasius farming", *Aquaculture Economics & Management*, **20(2)**, pp.185-200.

[34] G. Rowe and G. Wright (1999), "The Delphi technique as a forecasting tool: issues and analysis", *International Journal of Forecasting*, **15(4)**, pp.353-375.

[35] T.L. Saaty (1988), "What is the analytic hierarchy process? Mathematical models for decision support", *Mathematical Models for Decision Support*, pp.109-121.

[36] T.L. Saaty (1994), "How to make a decision: the analytic hierarchy process", *Interfaces*, **24(6)**, pp.19-43.

Vietnam Journal of Science, Technology and Engineering (VJSTE): Manuscript Template

General Instructions on using this template and submitting a manuscript to VJSTE: Thank you for preparing a manuscript for submission to VJSTE. Using this template, or following the guidelines below, will help us in processing your paper. Our goal is to be able to identify each section of your manuscript so that we can accurately record the title, authors, abstract, etc. and also be able to enrich it by including reference links and an accurate layout.

You can submit your paper at http://vietnamscience.vn

So that we can identify the parts of your paper, and even if you do not use our template, please begin each section with the specific key words listed below. Please do not use paragraph breaks in the title, author list, or abstract.

Title

Authors

Affiliations

Abstract

One Sentence Summary

Main Text

Acknowledgements

References

Several of these headings are optional, for example, not all papers will include a one-sentence summary, figures or tables.

Please use the .docx format (all version after Word 2007).

More specific formatting instructions are provided in the actual template, which follows.

Title: How to Format a Science Paper (replace with your real title)

Authors: The author list should be one single paragraph (no breaks). Authors should be listed by first name or initial followed by last name and separated by commas. Use superscript numbers to link affiliations, and symbols *†‡ for author notes. For example, X. Jones[1]*, P. Smith[1,2]

Affiliations:

[1]Affiliations should be preceded by superscript numbers corresponding to the author list, and each affiliation should end with a period.

[2]Each affiliation should be a separate paragraph.

*Correspondence to: include the email addresses or telephone number of the corresponding author(s). Please use the asterisk (*) symbol for the corresponding author information.

Abstract: The abstract should be about 100-150 words, and organized in this structure: An opening sentence that sets the question that you address and is comprehensible to the general reader, background content specific to this study, results, and a concluding sentence. It should be one paragraph only.

One Sentence Summary: A brief summary of the main result of your paper, without excessive jargon and less than 150 characters.

Main Text: In general, this should include a brief (1-2 paragraph) introduction, followed by a statement of the specific scope of the study, followed by results and then interpretations. Please avoid statements of future work or claims of priority, and avoid repeating the conclusions at the end.

All of the Figures and Tables should be cited in order (which should be cited as, for example, figure S1, and table S1). You can include page breaks if you would like to place the figures within the text.

Subheads: These can be included in Research Articles or Reviews and should be brief.

Equations can be included. We do not recommend using the native Word 2007, 2008, 2010 or 2011 equation editor. This can in some cases produce less reliable MathML, the online markup language we use, which may result in display errors. Instead, use the legacy equation editor in word (Insert menu; select insert object; select word equation) or use Mathtype (recommended). If you enter equations in simple LaTeX, check that they will convert accurately (Word 2007 and higher can convert simple LaTeX equations).

Fig. #: (Begin each figure caption with a label, "**Fig. 1.**" for example, as a new paragraph.).

Fig. 1. The figure caption should begin with an overall descriptive statement of the figure followed by additional text. They should be immediately after each figure. Figure parts are indicated with capital letters (**A**). If you prefer, you can place both the actual figures and captions logically through the text near where they are cited rather than at the end of the file (but not both). If a paragraph in the main text begins with the name of a figure, write out "Figure" in full (e.g., <para>"Figure 1 shows….").

Fig. 2. You can place graphics above each equation as part of this file.

Table #: (Begin each table caption with a label "**Table 1.**", etc.) as a new paragraph.

Table 1. Start this caption with a short description of your table. Format tables using the Word Table commands and structures. Do not create tables using spaces or tabs characters.

Acknowledgments: The acknowledgments should include a statement about where the data reported in the paper are presented, archived, or available. If in an archive, include the accession number or a placeholder for it. Please also include relevant funding information such as grant numbers and funding agencies. You can also include a statement of author contributions here. The acknowledgements can be multiple paragraphs.

References:

References should be cited in bracket with a number [1]. Multiple reference citations are separated by commas [2, 3] or if a series, dashes [4-6].

References are listed in numerical order, and in the same order in which they are cited in text. The reference list should include all and only those references you have cited in the text. The reference list appears at the end of the paper.

Please include the above heading "References".

Please do not mix in references with explanatory notes.

The reference consist of: Family name(s) and initials of all authors (year of publication), "Titles of journal articles" (optional), *Title of journal, book or other publication*, **volume(number)**, page numbers.

Example of a reference list:

[1] T. Binzoni, T.S. Leung, D. Boggett, D.T. Delpy (2002), "A new near infrared laser-Doppler flowmeter for deep tissue perfusion monitoring", *MAGMA*, **14,** pp.74-75.

[2] T. Binzoni, T.S. Leung, D. Boggett, D.T. Delpy (2003), "Non-invasive laser Doppler perfusion measurements of large tissue volumes and human skeletal muscle blood RMS velocity", *Phys. Med. Biol.*, **48(1)**, pp.2527-2549.

ISSN 2525-2461

Vietnam Journal of Science, Technology and Engineering

MARCH 2020 • VOL.62 NUMBER 1

EDITORIAL OFFICE

113 Tran Duy Hung Str., Cau Giay Dist., Hanoi
Tel: (84.24) 39436793; Fax: (84.24) 39436794
Email: khcnvn@most.gov.vn
Website: vietnamscience.vn

PUBLICATION LICENCE

No.1153/GP-BTTTT 26th July 2011
No.2528/GP-BTTTT 26th December 2012
No.592/GP-BTTTT 28th December 2016